Dynamic Modelling of Floating Wind Turbines

Jiayao Meng

Supervisor: Prof. Manolis Chatzis
Prof. Wouter Mostert

Department of Engineering Science
University of Oxford

This dissertation is submitted for the degree of
Doctor of Philosophy

Wolfson College
March 2025

I would like to dedicate this thesis to my beloved family

— *my grandparents, parents and Luoluo*.

Acknowledgements

I would like to express my sincere gratitude to my supervisors, Prof. Manolis Chatzis and Prof. Wouter Mostert, for their invaluable guidance and support throughout the course of my research. Special thanks to Manolis for his generous time commitment and all those stimulating discussions. His expertise and instincts in advanced dynamics and beyond, along with his meticulous attention to detail and clarity in theories, have deeply influenced me and set a high standard for my future endeavors. I am equally grateful to Wouter for his continuous insights in fluid mechanics and mathematics, which were critical for the successful completion of this work. I also want to thank both of them for their encouragement during this challenging academic journey, and for celebrating my every achievement. My thanks also go to Prof. Ross McAdam for his guidance during the first years of my study before he moved to industry.

I am deeply grateful to my friends in Oxford and back home. Many thanks to Yujiao, my best friend in Oxford, for always being there to share every happy moment and ease all the tough ones; to my best cooking buddy, Qian; my meme team buddies, Jorge and Harry; my sanity checkers, Chenying, Jingyi, and Misha; my best desk buddies, Markella and Jane; my lovely tennis buddy, Rui; my funny buddy, Zhengyou; my late-night working companion in Room 11, Xiongfeng; and a special mention to Port Meadow for never failing to lift my spirits — this journey would not have been as fun and memorable without you all. Shout out to my friends at home for more than ten years of friendship: Luyao, Yu, and Hanjing.

Finally, I would like to thank my beloved family and extended family of aunts and uncles. Heartfelt gratitude to my parents for their endless love, encouragement, and belief in me, which have been my constant source of strength and inspiration. They spent almost all their savings to fund my PhD — I only recently realized how brave they were. A special dedication to my late grandfather, my Gandalf, for always being proud of me.

Abstract

Floating Wind Turbines (FWTs) offer a promising solution to harnessing substantial offshore wind energy in deep waters. However, accurately modelling their complex dynamics is challenging due to the complex coupling between aerodynamics, hydrodynamics, structural elasticity, and controls. This thesis proposes an integrated FWT simulation framework in Simulink to investigate these dynamics, with a particular focus on nonlinear wave-platform interactions induced by large platform motions.

A comprehensive FWT model is developed in Simulink, featuring efficient state-space representations for linear wave radiation and excitation effects, a multibody formulation to account for large geometrically nonlinear blade deformations, a modified blade-element momentum method for unsteady aerodynamics, and a multi-loop ROSCO control strategy for power regulation and platform stabilization. Validation against the widely-used OpenFAST simulation tool demonstrates the ability of the developed Simulink model to capture the dominant FWT dynamic couplings under realistic environmental conditions.

To address the limitations of the conventional linear hydrodynamic model, which assumes small platform motion around the equilibrium position, an analytical solution to the 2D linear wave-platform boundary value problem (BVP) linearized at an arbitrary platform pose is proposed. The analytical method is compared against a numerical boundary element method, and the influence of platform pose on the hydrodynamic behaviour is investigated.

Additionally, a novel linear parameter varying (LPV) modelling framework is developed to capture the geometrically nonlinear wave radiation effect. The LPV system is constructed using state-space models identified from the BVPs linearized at various platform positions, with the instantaneous platform pose used to interpolate the state-space matrices. To ensure state-basis coherency across all linear models, a black-box method based on the balanced realization and a gray-box method that ties the state vector to physical parameters are proposed. Both LPV models are validated on the benchmark van Daalen floating cylinder, and they are then integrated into the Simulink FWT model. Results indicate that the LPV models effectively capture nonlinear hydrodynamic effects and offer significant computational efficiency, making them practical for early-stage FWT design and optimization.

Table of contents

List of figures

List of tables

Chapter 1

Introduction

1.1 Floating wind turbines (FWT)

The Paris Climate Change Agreement aims to limit global temperature rise to 1.5°C and achieve net-zero CO_2 emissions by 2050 [57]. Meeting this goal requires a substantial increase in global renewable electricity generation. Offshore wind energy presents a significant potential due to its high energy output from strong and consistent winds at sea, proximity to densely populated coastal areas, scalability to gigawatt (GW) levels, and relatively low social and environmental impact [58]. Currently, offshore wind contributes 75.2 GW energy production, accounting for just 7.1% of the global wind capacity; this share is expected to grow to 40% by 2050 [46].

Most existing offshore wind projects are located in waters less than 60 m deep within 60 km from the coast [58]. However, enormous wind resources, with an estimated capacity exceeding 13 terawatts (TW), are available in deeper waters farther from shore, where the deployment of bottom-fixed wind turbines is not economically viable. Floating wind turbines (FWTs) offer a promising solution for these deep water regions. For example, the Hywind Tampen project, the world's largest floating wind farm to date, became fully operational with a power generation capacity of 88 megawatt (MW) in August 2023 [32]. This floating wind farm is located 140 km offshore at water depths between 260 m and 300 m.

As a relatively new technology with only around 270 MW of operational capacity as of 2023, floating wind is not as cost-competitive as the established bottom-fixed wind technology. The average levelized cost of energy (LCoE) for floating wind in 2030 is projected to be around three times higher than that of bottom-fixed offshore wind, i.e., \$300/MWh vs. \$110/MWh. In contrast, land-based wind is expected to have an average LCoE of just \$42/MWh by 2030 [28]. To accelerate the expansion of the floating wind industry, it is crucial to achieve significant cost reduction. By 2050, the global average LCoE for floating wind is forecasted to drop to around \$95/MWh, though this will vary depending on regions and projects [28]. One key driver for this cost reduction is the deployment of larger turbines.

A FWT is a complex mechanical system comprising several key components: a rotor and nacelle assembly (RNA) that converts wind energy to electricity, a tower that holds the RNA at a height with high wind potential, a floating platform that supports the superstructure, and a station-keeping system that includes mooring lines, connectors, and anchors to constrain platform motions. Various FWT concepts have been developed using different stabilizing methods, including spar, barge, semi-submersible, and tension-leg platform (TLP) designs, as illustrated in Fig. 1.1.

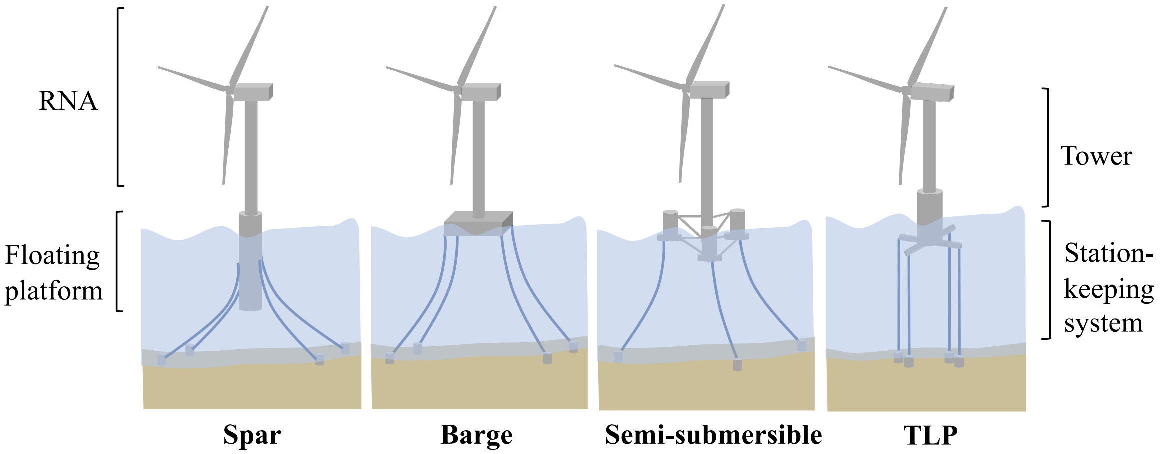

Fig. 1.1 Popular floating wind turbine concepts.

The IEC's most recent technical specification outlines comprehensive design requirements for FWTs to ensure structural integrity and serviceability. These requirements include the evaluation of multiple loads, such as gravitational and inertial loads, aerodynamic loads, hydrodynamic loads, mooring loads, and ice loads (where applicable) [56]. Additionally, factors such as aero-elastic and hydro-elastic interactions, control system behaviour, and the interaction between mooring lines, anchors, and the seabed must also be considered when necessary [56, 25, 26, 2]. These complex effects pose significant challenges in accurately predicting the dynamic behaviour of FWTs, often leading to unreliable or overly conservative FWT designs. Without a thorough understanding of the complex interactions within FWTs and their surrounding environment, the industry's progress toward larger turbines, which is essential for cost reduction, will be severely hindered.

1.2 Complex dynamics of FWTs

Acting as the base excitation for the superstructure and the top excitation for the station-keeping system, the dynamic behaviour of the floating platform predominantly determines the overall performance of the FWT system. While the relatively mature technologies from the offshore oil and gas industry can be leveraged to enhance the understanding of wave effects on FWT platforms, notable differences exist. Under most sea conditions, established theories based on linear assumptions of small wave amplitudes and small platform movements have proven effective in capturing the leading-order factors of hydrodynamic loads on floating platforms [97]. In extreme sea states, where the wave steepness (i.e., wave amplitude relative to wave length) becomes larger, nonlinear wave kinematics and wave-wave interactions are of significant importance [142]. In such cases, the established second-order hydrodynamics theory can be adopted for more accurate wave load evaluation than linear hydrodynamics. However, unlike oil and gas platforms, FWT platforms experience additional complexities due to the presence of the superstructure. The large aerodynamic forces acting on the hub height can lead to large platform rotations and displacements, resulting in complex **nonlinear wave-structure interaction** that can significantly influence the dynamic behaviour of the entire FWT system [4, 76].

The potentially large 3D movements of the floating platform also produce multiple novel challenges in understanding FWT physics compared to the more mature bottom-fixed wind turbines. Firstly, the large translational and rotational motions of the floating platform give rise to strong interactions between the rotor and its wake, leading to **unsteady aerodynamic effects** and drastic fluctuations in the power output [45]. Under the extreme situation when the platform moves downwind with a high velocity, the possible negative relative wind velocity on the rotor can even turn the turbine into a propeller, which outputs energy to the flow field [12]. To gain more insights into the unsteady aerodynamics induced by platform motions, researchers have conducted numerical [45, 12, 80, 41, 13, 18] and experimental [40, 9] studies. However, the aforementioned works mainly focus on the aerodynamic effect itself and simplify the overall FWT dynamics by prescribing harmonic platform motions in specific degrees of freedom (DoF), such as surge [80, 9], pitch [12, 41, 9], combined surge-pitch [45, 18], roll [40] or yaw [13].

The interaction between aerodynamics and control systems becomes particularly critical under the above-rated operating conditions for FWTs. As the platform undergoes large motions, especially rotational movements, it introduces an additional wind velocity component felt by the rotor. When the platform rotates in a downwind direction, the relative wind speed experienced by the rotor decreases, resulting in a lower blade pitch command and consequently higher aerodynamic thrust, which further accelerates the downwind motion, and vice versa. This adverse coupling effect brings about **negative damping**, which can destabilize the platform's response [129]. Meng et al. [88] conducted a 1:60-scale model test of the DTU 10-MW FWT and observed unstable platform pitch responses at above-rated wind speeds. To address the instability issue, two control strategies are commonly employed: (1) detuning the blade-pitch control gain to reduce the controller bandwidth below the platform pitch natural frequency [62], or (2) introducing an additional feedback loop to counteract the effect of platform motions on the controller. However, the first approach causes too slow control response to wind disturbances and potentially large generator speed excursions [88], while the second approach involves multiple control loops which further complicate the dynamics of the FWT system [119, 118]. Their effects should be investigated carefully with all other FWT dynamic domains.

Another significant challenge for FWTs analysis lies in the geometric and kinematic nonlinearities associated with **highly flexible blades** undergoing large deformations and overall rigid-body motions of the blade rotation and platform movement [124]. These nonlinear effects become more important for increasingly longer and slender blades [75]. An out-of-plane blade-tip deflection of 10% of the blade length (61.5 m) has been reported in [80] for a standard NREL 5-MW FWT operating at the rated wind speed. In contrast, for an up-to-date IEA 15-MW FWT with a much longer blade length of 117 m, the blade-tip deflection can reach 16% of the blade length at the rated operating condition [144]. While both works successfully capture the nonlinear blade dynamics, they again simplify the overall system by prescribing sinusoidal platform motions, without considering the complex interactions between wave-induced platform motions and the aerodynamic forces on the blades.

In addition to the aforementioned FWT physics, other factors such as the geometric nonlinearity of highly compliant mooring lines and anchor-soil interactions further complicate the overall FWT dynamics. To gain deeper insights into these complex couplings, researchers have conducted in-situ observations [15, 105, 59], scale model tests [135, 132], and hybrid experimental studies [39]. Alongside these field and experimental studies, there is a growing demand for advanced simulation tools capable of performing fully coupled aero-hydro-elastic-control dynamic analyses, which are essential for the reliable and cost-effective design and optimization of FWT systems.

1.3 Popular simulation tools for FWTs

Several popular simulation tools are available for fully coupled dynamic analysis of FWTs, e.g., OpenFAST [101], Bladed [10], and HAWC2 [50].

OpenFAST [101], previously known as FAST, is a nonlinear aero-hydro-elastic-control wind turbine simulation framework developed by the National Renewable Energy Laboratory (NREL). It is widely used for the time-domain dynamic analysis of FWTs and is one of the very few open-source simulation tools available. OpenFAST provides multiple options of modelling fidelity through a number of subroutine packages, as illustrated in Fig. 1.2. A typical FWT simulation routine in OpenFAST involves the following core modules: HydroDyn that determines the hydrodynamic loads, AeroDyn that calculates aerodynamic loads, ElastoDyn/BeamDyn/SubDyn that describes the multi-rigid-body dynamics and structural elasticity, ServoDyn that defines the blade-pitch and generator-torque controllers, and MAP++/MoorDyn/FEAM that models moorings' behaviour. Each module captures important FWT physics and is discussed in more detail as follows.

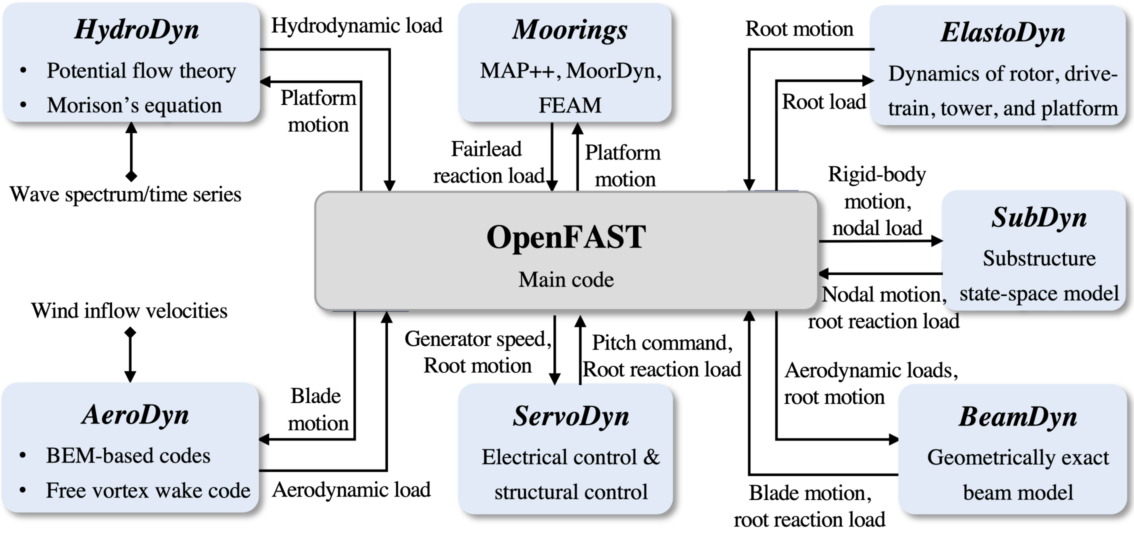

Fig. 1.2 Schematic of OpenFAST simulation framework.

- ***Hydrodynamics.*** **HydroDyn** combines potential flow theory and Morison's Equation to compute the hydrodynamic forces acting on the floating platform. In the potential flow theory, the wave-platform boundary value problem (BVP) is typically solved using numerical boundary element methods, such as WAMIT [131], in the frequency domain. This approach involves up to a second-order perturbation expansion around the mean free surface and a first-order perturbation around the mean wetted body surface, corresponding to the platform's static equilibrium position. The frequency-domain hydrodynamic coefficients (e.g., added mass, radiation damping, linear and quadratic wave excitation force transfer functions) obtained from these computations are then transformed into corresponding time-domain representations [110]. Given the platform kinematics, the hydrodynamic forces can be calculated at each time step for the FWT dynamic simulation, as shown in Fig. 1.2. This method offers a reasonable assessment of the wave-platform interaction when the platform movements are small relative to its characteristic length and the wave steepness remains below the breaking limit. Morison's Equation, on the other hand, is used to estimate the inertial and viscous drag forces on slender structural elements (e.g., columns or braces) within the floating platform. The accuracy of Morison's Equation largely depends on selecting appropriate inertia and drag coefficients, which are typically derived from experimental data or high-fidelity Computational Fluid Dynamics (CFD) simulations.

- ***Aerodynamics***. The **AeroDyn** package provides two methods to determine the aerodynamic loads on the rotor blades: the blade-element momentum (BEM) method and the free vortex wake method. In the BEM method, the aerodynamic forces are computed based on a quasi-steady representation of the wake around the rotor blades. This method is further enhanced by considering the skewed wake, dynamic inflow and dynamic stall effects, induced by the change of inflow and/or operating condition [64]. In contrast, the free vortex wake method uses lifting lines to represent the blades, which can capture the detailed structure and deformation of the wake vortices with higher fidelity but at an increased computational cost [115]. Prior to the aerodynamic load calculation in AeroDyn, the pre-processing tool TurbSim is used to generate a 3D turbulent wind field, and InflowWind is used to compute the local undisturbed wind velocities at each blade element [101]. With the undisturbed wind velocities and blade velocities inputs, the aerodynamic loads on the rotor blades can be computed for the FWT dynamic analysis, as shown in Fig. 1.2.

- ***Structural modelling***. The structure-related dynamics in OpenFAST are handled by three packages: ElastoDyn, BeamDyn, and SubDyn, as illustrated in Fig. 1.2. **ElastoDyn** evaluates the dynamics of the multibody system, including blades, tower, floating platform, and drivetrain. For blades and tower, a truncated modal representation is used, which includes two flapwise and one edgewise bending modes for each blade, and two fore-aft and two side-to-side bending modes for the tower. The mode shapes can be generated using a generic beam finite-element model (FEM) in the pre-processing step. The floating platform is represented as a rigid body with 6 DoFs, while the drivetrain is simplified as a single-DoF linear spring-damper system. ElastoDyn assumes the blades to be straight and isotropic, and only permits small deflections dominated by bending DoFs. **BeamDyn** [133] extends ElastoDyn's capabilities by replacing the simplified blade model with a geometrically exact beam model. This allows BeamDyn to capture full geometric nonlinearities and large deflections of blades, incorporating bending, torsion, shear, and axial extension DoFs. As a result, BeamDyn is more suitable for modelling FWTs with long slender blades, which can experience large deflections due to high wind thrust and large platform rotations. **SubDyn** [101] further enhances the structural modelling capability by allowing for platform flexibility using a finite-beam-element formulation. The modal reduction method is applied to reduce computational complexity. SubDyn is coupled with HydroDyn by passing the platform's nodal kinematics to HydroDyn, where hydrodynamic loads are calculated using Morison's Equation. These loads are then fed back to SubDyn to update platform dynamics at each time step. Additionally, SubDyn uses a rotating reference frame that follows the rigid-body motion of the floating platform obtained from ElastoDyn. The reaction forces calculated in SubDyn are transferred back to ElastoDyn at the interface nodes, ensuring an accurate description of the interface force under large platform movements.

- ***Controls***. The **ServoDyn** module enables the implementation of both electrical and structural control strategies. Electrical control includes blade pitch control and generator torque control, which can be defined internally within ServoDyn or externally through a user-defined dynamic link library (DLL). Specifically, an additional floating feedback loop is introduced to the blade pitch control to overcome the negative damping issue. Structural control, such as tuned mass dampers and tuned liquid column dampers, can be optionally installed at the nacelle, tower, blades, or platform to mitigate excessive vibrations and enhance system stability.

- ***Moorings***. Three different packages can be coupled to OpenFAST to simulate the mooring system, as shown in Figure 1.2. **MAP++** [83] uses a quasi-static model based on classic catenary theory to rapidly compute the mooring line response, accounting for weight, buoyancy, axial extension, and seabed friction represented by a constant friction coefficient. **MoorDyn** [47, 48] employs a lumped-mass approach to capture the inertia of mooring cables and represents seabed contact using vertical springs and dampers. **FEAM** [5] adopts a finite-rod-element formulation to represent the mooring lines and calculates inertia and drag forces at each element. It models the elastic foundation as a continuous quadratic spring but neglects horizontal friction between the moorings and the seabed. Additionally, OpenFAST can be integrated with the commercial code OrcaFlex [102] for more advanced mooring and seabed interaction modelling.

Other tools integrating offshore structure analysis programs with OpenFAST, such as TimeFloat-FAST [14], Charm3D-FAST [6], F2A (FAST-AQWA) [136], employ similar hydrodynamic analysis methods as those used in OpenFAST HydroDyn, and therefore are not introduced in detail.

Several commercial simulation tools are also widely used for FWT modelling. Bladed [10], developed by DNV GL, can be integrated with the hydrodynamic analysis tool, Sima (Simo and Riflex) [27], to perform fully coupled nonlinear dynamic analysis for FWTs. **Bladed-Sima**'s modelling approaches to hydrodynamics, aerodynamics, controls, and tower elasticity are similar to the methodologies used in OpenFAST. The primary difference between the two lies in blade modelling. Bladed implements a multibody framework by segmenting the blades into multiple substructures, each represented by linear Timoshenko beam elements. This formulation enables Bladed to effectively capture geometric nonlinearities due to large blade deflections. Another FWT simulation tool, **HAWC2** [50], developed by DTU, follows a similar approach but extends the multibody formulation to include both blades and the tower structure, enabling more accurate structural modelling of FWTs.

1.4 Toward enhanced FWT modelling: fidelity, affordability and adaptability

Most of the complex FWT physics discussed in Section 1.2, such as unsteady aerodynamics induced by large platform motions, interactions between the blade-pitch controller and platform dynamics, and nonlinear behaviour of highly flexible rotating blades, can be reasonably captured using the popular FWT simulation tools described in Section 1.3. However, these tools rely on linear potential flow theory for the hydrodynamic calculation, which only accounts for linear wave-platform interactions under the assumption of small platform displacements and rotations around the equilibrium position. Under extreme environmental conditions, when the platform experiences large movements, this linearization assumption breaks down, and the dynamic behaviour of the FWT system can potentially be significantly influenced by the time-varying wetted body surface [111]. According to Feng [36], when the oscillating amplitude of a floating platform exceeds a certain threshold, nonlinear effects dominate the platform responses, leading to inaccurate predictions when using linearized models. Li and Bachynski [76] observed a 17% reduction in the vertical wave diffraction force on the 5-MW OC6 semi-submersible FWT when the platform is fixed at a 5° inclination in the wind action plane. These observations highlight the importance of incorporating geometrically nonlinear wave-platform interactions for accurate hydrodynamic analysis of FWTs [29].

Researchers have adopted high-fidelity approaches, e.g. fully-nonlinear potential flow theory [141], smoothed particle hydrodynamics [69, 123], and CFD [19, 79, 122], to accurately capture the instantaneous pressure distribution over the FWT platform surface and determine the nonlinear wave-structure interaction effects. Nematbakhsh et al. [94] developed a CFD model of a 5-MW spar-type FWT and analyzed its dynamic behaviour under moderate and severe sea states. The CFD model is found to successfully capture large platform pitch motions of up to 10° and complex nonlinear effects such as complete platform submergence and tether slacking under extreme conditions. These phenomena are not likely to be accurately predicted by simulation tools relying on linear hydrodynamics assumptions, such as OpenFAST.

Despite the accuracy of high-fidelity models, they come with enormous computational costs. Incorporating aerodynamics and structural flexibility in a CFD model further increases computational demands [125, 124]. For instance, a 1-hour CFD-FEM simulation for a FWT can require up to 3×10^4 core hours [43]. Given the time and resource constraints, high-fidelity models are more suitable for the final verification phase of a new FWT design concept, while the conventional linear method is recommended for the preliminary design phase, where thousands of simulations are typically required [20, 26]. However, the limitations of the linear method in describing the wave-platform interaction may lead to the selection of design candidates that are later found suboptimal [121]. To avoid costly design changes in the final stages, it is essential to use reliable nonlinear models that can capture the dominant FWT hydrodynamics at an affordable computational cost during early design phases [42].

Additionally, a simulation tool that can accommodate different modelling fidelities for each physical domain of FWTs is particularly useful for dynamic analysis and early design optimization. The popular simulation tools described in Section 1.3 are developed based on Procedural-Oriented Programming (POP) languages, e.g. Fortran used by OpenFAST, which follow a certain cause-and-effect sequence. When a set of new modelling assumptions is to be implemented, the developer has to manually re-derive the kinematics and conservation equations. In contrast, Object-Oriented Programming (OOP) languages represent models as objects based on their real-world connectivity, and enable developers to easily create new codes/modules by inheriting and modifying the existing ones. Several researchers [73, 30, 148, 31] have investigated FWT modelling using an open-source OOP environment, Modelica, and demonstrated its easy development and modification characteristics. However, Modelica is mainly designed for physical system modelling. When additional simulation objectives are desired, e.g., the two-way coupling with AeroDyn [31], control co-design [1, 99] or cost-effective design optimization [74], etc., a Functional Mock-Up Interface (FMI) is required to exchange information between OOP-based (physical system) and POP-based (aerodynamics, control, optimization, etc.) models.

Simulink offers a more integrated simulation environment for FWTs by supporting direct interaction between OOP-based physical system modelling through Simscape, and POP-based simulation with the help of extensive Simulink blocks/libraries/apps. In addition, Matlab/Simulink is well-equipped with a large number of control, optimization, identification, and signal processing toolboxes, to name a few, which cover almost every aspect of standard FWT analysis, from pre-processing to post-processing. Furthermore, S-Functions are used as the FMI in Simulink, which can interface with external tools to further extend the modelling capability. Most of the existing works on the FWT modelling via Simulink are POP-based, mainly for data processing and control modelling [93, 20, 134]. An exception is an in-house FWT simulation tool, MOST developed by Sirigu et al. [116], which utilizes Simscape Multibody for the FWT dynamic analysis. However, the simplifications of rigid blades/tower and aerodynamic calculations based on look-up tables greatly limit its modelling capability.

1.5 Overview

The objective of this thesis is to develop an integrated simulation framework in Simulink for the dynamic analysis of FWTs, with a particular emphasis on evaluating nonlinear wave-platform interactions caused by large platform motions. The developed FWT simulation tool aims to balance fidelity, affordability, and adaptability, ensuring that the dominant system dynamics are accurately captured with realistic computational expenses. Using this newly developed tool, complex interactions between various physical domains, including aerodynamics, hydrodynamics, control system, and structural dynamics, will be explored to provide deeper insights into the nonlinear behaviours of FWTs.

The content of this thesis is organized into three main chapters. **Chapter 2** details the development of an integrated FWT simulation tool, incorporating well-established modelling methodologies for linear hydrodynamics, aerodynamics, structural elasticity and controls, with innovative implementations of them in the Simulink environment. The wave-platform interaction is calculated using linear potential flow theory, with the wave radiation and excitation effects represented by state-space models that are directly estimated from multi-input multi-output hydrodynamic coefficients in the frequency domain. The unsteady aerodynamics are determined through the classical blade-element momentum method enhanced with dynamic inflow and stall models. An industry-standard control strategy is implemented to regulate the power generation and stabilize the FWT system via an additional floating feedback loop. The structural dynamics are handled in Simulink/Simscape, where the hub, nacelle and platform are modelled as separate rigid bodies; the blade and tower are represented as a series of either rigid or deformable Euler-Bernoulli beams following the multibody formulation; and the drivetrain is modelled using a three-stage compound gear system. As the mooring response is not within the scope of this work, its effects are simplified as linear stiffness and damping matrices. This Simulink model is used to systematically investigate dominant FWT dynamic coupling effects, with a comparison against OpenFAST on the example NREL 5-MW ITI-Barge FWT highlighting the strengths and limitations of the proposed modelling approaches.

Chapter 3 aims to lay the foundation for the geometric nonlinear analysis of FWT hydrodynamics that will be presented in Chapter 4. A general analytical solution to the 2D linear wave-platform BVP is developed in this chapter. The assumption of small platform motion around the equilibrium position in the conventional linear potential flow theory is modified to small motions around a general platform pose. Step approximation and eigenfunction expansion techniques are adopted to derive the analytical solution to this modified BVP. The proposed analytical method is validated against a 2D boundary element method formulation. A barge-type floating platform is used as a demonstration example, and its hydrodynamic behaviour under different platform positions, corresponding to various wetted body-surface geometries, is examined.

Finally, **Chapter 4** presents a linear parameter-varying (LPV) framework to capture the geometrically nonlinear wave-platform interaction effects due to large platform motions in the 2D space. The LPV system is constructed using the state-space models estimated from the BVP solutions at a broad range of platform heave and pitch positions. During simulation, the state-space models are linearly interpolated based on the instantaneous platform position to determine the nonlinear wave radiation forces. To address the basis incoherency issue for correct model interpolation, a black-box approach utilizing the balanced realization and an automatic state-basis correction technique is proposed. Additionally, a novel gray-box approach is developed, which inherently ensures basis coherency by assigning physical meaning to the state vector via a finite-element formulation of the wave-platform interaction system. The resulting LPV state-space models representing the nonlinear wave radiation forces, along with other pose-dependent hydrodynamic effects, are implemented in Matlab/Simulink and validated using the benchmark van Daalen cylinder model [128]. The validated LPV model is then integrated with other physical domains of the Simulink FWT model developed in Chapter 2 to investigate the impact of nonlinear hydrodynamic effects on the global dynamic behaviour of the example 5-MW ITI-Barge FWT under various loading conditions.

Chapter 2

A Simulink Model for the Dynamic Analysis of Floating Wind Turbines

2.1 Introduction

In this chapter, an integrated FWT modelling framework is developed in Simulink to systematically investigate the dominant dynamic coupling effects between various FWT physical domains, including the hydrodynamics, structural elasticity, aerodynamics, and controls, as detailed in Section 1.2. The hydrodynamic forces are calculated based on linear potential flow theory. The unsteady aerodynamics are determined using a combination of the classical blade-element momentum method and Øye's dynamic inflow and stall models [11, 49]. The industry-standard ROSCO control strategy [113] is implemented to regulate power generation, and to stabilize the FWT system through an additional floating feedback loop. Structural modelling is achieved using the Simscape multibody simulation environment, in which the hub, nacelle, and platform are represented as individual rigid bodies. The blades and tower are modelled as a series of either rigid or deformable Euler-Bernoulli beams, following the multibody formulation. The drivetrain is represented using a three-stage compound gear model. Since mooring dynamics are outside the scope of this work, their effects are simplified using linear stiffness and damping matrices.

In addition to the novel implementation of multiple FWT physical domains in Simulink, this chapter introduces new features that enhance the robustness and efficiency of wave-platform interaction modelling. Accurate representation of wave-platform interactions is crucial for predicting the overall system dynamics. Among multiple FWT hydrodynamic effects, the wave radiation effect, which results from the kinetic energy dissipation of an oscillating platform via radiated waves, affects the stiffness, and more significantly, damping of the whole FWT system [89]. An accurate wave radiation model is essential for reliable stability analysis and the synthesis of FWT control algorithms, for which a state-space representation is particularly suitable. The wave excitation force, which represents the effects of incident and diffracted waves acting on the platform, is another key hydrodynamic effect. While it can be pre-computed given a target wave spectrum, a state-space representation is preferable when control strategies [38, 120] or real-time wave excitation force predictions [66] are required.

However, it is difficult to directly obtain state-space representations of the wave radiation and excitation models. The common practice is to find an estimate from the results of the widely-used frequency-domain hydrodynamic software, e.g., WAMIT [131]. This transforms the problem into a system identification task. For wave radiation modelling, the frequency response samples directly obtained from the hydrodynamic software are inherently multi-input multi-output (MIMO) systems, where platform velocities are inputs and radiation damping forces are outputs. On the other hand, wave excitation frequency response samples correspond to a single-input multi-output (SIMO) system, where the wave elevation at a reference point is the input, and wave excitation forces are the outputs. Conventional identification methods for floating structures often use separate single-input single-output (SISO) approaches, either through least-squares (LS) fitting [53, 33] or subspace methods [30], to develop a composite state-space model. The obtained multiple SISO state-space models are then assembled to get the final state-space model to represent the intrinsic MIMO/SIMO system. The total number of states (poles) is the sum of individual states for each SISO coupling. The wave excitation model using wave elevation at a specific point as input corresponds to a non-causal process [34]. In existing state-space identification attempts [140, 44], the wave excitation frequency response samples are first converted to impulse response samples, which are then causalized by introducing a time shift. The causalized impulse response samples are used to estimate a state-space model using the multi-SISO approach.

Although the number of states can be reduced by removing some zero couplings thanks to platform symmetry, the multi-SISO representation still has high redundancy and lacks efficiency [60]. Furthermore, using separate sets of poles for different input-output couplings fails to capture the congruent nature of the linear hydrodynamic analysis results. This congruency guarantees that the system poles remain invariant to the selection of reference origin and/or rotation of reference axes [65]. In light of this, a direct-MIMO identification that yields a common set of poles for all input-output couplings is more advantageous. Again, either the LS-based method [112] or the subspace method can be employed for the direct-MIMO identification. The latter, which makes use of the geometrical properties of the input-output sequences, outperforms the LS method in that it avoids the need for iteration and exhibits higher robustness. It is thus adopted in the present work for the state-space identification of the FWT wave radiation and excitation models. To the authors' knowledge, this direct-MIMO state-space subspace identification method has not been reported to be used on FWTs so far.

With the help of the newly developed Simulink model, the following important FWT dynamics are examined in first an individual then a holistic manner: wave-platform interaction effects, unsteady aerodynamics induced by platform rotations, negative damping issue due to the unfavorable coupling between the controller and platform rotation, nonlinear blade dynamics, and the coupling among different degrees of freedom (DoF) with all FWT domains involved. In addition, the strengths and limitations of the proposed FWT modelling methods in Simulink are critically assessed through comparisons with the popular OpenFAST simulation tool, as described in Section 1.3, and practical suggestions are provided.

2.2 Aero-hydro-elastic-control Modelling Methodology

The methodology employed to represent major physical domains of the FWT system is described in detail in the following subsections, including the wave-platform interaction, highly flexible blade modelling, aerodynamics and controls.

To describe the 3D movements of the FWT platform, two right-handed Cartesian coordinate systems are introduced (as shown in Fig. 2.1(a)). The earth-fixed O-XYZ is defined with the plane O-XY lying on the still wave surface, OX pointing downwind, and OZ pointing upwards. The body-fixed O'-$X'Y'Z'$ follows the movement of the platform under wind/wave actions. The translational displacement from O to O' in the surge, sway, and heave DoFs are denoted as ξ_1, ξ_2, ξ_3, respectively, and the rotation of roll, pitch and yaw DoF as ξ_4, ξ_5, ξ_6, respectively. The Euler angle sequence is defined as: Cartesian $X \rightarrow$ rotated Y following the ξ_4 transformation $\rightarrow$ rotated Z following the ξ_4 and ξ_5 transformations. In terms of the blade deformation and aerodynamics calculation, the blade-root O_b-$x_b y_b z_b$ coordinate system and local airfoil O_a-$x_a y_a z_a$ system are introduced, respectively. As shown on an example blade in Fig. 2.1(b), O_b is fixed at the blade root, $O_b z_b$ points towards the blade tip along the pitch axis (which is $1/4$ chord length away from the leading edge of each blade section), $O_b x_b$ towards the trailing edge of the zero-twist blade section, and $O_b y_b$ towards upwind. O_b-$x_b y_b z_b$ pitches and rotates with the blade. O_a is the aerodynamic center with respect to which the aerodynamic coefficients of a blade section are defined, and there is usually an offset along the chord-line between O_a and the pitch axis. O_a-$x_a y_a z_a$ does not pitch but does rotate with the blade, and it is parallel with O_b-$x_b y_b z_b$ under the zero-pitch condition.

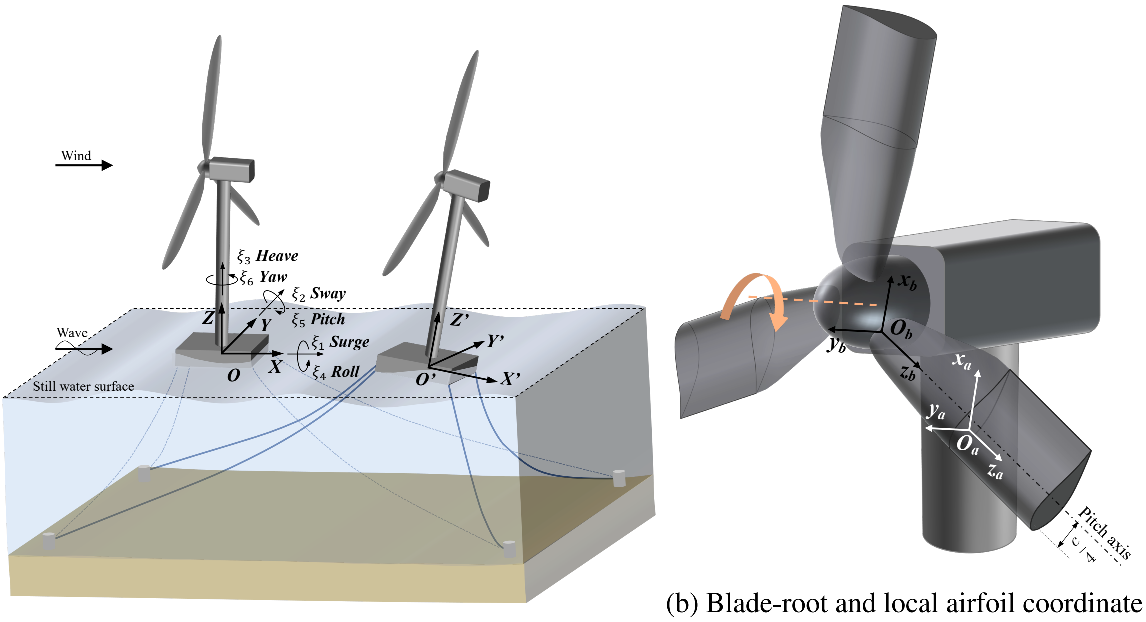

(a) Earth-fixed and platform-fixed coordinate systems

(b) Blade-root and local airfoil coordinate systems

Fig. 2.1 Coordinate systems to describe (a) the 3D floating platform movement and (b) the blade deformation and aerodynamic loads.

2.2.1 Wave-platform interaction

According to linear potential flow theory [97], the total linear hydro-mechanical force exerted by water onto the floating platform can be expressed in the time-domain as

$$\mathbf{F}_{hydro}(t) = \mathbf{F}_{b0} - \mathbf{K}_{hs}\boldsymbol{\xi}(t) - \boldsymbol{\lambda}_{\infty}\ddot{\boldsymbol{\xi}}(t) - \mathbf{F}_r(t) + \mathbf{F}_e(t). \tag{2.1}$$

The first two terms of Eq. (2.1) are hydrostatic forces, with the former $\mathbf{F}_{b0}$ being the static buoyancy force, which balances the FWT weight under the static equilibrium state, and the latter being the restoring force under a displaced state $\boldsymbol{\xi}$, where $\mathbf{K}_{hs}$ denotes the hydrostatic restoring stiffness depending on the water-plane area and center of buoyancy location. The third and fourth terms of Eq. (2.1) are radiation forces resulting from the momentum change in fluid induced by the platform motion, with the former capturing the additional inertia effects, where $\boldsymbol{\lambda}_{\infty}$ denotes the infinite-frequency added mass, and the latter being the radiation damping force $\mathbf{F}_r$ describing the kinetic energy loss of the platform due to the radiated wave propagating on the free surface away from the platform to the far field. The last term of Eq. (2.1) is the wave excitation force $\mathbf{F}_e$, which describes the effects of incident wave and diffracted wave due to the presence of the platform, and hence it is independent of the platform movement.

To determine the radiation damping force $\mathbf{F}_r$, Cummins' equation [22] is usually adopted, which takes into account the platform velocity history, i.e. the fluid memory effect, through a convolution integral:

$$\mathbf{F}_r(t) = \int_0^t \mathbf{k}_r(t-\tau)\dot{\boldsymbol{\xi}}(\tau)d\tau, \tag{2.2}$$

where the impulse response function $\mathbf{k}_r(t)$ can be calculated by:

$$\mathbf{k}_r(t) = \frac{2}{\pi}\int_0^\infty \boldsymbol{\mu}(\omega)\cos(\omega t)d\omega. \tag{2.3}$$

$\mathbf{k}_r(t)$ is the Fourier transform of the frequency response function $\mathbf{K}_r(i\omega)$ mapping from the platform velocity $\dot{\boldsymbol{\xi}}$ to the fluid-memory radiation damping force $\mathbf{F}_r$:

$$\mathbf{K}_r(i\omega) = \boldsymbol{\mu}(\omega) + i\omega\left[\boldsymbol{\lambda}(\omega) - \boldsymbol{\lambda}_\infty\right], \tag{2.4}$$

where $\boldsymbol{\lambda}, \boldsymbol{\mu}$ denote the frequency-dependent added mass and radiation damping matrix, respectively. Under the assumption of linear wave theory and uni-directional incident wave, the wave excitation force $\mathbf{F}_e$ can be calculated via inverse Fourier transform, given a wave spectrum $S_\eta(\omega)$:

$$\mathbf{F}_e(t) = \Re\left\{\frac{1}{2\pi}\int_{-\infty}^{\infty} W(\omega)\sqrt{2\pi S_\eta(\omega)}\mathbf{K}_e(i\omega)e^{i\omega t}\,d\omega\right\}, \tag{2.5}$$

where $W(\omega)$ is the white Gaussian noise representing random phases, and $\mathbf{K}_e$ the frequency-dependent wave excitation force frequency response function, which, together with $\boldsymbol{\lambda}_\infty, \boldsymbol{\lambda}, \boldsymbol{\mu}$ and $\mathbf{K}_{hs}$, are usually obtained from frequency-domain boundary element codes, such as WAMIT [131].

2.2.1.1 Wave radiation state-space model

Calculating the convolution integral at each time step with the velocity history, as shown in Eq. (2.2), is computationally intensive. To enhance efficiency, the state-space approximation has been proposed for the wave radiation model, with the platform velocity vector $\dot{\boldsymbol{\xi}}$ as inputs and radiation force $\mathbf{F}_r$ as outputs:

$$\begin{cases} \dot{\mathbf{x}}_r(t) = \mathbf{A}_r\mathbf{x}_r(t) + \mathbf{B}_r\dot{\boldsymbol{\xi}}(t) \\ \mathbf{F}_r(t) = \mathbf{C}_r\mathbf{x}_r(t) + \mathbf{D}_r\dot{\boldsymbol{\xi}}(t), \end{cases} \tag{2.6}$$

from which the estimated impulse response and frequency response functions can be expressed as

$$\hat{\mathbf{k}}_r(t) = \mathbf{C}_r e^{\mathbf{A}_r t}\mathbf{B}_r + \mathbf{D}_r\delta(t), \text{ and } \hat{\mathbf{K}}_r(i\omega) = \mathbf{C}_r\left(i\omega\mathbf{I} - \mathbf{A}_r\right)^{-1}\mathbf{B}_r + \mathbf{D}_r, \tag{2.7}$$

respectively, where $\delta(t)$ is the unit impulse function. It is note-worthy that the feedthrough matrix $\mathbf{D}_r$ is usually enforced to be zero such that the strict properness of $\mathbf{K}_r(i\omega)$ is satisfied, i.e., $\mathbf{K}_r(i\omega) \to 0$ as $\omega \to \infty$ [103].

As discussed in Section 2.1, the direct-MIMO subspace identification method is adopted to estimate the state-space fluid-memory radiation model of Eq. (2.6). This can be performed via either the time-domain (TD) or frequency-domain (FD) approaches. TD identification requires the impulse response samples $\mathbf{k}_r(t_j)$, (j=1,2,3,...), which can be computed from the Cosine transform of $\boldsymbol{\mu}(\omega_k)$ at discrete wave frequencies ω_k (k=1,2,3,...) from 0 to infinity (Eq. (2.3)). In practice, $\boldsymbol{\mu}(\omega_k)$ can only be accurately calculated within a frequency range up to ω_{Nw} due to the limit of mesh resolution. The extension from ω_{Nw} to a sufficiently large wave frequency is usually performed in the exponential or ω^{-2} manner. However, this extension has been reported to change the $\mathbf{k}_r(0)$ values and thus the hydrodynamic behaviour of the floating structure [65]. In contrast, FD identification which directly uses the frequency-response samples $\mathbf{K}_r(i\omega_k)$ calculated from $\boldsymbol{\lambda}(\omega_k), \boldsymbol{\mu}(\omega_k)$ and $\boldsymbol{\lambda}_\infty$ (Eq. (2.4)) avoids the frequency extension and thus is more reliable.

In this work, the well-established numerical subspace-based state-space system identification (N4SID) method using MIMO frequency response samples $\mathbf{K}_r(i\omega_k)$ is adopted. Before performing the identification, $\mathbf{K}_r(i\omega_k)$ obtained from Eq. (2.4) are suggested to be scaled via the element-wise division by a matrix $\mathscr{K}$ due to the relatively large magnitude difference in $\mathbf{K}_r(i\omega_k)$ between the translational and rotational DoFs. The state-space matrices $[\mathbf{A}_i, \mathbf{B}_i, \mathbf{C}_i]$ identified from the scaled $\mathbf{K}_r(i\omega_k)$ can then be converted to its modal form $[\mathbf{A}_m, \mathbf{B}_m, \mathbf{C}_m]$ through a transformation matrix $\mathbf{T}_{i/m}$ which comprises the eigenvectors of $\mathbf{A}_i$. The eigenvalues (poles) of $\mathbf{A}_i$, $p_1, p_2, \ldots, p_n$, are either real or complex conjugate pairs. To eliminate the possible spikes in $\mathbf{K}_r(i\omega_k)$ due to, e.g., irregular frequency phenomenon as described in [100], the poles whose damping ratio $-\Re(p_n)/|p_n|$ is lower than a specified value are removed by getting rid of the corresponding rows and columns in $[\mathbf{A}_m, \mathbf{B}_m, \mathbf{C}_m]$. The reduced state-space model $[\mathbf{A}'_m, \mathbf{B}'_m, \mathbf{C}'_m]$ can subsequently be converted to a real-valued state-space model in the real Jordan form $[\mathbf{A}_r, \mathbf{B}_r, \mathbf{C}_r]$ through a transformation matrix $\mathbf{T}_{m/r}$:

$$\mathbf{A}_r = \mathbf{T}_{m/r}^{-1}\mathbf{A}'_m\mathbf{T}_{m/r}, \;\; \mathbf{B}_r = \mathbf{T}_{m/r}^{-1}\mathbf{B}'_m, \;\; \mathbf{C}_r = \mathbf{C}'_m\mathbf{T}_{m/r}. \tag{2.8}$$

To better illustrate the complex-to-real transformation, an example of p_1 being a real pole and p_2, p_3 a complex conjugate pair ($p_2 = \sigma + i\varsigma, p_3 = \sigma - i\varsigma$) is taken. $\mathbf{T}_{m/r}$ and its inverse are written as:

$$\mathbf{T}_{m/r} = \begin{bmatrix} 1 & 0 & 0 \\ 0 & \frac{1}{2} & -\frac{1}{2}i \\ 0 & \frac{1}{2} & \frac{1}{2}i \end{bmatrix} \text{ and } \mathbf{T}_{m/r}^{-1} = \begin{bmatrix} 1 & 0 & 0 \\ 0 & 1 & 1 \\ 0 & i & -i \end{bmatrix}. \tag{2.9}$$

The system matrices before and after the transformation are

$$\mathbf{A}'_m = \begin{bmatrix} p_1 & 0 & 0 \\ 0 & \sigma + i\varsigma & 0 \\ 0 & 0 & \sigma - i\varsigma \end{bmatrix} \text{ and } \mathbf{A}_r = \begin{bmatrix} p_1 & 0 & 0 \\ 0 & \sigma & \varsigma \\ 0 & -\varsigma & \sigma \end{bmatrix}. \tag{2.10}$$

The direct-MIMO state-space identification from $\mathbf{K}_r(i\omega_k)$ proposed in this work is summarized and compared with the conventional multi-SISO method in Fig. 2.2. In the multi-SISO method, the state-space model can be identified either from each entry of the frequency-response samples $K_{r,mn}(i\omega_k)$ $(m,n = 1,2,...,6)$ via the LS fitting method followed by the transfer-function-to-state-space conversion (implemented using `invfreqs` and `tf2ss` functions in MATLAB), or from the impulse response samples $k_{r,mn}(t_j)$ via the realization theory followed by the model truncation (implemented using `imp2ss` and `balmr` functions in MATLAB). The obtained multiple SISO state-space models are then assembled and possibly truncated again to get the final state-space model $[\mathbf{A}_r, \mathbf{B}_r, \mathbf{C}_r]$. In contrast, the direct-MIMO method is much more straightforward and efficient, the reliability of which will be demonstrated later in Section 2.4.1.1.

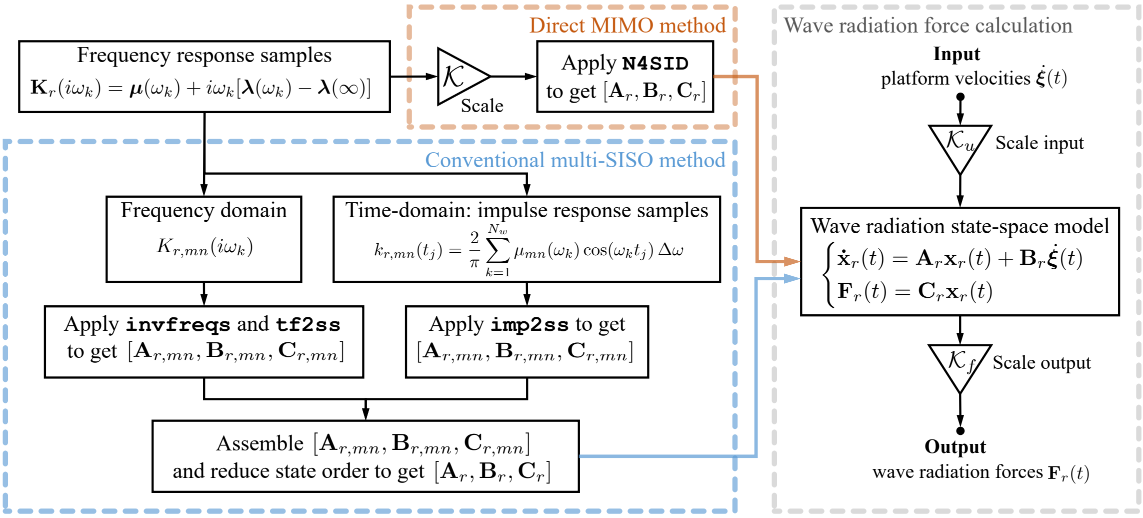

Fig. 2.2 Direct MIMO state-space identification vs. conventional multi-SISO identification for wave radiation, and the time-domain calculation of the radiation force $\mathbf{F}_r(t)$ with the identified state-space model $[\mathbf{A}_r, \mathbf{B}_r, \mathbf{C}_r]$.

The time-domain calculation of fluid-memory radiation force $\mathbf{F}_r(t)$ is also illustrated in Fig. 2.2. It should be noted that the input velocities $\dot{\boldsymbol{\xi}}(t)$ and output forces $\mathbf{F}_r(t)$ need to be scaled back by multiplying $\mathscr{K}_u$ and $\mathscr{K}_f$ vectors, respectively, such that the state-space model identified from the scaled $\mathbf{K}_r(i\omega_k)$ (the scaling matrix $\mathscr{K} = \mathscr{K}_f\mathscr{K}_u^{\mathsf{T}}$) is used with correct units in the time-domain calculation.

2.2.1.2 Wave excitation state-space model

Similarly as in the wave radiation problem (Eq. (2.6)), the wave excitation state-space model can be written as:

$$\begin{cases} \dot{\mathbf{x}}_e(t) = \mathbf{A}_e\mathbf{x}_e(t) + \mathbf{B}_e\eta_o(t) \\ \mathbf{F}_e(t) = \mathbf{C}_e\mathbf{x}_e(t) + \mathbf{D}_e\eta_o(t), \end{cases} \tag{2.11}$$

where the input η_o denotes wave elevation at the origin of the earth-fixed coordinate system O, and $\mathbf{D}_e$ is zero due to the strict properness of $\mathbf{K}_e$. A well-acknowledged issue of this wave excitation model is its non-causality [34], which manifests itself as an impulse response function with relatively large non-zero values at $t < 0$, meaning that the current force calculation requires future wave elevation input. This non-causality is attributed to the fact that the real cause of the output force $\mathbf{F}_e$ is not the chosen input η_o, instead, it is a distant wave maker as illustrated in Fig. 2.3. From the wave elevation at a single point η_o, it is impossible to infer the velocity profile of the wave maker along the water depth $v(z,t)$. The loss of information results in a non-causal mathematical mapping from η_o to $\mathbf{F}_e$, despite that the physical process of wave propagation is strictly causal.

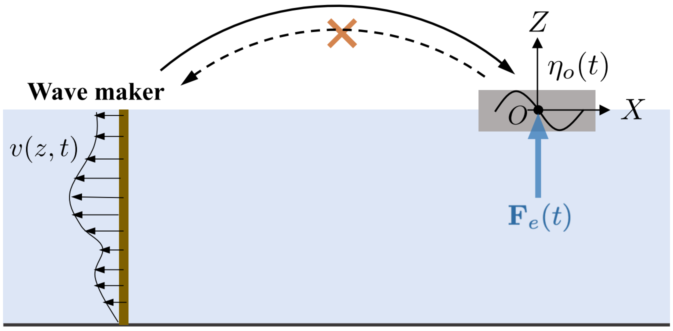

Fig. 2.3 Sketch to illustrate the non-causality issue in the wave excitation model.

Conventionally, as summarized in Fig. 2.4, the multiple SISO impulse response samples $k_{e,m}$ ($m = 1,2,...,6$) are first calculated from the inverse Fourier transform of $K_{e,m}$. They are then causalized by being shifted to the right by a certain time offset t_c, such that the values at negative times are sufficiently small, for example, within 2% of the peak impulse response value. The causalized impulse responses are used to estimate state-space models through the commonly used realization theory (`imp2ss` in MATLAB), which are then assembled and truncated to get the final state-space representation $[\mathbf{A}_e, \mathbf{B}_e, \mathbf{C}_e]$. It should be noted that when calculating in the time domain, the wave elevation input η_o should be shifted accordingly. In the present work, the identification process is streamlined using the direct-MIMO subspace-based identification method proposed in Section 2.2.1.1. The N4SID algorithm can be directly applied on the frequency response samples $\mathbf{K}_e(i\omega_k)$ and the time offset is handled by specifying a negative time delay ($-t_c$). As the time offset has been taken into account, there is no need to shift η_o, as illustrated in Fig. 2.4. Therefore, it provides a more robust and efficient tool for the evaluation of the wave excitation force.

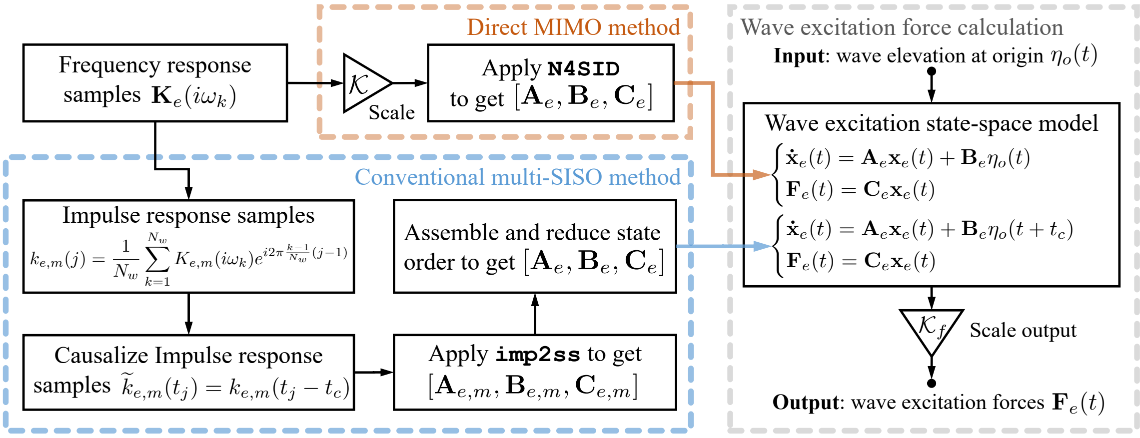

Fig. 2.4 Direct MIMO state-space identification vs. conventional multi-SISO identification for wave excitation, and the time-domain calculation of the excitation force $\mathbf{F}_e(t)$ with the identified state-space model $[\mathbf{A}_e, \mathbf{B}_e, \mathbf{C}_e]$.

2.2.2 Blade Modelling

A multibody formulation is employed to describe the dynamics of FWT blades. By splitting the blade into a series of flexible substructures, and introducing a floating frame of reference to each substructure, the geometric and kinematic nonlinearities induced by large 3D translational and rotational displacements can be captured. Within each substructure, the displacements are sufficiently small such that the linearization assumption holds. Given the cross-sectional stiffness and inertia properties at different radial distances, the substructure can be described by the finite element (FE) beam model. The slender and closed-section blade tends to show negligible shear and warping deformations, making the classical Euler-

Bernoulli beam theory with Saint-Venant torsion theory appropriate for the substructure modelling.

Fig. 2.5 illustrates the multibody formulation in which the blade is split into N substructures, each being represented with multiple beam elements. The local floating reference frame of the n^{th} substructure follows the translation and rotation of the last boundary node from the $n-1^{th}$ substructure. This section takes the n^{th} substructure, which contains M blade elements, as an example to demonstrate the reduced-order FE modelling. As shown in Fig. 2.5, the O_n-$x_n y_n z_n$ and O_e-$x_e y_e z_e$ coordinate systems are introduced to describe the kinematics of local n^{th} blade substructure, and local m^{th} blade element, respectively. The blade element reference point O_e lies on the pitch axis with $O_e x_e$ pointing in the chord direction. Tension center (T), shear center (S) and gravity center (G) are all located on plane O_e-$x_e y_e$, with their offsets from O_e being $(x_t, y_t), (x_s, y_s), (x_g, y_g)$, respectively. T-$x_t y_t z_t$ axes are obtained via rotating O_e-$x_e y_e z_e$ by an angle α_t along axis $O_e z_e$ such that Tx_t and Ty_t coincide with the cross-section principal axes of bending, while G-$x_g y_g z_g$ by an angle α_g such that Gx_g and Gy_g coincide with principal axes of inertia. The internal axial force (N_z), moment about Tx_t axis (M_x), moment about Ty_t axis (M_y) and their corresponding strains $u_{z,z}, \theta_{x,z}, \theta_{y,z}$ are defined around the tension center T, whereas the internal torsion M_z and the corresponding strain $\theta_{z,z}$ is defined around the shear center S.

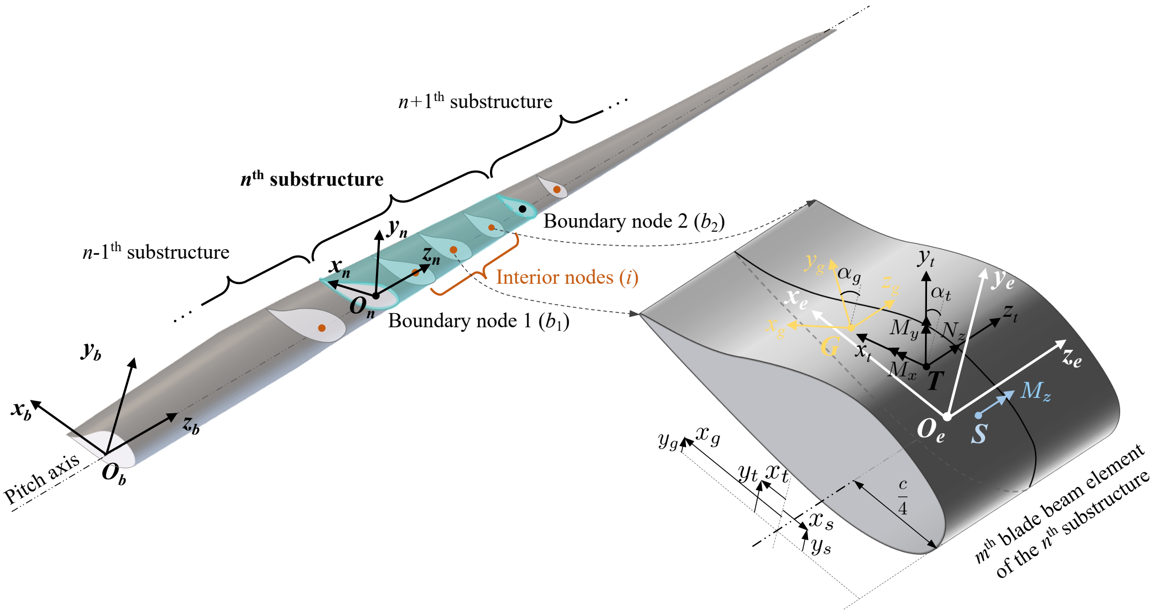

Fig. 2.5 Schematics for the blade multibody formulation with reduced-order finite-element modelling. O_b-$x_b y_b z_b$, O_n-$x_n y_n z_n$ and O_e-$x_e y_e z_e$ denote the blade-root, local n^{th} blade substructure, and local m^{th} blade element reference coordinates, respectively.

Principle of virtual work is adopted to derive the Equations of Motion (EoM) of the m^{th} element of the n^{th} blade substructure. The external virtual work is represented as:

$$W_{ext}^{*} = \int_0^{l_e} \mathbf{r}_e^{*\mathsf{T}} \mathbf{f}_e dz + \int_0^{l_e} \mathbf{r}_g^{*\mathsf{T}} \left(-\boldsymbol{\rho}_g \ddot{\mathbf{r}}_g\right) dz, \tag{2.12}$$

where $()^{*}$ denotes the virtual variable, l_e the length of the current element, $\mathbf{r}_e$ the general displacement vector of the element reference point O_e, which can be approximated by the cubic Hermite polynomial shape functions $\mathscr{N}$ and displacements of two nodes $\mathbf{u}_e = [\mathbf{u}_{e1}; \mathbf{u}_{e2}]$, i.e. $\mathbf{r}_e = \mathscr{N}\mathbf{u}_e$, $\mathbf{f}_e$ the external force per unit length, $\boldsymbol{\rho}_g$ the cross-section mass matrix containing mass density and rotational inertias per unit length $\boldsymbol{\rho}_g = \mathrm{diag}(\rho, \rho, \rho, i_x, i_y, i_z)$, $\mathbf{r}_g$ the displacement of gravity center G which is given by $\mathbf{r}_g = \mathbf{T}_{g/e}\mathbf{r}_e$, where $\mathbf{T}_{g/e}$ is the kinematics transformation matrix between G-$x_g y_g z_g$ and O_e-$x_e y_e z_e$ axes with first translational and then rotational transformations:

$$\mathbf{T}_{g/e} = \begin{bmatrix} \mathbf{q}_{g/e} & \mathbf{0} \\ \mathbf{0} & \mathbf{q}_{g/e} \end{bmatrix} \begin{bmatrix} \mathbf{I} & \mathbf{t}_{g/e} \\ \mathbf{0} & \mathbf{I} \end{bmatrix}, \text{where } \mathbf{t}_{g/e} = \begin{bmatrix} 0 & 0 & -y_s \\ 0 & 0 & x_s \\ y_g & -x_g & 0 \end{bmatrix}, \mathbf{q}_{g/e} = \begin{bmatrix} \cos\alpha_g & \sin\alpha_g & 0 \\ -\sin\alpha_g & \cos\alpha_g & 0 \\ 0 & 0 & 1 \end{bmatrix}. \tag{2.13}$$

The external virtual work can then be expressed in terms of the nodal displacements $\mathbf{u}_e$ as:

$$W_{ext}^{*} = \mathbf{u}_e^{*\mathsf{T}} \int_0^{l_e} \mathscr{N}^{\mathsf{T}} \mathbf{f}_e dz - \mathbf{u}_e^{*\mathsf{T}} \int_0^{l_e} \mathscr{N}^{\mathsf{T}} \mathbf{T}_{g/e}^{\mathsf{T}} \boldsymbol{\rho}_g \mathbf{T}_{g/e} \mathscr{N} dz \, \ddot{\mathbf{u}}_e. \tag{2.14}$$

Considering a generic composite blade with anisotropic and inhomogeneous material, the cross-section force-strain relation in the T-$x_t y_t z_t$ coordinates, as depicted in Fig. 2.5, is given as:

$$\mathbf{F}_t = \mathbf{C}_t \boldsymbol{\varepsilon}_t, \text{ i.e., } \begin{bmatrix} N_z \\ M_x \\ M_y \\ M_z \end{bmatrix} = \begin{bmatrix} EA & 0 & 0 & 0 \\ & EI_x & 0 & B_xT \\ & sym. & EI_y & B_yT \\ & & & GJ \end{bmatrix} \begin{bmatrix} u_{z,z} \\ \theta_{x,z} \\ \theta_{y,z} \\ \theta_{z,z} \end{bmatrix}. \tag{2.15}$$

The diagonal term EA, EI_x, EI_y, GJ of the symmetric cross-section stiffness matrix $\mathbf{C}_t$ represent axial rigidity, flapwise bending stiffness, edgewise bending stiffness, and torsional rigidity, respectively. The off-diagonal term B_xT, B_yT represent the coupled flapwise bending-torsion, and edgewise bending-torsion stiffness, respectively. The strain vector $\boldsymbol{\varepsilon}_t$ can be determined from the nodal displacements via $\boldsymbol{\varepsilon}_t = \hat{\mathscr{B}}\mathbf{u}_t = \hat{\mathscr{B}}[\mathbf{u}_{t1}; \mathbf{u}_{t2}] = \hat{\mathscr{B}}\left[\mathbf{T}_{t/e}\mathbf{u}_{e1}; \mathbf{T}_{t/e}\mathbf{u}_{e2}\right]$, where $\hat{\mathscr{B}}$ is the strain-displacement matrix containing derivative terms of the shape function $\mathscr{N}$, and $\mathbf{T}_{t/e}$ is the transformation matrix between T-$x_t y_t z_t$ and O_e-$x_e y_e z_e$, which takes the similar form as Eq. (2.13):

$$\mathbf{T}_{t/e} = \begin{bmatrix} \mathbf{q}_{t/e} & \mathbf{0} \\ \mathbf{0} & \mathbf{q}_{t/e} \end{bmatrix} \begin{bmatrix} \mathbf{I} & \mathbf{t}_{t/e} \\ \mathbf{0} & \mathbf{I} \end{bmatrix}, \text{where } \mathbf{t}_{t/e} = \begin{bmatrix} 0 & 0 & -y_s \\ 0 & 0 & x_s \\ y_t & -x_t & 0 \end{bmatrix}, \mathbf{q}_{t/e} = \begin{bmatrix} \cos\alpha_t & \sin\alpha_t & 0 \\ -\sin\alpha_t & \cos\alpha_t & 0 \\ 0 & 0 & 1 \end{bmatrix}. \tag{2.16}$$

Defining $\overline{\mathbf{T}}_{t/e} = \mathrm{diag}(\mathbf{T}_{t/e}, \mathbf{T}_{t/e})$, the internal virtual work of the element can be expressed as:

$$W_{int}^* = \int_0^{l_e} \boldsymbol{\varepsilon}_t^{*\mathsf{T}} \mathbf{C}_t \boldsymbol{\varepsilon}_t dz = \mathbf{u}_e^{*\mathsf{T}} \overline{\mathbf{T}}_{t/e}^{\mathsf{T}} \int_0^{l_e} \hat{\mathscr{B}}^{\mathsf{T}} \mathbf{C}_t \hat{\mathscr{B}} dz \, \overline{\mathbf{T}}_{t/e} \mathbf{u}_e. \tag{2.17}$$

Applying the principle of virtual work $W_{ext}^* = W_{int}^*$ and factoring out $\mathbf{u}_e^{*\mathsf{T}}$ yield the EoM:

$$\int_0^{l_e} \mathscr{N}^{\mathsf{T}} \mathbf{T}_{g/e}^{\mathsf{T}} \boldsymbol{\rho}_g \mathbf{T}_{g/e} \mathscr{N} dz \, \ddot{\mathbf{u}}_e + \overline{\mathbf{T}}_{t/e}^{\mathsf{T}} \int_0^{l_e} \hat{\mathscr{B}}^{\mathsf{T}} \mathbf{C}_t \hat{\mathscr{B}} dz \, \overline{\mathbf{T}}_{t/e} \mathbf{u}_e = \int_0^{l_e} \mathscr{N}^{\mathsf{T}} \mathbf{f}_e dz. \tag{2.18}$$

By defining the m^{th} blade-element mass, stiffness matrix as

$$\mathbf{m}^{[m]} = \int_0^{l_e} \mathscr{N}^{\mathsf{T}} \mathbf{T}_{g/e}^{\mathsf{T}} \boldsymbol{\rho}_g \mathbf{T}_{g/e} \mathscr{N} dz, \ \mathbf{k}^{[m]} = \overline{\mathbf{T}}_{t/e}^{\mathsf{T}} \int_0^{l_e} \hat{\mathscr{B}}^{\mathsf{T}} \mathbf{C}_t \hat{\mathscr{B}} dz \, \overline{\mathbf{T}}_{t/e}, \tag{2.19}$$

and stiffness-proportional damping matrix as

$$\mathbf{c}^{[m]} = \overline{\mathbf{T}}_{t/e}^{\mathsf{T}} \int_0^{l_e} \hat{\mathscr{B}}^{\mathsf{T}} \boldsymbol{\mu}_d \mathbf{C}_t \hat{\mathscr{B}} dz \, \overline{\mathbf{T}}_{t/e} \tag{2.20}$$

via coefficient $\boldsymbol{\mu}_d = \mathrm{diag}(\mu_z, \mu_{\theta_x}, \mu_{\theta_y}, \mu_{\theta_z})$, the n^{th} blade-substructure mass $\mathbf{M}_n$, stiffness $\mathbf{K}_n$ and damping $\mathbf{C}_n$ matrices can be obtained by assembling $\mathbf{m}^{[m]}, \mathbf{k}^{[m]}, \mathbf{c}^{[m]}$, $(m = 1, 2, 3, \ldots, M)$ following typical finite element assembly methods. The corresponding EoM of the n^{th} blade substructure can be written as:

$$\mathbf{M}_n \ddot{\mathbf{u}}_n + \mathbf{C}_n \dot{\mathbf{u}}_n + \mathbf{K}_n \mathbf{u}_n = \mathbf{f}_n. \tag{2.21}$$

It is worth mentioning that the aerodynamic pre-twist between adjacent blade elements should be taken into account through rotational transformations when assembling $\mathbf{m}^{[m]}, \mathbf{k}^{[m]}, \mathbf{c}^{[m]}$ matrices.

The Craig-Bampton (C-B) method [21] is adopted to reduce the FE model of the n^{th} blade substructure, in which M blade elements yield M+1 nodes and 6(M+1) DoFs in total. By partitioning all DoFs into boundary (b_1, b_2) and interior (i) ones, Eq. (2.21) without damping can be rewritten as:

$$\begin{bmatrix} \mathbf{M}_{b_1b_1} & \mathbf{M}_{b_1i} & \mathbf{M}_{b_1b_2} \\ \mathbf{M}_{ib_1} & \mathbf{M}_{ii} & \mathbf{M}_{ib_2} \\ \mathbf{M}_{b_2b_1} & \mathbf{M}_{b_2i} & \mathbf{M}_{b_2b_2} \end{bmatrix} \begin{bmatrix} \ddot{\mathbf{u}}_{b_1} \\ \ddot{\mathbf{u}}_i \\ \ddot{\mathbf{u}}_{b_2} \end{bmatrix} + \begin{bmatrix} \mathbf{K}_{b_1b_1} & \mathbf{K}_{b_1i} & \mathbf{K}_{b_1b_2} \\ \mathbf{K}_{ib_1} & \mathbf{K}_{ii} & \mathbf{K}_{ib_2} \\ \mathbf{K}_{b_2b_1} & \mathbf{K}_{b_2i} & \mathbf{K}_{b_2b_2} \end{bmatrix} \begin{bmatrix} \mathbf{u}_{b_1} \\ \mathbf{u}_i \\ \mathbf{u}_{b_2} \end{bmatrix} = \begin{bmatrix} \mathbf{f}_{b_1} \\ \mathbf{f}_i \\ \mathbf{f}_{b_2} \end{bmatrix}. \tag{2.22}$$

Fixing all boundary DoFs and assuming no external forces are applied at interior nodes, i.e., $\mathbf{f}_i = 0$, the static displacements of interior nodes are given as $\mathbf{u}_i^{static} = -\mathbf{K}_{ii}^{-1}\mathbf{K}_{ib_1}\mathbf{u}_{b_1} - \mathbf{K}_{ii}^{-1}\mathbf{K}_{ib_2}\mathbf{u}_{b_2}$, with which the static displacements of all DoFs can be expressed in terms of boundary displacements as:

$$\mathbf{u}_n^{static} = \mathbf{S}\mathbf{u}_b = \begin{bmatrix} \mathbf{I}_{b_1b_1} & \mathbf{0}_{b_1b_2} \\ -\mathbf{K}_{ii}^{-1}\mathbf{K}_{ib_1} & -\mathbf{K}_{ii}^{-1}\mathbf{K}_{ib_2} \\ \mathbf{0}_{b_2b_1} & \mathbf{I}_{b_2b_2} \end{bmatrix} \begin{bmatrix} \mathbf{u}_{b_1} \\ \mathbf{u}_{b_2} \end{bmatrix}, \tag{2.23}$$

where $\mathbf{S}$ is the static condensation transformation matrix. By solving the eigenvalue problem for all interior DoFs with the boundary DoFs being fully constrained $\left(\mathbf{K}_{ii} - \omega^2\mathbf{M}_{ii}\right)\mathbf{\Phi}_{ii} = 0$, and applying modal truncation, the dynamic displacements of interior DoFs can be approximated with a reduced number of modal coordinates $\mathbf{q}_p$ $(p \leq 6(M-1))$: $\mathbf{u}_i^{dyn} = \mathbf{\Phi}_{ip}\mathbf{q}_p$, where $\mathbf{\Phi}_{ip}$ is the mass-normalized mode shape matrix. The dynamic displacements of all DoFs can then be expressed as:

$$\mathbf{u}_n^{dyn} = \mathbf{D}\mathbf{q}_p = \begin{bmatrix} \mathbf{0}_{b_1p} \\ \mathbf{\Phi}_{ip} \\ \mathbf{0}_{b_2p} \end{bmatrix} \mathbf{q}_p, \tag{2.24}$$

where $\mathbf{D}$ is the modal reduction transformation matrix. The displacements of all DoFs can eventually be written as the linear superposition of boundary displacements and the reduced modal coordinates: $\widetilde{\mathbf{u}}_n = \mathbf{u}_n^{static} + \mathbf{u}_n^{dyn} = \mathbf{S}\mathbf{u}_b + \mathbf{D}\mathbf{q}_p$. Defining the total Craig-Bampton transformation matrix $\mathbf{T} = [\mathbf{S}\ \mathbf{D}]$, the displacements can be expressed as $\widetilde{\mathbf{u}}_n = \mathbf{T}[\mathbf{u}_b; \mathbf{q}_p]$, which yields the reduced-order mass, stiffness and damping matrices:

$$\widetilde{\mathbf{M}}_n = \mathbf{T}^\mathsf{T}\mathbf{M}_n\mathbf{T} = \begin{bmatrix} \mathbf{S}^\mathsf{T}\mathbf{M}_n\mathbf{S} & \mathbf{S}^\mathsf{T}\mathbf{M}_n\mathbf{D} \\ \mathbf{D}^\mathsf{T}\mathbf{M}_n\mathbf{S} & \mathbf{I}_{pp} \end{bmatrix}, \tag{2.25}$$

$$\widetilde{\mathbf{K}}_n = \mathbf{T}^\mathsf{T}\mathbf{K}_n\mathbf{T} = \begin{bmatrix} \mathbf{S}^\mathsf{T}\mathbf{K}_n\mathbf{S} & \mathbf{0}_{bp} \\ \mathbf{0}_{bp} & \mathbf{\Lambda}_{pp} \end{bmatrix}, \tag{2.26}$$

$$\widetilde{\mathbf{C}}_n = \mathbf{T}^\mathsf{T}\mathbf{C}_n\mathbf{T}, \tag{2.27}$$

where $\mathbf{\Lambda}_{pp}$ contains all the retained eigenvalues (modes). With the obtained reduced-order $\widetilde{\mathbf{M}}_n, \widetilde{\mathbf{K}}_n, \widetilde{\mathbf{C}}_n$ matrices of all blade substructures, the blade multibody formulation can be implemented.

2.2.3 Aerodynamics

A dynamic blade-element momentum method is adopted to determine aerodynamic loads, which are assumed to act along the blade span at a finite number of sections, with no interference between each other. Therefore, the aerodynamic calculation can be performed on each blade section, by resolving the flow velocities onto the local airfoil plane O_a-$x_a y_a$ as depicted in Fig. 2.6. The blade rotates clockwise around the low-speed shaft at a rotor speed of Ω_r. The free-stream wind velocity, taking into account the wind turbulence and shear, is converted to the rotating O_a-$x_a y_a$ plane, and is denoted by $\mathbf{V}_w$ as shown in Fig. 2.6. Similarly, the blade velocity, accounting for the overall rigid-body motion and elastic blade/tower deformations, is also converted to O_a-$x_a y_a$ and the corresponding flow velocity which is opposite to the blade velocity is denoted by $\mathbf{V}_b$. The relative velocity $\mathbf{V}_{rel}$ seen by the local blade section is the vector sum of $\mathbf{V}_w, \mathbf{V}_b$, and the induced velocity $\mathbf{W}$. Upon getting $\mathbf{V}_{rel}$, the inflow angle ϕ and thus angle of attack α can be obtained, knowing the difference between ϕ and α is the sum of the local pre-twist angle θ and global blade pitch angle β_p. The lift (C_l) and drag (C_d) coefficients can then be interpolated from the C_l,C_d-α database based on the local α value, and the resulting lift force $d\mathbf{L}$ is perpendicular to and drag force $d\mathbf{D}$ parallel to $\mathbf{V}_{rel}$. Resolving the total force $d\mathbf{F}_a$ onto the $O_a x_a, O_a y_a$ axes yields the normal and tangential aerodynamic force dF_a^n and dF_a^t, respectively. Integrating the distributed dF_a^n along the blade length for all three blades gives the total aerodynamic thrust F_a, and integrating the torque caused by dF_a^t around the low-speed shaft for three blades gives total aerodynamic torque T_a. This aerodynamics calculation process is summarized in Fig. 2.7, and more detailed descriptions can be found in [49].

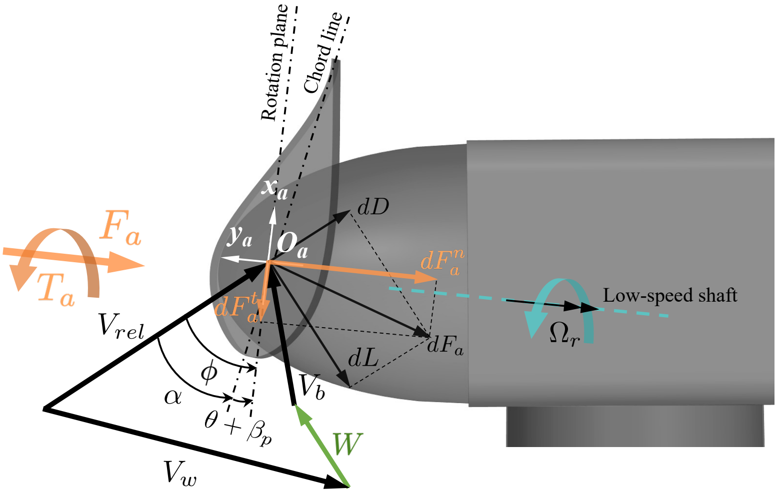

Fig. 2.6 Flow velocities and aerodynamic forces in the local airfoil plane (O_a-$x_a y_a$) for an example blade section.

The key to the above-described aerodynamic force calculation approach is to determine the induced velocity $\mathbf{W}$ resulting from the trailing vortices effect. The blade-element momentum method utilizes the steady-state conservation of momentum theory to obtain the quasi-steady induced flow field $\mathbf{W}_{qs}$. The algorithm proposed in [98] is adopted in this work and the associated equations are listed in the “Quasi-steady calculation of induced velocity” block in Fig. 2.7. The induction factors a, a' which denote the normalized axial and tangential components of $\mathbf{W}_{qs}$, respectively, are functions of ϕ. They are computed taking into account the Prandtl’s tip- and hub-loss corrections (F_{tip} and F_{hub}) and empirical Glauert’s correction (based on the region that ϕ and $\kappa(\phi)$ fall in). For the sake of brevity, the intermediate variables involved in the calculation of induced velocity are not detailed here and the readers are referred to Nomenclature for further information. The quasi-steady calculation is eventually formulated into solving a nonlinear algebraic equation of just one variable ϕ: $f(\phi) = 0$. Due to the complex correction functions involved, usually only numerical solutions are possible via methods such as Newton’s method. On the other hand, if the change in the flow behaviour is sufficiently small such that the previous $\phi = \phi_{t-dt}$ satisfies current $f(\phi) = 0$ within a tolerance tol, the nonlinear equation solving step is skipped and the previous $\mathbf{W}_{t-dt}$ is used.

Due to the atmospheric turbulence, wind shear, time-varying operating conditions, blade vibrations, and most importantly, platform motions, the shed vorticity at the rotor plane (mid-wake dynamics) as well as 2D flow structure at the local blade section (near-wake dynamics) change constantly for FWTs, making the aerodynamic force significantly different than that calculated from the steady-state and fully-attached flow [24]. The mid-wake effect is described by a state-space representation modified from Øye’s model [11], which is listed in the “Dynamic inflow model” block in Fig. 2.7. It captures the lag effect that the wake experiences before settling to a new steady state upon the change of inflow and/or operating condition. $\mathbf{W}_{qs}$ calculated from the quasi-steady model is taken as the input and dynamic $\mathbf{W}$ as the output. The near-wake effect is represented by Øye’s one-state dynamic stall model [49], as listed in the “Dynamic stall model” block in Fig. 2.7. It describes the buildup of trailing-edge separation as the angle of attack (α) increases. The unsteady separation function f_s is defined as the only state, and the output dynamic lift coefficient (C_l^{dyn}) is the weighted sum of the fully-attached and fully-separated lift coefficients, both calculated from the static lift coefficient C_l. Again, see Nomenclature for the descriptions of the associated variables.

The dynamic inflow and stall models are uncoupled in Fig. 2.7, which is justified by the fact that their characteristic time scales are of different orders, i.e., $\sim$ 10s vs. $\sim$ 0.5s for modern multi-MW wind turbines [24], which means that the wake tends not to respond instantaneously to the flow separation. Therefore, the dynamic stall can be calculated after obtaining α from the output of the dynamic inflow model $\mathbf{W}$, and C_l^{dyn} is then used to determine the distributed aerodynamic loads at each blade section. It should be noted that the skewed flow correction, which takes into account the effect induced by the misalignment between the rotor and the main inflow wind direction, is not included in this paper. The influence of this simplification will be discussed later in Section 2.4.2.

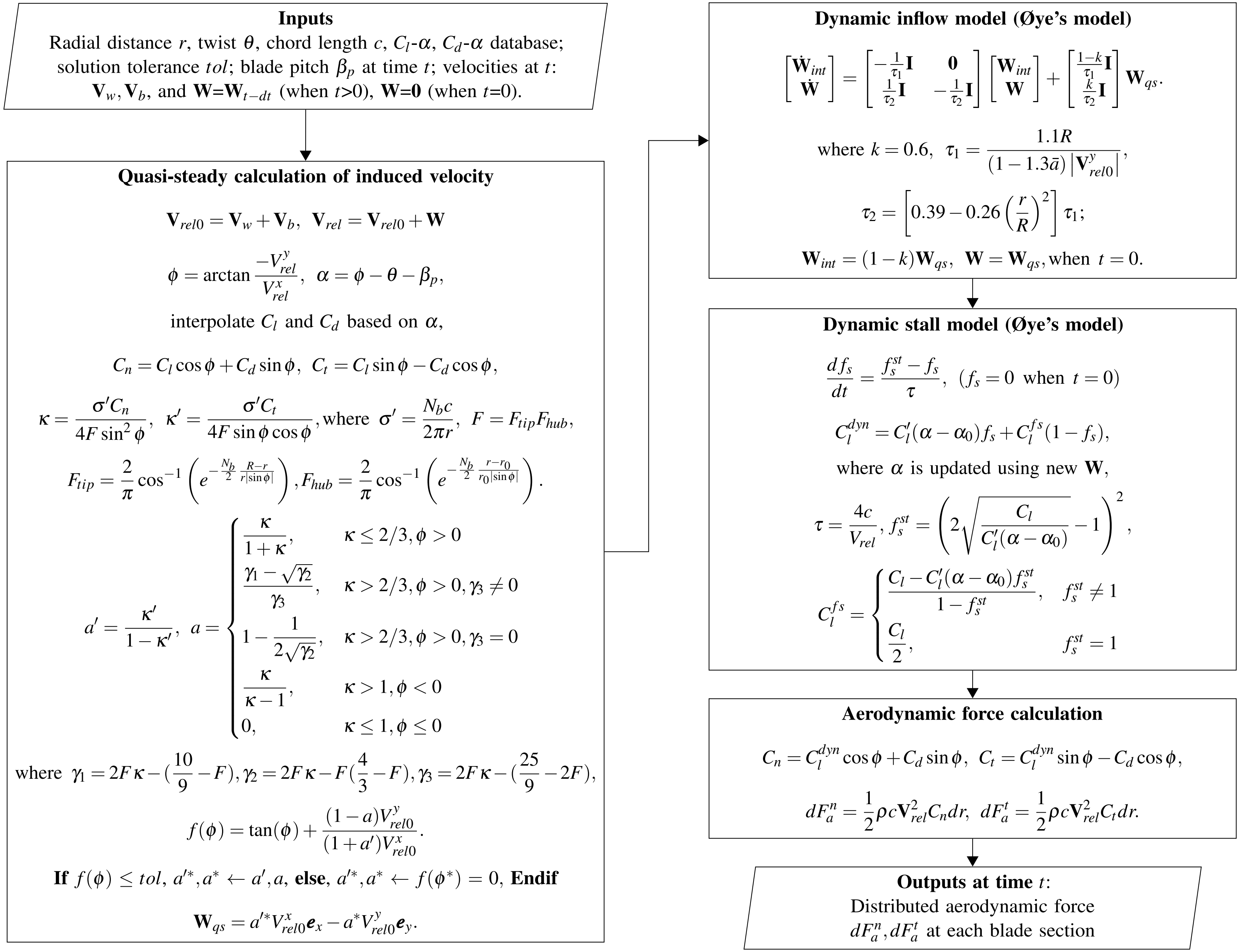

Inputs

Radial distance r, twist θ, chord length c, C_l-α, C_d-α database; solution tolerance tol; blade pitch β_p at time t; velocities at t: $\mathbf{V}_w, \mathbf{V}_b$, and $\mathbf{W}=\mathbf{W}_{t-dt}$ (when t>0), $\mathbf{W}=\mathbf{0}$ (when t=0).

Quasi-steady calculation of induced velocity

$$\mathbf{V}_{rel0} = \mathbf{V}_w + \mathbf{V}_b,\ \ \mathbf{V}_{rel} = \mathbf{V}_{rel0} + \mathbf{W}$$

$$\phi = \arctan\frac{-V_{rel}^y}{V_{rel}^x},\ \ \alpha = \phi - \theta - \beta_p,$$

interpolate C_l and C_d based on α,

$$C_n = C_l\cos\phi + C_d\sin\phi,\ \ C_t = C_l\sin\phi - C_d\cos\phi,$$

$$\kappa = \frac{\sigma' C_n}{4F\sin^2\phi},\ \ \kappa' = \frac{\sigma' C_t}{4F\sin\phi\cos\phi}, \text{where } \sigma' = \frac{N_b c}{2\pi r},\ \ F = F_{tip}F_{hub},$$

$$F_{tip} = \frac{2}{\pi}\cos^{-1}\left(e^{-\frac{N_b}{2}\frac{R-r}{r|\sin\phi|}}\right), F_{hub} = \frac{2}{\pi}\cos^{-1}\left(e^{-\frac{N_b}{2}\frac{r-r_0}{r_0|\sin\phi|}}\right).$$

$$a' = \frac{\kappa'}{1-\kappa'},\ \ a = \begin{cases} \dfrac{\kappa}{1+\kappa}, & \kappa \le 2/3, \phi > 0 \\ \dfrac{\gamma_1 - \sqrt{\gamma_2}}{\gamma_3}, & \kappa > 2/3, \phi > 0, \gamma_3 \neq 0 \\ 1 - \dfrac{1}{2\sqrt{\gamma_2}}, & \kappa > 2/3, \phi > 0, \gamma_3 = 0 \\ \dfrac{\kappa}{\kappa - 1}, & \kappa > 1, \phi < 0 \\ 0, & \kappa \le 1, \phi \le 0 \end{cases}$$

where $\gamma_1 = 2F\kappa - (\frac{10}{9} - F), \gamma_2 = 2F\kappa - F(\frac{4}{3} - F), \gamma_3 = 2F\kappa - (\frac{25}{9} - 2F)$,

$$f(\phi) = \tan(\phi) + \frac{(1-a)V_{rel0}^y}{(1+a')V_{rel0}^x}.$$

If $f(\phi) \le tol$, $a'^*, a^* \leftarrow a', a$, **else**, $a'^*, a^* \leftarrow f(\phi^*) = 0$, **Endif**

$$\mathbf{W}_{qs} = a'^* V_{rel0}^x \boldsymbol{e}_x - a^* V_{rel0}^y \boldsymbol{e}_y.$$

Dynamic inflow model (Øye's model)

$$\begin{bmatrix} \dot{\mathbf{W}}_{int} \\ \dot{\mathbf{W}} \end{bmatrix} = \begin{bmatrix} -\frac{1}{\tau_1}\mathbf{I} & \mathbf{0} \\ \frac{1}{\tau_2}\mathbf{I} & -\frac{1}{\tau_2}\mathbf{I} \end{bmatrix} \begin{bmatrix} \mathbf{W}_{int} \\ \mathbf{W} \end{bmatrix} + \begin{bmatrix} \frac{1-k}{\tau_1}\mathbf{I} \\ \frac{k}{\tau_2}\mathbf{I} \end{bmatrix} \mathbf{W}_{qs}.$$

$$\text{where } k = 0.6,\ \ \tau_1 = \frac{1.1R}{(1-1.3\bar{a})\left|\mathbf{V}_{rel0}^y\right|},$$

$$\tau_2 = \left[0.39 - 0.26\left(\frac{r}{R}\right)^2\right]\tau_1;$$

$$\mathbf{W}_{int} = (1-k)\mathbf{W}_{qs},\ \ \mathbf{W} = \mathbf{W}_{qs}, \text{when } t = 0.$$

Dynamic stall model (Øye's model)

$$\frac{df_s}{dt} = \frac{f_s^{st} - f_s}{\tau},\ \ (f_s = 0 \text{ when } t = 0)$$

$$C_l^{dyn} = C_l'(\alpha - \alpha_0)f_s + C_l^{fs}(1 - f_s),$$

where α is updated using new $\mathbf{W}$,

$$\tau = \frac{4c}{V_{rel}}, f_s^{st} = \left(2\sqrt{\frac{C_l}{C_l'(\alpha - \alpha_0)}} - 1\right)^2,$$

$$C_l^{fs} = \begin{cases} \dfrac{C_l - C_l'(\alpha - \alpha_0)f_s^{st}}{1 - f_s^{st}}, & f_s^{st} \neq 1 \\ \dfrac{C_l}{2}, & f_s^{st} = 1 \end{cases}$$

Aerodynamic force calculation

$$C_n = C_l^{dyn}\cos\phi + C_d\sin\phi,\ \ C_t = C_l^{dyn}\sin\phi - C_d\cos\phi,$$

$$dF_a^n = \frac{1}{2}\rho c\mathbf{V}_{rel}^2 C_n dr,\ \ dF_a^t = \frac{1}{2}\rho c\mathbf{V}_{rel}^2 C_t dr.$$

Outputs at time t:

Distributed aerodynamic force

dF_a^n, dF_a^t at each blade section

Fig. 2.7 Flowchart of the aerodynamics calculation.

2.2.4 Controls

A variable-speed generator-torque controller and a rotor-collective blade-pitch controller are incorporated in the FWT control system. The former regulates the generator rotational speed Ω_g to maximize power generation P_g when the turbine is operating below the rated wind speed, and the latter maintains the generator speed at its rated value when above the rated wind speed. The industry-standard ROSCO strategy [113] is adopted, the control diagram of which is shown in Fig. 2.8. The generator-torque controller includes three main regions and two transition regions in between, based on the low-pass filtered generator speed Ω_g'. Region 1 is before cut-in wind speed, in which the generator torque T_g is fixed to the minimum value. Region 2 is to maximize the power harvesting by forcing the generator torque to be proportional to the square of generator speed by a constant K_{opt}. Region 3 is above the rated wind speed, in which the generator torque is either inversely proportional to generator speed for constant power output (constant power mode, as shown in Fig. 2.8) or kept constant at its rated torque value (constant torque mode). A power generation efficiency of η_g is considered in the power calculation. In the transition regions 1.5 and 2.5, proportional-integral (PI) controllers are used to maintain the minimum optimal generator speed Ω_g^{opm} and reference generator speed Ω_g^{ref}, respectively. The blade-pitch controller is activated when Ω_g' is above Ω_g^{ref} (region 2.5 and 3), and the pitch command β_p^{base} is determined by a gain-scheduling PI law. To avoid the conflict between the generator-torque controller and blade-pitch controller in the near-rated region 2.5, a set-point smoother is adopted to shift their reference values Ω_g^{ref} apart.

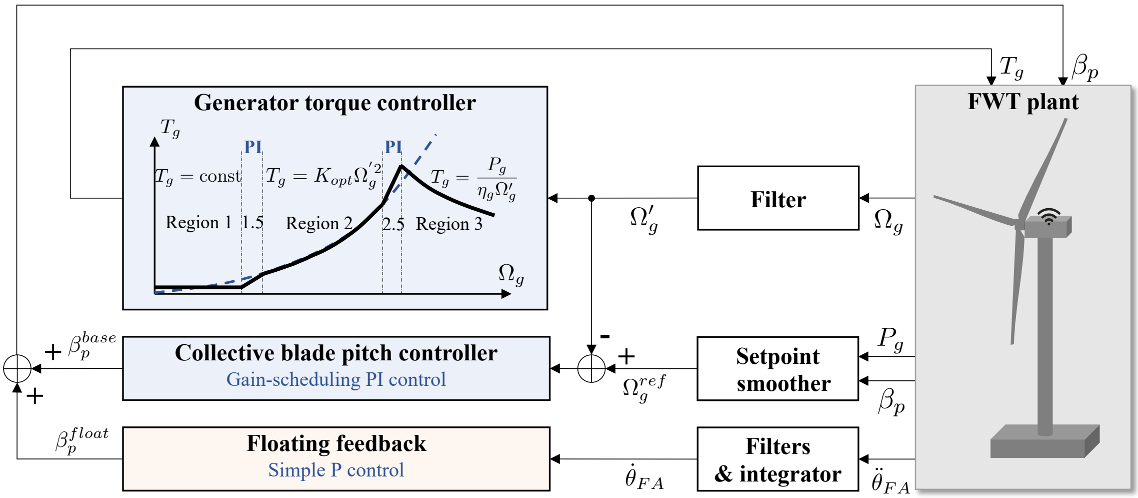

Fig. 2.8 Control diagram for FWTs following the ROSCO strategy with constant power.

When the turbine is operating above the rated wind speed, i.e., the blade-pitch controller is activated, the platform pitch rotation introduces an additional wind velocity felt by the rotor. When the platform is rotating in a downwind direction, the relative wind velocity on the rotor is reduced, leading to a lower blade pitch command and thus higher aerodynamic thrust, which drives the rotor further downwind, and vice versa. This unfavorable coupling effect between the blade pitch controller and platform pitch rotation brings about negative damping to the platform pitch motion. If the fluid radiation damping and moorings damping are not sufficient to counteract this effect, the FWT system becomes unstable.

To overcome this instability issue, a floating feedback control using a simple P gain is introduced in ROSCO, which eliminates the influence of the platform rotation onto the blade-pitch controller. This feedback loop provides an additional pitch command β_p^{float} based on the tower-top fore-aft rotation velocity $\dot{\theta}_{FA}$, as shown in Fig. 2.8. It is worth mentioning that $\dot{\theta}_{FA}$ is not directly measured, instead, it is integrated from the more accessible tower-top rotation acceleration measurements $\ddot{\theta}_{FA}$. To guarantee that only the signal carrying the platform pitch rotation frequency is passed into the floating feedback loop, high-frequency contents in the $\ddot{\theta}_{FA}$ measurement involving, e.g., the tower/blades vibration natural frequencies and blade passing frequencies, must be filtered in advance. On the other hand, $\ddot{\theta}_{FA}$ can be replaced with the platform pitch rotation velocity $\dot{\xi}_5$ directly measured from the onboard inertial measurement unit (IMU) [132], if available. However, whether $\dot{\xi}_5$ is affected by the superstructure behaviour needs further investigation.

2.3 Simulink Implementation

The FWT is a complex assembly of mechanical components including blades, hub, nacelle and tower that are subject to wind loads, floating platform and moorings subject to wave loads, as well as generator and gearbox that operate under the regulation of controllers. Simscape Multibody, a package of MATLAB/Simulink, is utilized in this work to establish the FWT assembly, to apply environmental and operational loads, as well as to measure system responses, through various Simscape blocks summarized in Table 2.1. The loads are determined via the aerodynamics, hydrodynamics and control subsystems created using extensive Simulink libraries. The framework of a generic Simulink FWT model proposed in this work is illustrated in Fig. 2.9, and the visualization is shown in Fig. 2.10.

Table 2.1 Summary of Simscape Multibody blocks used in the developed FWT Simulink model.

Simscape/Multibody block		Usage in the FWT model
Bodies	`Spherical Solid`	Hub, nacelle (lumped mass)
	`Cylindrical Solid`	Hub (rotational inertia)
	`Revolved Solid`	Rigid tower (mass and inertia tensor)
	`Flexible Cylindrical Solid`	Flexible tower substructure (Euler-Bernoulli beam)
	`Extruded Solid`	Rigid blade (distributed lumped mass)
	`Reduced Order Flexible Solid`	Flexible blade substructure (C-B reduced-order FE)
	`File Solid`	Platform from CAD file (mass and inertia tensor)
Joints	`6-DOF Joint`	Platform-water joint to define 3D platform motions
	`Revolute Joint`	Blade pitch, hub rotation, gears for turbine operation
Frames and Constraints	`World Frame`	Earth-fixed coordinate system *O-XYZ*
	`Rigid Transform`	Translation and rotation between connected frames
	`Common Gear Constraint`	Kinematic constraint for gears
Loads and sensors	`External Force and Torque`	Aero/hydro forces and generator torque application
	`Transform Sensor`	Local blade pos/vel, world to rotating-blade frame transformation

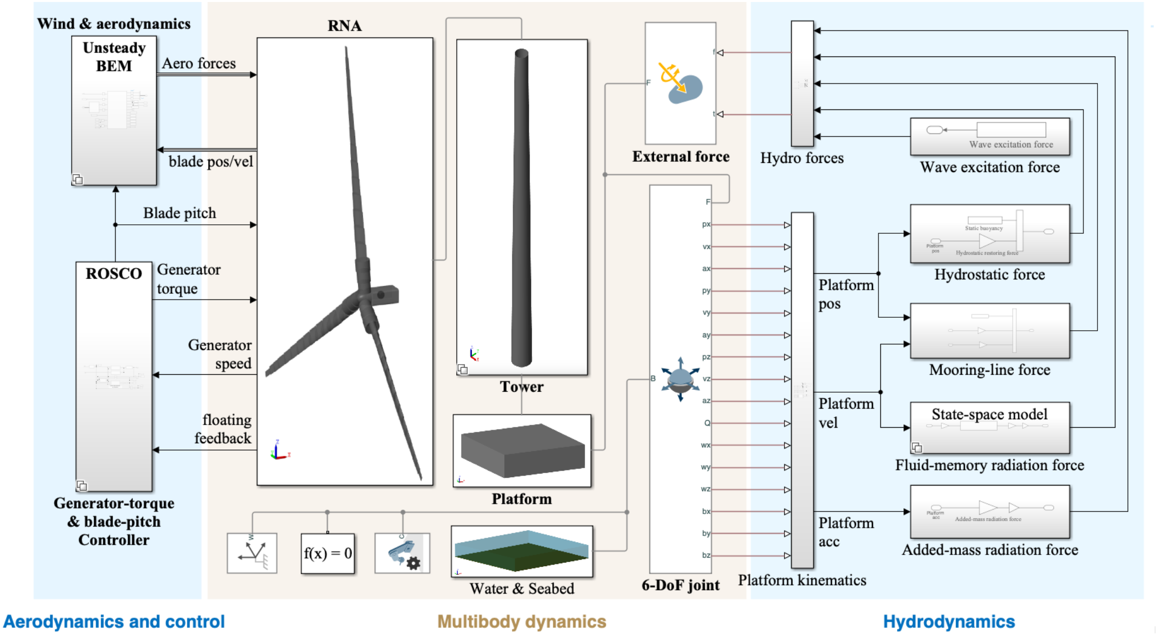

Fig. 2.9 Topology of a generic FWT model implemented in the MATLAB/Simulink environment.

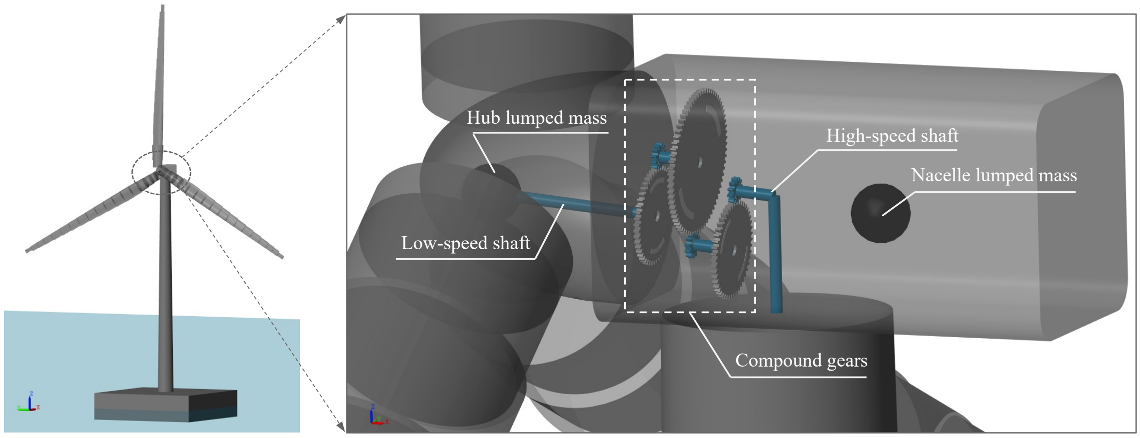

Fig. 2.10 Visualization of the developed Simulink FWT model with a detailed view of the nacelle.

2.3.1 Multibody implementation

As summarized in Table 2.1, the hub, nacelle and platform that have relatively small elastic deformation are modelled as rigid bodies with lumped masses and inertias defined at their centers of mass. The tower and blades can be modelled as a series of either rigid or flexible bodies. The flexible tower body that has a circular hollow cross-section can be represented with a `Flexible Cylindrical Beam`. Given the geometry, material and damping properties, the cross-sectional stiffness and inertia are automatically derived, and the mass, stiffness and damping matrices are subsequently calculated based on the Euler-Bernoulli beam theory. In contrast, the flexible blade body, which typically has an irregular cross-section is modelled as a `Reduced Order Flexible Body`, which defines 6 DoFs for each boundary node and p DoFs for the retained modal coordinates within the body. The required reduced-order mass, stiffness and damping matrices are determined from the Craig-Bampton reduced-order FE modelling described in Section 2.2.2. Simulink allows for multiple subsystem variants, enabling easy switch between rigid and flexible blade/tower models.

All the above mechanical components represented by Simscape blocks are connected to construct the entire FWT system in Simulink following the real-world connectivity, as highlighted in the orange area in Fig. 2.9. Three different connections are used depending on the kinematic relations between the two connected frames. The first connection type, `Rigid Transform`, specifies a fixed translation and/or rotation relations. It is used to connect the platform to tower bottom; to connect the nacelle to tower top; to assemble rigid/flexible tower/blade bodies; to assemble the compound gearbox; and to implement the aerodynamic center offset and gravity center offset of each blade body from the blade pitch axis (see Fig. 2.1 and 2.5), pre-twist angle offset between neighboring blade bodies, pre-cone angle of each blade, and pre-tilt angle of the shafts. The second connection type, joint, specifies the maximum DoFs permitted between the connected bodies. A `6-DOf Joint` is used to define the 3D platform motion with respect to the world frame (O-XYZ in Fig. 2.1), which contains 3 translations and a 3D rotation that is in the singularity-free form of quaternion, allowing for arbitrarily large platform rotations. The `Revolute Joint` is used to implement 1D rotation, including the blade pitch rotation, hub (low-speed shaft) rotation, gears rotation, and generator (high-speed shaft) rotation, as shown in Fig. 2.10. In addition, sensors and actuators built in the joint enable the output of kinematics and the enforcement of joint motions, respectively. The former is used to provide platform position $\boldsymbol{\xi}$, velocity $\dot{\boldsymbol{\xi}}$ and acceleration $\ddot{\boldsymbol{\xi}}$ as inputs to the hydrodynamics subsystem, and generator speed Ω_g as the control input. The latter is used to implement the blade pitch command β_p obtained from the control subsystem. The third connection type, `Common Gear Constraint`, is only used to connect gears. In this work, a simplified three-stage planetary gearbox, as shown in Fig. 2.10, is adopted to convert the low-speed rotation of blades Ω_r driven by wind to the high-speed rotation of the generator Ω_g to harvest electrical energy.

In addition to inbuilt joint sensors, Simscape allows for measuring the spatial relations between any two frames via `Transform Sensor`. To obtain the time-varying absolute position and velocity at local blade cross-sections as the inputs for the aerodynamics calculation, a series of sensors are deployed along the blade, each with one port connected to the boundary node of a blade body and the other to the world frame. Note that, as described in Section 2.2.3, the flow velocities $\mathbf{V}_w$ and $\mathbf{V}_b$ are both in the local blade airfoil coordinate system O_a-$x_a y_a z_a$. To convert the flow velocities from the world frame to the rotating O_a-$x_a y_a z_a$ frame, the Transform Sensor is used to output the instantaneous rotation transform matrix for each blade. The tower-top fore-aft rotating acceleration $\ddot{\theta}_{FA}$ is also measured using a Transform Sensor to provide floating feedback input for the controller. The calculated aerodynamic loads dF_a^n, dF_a^t at each blade section, hydrodynamic loads $\mathbf{F}_{hydro}$ at the platform origin O, as well as generator torque T_g at the high-speed shaft, are applied to the corresponding components via `External Force and Torque` blocks.

2.3.2 Aerodynamics implementation

In the wind & aerodynamics subsystem, 4-D look-up tables are used to store the time series of a spatial wind velocity field generated by pre-processing tools, e.g., TurbSim [127]. The local blade absolute positions passed from the multibody subsystem are used to interpolate the instantaneous inflow wind velocities on each blade section. The interpolated local wind velocities and measured blade velocities are converted to the local airfoil coordinates O_a-$x_a y_a z_a$ via the instantaneous rotation transform matrix described in Section 2.3.1. The converted local flow velocities $\mathbf{V}_w$ and $\mathbf{V}_b$, together with the blade pitch angle β_p, are subsequently used to determine the aerodynamic force based on the dynamic blade-element momentum method described in Fig. 2.7. The obtained distributed aerodynamic forces are then passed back to the multibody subsystem and applied to each blade section.

2.3.3 Hydrodynamics implementation

In the pre-processing step, hydrodynamic coefficients $\boldsymbol{\lambda}_\infty, \boldsymbol{\lambda}(\omega), \boldsymbol{\mu}(\omega), \mathbf{K}_{hs}$ and $\mathbf{K}_e(i\omega)$ are usually obtained from boundary element codes, e.g., WAMIT [131]. The wave radiation damping force $\mathbf{F}_r$ can be computed via either convolution integral (Eq. (2.2)) or the state-space model $[\mathbf{A}_r, \mathbf{B}_r, \mathbf{C}_r]$ identified from $\mathbf{K}_r(i\omega_k)$ using the direct-MIMO N4SID method, as illustrated in Fig. 2.2. The wave excitation force $\mathbf{F}_e$ can be calculated via either the inverse Fourier transform (Eq. (2.5)), or the state-space model $[\mathbf{A}_e, \mathbf{B}_e, \mathbf{C}_e]$ identified from $\mathbf{K}_e(i\omega_k)$ using the direct-MIMO N4SID method, as illustrated in Fig. 2.4. The implementation is then carried out via independent subsystems, each corresponding to a force component in Fig. 2.1. The hydrostatic stiffness $\mathbf{K}_{hs}$ and infinite-frequency added mass $\boldsymbol{\lambda}_\infty$ are multiplied by the instantaneous platform displacement $\boldsymbol{\xi}$ and acceleration $\ddot{\boldsymbol{\xi}}$ to get the hydrostatic restoring force and added-mass radiation force, respectively. The wave radiation convolution-integral/state-space model receives the platform velocity $\dot{\boldsymbol{\xi}}$ as input to calculate the fluid-memory radiation force $\mathbf{F}_r$. The wave excitation force $\mathbf{F}_e$ can be either imported as time-series data in Simulink, or calculated by passing the wave elevation η_o to the wave excitation state-space model. The mooring lines are simplified as linear 6×6 stiffness and damping matrices. The aforementioned forces as well as the weight of moorings and displaced water by the platform are summed and applied to the 6-DoF water-platform joint, as shown in Fig. 2.9.

2.3.4 Controls implementation

As described in Section 2.2.4, the low-pass filtered Ω_g fed into the control subsystem is taken as the input to determine the blade pitch β_p^{base} and generator torque T_g commands. To avoid the negative damping issue, a floating feedback with the input of the filtered and integrated tower-top $\ddot{\theta}_{FA}$ is implemented, which yields an additional blade pitch command β_p^{float}. The total blade pitch β_p is passed to each blade-root revolute joint as the actuation input, and the torque command T_g is passed to the high-speed shaft as an external load to regulate the generator rotation. Given the negligible difference in the system reponses between constant power and constant torque modes when a floating feedback control loop is introduced, the constant power mode is adopted in this work.

2.3.5 Equations of Motion

After building the full FWT system and specifying wind and wave excitations, the dynamic analysis can be carried out. The different nature of POP-based mathematical model (aero-hydro-control subsystems, i.e., blue area in Fig. 2.9) and OOP-based physical model (multibody subsystems, i.e., orange area) determines different approaches to obtaining their EoMs. The mathematical model follows a certain input-output logic sequence, and uses wires with arrows to indicate the signal flow. The EoMs are established explicitly through the specified inputs and outputs. In contrast, no explicit cause-and-effect relations are defined in the physical model and thus wires without arrows are used as connections. Simulink determines the causality and integrates the EoMs from individual physical subsystems during the model compilation based on their interconnections. The communication between the mathematical and physical models requires `Simulink-PS Converter` and `PS-Simulink Converter` blocks. Eventually, the incorporated EoMs can be numerically solved using Simulink inbuilt ODE solvers. As the use of flexible blade/tower substructures greatly increases the numerical stiffness of the system, a stiff solver such as `ode15s` is suggested.

2.4 Investigation of Individual Dominant FWT Physics

The FWT dynamic system is multi-physics involved and the following sections investigate them individually to provide deeper insights on each process. The dominant FWT physics discussed in this work mainly encompass the wave-platform interaction; unsteady aerodynamics induced by platform motions; interaction between the blade-pitch controller and platform motions; and the nonlinear behaviour of highly flexible rotating blades. The developed Simulink model allows for the inspection of each process by only activating the associated subsystems. The NREL 5-MW ITI-Barge floating wind turbine is taken as an example. For detailed geometrical and mechanical properties, as well as operating parameters, the readers are referred to [63]. The dynamic behaviour of the example FWT predicted by the Simulink model on each of the afore-mentioned processes are compared against that calculated from OpenFAST (v3.5.3), and practical suggestions are provided.

2.4.1 Wave-platform interaction

The effectiveness of the developed direct-MIMO state-space identification approach for both the wave radiation and excitation models, as detailed in Section 2.2.1.1 and Section 2.2.1.2, respectively, are investigated on the example ITI-Barge floating platform. The advantages of the newly proposed direct-MIMO approach in evaluating both wave-platform interaction effects are demonstrated through comparisons with the conventional multi-SISO approach.

2.4.1.1 Wave radiation model

The radiation state-space identification approach proposed in Section 2.2.1.1 is demonstrated on the example ITI-Barge platform. The non-zero entries of the frequency response matrix $\mathbf{K}_r(i\omega_k)$ calculated from WAMIT at $\omega_k = 0.05, 0.1, 0.15, \ldots 5$ rad/s are shown in Fig. 2.11. For better identification quality, the original $\mathbf{K}_r(i\omega_k)$ are scaled by a matrix $\mathscr{K}=\mathscr{K}_f\mathscr{K}_u{}^{\mathsf{T}}$, where $\mathscr{K}_f=\mathscr{K}_u=\begin{bmatrix}1 & 1 & 2 & r_g & r_g & r_g\end{bmatrix}^{\mathsf{T}}$ and r_g is the approximate radii of gyration of the platform pitch/roll/yaw DoF which is around 10 m. The function `ssest` from the system identification toolbox of MATLAB (2023b) is utilized to perform the direct-MIMO identification, and a tentative state number of 18 is selected. In order to suppress the effects of large oscillations in WAMIT $\mathbf{K}_r(i\omega_k)$ at $\omega > 3$ rad/s (see Fig. 2.11), a small weight of 0.001 is applied to samples above 3 rad/s in the `ssest` function. The identified poles whose damping ratios are smaller than 0.05 are also removed, yielding the final 16 states for the identified frequency response, which is shown in Fig. 2.11. The frequency response identified using the multi-SISO method via SS_Fitting [117], which is suggested in OpenFAST, is also compared in Fig. 2.11. A total of 30 states are used in the multi-SISO method which is the sum of states identified from each non-zero entry of $\mathbf{K}_r(i\omega_k)$. The MIMO identification is demonstrated to offer a more efficient representation of the radiation model by using only about half the number of states compared to the multi-SISO method (16 vs. 30) and capturing even more resonance peaks, e.g. around 1.8 rad/s in the yaw-yaw $\mathbf{K}_r(i\omega_k)$ as shown in Fig. 2.11. Therefore, the MIMO method is recommended for the state-space identification of the wave radiation model.

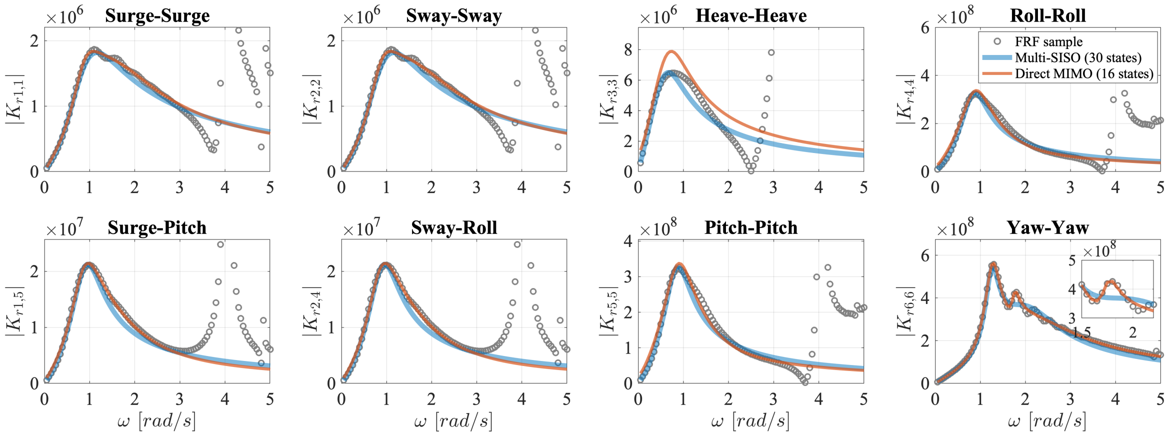

Fig. 2.11 Comparison of the wave radiation frequency response function (FRF) samples of the ITI-Barge floating platform obtained from WAMIT, and the FRFs identified using multi-SISO and direct-MIMO approaches.

The state-space matrices $[\mathbf{A}_r, \mathbf{B}_r, \mathbf{C}_r]$ identified via the proposed direct-MIMO method are used to calculate the fluid-memory radiation damping force $\mathbf{F}_r$ in the Simulink model. A free decay test is examined to compare the platform response of the Simulink model with that calculated from OpenFAST, which uses the conventional multi-SISO identification method. To narrow the difference of the wave-platform interaction modelling between the Simulink model and OpenFAST to only the identified radiation state-space matrices, the same $\mathbf{F}_{b0}, \boldsymbol{\lambda}_\infty$ and $\mathbf{K}_{hs}$ are used in both models to calculate the corresponding hydro-mechanical force in Eq. (2.1). In addition, the linear stiffness K_{moor} and damping C_{moor} matrices

$$K_{moor} = \begin{bmatrix} 15900 & 0 & 0 & 0 & 205100 & 0 \\ 0 & 15900 & 0 & -205200 & 0 & 0 \\ 0 & 0 & 24900 & 0 & 11400 & 0 \\ 0 & -208000 & 0 & 26445800 & -10800 & -3100 \\ 208000 & 0 & 0 & 10700 & 26443100 & 0 \\ 0 & 0 & 0 & -666000 & 0 & 24657900 \end{bmatrix}, \tag{2.28}$$

$$C_{moor} = \begin{bmatrix} 33100 & 0 & 0 & 0 & 231500 & 0 \\ 0 & 33100 & 0 & -231600 & 0 & 0 \\ 0 & 0 & 1997900 & 0 & 5500 & 0 \\ 0 & -232300 & 0 & 294004300 & -1000 & -94800 \\ 232300 & 0 & 4700 & 1000 & 293586500 & 0 \\ 0 & 0 & 0 & 11800 & 0 & 19846000 \end{bmatrix} \tag{2.29}$$

that are used to represent the moorings in the Simulink model are set as additional matrices in HydroDyn, the hydrodynamic solver in OpenFAST, and thus no separate mooring calculation solver is required in the OpenFAST simulation. In the free decay test, only 6 platform

DoFs are activated and the FWT oscillates freely in still water from an initial pitch rotation angle of 4° without wind/wave actions and aerodynamic calculation. An initial platform heave displacement of $-0.127m$ is assumed to account for the additional displaced water by moorings weight and thus reduce initial transients. The platform motions obtained from the Simulink model and OpenFAST are compared in Fig. 2.12. It can be seen that the platform shows almost planar movement and the pitch motion (ξ_5) matches very well between the two models. The slight mismatch in heave ξ_3 can be explained by the discrepancy in the identified heave-heave $K_{r3,3}(\omega)$ of the two models as shown in Fig. 2.11, and the slight difference in surge ξ_1 is due to the coupling between surge-heave-pitch DoFs in the mooring stiffness (Eq. (2.28)).

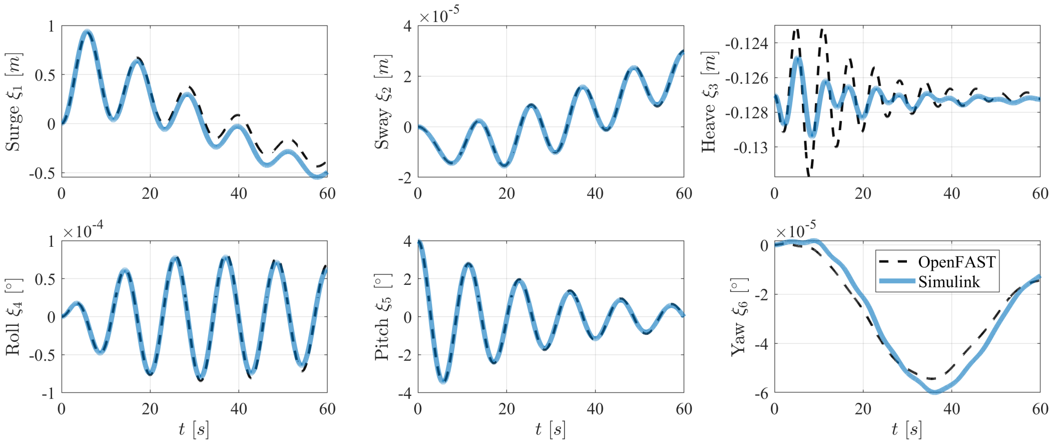

Fig. 2.12 Comparison of the platform motions obtained from the Simulink model and OpenFAST (HydroDyn) for the example NREL 5-MW ITI-Barge FWT under an initial platform pitch rotation of 4° in still water.

2.4.1.2 Wave excitation model

The excitation state-space identification approach described in Section 2.2.1.2 is demonstrated on the example ITI-Barge platform, and the excitation frequency response samples are also obtained from WAMIT at $\omega_k = 0.05, 0.1, 0.15, \ldots 5$ rad/s. The incident wave is assumed to be along the positive X direction, and thus only the forces in surge, heave, and pitch DoFs are non-zero. The impulse response functions $\mathbf{k}_e(t)$ processed using the conventional multi-SISO approach are shown in Fig. 2.13, which compares the original impulse response samples computed from the inverse Fourier transform of $\mathbf{K}_e(i\omega_k)$, the impulse response samples that are time-shifted by $t_c = 12$s from the original ones, and the impulse responses of the state-space model $[\mathbf{A}_e, \mathbf{B}_e, \mathbf{C}_e]$ estimated via the realization theory (`imp2ss` function of

MATLAB) with 30 states retained. The results indicate that the causalized impulse response samples are effectively captured by the multi-SISO state-space model.

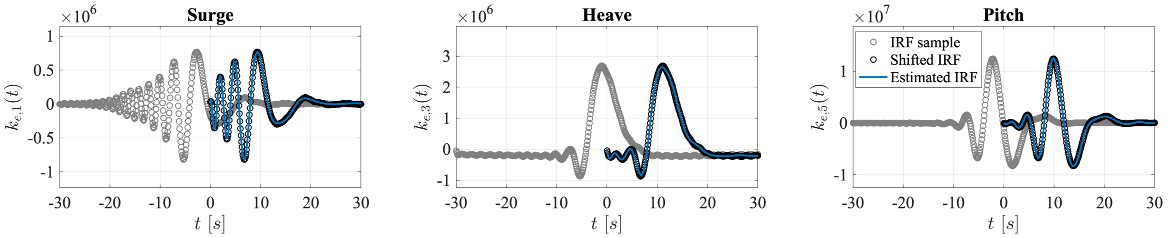

Fig. 2.13 Causalization of the wave excitation impulse response function (IRF) samples and the IRFs estimated by the multi-SISO approach.

The direct-MIMO identification method proposed in this work is implemented on $\mathbf{K}_e(i\omega_k)$ using the `ssest` function of MATLAB (2023b), with a negative time delay of -12s and a state number of 14. The magnitude and phase angle of frequency responses estimated via the direct-MIMO approach are shown in Fig. 2.14, which are compared with the original frequency response samples obtained from WAMIT, and those estimated using the conventional multi-SISO method. It can be found from Fig. 2.14 that the newly proposed direct-MIMO identification method outperforms the multi-SISO method with better fitting quality especially in low frequencies and a smaller number of model states (14 vs. 30).

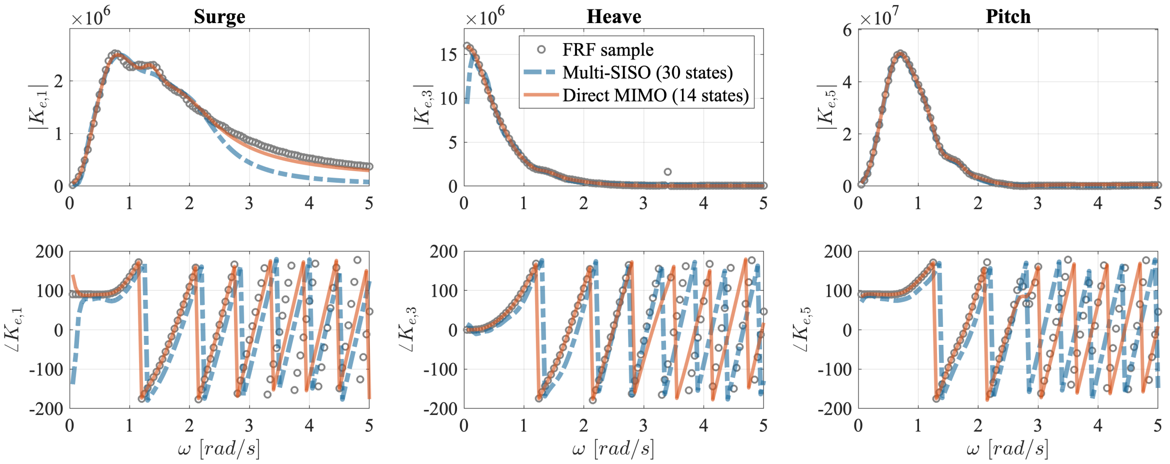

Fig. 2.14 Comparison of the wave excitation frequency response function (FRF) samples of the ITI-Barge floating platform obtained from WAMIT, and the FRFs identified using multi-SISO and direct-MIMO approaches.

The state-space matrices $[\mathbf{A}_e, \mathbf{B}_e, \mathbf{C}_e]$ estimated via both the proposed direct-MIMO method and the conventional multi-SISO method are used to calculate the wave excitation force $\mathbf{F}_e$ given a wave elevation. Fig. 2.15 compares the time series of the resulting wave excitation forces with those calculated directly from the benchmark inverse Fourier transform method, as described in Eq. (2.5). As the initial states are not estimated for both identification methods, discrepancies can be found at the beginning of the force time series. However, the direct-MIMO results approach the benchmark much faster than the multi-SISO results. Considering its higher accuracy and efficiency, the readers are suggested to use the direct-MIMO method for the state-space identification of the wave excitation model.

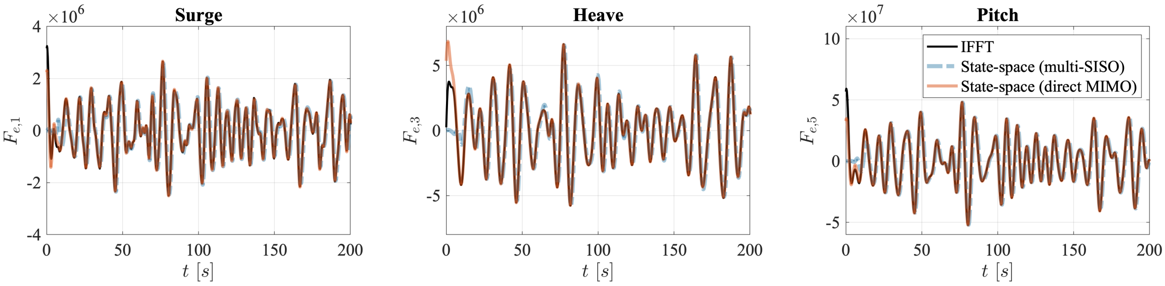

Fig. 2.15 Comparison of the wave excitation force time series of the ITI-Barge floating platform computed from the inverse Fourier transform in Eq. (2.5), and those computed from the state-space models estimated using the conventional multi-SISO and newly-proposed direct-MIMO approaches.

2.4.2 Aero-platform interaction

A platform pitching test on an operating FWT is conducted to examine the influence of platform rotations on the rotor aerodynamics. The relative wind seen by the rotor undergoes great changes under platform pitch rotations due to the long lever arm of the tower height, leading to time-varying wake and stall behaviours on local blade sections. As such, all aerodynamic calculation procedures illustrated in Fig. 2.7 are involved and are equally important. To validate the Simulink implementation of these procedures, AeroDyn (v15), the standalone aerodynamic solver of OpenFAST, is adopted as the benchmark, which includes the blade-element momentum calculation, dynamic inflow state-space model, and one-state dynamic stall model that are similar to those in the developed Simulink model, as well as the skewed-flow correction that is not taken into account in the Simulink model.

The rotor is operating at the rated conditions of constant uniform wind velocity $V_0 = 11.4$ m/s, rotor speed $\Omega_r = 12.1$ rpm, and blade pitch angle $\beta_p = 0°$. A sinusoidal rotation with the amplitude of 4° and period of 10s, as shown in Fig. 2.16, is applied to the platform pitch DoF ξ_5. All other platform DoFs are fixed, the blades and tower subsystems are switched to rigid, and the shaft tilt and blade pre-cone angles are set to 0, such that the changes in the relative wind only source from platform pitch rotations. The aerodynamic torque T_a calculated from the Simulink model and the benchmark AeroDyn solver are compared in Fig.

2.16. The time-varying axial induction factor a, dynamic stall state f_s and the C_l-α curve at the middle section of one blade are illustrated in Fig. 2.17.

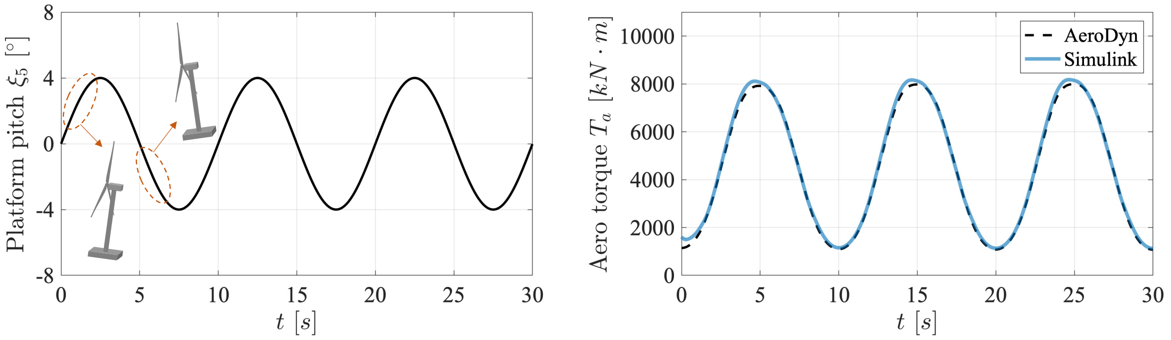

Fig. 2.16 The sinusoidal platform pitch rotation applied to the NREL 5-MW turbine, and the comparison of aerodynamic torque T_a calculated from Simulink model against AeroDyn, under constant wind $V_0 = 11.4$ m/s, $\Omega_r = 12.1$ rpm, and $\beta_p = 0°$.

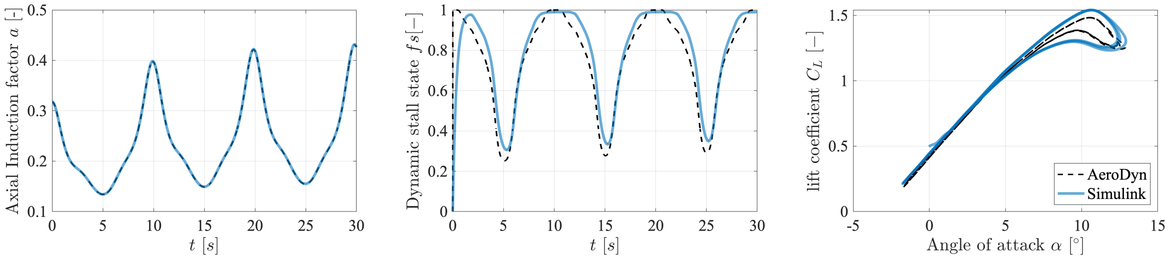

Fig. 2.17 Comparison of the aerodynamic behaviours of the NREL 5-MW turbine calculated from Simulink model against AeroDyn under sinusoidal platform pitch rotation. The axial induction factor (a), dynamic stall state (f_s), angle of attack (α) and lift coefficient (C_l) are values at the middle section (i.e. $r = 30.75$ m from the blade root).

It can be observed from Fig. 2.16-2.17 that the aerodynamic torque T_a, induction factor a and dynamic stall state f_s vary periodically with the platform pitch rotation ξ_5 in the same frequency. The local minimum T_a occurs at the positive maximum pitch rotation velocity when e.g. $t = 0$s, as the downwind pitch rotation introduces an opposite component to the inflow wind velocity, leading to a minimum $|V_{rel}^y|$, and thus local minimum ϕ, α, C_l whereas local maximum a. Flow around the blade section tends to be fully-attached and hence increases f_s to 1 from the initial 0 state. In contrast, the local maximum T_a, as well as local minimum a, occur at the negative maximum pitch rotation velocity when e.g. $t = 5$s, as $|V_{rel}^y|, \phi, \alpha, C_l$ reach their peak values when the rotor is moving against wind with the greatest velocity. Flow around the blade section tends to be more separated due to the increase of α, which yields a local minimum f_s. The C_l hysteresis resulting from the dynamic stall effect under large α is captured by both models. The C_l here represents C_l^{dyn} described in

Fig. 2.7. The discrepancies of f_s and the C_l-α hysteresis loop size between the two models are caused by different equations used in calculating the separation parameters and time constant. Despite the discrepancies in dynamic stall, the two aerodynamic torque T_a results show excellent agreement, which verifies the accuracy of the Simulink implementation of the aerodynamic model. It can also be concluded that the neglected skewed-flow effect in the Simulink model shows limited influence on the aerodynamic performance under the rotor tilt as large as 4° for this example FWT.

2.4.3 Controller-platform interaction

To investigate the interaction between the blade-pitch controller and platform rotation, a FWT simulation test under a constant uniform above-rated wind speed of 14 m/s is performed on the Simulink model, with the aerodynamic, hydrodynamic and control subsystems activated. Only the 6 platform DoFs are enabled and the irregular wave excitation forces shown in Fig. 2.15 are applied. The FWT behaviours are compared against those obtained from OpenFAST coupled with ROSCO (v2.8.0). The filter parameters used in both models are summarized in Table 2.2. Fig. 2.18 compares the total blade pitch β_p, platform pitch rotation ξ_5, rotor speed Ω_r and generator power output P_g simulated from the Simulink model and OpenFAST, under the baseline control (without floating feedback) and the augmented control with floating feedback. The results indicate that the two models match well for both configurations, verifying the controls implementation in Simulink.

Table 2.2 Parameters of controller filters.

Filter	Generator speed LPF	Set-point smoother LPF	Floating feedback LPF	Floating feedback HPF	Floating feedback NF
Representation	$\frac{\omega_c}{s+\omega_c}$	$\frac{\omega_c}{s+\omega_c}$	$\frac{\omega_c^2}{s^2+2\omega_c\zeta_c s+\omega_c^2}$	$\frac{s}{s+\omega_c}$	$\frac{s^2+\omega_c^2}{s^2+2\omega_c\zeta_c s+\omega_c^2}$
Frequency ω_c $[rad/s]$	1.5708	0.6283	0.55	0.0104	3.355
Damping ζ_c $[-]$	/	/	1	/	0.25

LPF: low-pass filter; HPF: high-pass filter; NF: notch filter.

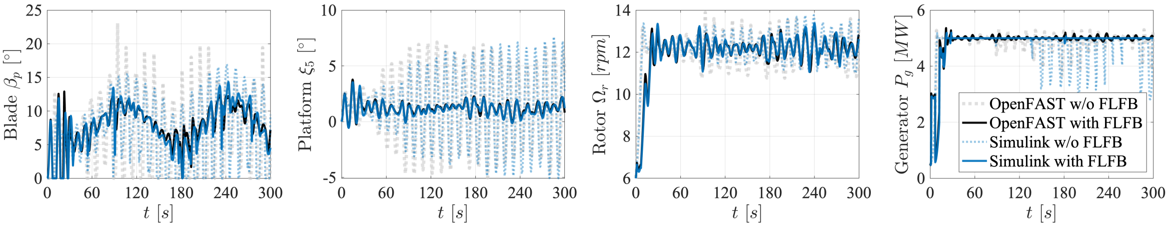

Fig. 2.18 Comparison of the blade pitch β_p, platform pitch rotation ξ_5, rotor speed Ω_r, and generator power output P_g between the Simulink model and OpenFAST-ROSCO, each with and without floating feedback (FLFB), under constant wind $V_0 = 14$ m/s and irregular wave excitation forces shown in Fig. 2.15.

The negative damping effect described in Section 2.2.4 can be found through the large oscillations in platform pitch response ξ_5 and power output P_g in Fig. 2.18. A floating feedback loop with a simple proportional (P) gain of 20s is introduced, which gives an additional blade pitch command β_p^{float} to counteract the negative effect induced by platform rotations. For example, during $0-8$s when the baseline control is not activated as Ω_r has not reached its rated value (12.1 rpm), the floating feedback outputs a positive β_p^{float} which alleviates the increased aerodynamic loads due to the platform rotation, and in turn reduces the platform rotation response. When Ω_r reaches its rated value, the floating feedback effectively works with the baseline control to stabilize the platform response and regulate the power output to its rated value, as shown in Fig. 2.18.

2.4.4 Large deformation of flexible rotating blades

To evaluate the dynamic behaviour of flexible blades undergoing large rigid-body motions, a blade rotation test is performed. The tower and platform DoFs are fully constrained, no winds and waves are applied, and the blades rotate constantly in the vertical plane at the rated speed of 12.1 rpm solely subject to gravity as the external load. The ability of the multibody formulation described in Section 2.2.2 to capture the nonlinear dynamics of the rotating blade is examined on the developed Simulink model. A total of 49 cross-section geometric, stiffness and inertial properties of the 61.5-meter NREL 5-MW FWT blade are provided. These 49 sections give at least 2 and at most 48 substructures for the multibody modelling of each blade. Fig. 2.19 demonstrates a single blade using two example numbers of substructures (i.e. Simscape reduced-order flexible bodies). The required reduced-order mass, stiffness and damping matrices for each substructure are determined from Eq. (2.22). To simplify the FE formulation, the cross-section tension center T, shear center S and gravity center G are all assumed to be located at the reference point O_e, and T-$x_t y_t z_t$, G-$x_g y_g z_g$

coordinates to be coincident with O_e-$x_e y_e z_e$ (i.e. x_t=y_t=x_s=y_s=x_g=y_g=0, and α_t=α_g=0 in Fig. 2.5).

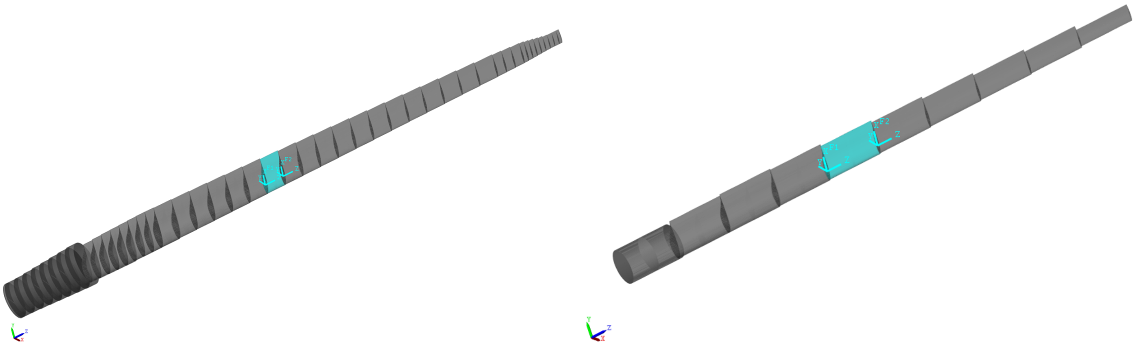

(a) 48 substructures

(b) 10 substructures

Fig. 2.19 Multibody formulation of a single blade using (a) 48 and (b) 10 substructures, with an example substructure highlighted in both cases.

To decide the appropriate number of substructures (N) and the retained number of modal coordinates (p) within each substructure to be used in the Simulink model, a convergence test is carried out. BeamDyn, a blade dynamics solver in OpenFAST, employs the geometrically exact nonlinear beam theory which accurately captures nonlinear displacement-strain relations and beam kinematics [133], and is thus taken as the benchmark. Each blade in BeamDyn is represented by a single 5^{th}-order Legendre spectral finite element. Fig. 2.20 compares the elapsed time and blade-tip responses error of the Simulink blade models with different combinations of $N's$ and $p's$ against BeamDyn. Generally speaking, the more substructures the blade is split into (larger N), the more accurate the Simulink multibody blade model is, and for a specific number of substructures, the more modes that are retained (larger p), the longer the simulation runs. As a trade-off between computational cost and accuracy, the 10-substructure Simulink blade model with each substructure retaining the first 1/8 internal modes is selected, which is highlighted in Fig. 2.20.

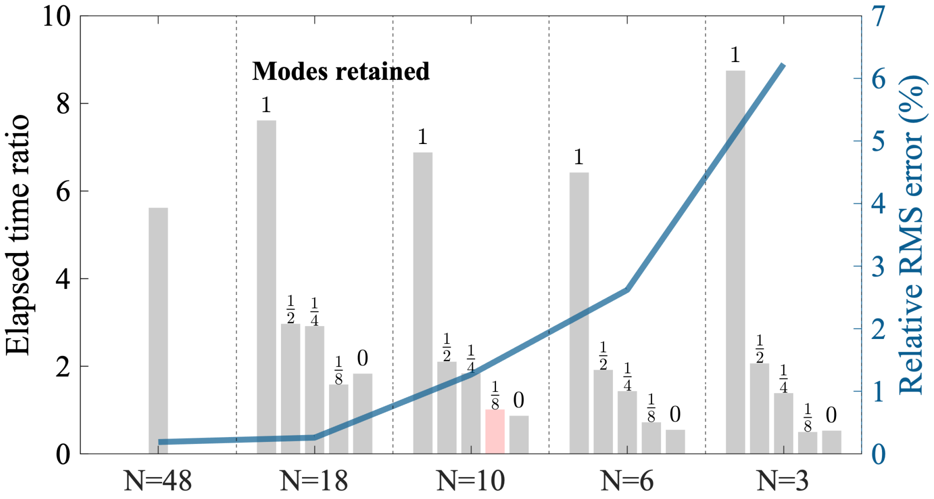

Fig. 2.20 Comparison of elapsed time and blade-tip responses error between Simulink blade models and BeamDyn. Simulink models involve the blade represented with 48, 18, 10, 6 and 3 substructures, and each substructure with all (1), first one-half (1/2), first one-fourth (1/4), first one-eighth (1/8) and none (0) internal modes retained. Elapsed time ratio = Simulink/BeamDyn, and relative root mean square (RMS) error = RMS(Simulink−BeamDyn)/RMS(BeamDyn).

The blade-tip deformations of the "$N = 48$" and "$N = 10, p = 1/8$-modes" Simulink models are compared against BeamDyn in Fig. 2.21. The "$N = 48$" Simulink model shows excellent agreement with BeamDyn, which indicates the ability of the developed Simulink multibody blade model in accurately capturing the geometric nonlinearity. The "$N = 10$" model agrees with BeamDyn in general except for a twist offset of around $0.25°$, which is the rounding error due to taking the mean pre-twist angle for the outermost (10^{th}) substructure. Fig. 2.21 also compares the results simulated from ElastoDyn, which has been widely used as a computationally efficient tool to model the wind turbine structure. In ElastoDyn, the blade deformation displacement field is integrated from the linear superposition of local curvatures induced by the first two flapwise-bending and first edgewise-bending modes of the whole blade. In order for the curvatures to be additive, small translation and rotation assumptions must hold. Whilst ElastoDyn considers some geometric and kinematic nonlinearities (such as centrifugal stiffening, Coriolis and gyroscopic effects), the inherent small deformation assumption still leads to discrepancies in the in-plane and out-of-plane rotations between ElastoDyn and BeamDyn, as shown in Fig. 2.21. In contrast, the multibody formulation enables the Simulink blade models to accommodate large translations and rotations. Additionally, the axial and torsion DoFs are neglected in ElastoDyn, which is another important source of discrepancies in the axial extensions between ElastoDyn and the other three models.

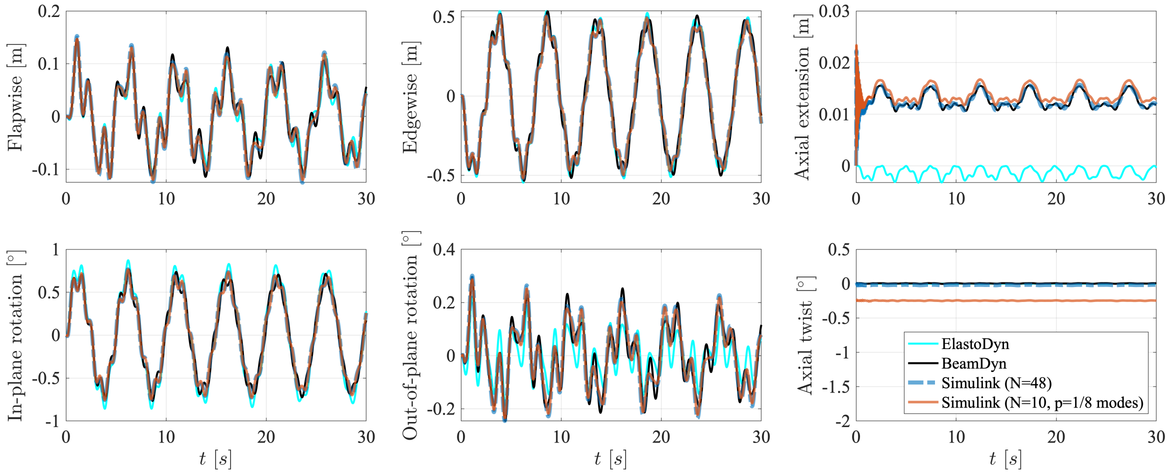

Fig. 2.21 Comparison of 6 blade-tip deflections in the blade-root coordinates O_b-$x_b y_b z_b$ between ElastoDyn, BeamDyn, 48-substructure Simulink model, and 10-substructure 1/8-modes-retained Simulink model.

2.5 Full-system Dynamic Analysis

After a close inspection of the dominant physics associated with FWTs individually, the full-system dynamic analysis is conducted on the developed Simulink FWT model. A modal analysis is first carried out under the parked rotor condition to examine the coupling between blades, tower and platform. It is followed by the FWT responses analysis under realistic environmental conditions of turbulent winds and irregular waves, with the aim to further investigate the findings that are shown in Section 2.4 on the interaction between different FWT subsystems in a holistic manner. The NREL 5-MW ITI-Barge FWT is again taken as an example and the simulation results are compared against those obtained from OpenFAST (v3.5.3). All DoFs of the platform, flexible tower, and flexible blades are taken into account. The tower is split into 11 substructures, and each blade is split into 10 substructures and within each the first 1/8 internal modes are retained, as described in Section 2.4.4.

2.5.1 Modal analysis

The linearization analysis of the nonlinear Simulink FWT model is performed through the `Model Linearizer App` in Simulink. No wind and wave excitations are applied, the rotor is parked by fixing the drivetrain torsion, and the aerodynamic and control subsystems are disabled. The benchmark OpenFAST model is configured accordingly, with ElastoDyn and BeamDyn enabled, with moorings weight, stiffness and damping matrices modelled in HydroDyn, and with AeroDyn and ServoDyn disabled. The natural frequencies of 6 platform modes, the first 2 tower fore-aft (FA) and side-to-side (SS) modes, as well as the first 3 blade flapwise and edgewise modes of the example FWT obtained from Simulink and OpenFAST linearization analyses are compared in Table 2.3. The corresponding tower and blade modeshapes post-processed from the Simulink linearization results are shown in Fig. 2.22. Pronounced couplings can be observed between the platform pitch rotation, 1^{st} tower FA bending and 1^{st} blade flapwise bending modes; between the platform roll rotation, 1^{st} tower SS bending and 1^{st} blade edgewise bending modes; between the 2^{nd} tower FA and 2^{nd} blade flapwise bending modes; and between the 2^{nd} tower SS and 2^{nd} blade edgewise bending modes.

Table 2.3 Natural frequencies of the 5-MW ITI-Barge FWT model.

Modes	OpenFAST (Hz)	Simulink (Hz)	Difference (%)
Platform surge	0.0071	0.0071	0
Platform sway	0.0071	0.0071	0
Platform heave	0.1452	0.1274	-12.2590
Platform roll	0.0844	0.0839	-0.5924
Platform pitch	0.0840	0.0841	0.1190
Platform yaw	0.0190	0.0190	0
1^{st} Tower fore-aft (FA)	0.5316	0.5307	-0.1693
1^{st} Tower side-to-side (SS)	0.5754	0.5355	-6.9343
2^{nd} Tower fore-aft (FA)	2.9476	2.9272	-0.6921
2^{nd} Tower side-to-side (SS)	2.8695	2.8874	0.6238
1^{st} Blade asymmetric flapwise 1	0.6784	0.6452	-4.8939
1^{st} Blade asymmetric flapwise 2	0.6839	0.6744	-1.3891
1^{st} Blade collective flap (flapwise 3)	0.7048	0.7019	-0.4115
1^{st} Blade collective lag (edgewise 1)	1.0374	1.0145	-2.2074
1^{st} Blade asymmetric edgewise 2	1.0648	1.0836	1.7656
1^{st} Blade asymmetric edgewise 3	1.0830	1.0977	1.3573

The slight discrepancies in natural frequencies calculated from the developed Simulink model and OpenFAST model are induced by the following reasons:

- *Different blades/tower modelling methods*

  The tower deformation of the OpenFAST model is represented using the first 2 FA and first 2 SS tower modes in ElastoDyn, which does not account for the axial extension and torsion. As a result, it fails to capture the interaction between the tower axial extension and platform heave modes, as well as the interaction between the blade asymmetric flapwise vibration, tower torsion, and platform yaw rotation modes. In contrast, the

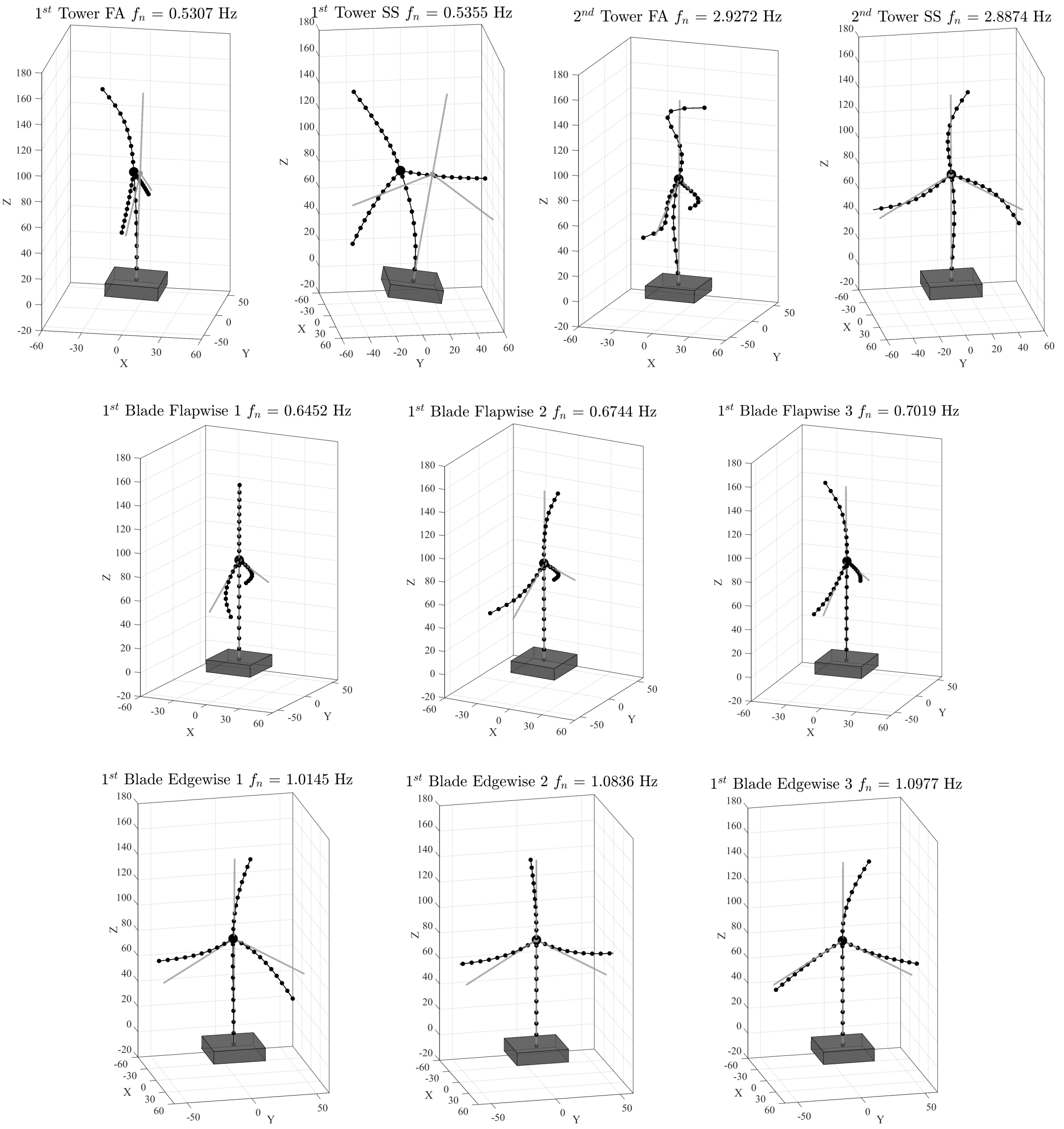

Fig. 2.22 Tower and rotor mode shapes of the Simulink FWT model.

Simulink tower model employs the multibody FE formulation that takes into account extension, torsion, and FA, SS bending, in which sense yields more accurate tower modelling than ElastoDyn. Regarding the blade modelling, both the Simulink multibody model and BeamDyn can describe the large blade deformation in all 6 DoFs. However, the Simulink blade substructure uses a reduced-order model which might exclude some high-frequency torsion and/or extension modes and thus affect the overall rotor natural frequencies. Having said that, the difference between the Simulink blade model and BeamDyn has been demonstrated to be negligible (see Fig. 2.21).

- *Different hydrodynamic fluid-memory radiation state-space models*

HydroDyn in OpenFAST and Simulink hydrodynamics subsystem use different state-space models to represent the fluid-memory radiation force. HydroDyn uses the one identified via the popular multi-SISO method while Simulink uses that identified via the suggested direct-MIMO method, as compared in Fig. 2.11. The difference in the heave-heave transfer function between the two identified models affects the natural frequency of the platform heave mode directly and alters other modes via coupling effects.

- *Different linearization methods*

  In the linearization analysis of both OpenFAST and Simulink models, the full-system linear state-space model, from which the eigenvalues (natural frequencies) are calculated, is the assembly of the state-space model linearized from each module/subsystem. The difference is that, in OpenFAST, a combination of analytical and numerical linearization are adopted, with the former being applied on the hydrodynamic radiation state-space model, added mass and stiffness matrices, etc., and the latter on most of the other equations in ElastoDyn and BeamDyn via the central-difference perturbation. In contrast, the pre-programmed linearization feature in most Simulink blocks allows for the analytical linearization for all subsystems and hence provides more accurate eigenanalysis results.

2.5.2 System response under realistic environmental conditions

The aero-hydro-elastic-control simulation is performed on the example FWT to demonstrate the ability of the developed Simulink model to predict the 3D dynamic behaviour of the entire FWT system, and more importantly, to further investigate the interaction among all subsystems. In the benchmark OpenFAST model, modules of ElastoDyn, BeamDyn, InflowWind, AeroDyn, HydroDyn and ServoDyn modules are enabled and their settings are configured accordingly as in corresponding Simulink subsystems. An initial platform heave displacement of -0.127 m and an initial rotor speed of 6 rpm are assumed in both models.

The IEC-Kaimal model is used in TurbSim to generate the time series of 3D turbulent wind fields for two simulation cases, one with the hub-height reference wind speed below the rated wind speed (11.4 m/s) and the other above the rated. A developing sea state defined by the Jonswap spectrum is applied in both cases. The wave is assumed to propagate along the downwind (positive X) direction with the significant wave height of 2 m and peak spectral wave period of 10s. The generated wave elevation time history, its power spectrum density (PSD) and the target Jonswap spectrum are presented in Fig. 2.23. As the wave excitation force $\mathbf{F}_e$ is independent of the platform behaviour, the force time series calculated from OpenFAST according to Eq. (2.5) are directly applied in the Simulink model, to focus the analysis on the subsystem interactions for both models. $\mathbf{F}_e$ are only nonzero in the wave application plane (surge, heave, and pitch DoFs) and their PSDs are shown in Fig. 2.23. The dominant frequency content is around 0.1 Hz, which is consistent with the peak spectral incident wave frequency f_{wave}.

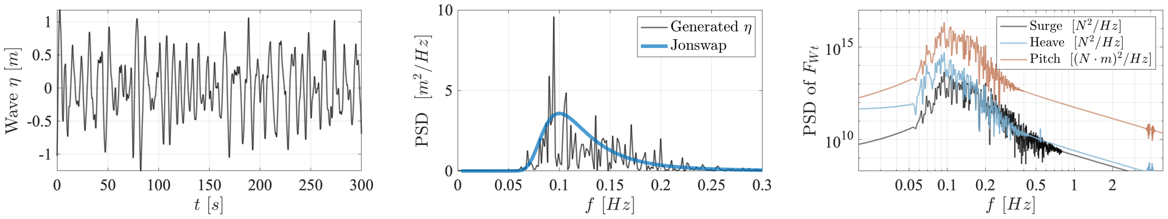

Fig. 2.23 The wave elevation (η) time history, its PSD vs. the target Jonswap spectrum, and the PSDs of non-zero wave excitation forces ($\mathbf{F}_e$).

2.5.2.1 System response below rated wind speed

A 3D wind field with the reference hub-height wind speed ($V_{hub}^{ref} = 8$ m/s) below the rated wind speed is applied to the Simulink FWT model to investigate the interaction between different dynamic subsystems. The hub-height wind speed time history and the operational responses of the turbine obtained from the developed Simulink model and OpenFAST model are depicted in Fig. 2.24. Despite the high blade modelling fidelity of BeamDyn, the modular coupling in OpenFAST is more robust when using ElastoDyn to represent blades. Therefore, BeamDyn and ElastoDyn are adopted separately in OpenFAST for the blade modelling as a cross-check, and the Simulink model is compared to both OpenFAST-ElastoDyn and OpenFAST-BeamDyn models henceforth. It can be seen from Fig. 2.24 that the rotor speed and power generation vary in the same tendency as the wind excitation. As the rotor speed is always below the rated value (12.1 rpm), the blade pitch controller stays disabled. The operational responses of the Simulink model match well with both OpenFAST models, again verifying the modelling accuracy of the developed Simulink model.

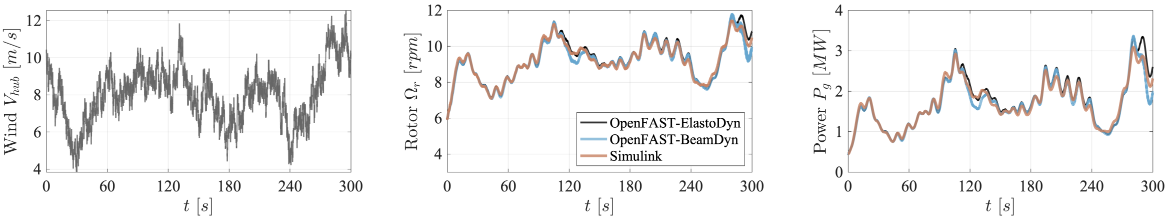

Fig. 2.24 Hub-height wind speed (V_{hub}), rotor speed (Ω_r) and power generation (P_g) of the below-rated wind simulation.

The structural responses within the wind/wave application plane, including the platform surge (ξ_1), heave (ξ_3), pitch (ξ_5) motions, and tower-top FA (x_{FA}), blade flapwise (x_{flap})

deflections with respect to their undeformed configurations, of the Simulink model and both OpenFAST models are illustrated in Fig. 2.25. An overall good agreement is found among the three models. The discrepancy in platform heave motions (ξ_3) is due to the different state-space identification methods used in the Simulink and OpenFAST models, as described in Section 2.4.1. The blade flapwise deflection (x_{flap}) predicted by the Simulink blade model tends more to the BeamDyn result than ElastoDyn, especially after 200s. This is due to the limited ability of ElastoDyn in capturing the geometric nonlinearities induced by large blade motions, which is consistent with the discussion in Section 2.4.4. The significant coupling between blade-tower-platform DoFs that have been discussed in the modal analysis results in Section 2.5.1 can be observed from the PSDs in Fig. 2.25. The predominant wave frequency $f_{wave} = 0.1$ Hz is very close to the platform pitch $f_{pitch} = 0.0841$ Hz and heave $f_{heave} = 0.1274$ Hz natural frequencies (see Table 2.3), and thus the platform pitch and heave modes are excited. Energy is also supplied to the platform surge mode due to the surge-pitch coupling (see the pitch PSD in Fig. 2.25). In contrast, the surge-heave coupling is unnoticeable, as implied in the platform heave PSD in Fig. 2.25. These low-frequency platform motions affect the aerodynamic loads by altering the relative wind velocity seen by the rotor as discussed in Section 2.4.2, and thus transmitting energy of the same frequencies from the platform up to the tower and blade vibrations, as shown in Fig. 2.25. Conversely, the blade flapwise bending mode ($f_{bld} = 0.6 - 0.7$ Hz) and blade passing frequencies under the average 9 rpm rotor speed ($f_{1P} = 0.158$ Hz, $f_{2P} = 0.317$ Hz, $f_{3P} = 0.475$ Hz, etc.) have negligible effect on platform motions due to the large inertia difference between the rotor and platform. However, the tower FA bending mode ($f_{twr} = 0.5307$ Hz) can transmit to the platform pitch rotation, as they are directly connected. This indicates that, when the platform pitch velocity is used as the control input of the floating feedback loop, as described in Section 2.2.4, the high-frequency tower vibration mode should be filtered in advance.

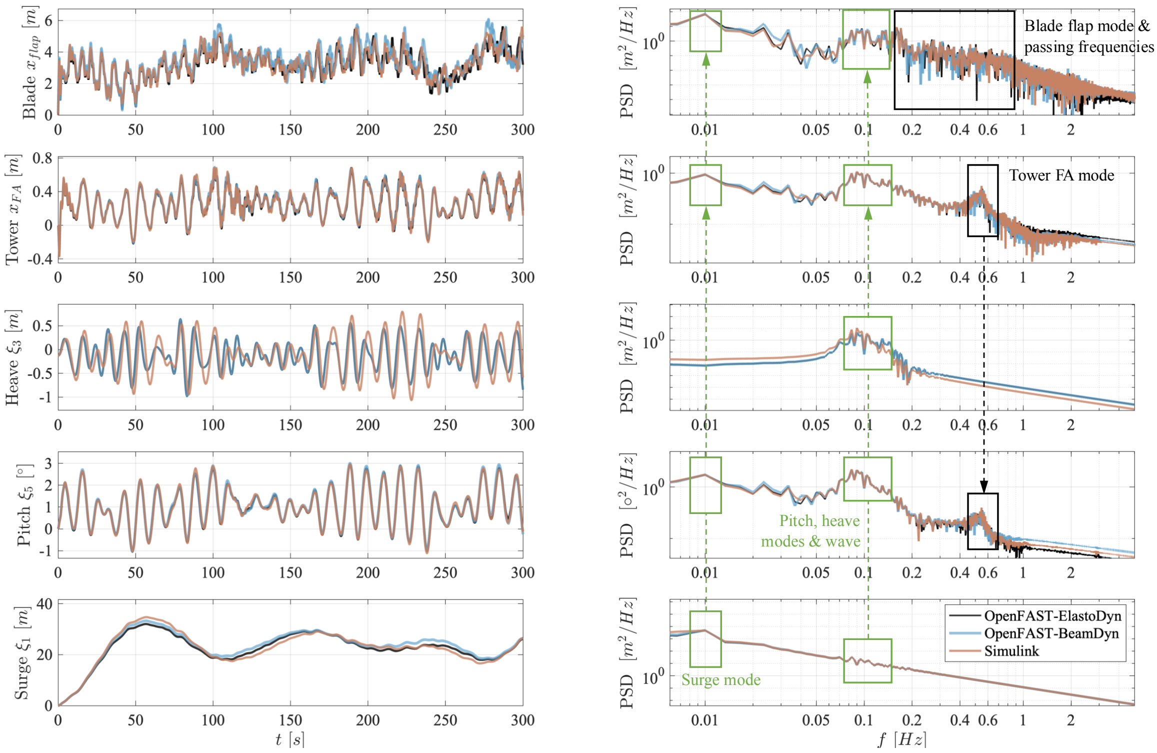

Fig. 2.25 Time-domain and frequency-domain along-wind structural responses of the Simulink FWT model and OpenFAST models under below-rated wind speed $V_{hub}^{ref} = 8$ m/s and irregular wave H_s = 2m, T_p = 10s.

Despite the aligned direction of wind and wave actions, platform motions in the cross-wind direction, i.e. sway (ξ_2), roll (ξ_4) and yaw (ξ_6) DoFs, are observed, as shown in Fig. 2.26. The platform yaw rotation, which can be as large as 5°, is mainly induced by the non-axisymmetric aerodynamic force distribution on the rotor plane. This non-axisymmetric load stems from: the turbulent and shear nature of the wind field; the non-axisymmetric deflection of the blades due to gravity, shaft tilt, pre-cone angle, etc.; and the unevenly induced relative wind velocity due to the platform rigid-body motions, especially the platform pitch rotation. As pointed out in Section 2.2.3, the skewed wake effect introduced by platform rotations is not taken into account in the developed Simulink model, which causes discrepancies in the structural and operational responses between the Simulink model and OpenFAST models. However, the discrepancies are negligible under small platform pitch and yaw rotations, which is consistent with the observations in Section 2.4.2.

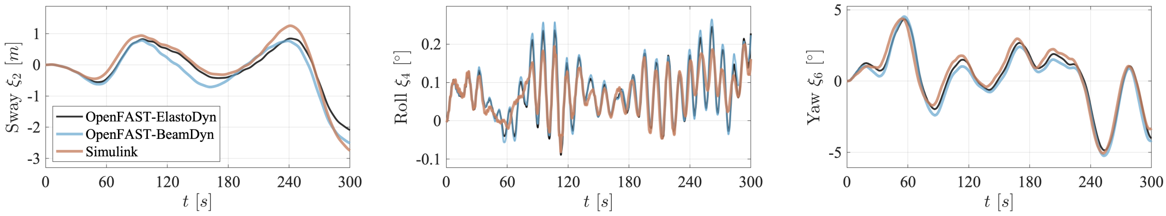

Fig. 2.26 Cross-wind platform responses of the Simulink FWT model and OpenFAST models under below-rated wind speed $V_{hub}^{ref} = 8$ m/s and irregular wave H_s = 2m, T_p = 10s.

2.5.2.2 System response above rated wind speed

To investigate the overall dynamic interactions of the FWT system with the involvement of the blade-pitch controller, a 3D wind field with above-rated hub-height reference wind speed ($V_{hub}^{ref} = 14$ m/s) is applied. The hub-height wind speed time history and the operational responses of the blade pitch angle (β_p) and rotor speed (Ω_r) obtained from the developed Simulink model and OpenFAST models are depicted in Fig. 2.27. It's worth mentioning that OpenFAST (v3.5.3) fails to give correct results when the one-state dynamic stall model in AeroDyn (`UAMod=6`) and BeamDyn are coupled. As a workaround, the more sophisticated four-state dynamic stall model (`UAMod=4`) is used in both OpenFAST-ElastoDyn and OpenFAST-BeamDyn models. This explains the discrepancies in the operational response in Fig. 2.27 between OpenFAST models and the developed Simulink model, which still adopts the one-state dynamic stall model in the aerodynamics subsystem as described in Fig. 2.7. The floating feedback loop used in the blade-pitch controller in all three models starts to provide a non-zero blade pitch command at $0-10$s before the rotor speed reaches its rated value (12.1 rpm), to avoid the potential negative damping issue and thus stabilize the FWT system, which is consistent with the findings in Section 2.4.3. After Ω_r reaches the rated value, the blade pitch controller effectively maintains the rotor speed, and the blade pitch command shows the same tendency as the wind speed, especially after 120s.

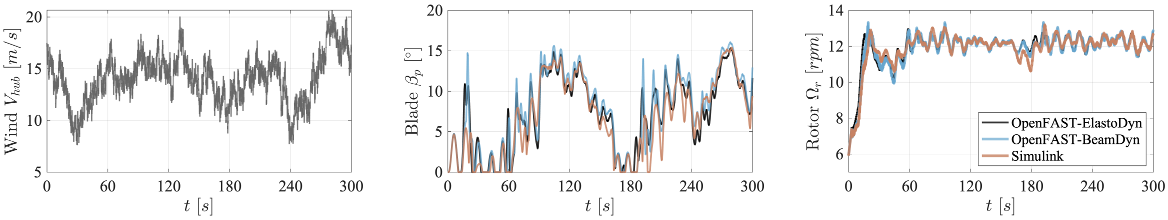

Fig. 2.27 Hub-height wind speed (V_{hub}), blade pitch angle (β_p), and rotor speed (Ω_r) of the above-rated wind simulation.

The along-wind structural response time histories and their PSDs of the Simulink and OpenFAST models are shown in Fig. 2.28. Similar to the discussion of Fig. 2.25 in Section

2.5.2.1, strong one-way coupling from the platform surge-heave-pitch, to the tower FA, and eventually to the blade flapwise vibrations can be observed in Fig. 2.28. In contrast, the influence of the blade bending modes as well as blade passing frequencies under the rated rotor speed ($f_{1P} = 0.2$ Hz, $f_{2P} = 0.4$ Hz, $f_{3P} = 0.6$ Hz, etc.) is not noticeable in the platform motion. Comparing Fig. 2.29 and Fig. 2.26, the cross-wind platform response within the above-rated wind simulation is found to be much larger than the below-rated case, due to the greater non-axisymmetric aerodynamic loads as the increase of wind speed and platform rotations. The potentially strong skewed flow effects induced by the large platform pitch rotation (up to 5°) and yaw rotation (up to 10°) also contribute to the discrepancies in dynamic response between the developed Simulink model and OpenFAST models.

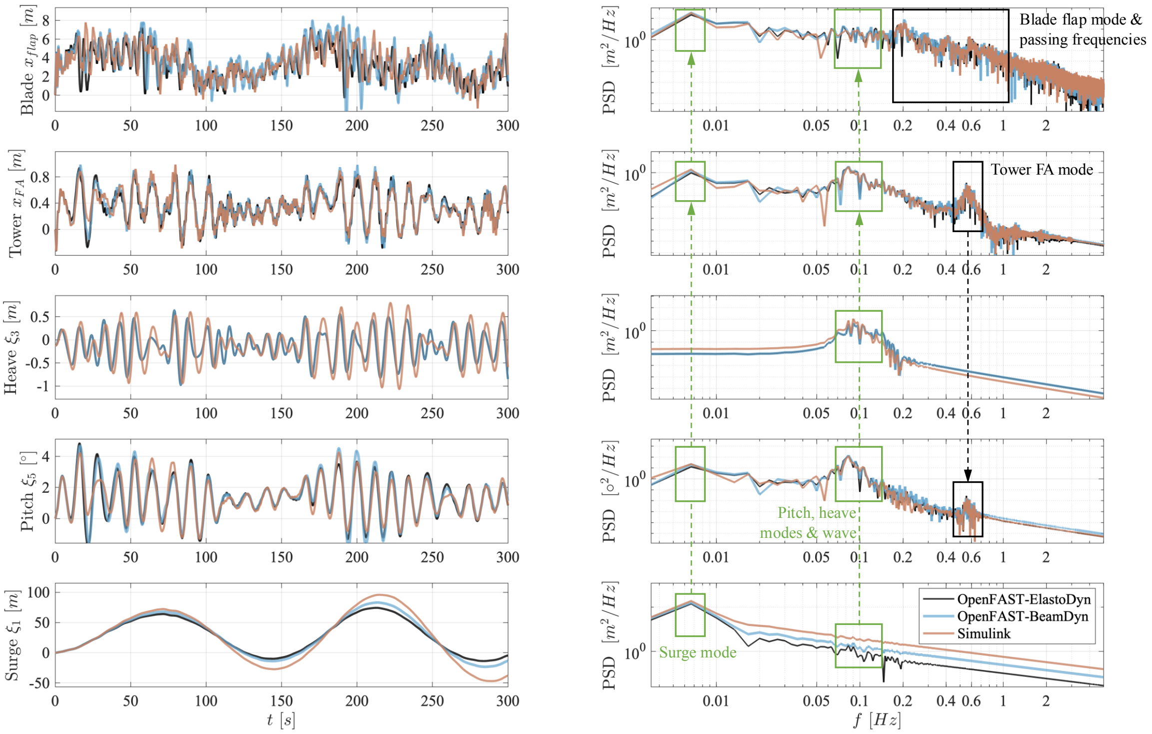

Fig. 2.28 Time-domain and frequency-domain along-wind structural responses of the Simulink FWT model and OpenFAST models under above-rated wind speed $V_{hub}^{ref} = 14$ m/s and irregular wave H_s = 2m, T_p = 10s.

2.5.3 Computational efficiency

To better evaluate the computational efficiency of the developed Simulink FWT model, CPU times are compared between Simulink and OpenFAST with three modelling fidelities regarding tower and blade flexibility. All simulations are conducted under the above-rated

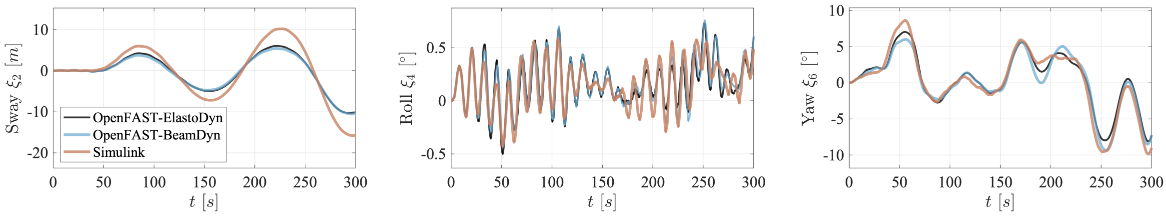

Fig. 2.29 Across-wind platform responses of the Simulink FWT model and OpenFAST models under above-rated wind speed $V_{hub}^{ref} = 14$ m/s and irregular wave $H_s = 2$ m, $T_p = 10$s.

wind and irregular wave excitations (as described in Section 2.5.2.2). Table 2.4 presents the number of DoF for different models and their CPU times. Notably, the Simulink model was run in Rapid Accelerator mode, which compiles the model into C code to enhance efficiency.

Table 2.4 Comparison of DoFs and CPU time for OpenFAST vs. Simulink (300-s simulation).

Settings	OpenFAST-ElastoDyn		OpenFAST-BeamDyn		Simulink	
	No. DoFs	CPU time	No. DoFs	CPU time	No. DoFs	CPU time
Rigid blades/tower	7	25s	/	/	7	2 min
Rigid blades, flexible tower	11	25s	/	/	73	4 min
Flexible blades/tower	20	25s	/	21 min	358	110 min

The results indicate that the CPU time of the Simulink model is generally much longer than that of OpenFAST, which is primarily attributed to the higher number of DoFs. Additionally, OpenFAST employs a fourth-order Adams-Bashforth-Adams-Moulton (ABM4) fixed-step implicit integrator, whereas Simulink uses the general-purpose stiff solver ode15s, which is a variable-order variable-step implicit integrator. `Solver Profiler` App of Simulink revealed that the example Simulink model's average step size (2.5×10^{-4}s) is much smaller than OpenFAST's fixed time step (0.01 s for ElastoDyn, 0.00125 s for BeamDyn), which further increases computational cost.

Notably, the computation time increased dramatically when including blade flexibility (110 min vs. 4 min). `Solver Profiler` detected dense solver exceptions at the outermost substructures of each blade, suggesting that the retained modes' stiffness might be too high for the solver to handle within the set tolerance. A re-examination of the reduced-order modelling settings for blades could significantly reduce computational costs.

2.6 Conclusions

A new Simulink FWT model is developed in this work, leveraging the object-based Simscape environment for the implementation of the physical multibody system, as well as the procedure-based Simulink environment for the calculation of aerodynamics, hydrodynamics, and controls. With the help of this newly proposed Simulink model, the dominant dynamics of the FWT system are carefully examined individually on an example 5-MW ITI-Barge FWT. Specifically, the unsteady aerodynamics in the Simulink model are evaluated via efficient dynamic inflow and stall models. The large variation in the aerodynamic behaviour due to the platform pitch rotations is accurately captured. The FWT hydrodynamics are determined under linear potential flow assumptions, with wave radiation and excitation effects represented with state-space models. A novel N4SID MIMO state-space identification and post-processing approach based on frequency response samples is proposed in this work, which offers a more efficient and robust state-space representation compared to the popular multi-SISO method used in OpenFAST. The proposed frequency-domain MIMO identification approach provides another advantage of circumventing the need for causalization in the conventional wave excitation state-space identification. The multibody formulation is employed for the blades/tower modelling in Simulink, which has been demonstrated to be able to accommodate large geometrically nonlinear blade deformations by comparing against the high-fidelity nonlinear blade dynamics solver BeamDyn in OpenFAST. The multi-loop ROSCO control strategy featuring the combination of generator speed feedback and floating feedback is implemented in the Simulink model, and is demonstrated to effectively regulate the power output and overcome the instability issue in the platform responses.

Furthermore, the above important FWT dynamics are investigated holistically in the Simulink model of the example FWT through a modal analysis and a fully-coupled dynamic analysis under realistic ocean wind and wave environments. The overall good agreement between the Simulink model and OpenFAST verifies the ability of Simulink to estimate the FWT dynamic behaviour. The comparison of the computational efficiency between the Simulink and OpenFAST models reveals the reasons for high computational costs of the developed Simulink model. It also suggests the possibility of further reducing the computational cost of the Simulink model while maintaining the modelling accuracy.

On the example 5-MW ITI-Barge FWT, significant one-way coupling from the platform surge-heave-pitch, to the tower fore-aft, and eventually to the blade flapwise vibrations are observed, whereas, except for the first tower bending mode, the high-frequency contents from the superstructure have negligible influence on the platform motion. The neglected skewed wake effects in the developed Simulink aerodynamic model are shown to have limited influence on the structural and operational responses of the example ITI-Barge FWT for the below-rated wind condition. However, the conclusions drawn from the example barge-type FWT may not be directly applicable to other FWT platform concepts due to their distinct dynamic characteristics from the barge. The full system coupling effects, potentially large platform yaw motion, etc. should be carefully re-investigated for turbines mounted on spar, semi-submersible, and tension-leg platforms (TLP). This can be readily achieved by providing the hydro-mechanical coefficients (hydrostatic stiffness, added mass, radiation damping, wave excitation, etc.) of a specific platform to the Simulink model.

The developed Simulink model features easy modification and integration of different domains in FWTs. Another important work in this thesis upgrades the linear hydrodynamic subsystem to account for the geometric nonlinearities caused by large platform movements. Apart from that, the established Simulink FWT model can be readily coupled in future works with other mechanical and electrical features, such as a more advanced dynamic mooring line solver, the incorporation of tuned mass dampers for excessive response suppression, the implementation of individual pitch control for more sophisticated load mitigation, etc. The extensive MATLAB toolboxes are also anticipated to assist with the control co-design and FWT design optimization, as well as to offer digital twins that aid Operation & Maintenance to extend FWT service life.

Nomenclature for Aerodynamics Calculation in Fig. 2.7

Quasi-steady calculation

α	local angle of attack
β_p	blade pitch angle
γ_i	Glauert's correction parameters ($i = 1,2,3$)
ϕ	local inflow angle
κ	nondimensional axial parameter
κ'	nondimensional tangential parameter
σ'	local blade solidity
θ	local blade pre-twist angle
a	local axial induction factor
a'	local tangential induction factor
c	local blade chord length
C_l	static lift coefficient
C_d	static drag coefficient
C_n	normal force coefficient
C_t	tangential force coefficient
F	Prandtl's loss factor (tip: F_{tip}, hub: F_{hub})
r_0, R	hub and blade tip radius, respectively
r	local blade radial distance
N_b	number of blades
$f(\phi)$	residual equation
$\mathbf{W}_{qs}$	quasi-steady induced flow velocity
$\mathbf{V}_{rel0}$	relative flow velocity without induction. V^x_{rel0}, V^y_{rel0}: component along $O_a x_a$ and $O_a y_a$ axis, respectively
$\mathbf{V}_{rel}$	relative flow velocity with induction. V^x_{rel}, V^y_{rel}: component along $O_a x_a$ and $O_a y_a$ axis, respectively

Dynamic inflow model

τ_1, τ_2	time constants
$\bar{a}$	average axial induction over the rotor plane
k	coupling constant
$\mathbf{W}_{int}$	intermediate induced flow velocity
$\mathbf{W}$	actual induced flow velocity

Dynamic stall model

α_0	zero-lift angle of attack, i.e., $C_l(\alpha_0) = 0$
τ	time constant
C_l'	slope of $C_l - \alpha$ curve at α_0
C_l^{fs}	fully separated lift coefficient
C_l^{dyn}	dynamic lift coefficient
f_s^{st}	steady separation parameter
f_s	separation parameter

Chapter 3

Analytical Solution to Linear Wave-Platform Interaction Problem

3.1 Introduction

Accurately modelling the wave-platform interaction is crucial for the dynamic analysis of floating wind turbines (FWTs). Conventionally, these effects are evaluated only around the original equilibrium platform position, disregarding the potentially large translation and especially rotation of the platform under combined wind and wave actions. The effect of large platform movements on wave-platform interactions and consequently the global dynamic behaviour of FWTs remains an open question. This question will be investigated in this work using a piecewise linearization framework, in which the general nonlinear wave-platform boundary value problem (BVP) is locally linearized at various platform positions. The assumption of small platform displacement around the equilibrium position in the original linear BVP is replaced by that of small displacement around the local platform position during each linearization, while the small wave amplitude assumption is retained. The resultant locally linearized models are combined to estimate the geometric nonlinear effects induced by large platform movements. The reliability of this newly proposed nonlinear analysis approach depends directly on the accuracy of each locally linearized wave-platform interaction model. Finding a local model involves solving the wave-platform BVP for an arbitrary platform position. Essentially, this modified BVP boils down to a mathematical problem of solving Laplace's equation of velocity potential function over a semi-infinite fluid domain, with non-homogeneous boundary conditions specified on an arbitrary wetted body surface, and homogeneous ones on the still water surface, sea bed and far field.

Numerical methods such as the Boundary Element Method (BEM) [138], Finite Element Method (FEM) [7, 71], and Multipole Expansion Method (MEM) [77] have been developed to solve the linear wave-platform BVP described above. Among these methods, BEM is the most frequently used one and particularly suitable for floating bodies with arbitrary geometries. In BEM, Laplace's equation throughout the entire fluid domain is reformulated into an integral equation over the fluid boundaries, and a system of linear algebraic equations are obtained after discretizing the boundaries. Popular BEM codes, such as WAMIT [131] and NEMOH [96], commonly employ the free-surface Green's function that automatically satisfies boundary conditions on the free surface, sea bed and far field, as such the integral equation only involves the body-surface boundary condition and only the discretization on the wetted body surface is required. However, the mathematical complexity of the free-surface Green's function makes the computation of the function itself and its derivatives time-consuming. In addition, special treatment is required to circumvent the irregular frequency issue due to the specific free-surface Green's function [70]. To overcome these challenges, BEM formulations using simple Green's function of the form $\ln\frac{1}{r}$ in two-dimension (2D) and $\frac{1}{r}$ in three-dimension (3D) domains have been re-examined [37, 78]. These simpler kernels effectively reduce computational complexity but at the expense of accounting for all boundaries in the integral equation. Inspired by [8], Poul and He [107] reduced the computational cost of BEM for a 2D wave-platform BVP by truncating the fluid domain with vertical imaginary boundaries, beyond which the potentials are represented by eigenfunction expansions.

Despite the advantage of BEMs in handling wave-platform BVPs for bodies with arbitrary geometries, these methods are sensitive to mesh resolution. For floating bodies with relatively simple geometries, analytical solutions can be sought to provide benchmarks for validating numerical codes. Analytical methods offer deeper insights into the underlying physics and can potentially achieve higher computational efficiency compared to numerical methods. In a typical analytical formulation, the fluid domain is divided into multiple subdomains, and the method of separation of variables is used to express the velocity potential in each subdomain as a sum of eigenfunctions with unknown coefficients. Continuity conditions for pressure and normal velocity at the interface between different subdomains are then applied to determine these coefficients. Analytical methods were first investigated for wetted body surfaces with regular shapes, such as rectangles [72, 146], circular cylinders [137, 54] and spheres [55], which are conveniently addressed in Cartesian, cylindrical and spherical coordinates, respectively. Kokkinowrachos et al. [68] extended the analytical method to include vertical axisymmetric cylinders with non-circular cross-sections. Yu et al. [139] further extended it to vertical cylinders with arbitrary cross-sections, such as cosine, elliptical and quasi-elliptical shapes. Additional extensions have been made to combinations of vertical cylinders with arbitrary cross-sections, both coaxially [145] and heteroaxially [51]. However, these studies are limited to floating platforms with vertical walls, and no analytical solution has yet been attempted for wave-platform BVPs involving arbitrary body geometries. Even a relatively simple 2D tilted rectangle floating on a fluid domain of constant depth presents complex mathematical challenges. The primary difficulty arises from the non-orthogonal and inseparable boundary conditions due to the slanting wetted body surfaces, which preclude the direct use of the separation of variables method.

Valuable insights can be gained from the surface-wave propagation problem, in which an arbitrary sea bed profile is usually approximated by a series of horizontal and vertical steps [106]. This step approximation results in orthogonal boundaries for all fluid subdomains, and thus enables the application of separation of variables. A few researchers examined the use of step approximation in the wave-platform interaction problem. Tsai et al. [126] investigated the wave scattering effect on 2D stationary bodies with triangular and trapezoidal shapes, which are approximated by a series of steps, and analytical solutions are derived following the typical eigenfunction expansion formulation. Zhou et al. [147] extended this method to include the analytical solution for a heaving body with arbitrary bottom shapes. However, the body movement is either fully constrained or only allowed in the vertical direction in the two works, and both of them require that the body intersects with the water surface at an angle less than 90°, which means no fluid subdomains exist above the body.

In this work, a general analytical solution to the 2D linear wave-platform BVP is investigated, utilizing step approximation and eigenfunction expansion techniques. No assumptions are made about the body geometry which can have a general pose in a 2D space, i.e., displacement and rotation. The newly proposed analytical method is cross-validated with a 2D BEM formulation, which employs the simple Green's function and a truncated fluid domain, as described in [107]. To demonstrate the methodology, a barge-type floating platform is used. The hydrodynamic behaviours of the barge under three representative positions, which result in rectangular, trapezoidal, and triangular wetted body-surface geometries, are examined, with the aim of laying the foundation for the geometric nonlinear analysis of the example barge-type FWT in the subsequent chapter.

3.2 Mathematical formulation

Two right-handed coordinate systems are defined to describe the planar movements of the floating rectangular platform and the wave kinematics in an open sea of finite depth h (as shown in Fig. 3.1). The earth-fixed Cartesian coordinate system Oxz is defined with the origin O lying on the still water level ($z = 0$), with Ox pointing towards the incident wave direction, and Oz pointing upwards. The body-fixed coordinate system $O'x'z'$ follows the movement of the platform, with O' being the center of gravity whose coordinates in Oxz are (x_0, z_0). The $O'x'$ and $O'z'$ axes are parallel to the width and height of the barge. When the rotation of the barge, i.e., the pitch is zero, the two sets of axes are parallel. The translational displacements from O to O' in the surge and heave Degrees of Freedom (DoF), and the rotation in the pitch DoF, are denoted as ξ_1, ξ_3, ξ_5, respectively, which are consistent with the definition in Fig. 2.1. The platform rigid-body velocity is defined as $\mathbf{V}_{o'} = [\dot{\xi}_1 \ \dot{\xi}_3 \ \dot{\xi}_5]^\intercal$.

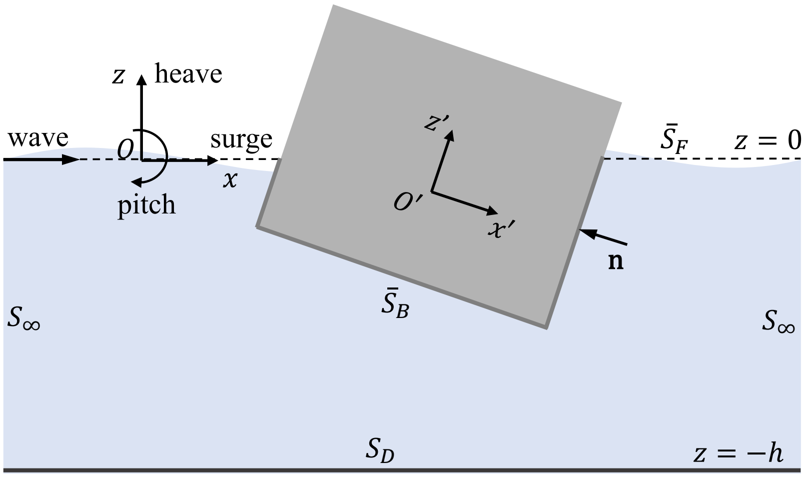

Fig. 3.1 Coordinate system of a 2D wave-platform interaction problem.

3.2.1 Nonlinear boundary value problem

An ideal fluid (homogeneous, inviscid, and incompressible) without rotational motion and surface tension is assumed in this work. In this case, the flow can be completely described by a velocity potential $\Phi(x,z,t)$ satisfying Laplace's equation throughout the whole fluid domain Ω. Φ can be determined given the combined nonlinear kinematic and dynamic boundary condition on the instantaneous free surface $S_F(t)$, the impermeability condition on the body surface $S_B(t)$ and the sea bed S_D, the non-reflecting condition on the far-field S_∞, as well as the initial conditions, which are summarized as follows:

$$\begin{cases} \nabla^2\Phi = 0, & \mathbf{X} \in \Omega \\ \left(\dfrac{\partial}{\partial t} + \nabla\Phi\cdot\nabla\right)\left(\dfrac{\partial\Phi}{\partial t} + \dfrac{1}{2}\nabla\Phi\cdot\nabla\Phi + gz\right) = 0, & \mathbf{X} \in S_F(t):\ z = \eta(x,t) \\ \nabla\Phi\cdot\mathbf{n} = \mathbf{V}\cdot\mathbf{n}, & \mathbf{X} \in S_B(t) \\ \nabla\Phi\cdot\mathbf{n} = 0, & \mathbf{X} \in S_D \\ |\nabla\Phi| \to 0, & \mathbf{X} \in S_\infty \\ \Phi|_{t=0} = 0,\ \left.\dfrac{\partial\Phi}{\partial t}\right|_{t=0} = 0, & \end{cases} \tag{3.1}$$

where $\nabla^2 = \frac{\partial^2}{\partial x^2} + \frac{\partial^2}{\partial z^2}$, g is the gravitational constant, $\eta(x,t)$ is the wave elevation with respect to the still water level, $\mathbf{n} = [n_x\ n_z]^\intercal$ denotes the normal vector at the platform surface pointing out of the fluid, $(\cdot)$ denotes the inner product, and $\mathbf{V}$ is the velocity of a point (x,z) on the platform surface, which can be calculated from the following equation:

$$\mathbf{V}(x,z,t) = \begin{bmatrix} \dot{\xi}_1(t) + (z - z_0)\dot{\xi}_5(t) \\ \dot{\xi}_3(t) - (x - x_0)\dot{\xi}_5(t) \end{bmatrix}. \tag{3.2}$$

Note that the reference point of the position vector is taken at the center of gravity (x_0, z_0).

3.2.2 Linearized boundary value problem

The fully nonlinear dynamic and kinematic conditions on the time-varying free surface $z = \eta(x,t)$, as well as the coupling between fluid behaviour and floating body dynamics, pose significant difficulties in finding the solution to $\Phi(x,z,t)$. By assuming small wave amplitudes relative to the wavelength, and small platform displacements and rotations around a specified pose, the nonlinear problem can be simplified to a linear one, with the boundary conditions being satisfied on the still water level ($\overline{S}_F$) and mean wetted body surface ($\overline{S}_B$). As indicated in Section 3.1, different from the conventional linear potential flow theory in which $\overline{S}_B$ refers to the static equilibrium of the floating body, in this work, $\overline{S}_B$ represents any platform position of interest around which small translations and rotations are assumed (as shown in Fig. 3.1). The linearized governing equation, boundary conditions, and initial conditions are summarized as follows:

$$\begin{cases} \nabla^2\Phi = 0, & \mathbf{X} \in \Omega \\ \dfrac{\partial^2\Phi}{\partial t^2} + g\dfrac{\partial\Phi}{\partial z} = 0, & \mathbf{X} \in \overline{S}_F : \ z = 0 \\ \dfrac{\partial\Phi}{\partial \mathbf{n}} = \mathbf{V}\cdot\mathbf{n}, & \mathbf{X} \in \overline{S}_B \\ \dfrac{\partial\Phi}{\partial z} = 0, & \mathbf{X} \in S_D : \ z = -h \\ |\nabla\Phi| \to 0, & \mathbf{X} \in S_\infty \\ \Phi|_{t=0} = 0, \ \dfrac{\partial\Phi}{\partial t}\Big|_{t=0} = 0. \end{cases} \tag{3.3}$$

This simplification enables the decomposition of Φ into an incident wave potential Φ_I, a radiation potential Φ_R and a diffraction potential Φ_D. Φ_R handles non-homogeneous body surface boundary conditions, Φ_I is an exogenous input to the fluid-body system and Φ_D is used to cancel out the influence of Φ_I onto the body surface. The total velocity potential can be written as:

$$\begin{aligned} \Phi(x,z,t) &= \Phi_R(x,z,t) + \Phi_I(x,z,t) + \Phi_D(x,z,t) \\ &= \Re\left\{ \frac{1}{2\pi} \int_{-\infty}^{\infty} \left\{ \overline{\mathbf{V}}_{o'}(\omega)\cdot\boldsymbol{\phi}_R(x,z,\omega) + \overline{\eta}_o(\omega)\left[\phi_I(x,z,\omega) + \phi_D(x,z,\omega)\right] \right\} e^{i\omega t}\, d\omega \right\}, \end{aligned} \tag{3.4}$$

where $\overline{\mathbf{V}}_{o'}(\omega), \overline{\eta}_o(\omega)$ are the Fourier transform of the platform rigid-body velocity $\mathbf{V}_{o'}(t)$ and wave elevation at the origin $\eta_o(t)$, respectively, $\boldsymbol{\phi}_R$ is the radiation potential vector $\begin{bmatrix} \phi_R^{surge} & \phi_R^{heave} & \phi_R^{pitch} \end{bmatrix}^{\mathsf{T}}$ corresponding to different platform DoFs, which is, however, independent of the platform velocity; ϕ_I, ϕ_D are the incident and diffraction wave potential, respectively, and they are independent of the wave elevation. According to Airy's wave theory, ϕ_I representing the incident wave propagating along positive x direction takes the following form:

$$\phi_I(x,z,\omega) = \frac{ig}{\omega}\cdot\frac{\cosh[k(z+h)]}{\cosh(kh)} e^{-ikx}, \tag{3.5}$$

where k is the wave number satisfying the dispersion relation:

$$\omega^2 = gk\tanh(kh). \tag{3.6}$$

Substituting Eq. (3.4) into Eq. (3.3), one can write the governing equation and boundary conditions of the linear BVP in the frequency domain as:

$$\begin{cases} \nabla^2 \boldsymbol{\phi} = 0, & \mathbf{X} \in \Omega \\ \dfrac{\partial \boldsymbol{\phi}}{\partial z} - \dfrac{\omega^2}{g} \boldsymbol{\phi} = 0, & \mathbf{X} \in \overline{S}_F : \; z = 0 \\ \dfrac{\partial \boldsymbol{\phi}}{\partial \mathbf{n}} = \widetilde{\mathbf{n}}, & \mathbf{X} \in \overline{S}_B \\ \dfrac{\partial \boldsymbol{\phi}}{\partial z} = 0, & \mathbf{X} \in S_D : \; z = -h \\ \lim\limits_{x \to \pm\infty} \left(\dfrac{\partial \boldsymbol{\phi}}{\partial x} \mp ik\boldsymbol{\phi} \right) = 0, & \end{cases} \tag{3.7}$$

where $\boldsymbol{\phi}$ denotes the augmented potential vector $\left[\phi_R^{surge} \quad \phi_R^{heave} \quad \phi_R^{pitch} \quad \phi_D\right]^\mathsf{T}$, and $\widetilde{\mathbf{n}}$ the non-homogeneous body surface boundary condition vector which is defined as:

$$\widetilde{\mathbf{n}} = \left[n_x \quad n_z \quad (z - z_0)n_x - (x - x_0)n_z \quad -\left(\frac{\partial \phi_I}{\partial x} n_x + \frac{\partial \phi_I}{\partial z} n_z \right) \right]^\mathsf{T}. \tag{3.8}$$

3.2.3 Wave forces calculation

Hydrodynamic forces acting on the body are determined by integrating the pressure over the body surface $\overline{S}_B$. With the velocity potential $\Phi(x,z,t)$ (Eq. (3.4)), hydrodynamic pressure $p(x,z,t)$ can be calculated using unsteady Bernoulli's equation:

$$p = -\rho \frac{\partial \Phi}{\partial t} - \frac{1}{2}\rho (\nabla \Phi)^2 - \rho g z, \tag{3.9}$$

where ρ is the fluid density. Under the linearization assumption, the higher-order term $\frac{1}{2}\rho(\nabla\Phi)^2$ is neglected. By substituting Eq. (3.4) into Eq. (3.9), one can obtain the dynamic buoyancy forces $\mathbf{F}_b$, wave radiation forces $\mathbf{F}_r$, and wave excitation forces $\mathbf{F}_e$ introduced in Eq. (2.1), and they are expressed as follows:

$$\begin{aligned} \mathbf{F}_b(t) &= -\rho g \int_{\overline{S}_B} z \overline{\mathbf{n}} \, dS = \mathbf{F}_{b0} - \mathbf{K}_{hs} \boldsymbol{\xi}(t), \\ \mathbf{F}_{rt}(t) &= -\rho \int_{\overline{S}_B} \frac{\partial \Phi_R}{\partial t} \overline{\mathbf{n}} \, dS = -\frac{1}{2\pi} \int_{-\infty}^{\infty} \left[\boldsymbol{\lambda}(\omega) i\omega \overline{\mathbf{V}}_{o'}(\omega) + \boldsymbol{\mu}(\omega) \overline{\mathbf{V}}_{o'}(\omega) \right] e^{i\omega t} \, d\omega, \\ \mathbf{F}_e(t) &= -\rho \int_{\overline{S}_B} \frac{\partial}{\partial t} (\Phi_I + \Phi_D) \overline{\mathbf{n}} \, dS = \Re \left\{ \frac{1}{2\pi} \int_{-\infty}^{\infty} \overline{\eta}_o(\omega) \mathbf{K}_e(i\omega) e^{i\omega t} \, d\omega \right\}, \end{aligned} \tag{3.10}$$

where $\overline{\mathbf{n}} = \left[n_x \quad n_z \quad (z - z_0)n_x - (x - x_0)n_z \right]^\mathsf{T}$ is the augmented normal vector corresponding to the horizontal force, vertical force and moment around y axis, respectively. The frequency-dependent hydrodynamic coefficient matrices — added mass $\boldsymbol{\lambda}$, radiation damping $\boldsymbol{\mu}$, and wave excitation transfer function $\mathbf{K}_e$ — can be determined once the potential solutions $\boldsymbol{\phi} = \begin{bmatrix} \phi_R^{surge} & \phi_R^{heave} & \phi_R^{pitch} & \phi_D \end{bmatrix}^\mathsf{T}$ are calculated:

$$\begin{aligned} \boldsymbol{\lambda}(\omega) &= \rho \int_{\overline{S}_B} \overline{\mathbf{n}} \left[\boldsymbol{\phi}_R^{Re}\right]^\mathsf{T} dS, \\ \boldsymbol{\mu}(\omega) &= -\rho\omega \int_{\overline{S}_B} \overline{\mathbf{n}} \left[\boldsymbol{\phi}_R^{Im}\right]^\mathsf{T} dS, \\ \mathbf{K}_e(i\omega) &= -\rho i\omega \int_{\overline{S}_B} (\phi_I + \phi_D)\,\overline{\mathbf{n}}\,dS, \end{aligned} \tag{3.11}$$

where $()^{Re}$ and $()^{Im}$ denote the real and imaginary parts of the radiation potential $\boldsymbol{\phi}_R$, respectively. It is worth noting that the wave radiation force $\mathbf{F}_{rt}$ in Eq. (3.10) is the sum of the radiation inertia $\boldsymbol{\lambda}_\infty \ddot{\boldsymbol{\xi}}$ and radiation damping force $\mathbf{F}_r$, as described in Eq. (2.1).

3.3 Analytical formulation

The analytical formulation for the 2D linear wave-platform BVP with an arbitrary platform pose, as defined in Eq. (3.7), is developed in this work. The methodology is demonstrated on a barge-type floating platform in the Oxz plane, assuming an infinite length along the y axis. The primary challenge in solving the BVP analytically arises from the non-homogeneous boundary conditions on the irregular submerged body surface $\overline{S}_B$. When the barge platform is in its upright position, i.e., with zero pitch rotation ($\xi_5 = 0$), the submerged area is rectangular, as shown in Fig. 3.2(a). This simple case has been extensively studied over the past few decades [137, 72, 146, 85], leading to a standard approach that involves splitting the fluid domain into three subdomains along the two vertical sides of the platform. This approach simplifies the original BVP, which has three non-homogeneous body-surface boundary conditions in a complex fluid domain, into three BVPs in simple rectangular subdomains, each with only one non-homogeneous body-surface boundary condition. The method of separation of variables is then applied to represent the solutions for $\boldsymbol{\phi}$ in each fluid subdomain as eigenfunction expansions, and the continuity conditions at the two vertical interfaces convert the original BVP into a system of linear equations with the coefficients of the eigenfunctions as unknowns.

However, when the platform is tilted ($\xi_5 \neq 0$), as shown in Fig. 3.2(b) and (c), the non-orthogonal boundaries resulting from the slanting sides of the platform prevent the fluid domain from being split into separable BVPs by this method. To address the non-orthogonal boundary issue, the step approximation inspired by surface-wave problems [126, 106] is implemented in this work. As illustrated in Fig. 3.2(b) and (c), the slanting sides of a tilted barge are replaced by a series of steps comprising only horizontal and vertical lines. The fluid domain can be discretized into rectangular subdomains along the vertical lines of the steps, such that the standard analytical method can be applied in each subdomain. Note again that this discretization is applicable to floating bodies with arbitrary geometry, and the rectangular cross section is only used for ease of presentation.

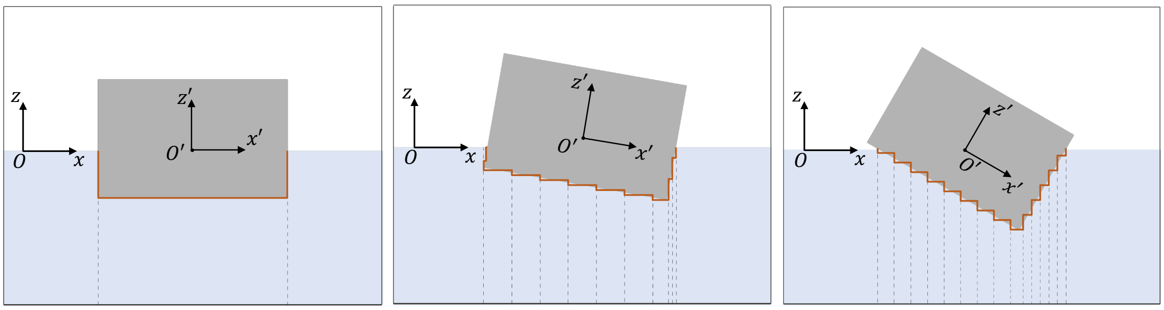

(a) Rectangular submergence (b) Trapezoidal submergence (c) Triangular submergence

Fig. 3.2 Step approximation for the 2D wetted body submergence of (a) rectangular, (b) trapezoidal, and (c) triangular shapes.

3.3.1 Step approximation

The pose of Fig. 3.2(b) is used as an example, resulting in the geometry of the submerged part of the body being trapezoidal. In that case, the fluid domain can be discretized into a series of rectangular subdomains, as shown in Fig. 3.3. The vertices of the submerged floating barge are labelled clockwise from the top right corner to top left, with coordinates $\mathrm{A}:(x_a,0)$, $\mathrm{B}:(x_b,z_b)$, $\mathrm{C}:(x_c,z_c)$, $\mathrm{D}:(x_d,0)$. These coordinates can be determined from the kinematics of the platform:

$$\begin{bmatrix} x \\ z \end{bmatrix} = \begin{bmatrix} x_0 \\ z_0 \end{bmatrix} + \begin{bmatrix} \cos\xi_5 & \sin\xi_5 \\ -\sin\xi_5 & \cos\xi_5 \end{bmatrix} \begin{bmatrix} x' \\ z' \end{bmatrix}, \tag{3.12}$$

where $[x' \; z']^\intercal$ is the position vector of an arbitrary point on the platform surface in the body-fixed reference frame $O'x'z'$. The fluid subdomains are also labelled clockwise, starting from the right open-ended region ($j=1$) to the one adjacent to vertex D ($j=N_d$). The subdomain under vertex B is labelled as $j=N_b$, and the left open-ended subdomain as $j=N_c$. Note that D disappears under the triangular submergence, as depicted in Fig. 3.2(c). The j^{th} fluid subdomain Ω_j is bounded by $x=x_{j+1}$ on the left, $x=x_j$ on the right, $z=-h$ at the bottom, and $z=z_j$ at the top for all subdomains beneath the barge ($j<N_c$). If side CD exists ($j>N_c$), the subdomains above the barge are bounded by $x=x_{j-1}$ on the left, $x=x_j$ on the right, $z=z_j$ at the bottom, and $z=0$ at the top.

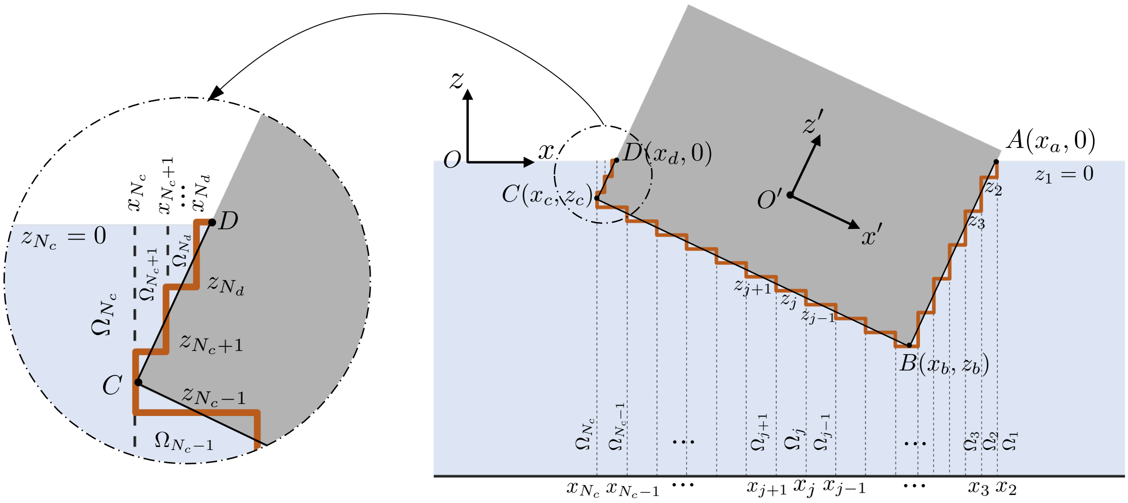

Fig. 3.3 Fluid subdomains and the associated coordinates for a tilted 2D floating platform.

3.3.2 General expressions of potential functions in different domains

In this subsection the expressions for the velocity potentials in all fluid subdomains are determined by applying the method of separation of variables.

- ***Potentials in the right open-ended subdomain* Ω_1**

  The potentials in subdomain Ω_1 can be written as the product of an unknown coefficient vector ($\boldsymbol{A}_1$), and an eigenfunction vector ($\boldsymbol{\Lambda}_{A,1}$) that satisfies Laplace's equation, and the free-surface, sea-bed and far-field boundary conditions:

$$\boldsymbol{\phi}_1=\boldsymbol{\Lambda}_{A,1}^{\mathsf{T}}\boldsymbol{A}_1 \text{ , where } \boldsymbol{\Lambda}_{A,1}=\begin{pmatrix} e^{-\beta_{1,1}(x-x_2)}\dfrac{\cos\left[\beta_{1,1}(z+h)\right]}{\cos\left(\beta_{1,1}h\right)} \\ \vdots \\ e^{-\beta_{1,n}(x-x_2)}\dfrac{\cos\left[\beta_{1,n}(z+h)\right]}{\cos\left(\beta_{1,n}h\right)} \\ \vdots \end{pmatrix} \text{ , } \boldsymbol{A}_1=\begin{pmatrix} A_{1,1} \\ \vdots \\ A_{1,n} \\ \vdots \end{pmatrix} . \quad (3.13)$$

  The eigenvalues $\beta_{1,n}$ satisfy

$$\omega^2=-g\beta_{1,n}\tan(\beta_{1,n}h), \quad (3.14)$$

  where $\beta_{1,1}=ik$ is the imaginary root, with k being the wave number defined in Eq. (3.6). The elements of the eigenfunction $\boldsymbol{\Lambda}_{A,1}$ are mutually orthogonal over $[-h,0]$ on the interface $x=x_2$, which yields the following equation:

$$\int_{-h}^{0} \frac{\cos\left[\beta_{1,m}(z+h)\right]}{\cos\left(\beta_{1,m}h\right)} \frac{\cos\left[\beta_{1,n}(z+h)\right]}{\cos\left(\beta_{1,n}h\right)} dz = C_{1,n}\delta_{mn}, \tag{3.15}$$

where:

$$C_{1,n} = \frac{\cos\left(\beta_{1,n}h\right)\sin\left(\beta_{1,n}h\right) + \beta_{1,n}h}{2\beta_{1,n}\cos^2\left(\beta_{1,n}h\right)}, \tag{3.16}$$

and δ is used for the Kronecker δ function:

$$\delta_{mn} = \begin{cases} 1, & m = n \\ 0, & m \neq n \end{cases} \tag{3.17}$$

with $m, n = 1, 2, 3, \ldots$ representing different eigenmodes.

- ***Potentials in subdomains below the barge*** Ω_j***,*** $(j = 2, \ldots, N_c - 1)$

  For the subdomains below the barge, the potentials can be expressed as the sum of a particular and a homogeneous solution. $\boldsymbol{\phi}_j^p$ is the particular solution satisfying Laplace's equation, sea-bed boundary condition, and the non-homogeneous boundary condition on the barge surface $(z = z_j)$: $\frac{\partial \boldsymbol{\phi}_j^p}{\partial z} = \begin{bmatrix} 0 & 1 & -(x - x_o) & -\frac{\partial \phi_I}{\partial z} \end{bmatrix}^\mathsf{T}$, as listed in Eq. (3.7). One possible set of solutions to $\boldsymbol{\phi}_j^p$ is:

$$\boldsymbol{\phi}_j^p = \begin{bmatrix} 0 & \dfrac{(z+h)^2 - (x - x_0)^2}{2(h + z_j)} & -\dfrac{(z+h)^2(x - x_0) - \frac{1}{3}(x - x_0)^3}{2(h + z_j)} & -\phi_I \end{bmatrix}^\mathsf{T}. \tag{3.18}$$

  $\boldsymbol{\phi}_j^h$ is the component corresponding to the homogeneous boundary condition on $z = z_j$: $\frac{\partial \boldsymbol{\phi}_j^h}{\partial z} = 0$. It can be expressed as $\boldsymbol{\phi}_j^h = \boldsymbol{\Lambda}_{A,j}^\mathsf{T}\boldsymbol{A}_j + \boldsymbol{\Lambda}_{B,j}^\mathsf{T}\boldsymbol{B}_j$, where the eigenfunctions

$$\boldsymbol{\Lambda}_{A,j} = \begin{pmatrix} x \\ e^{-\beta_{j,2}\left(x - x_{j+1}\right)} \dfrac{\cos\left[\beta_{j,2}(z+h)\right]}{\cos\left[\beta_{j,2}\left(z_j + h\right)\right]} \\ \vdots \\ e^{-\beta_{j,n}\left(x - x_{j+1}\right)} \dfrac{\cos\left[\beta_{j,n}(z+h)\right]}{\cos\left[\beta_{j,n}\left(z_j + h\right)\right]} \\ \vdots \end{pmatrix}, \quad \boldsymbol{\Lambda}_{B,j} = \begin{pmatrix} 1 \\ e^{\beta_{j,2}\left(x - x_j\right)} \dfrac{\cos\left[\beta_{j,2}(z+h)\right]}{\cos\left[\beta_{j,2}\left(z_j + h\right)\right]} \\ \vdots \\ e^{\beta_{j,n}\left(x - x_j\right)} \dfrac{\cos\left[\beta_{j,n}(z+h)\right]}{\cos\left[\beta_{j,n}\left(z_j + h\right)\right]} \\ \vdots \end{pmatrix}, \tag{3.19}$$

and the coefficients

$$\boldsymbol{A}_j = \begin{pmatrix} A_{j,1} \\ A_{j,2} \\ \vdots \\ A_{j,n} \\ \vdots \end{pmatrix}, \quad \boldsymbol{B}_j = \begin{pmatrix} B_{j,1} \\ B_{j,2} \\ \vdots \\ B_{j,n} \\ \vdots \end{pmatrix}.$$

The eigenvalues $\beta_{j,n} = \frac{(n-1)\pi}{h+z_j}$, $(n = 2,3,\ldots;\ j = 2,\ldots,N_c-1)$ are independent of the wave frequency ω, which is the major difference from the eigenvalues in the subdomains connected to the free surface, as presented in Eq. (3.14). The elements of eigenfunctions $\boldsymbol{\Lambda}_{A,j}$ and $\boldsymbol{\Lambda}_{B,j}$ are mutually orthogonal over $[-h, z_j]$ on the vertical interfaces $x = x_{j+1}$ and $x = x_j$, which can be summarized as:

$$\int_{-h}^{z_j} \begin{bmatrix} 1 \\ x \\ \dfrac{\cos\left[\beta_{j,m}(z+h)\right]}{\cos\left[\beta_{j,m}\left(z_j+h\right)\right]} \end{bmatrix} \begin{bmatrix} 1 & x & \dfrac{\cos\left[\beta_{j,n}(z+h)\right]}{\cos\left[\beta_{j,n}\left(z_j+h\right)\right]} \end{bmatrix} dz$$

$$= \begin{bmatrix} \left(h+z_j\right) & x\left(h+z_j\right) & 0 \\ x\left(h+z_j\right) & x^2\left(h+z_j\right) & 0 \\ 0 & 0 & \dfrac{h+z_j}{2}\delta_{mn} \end{bmatrix}. \tag{3.20}$$

The total velocity potential in domains Ω_j, $(j = 2,\ldots,N_c-1)$ can thus be expressed as the sum of $\boldsymbol{\phi}_j^p$ and $\boldsymbol{\phi}_j^h$:

$$\boldsymbol{\phi}_j = \boldsymbol{\phi}_j^p + \boldsymbol{\Lambda}_{A,j}^{\intercal}\boldsymbol{A}_j + \boldsymbol{\Lambda}_{B,j}^{\intercal}\boldsymbol{B}_j. \tag{3.21}$$

- ***Potentials in the left open-ended subdomain*** Ω_{N_c}

Similarly as in Ω_1, the potential function in Ω_{N_c} can be written as:

$$\boldsymbol{\phi}_{N_c} = \boldsymbol{\Lambda}_{B,N_c}^{\mathsf{T}} \boldsymbol{B}_{N_c} \text{ , where } \boldsymbol{\Lambda}_{B,N_c} = \begin{pmatrix} e^{\beta_{N_c,1}(x-x_{N_c})} \dfrac{\cos\left[\beta_{N_c,1}(z+h)\right]}{\cos\left(\beta_{N_c,1}h\right)} \\ \vdots \\ e^{\beta_{N_c,n}(x-x_{N_c})} \dfrac{\cos\left[\beta_{N_c,n}(z+h)\right]}{\cos\left(\beta_{N_c,n}h\right)} \\ \vdots \end{pmatrix}, \boldsymbol{B}_{N_c} = \begin{pmatrix} B_{N_c,1} \\ \vdots \\ B_{N_c,n} \\ \vdots \end{pmatrix}. \tag{3.22}$$

The eigenvalues $\beta_{N_c,n} = \beta_{1,n}$ and the eigenfunctions $\boldsymbol{\Lambda}_{B,N_c}$ satisfy an orthogonality condution that has the same form as Eq. (3.15), given the assumption of constant sea depth.

- ***Potentials in subdomains above the barge*** $\Omega_j,\ (j = N_c+1,\dots,N_d)$

  For subdomains above the barge, the potentials are again split into components of particular and homogeneous solutions. One possible set of the particular component, which simultaneously satisfies Laplace's equation, the free-surface boundary condition and the non-homogeneous body-surface boundary condition on $z = z_j$, is:

$$\boldsymbol{\phi}_j^p = \begin{bmatrix} 0 & z+\dfrac{g}{\omega^2} & -(x-x_0)(z+\dfrac{g}{\omega^2}) & -\phi_I \end{bmatrix}^{\mathsf{T}}. \tag{3.23}$$

The homogenous component can be written as $\boldsymbol{\phi}_j^h = \boldsymbol{\Lambda}_{A,j}^{\mathsf{T}} \boldsymbol{A}_j + \boldsymbol{\Lambda}_{B,j}^{\mathsf{T}} \boldsymbol{B}_j$, where the eigenfunctions are defined as:

$$\boldsymbol{\Lambda}_{A,j} = \begin{pmatrix} e^{-\beta_{j,1}(x-x_{j-1})} \dfrac{\cos\left[\beta_{j,1}(z-z_j)\right]}{\cos\left(\beta_{j,1}z_j\right)} \\ \vdots \\ e^{-\beta_{j,n}(x-x_{j-1})} \dfrac{\cos\left[\beta_{j,n}(z-z_j)\right]}{\cos\left(\beta_{j,n}z_j\right)} \\ \vdots \end{pmatrix}, \boldsymbol{\Lambda}_{B,j} = \begin{pmatrix} e^{\beta_{j,1}(x-x_j)} \dfrac{\cos\left[\beta_{j,1}(z-z_j)\right]}{\cos\left(\beta_{j,1}z_j\right)} \\ \vdots \\ e^{\beta_{j,n}(x-x_j)} \dfrac{\cos\left[\beta_{j,n}(z-z_j)\right]}{\cos\left(\beta_{j,n}z_j\right)} \\ \vdots \end{pmatrix}. \tag{3.24}$$

The corresponding eigenvalues $\beta_{j,n},\ (j = N_c+1,\dots,N_d)$ satisfy a new dispersion relation, which depends on both the wave frequency and the height of the fluid subdomain ($-z_j$):

$$\omega^2 = g\beta_{j,n}\tan(\beta_{j,n}z_j). \tag{3.25}$$

The elements of the eigenfunctions $\boldsymbol{\Lambda}_{A,j}$ and $\boldsymbol{\Lambda}_{B,j}$ are mutually orthogonal over $[z_j, 0]$ on the vertical interfaces $x = x_{j-1}$ and $x = x_j$, which yields:

$$\int_{z_j}^{0} \frac{\cos\left[\beta_{j,m}\left(z-z_j\right)\right]}{\cos\left(\beta_{j,m}z_j\right)} \frac{\cos\left[\beta_{j,n}\left(z-z_j\right)\right]}{\cos\left(\beta_{j,n}z_j\right)}\, dz = -\frac{\cos\left(\beta_{j,n}h\right)\sin\left(\beta_{j,n}z_j\right)+\beta_{j,n}z_j}{2\beta_{j,n}\cos^2\left(\beta_{j,n}z_j\right)}\delta_{mn}. \tag{3.26}$$

3.3.3 Determination of unknown coefficients

To determine the unknown coefficients $\boldsymbol{A}_j$ and $\boldsymbol{B}_j$, $(j = 1, 2, \ldots, N_d)$ in the potential expressions that were presented earlier, the continuity conditions of pressure and normal velocity at the vertical interfaces between neighboring fluid subdomains are used.

For the interfaces under the side AB ($x = x_j,\ j = 2, \ldots, N_b$), the continuity of pressure implies:

$$\boldsymbol{\phi}_j = \boldsymbol{\phi}_{j-1}, \text{ on } -h \leq z \leq z_j, \tag{3.27}$$

which can be expanded as:

$$\boldsymbol{\phi}_j^p + \boldsymbol{\Lambda}_{A,j}^{\mathsf{T}}\boldsymbol{A}_j + \boldsymbol{\Lambda}_{B,j}^{\mathsf{T}}\boldsymbol{B}_j = \boldsymbol{\phi}_{j-1}^p + \boldsymbol{\Lambda}_{A,j-1}^{\mathsf{T}}\boldsymbol{A}_{j-1} + \boldsymbol{\Lambda}_{B,j-1}^{\mathsf{T}}\boldsymbol{B}_{j-1}. \tag{3.28}$$

Multiplying both sides of Eq. (3.28) by $\boldsymbol{\Lambda}_{B,j}$ and integrating them over $[-h, z_j]$, one can rewrite the pressure continuity as:

$$\int_{-h}^{z_j} \boldsymbol{\Lambda}_{B,j}\left(\boldsymbol{\phi}_j^p + \boldsymbol{\Lambda}_{A,j}^{\mathsf{T}}\boldsymbol{A}_j + \boldsymbol{\Lambda}_{B,j}^{\mathsf{T}}\boldsymbol{B}_j\right)^{\mathsf{T}} dz = \int_{-h}^{z_j} \boldsymbol{\Lambda}_{B,j}\left(\boldsymbol{\phi}_{j-1}^p + \boldsymbol{\Lambda}_{A,j-1}^{\mathsf{T}}\boldsymbol{A}_{j-1} + \boldsymbol{\Lambda}_{B,j-1}^{\mathsf{T}}\boldsymbol{B}_{j-1}\right)^{\mathsf{T}} dz. \tag{3.29}$$

The continuity of the normal velocity implies:

$$\frac{\partial \boldsymbol{\phi}_{j-1}}{\partial x} = \begin{cases} \widetilde{\mathbf{n}}_j = \begin{bmatrix} 1 & 0 & (z-z_0) & -\frac{\partial \phi_I}{\partial x} \end{bmatrix}^{\mathsf{T}}, & z_j \leq z \leq z_{j-1} \\ \dfrac{\partial \boldsymbol{\phi}_j}{\partial x}, & -h \leq z \leq z_j \end{cases} \tag{3.30}$$

which can be expanded as:

$$\frac{\partial \boldsymbol{\phi}_{j-1}^p}{\partial x} + \frac{\partial \boldsymbol{\Lambda}_{A,j-1}^{\mathsf{T}}}{\partial x}\boldsymbol{A}_{j-1} + \frac{\partial \boldsymbol{\Lambda}_{B,j-1}^{\mathsf{T}}}{\partial x}\boldsymbol{B}_{j-1} = \begin{cases} \widetilde{\mathbf{n}}_j, & z_j \leq z \leq z_{j-1} \\ \dfrac{\partial \boldsymbol{\phi}_j^p}{\partial x} + \dfrac{\partial \boldsymbol{\Lambda}_{A,j}^{\mathsf{T}}}{\partial x}\boldsymbol{A}_j + \dfrac{\partial \boldsymbol{\Lambda}_{B,j}^{\mathsf{T}}}{\partial x}\boldsymbol{B}_j, & -h \leq z \leq z_j \end{cases} \tag{3.31}$$

Multiplying both sides of Eq. (3.31) by $\mathbf{\Lambda}_{A,j-1}$ and integrating them over $[-h, z_{j-1}]$, one can rewrite the velocity continuity as

$$\begin{aligned}
&\int_{-h}^{z_{j-1}} \mathbf{\Lambda}_{A,j-1}\left(\frac{\partial \boldsymbol{\phi}_{j-1}^{p}}{\partial x}+\frac{\partial \mathbf{\Lambda}_{A,j-1}^{\mathsf{T}}}{\partial x}\boldsymbol{A}_{j-1}+\frac{\partial \mathbf{\Lambda}_{B,j-1}^{\mathsf{T}}}{\partial x}\boldsymbol{B}_{j-1}\right)^{\mathsf{T}} dz \\
&\qquad = \int_{-h}^{z_j}\mathbf{\Lambda}_{A,j-1}\left(\frac{\partial \boldsymbol{\phi}_{j}^{p}}{\partial x}+\frac{\partial \mathbf{\Lambda}_{A,j}^{\mathsf{T}}}{\partial x}\boldsymbol{A}_{j}+\frac{\partial \mathbf{\Lambda}_{B,j}^{\mathsf{T}}}{\partial x}\boldsymbol{B}_{j}\right)^{\mathsf{T}} dz+\int_{z_j}^{z_{j-1}}\mathbf{\Lambda}_{A,j-1}\widetilde{\mathbf{n}}_j^{\mathsf{T}}dz. \qquad (3.32)
\end{aligned}$$

We write Eq. (3.29) and Eq. (3.32) into the matrix form for more compact expression:

$$\begin{aligned}
&\begin{bmatrix}
-\int_{-h}^{z_j}\mathbf{\Lambda}_{B,j}\mathbf{\Lambda}_{A,j-1}^{\mathsf{T}}dz & -\int_{-h}^{z_j}\mathbf{\Lambda}_{B,j}\mathbf{\Lambda}_{B,j-1}^{\mathsf{T}}dz & \int_{-h}^{z_j}\mathbf{\Lambda}_{B,j}\mathbf{\Lambda}_{A,j}^{\mathsf{T}}dz & \int_{-h}^{z_j}\mathbf{\Lambda}_{B,j}\mathbf{\Lambda}_{B,j}^{\mathsf{T}}dz \\
\int_{-h}^{z_{j-1}}\mathbf{\Lambda}_{A,j-1}\frac{\partial \mathbf{\Lambda}_{A,j-1}^{\mathsf{T}}}{\partial x}dz & \int_{-h}^{z_{j-1}}\mathbf{\Lambda}_{A,j-1}\frac{\partial \mathbf{\Lambda}_{B,j-1}^{\mathsf{T}}}{\partial x}dz & -\int_{-h}^{z_j}\mathbf{\Lambda}_{A,j-1}\frac{\partial \mathbf{\Lambda}_{A,j}^{\mathsf{T}}}{\partial x}dz & -\int_{-h}^{z_j}\mathbf{\Lambda}_{A,j-1}\frac{\partial \mathbf{\Lambda}_{B,j}^{\mathsf{T}}}{\partial x}dz
\end{bmatrix}
\begin{bmatrix}\boldsymbol{A}_{j-1}\\ \boldsymbol{B}_{j-1}\\ \boldsymbol{A}_{j}\\ \boldsymbol{B}_{j}\end{bmatrix} \\
&\qquad = \begin{bmatrix}
\int_{-h}^{z_j}\mathbf{\Lambda}_{B,j}\left(\boldsymbol{\phi}_{j-1}^{p}-\boldsymbol{\phi}_{j}^{p}\right)^{\mathsf{T}}dz \\
\int_{z_j}^{z_{j-1}}\mathbf{\Lambda}_{A,j-1}\widetilde{\mathbf{n}}_j^{\mathsf{T}}dz+\int_{-h}^{z_j}\mathbf{\Lambda}_{A,j-1}\left(\frac{\partial \boldsymbol{\phi}_{j}^{p}}{\partial x}\right)^{\mathsf{T}}dz-\int_{-h}^{z_{j-1}}\mathbf{\Lambda}_{A,j-1}\left(\frac{\partial \boldsymbol{\phi}_{j-1}^{p}}{\partial x}\right)^{\mathsf{T}}dz
\end{bmatrix}. \qquad (3.33)
\end{aligned}$$

Similarly, the continuity conditions of pressure and normal velocity on the interfaces under side BC ($x = x_j,\ j = N_b+1, \ldots, N_c$) yield

$$\begin{bmatrix} -\int_{-h}^{z_{j-1}} \mathbf{\Lambda}_{A,j-1}\mathbf{\Lambda}_{A,j-1}^{\mathsf{T}} dz & -\int_{-h}^{z_{j-1}} \mathbf{\Lambda}_{A,j-1}\mathbf{\Lambda}_{B,j-1}^{\mathsf{T}} dz & \int_{-h}^{z_{j-1}} \mathbf{\Lambda}_{A,j-1}\mathbf{\Lambda}_{A,j}^{\mathsf{T}} dz & \int_{-h}^{z_{j-1}} \mathbf{\Lambda}_{A,j-1}\mathbf{\Lambda}_{B,j}^{\mathsf{T}} dz \\ -\int_{-h}^{z_{j-1}} \mathbf{\Lambda}_{B,j}\frac{\partial \mathbf{\Lambda}_{A,j-1}^{\mathsf{T}}}{\partial x} dz & -\int_{-h}^{z_{j-1}} \mathbf{\Lambda}_{B,j}\frac{\partial \mathbf{\Lambda}_{B,j-1}^{\mathsf{T}}}{\partial x} dz & \int_{-h}^{z_{j}} \mathbf{\Lambda}_{B,j}\frac{\partial \mathbf{\Lambda}_{A,j}^{\mathsf{T}}}{\partial x} dz & \int_{-h}^{z_{j}} \mathbf{\Lambda}_{B,j}\frac{\partial \mathbf{\Lambda}_{B,j}^{\mathsf{T}}}{\partial x} dz \end{bmatrix} \begin{bmatrix} \boldsymbol{A}_{j-1} \\ \boldsymbol{B}_{j-1} \\ \boldsymbol{A}_{j} \\ \boldsymbol{B}_{j} \end{bmatrix}$$

$$= \begin{bmatrix} \int_{-h}^{z_{j-1}} \mathbf{\Lambda}_{A,j-1}\left(\boldsymbol{\phi}_{j-1}^{p} - \boldsymbol{\phi}_{j}^{p}\right)^{\mathsf{T}} dz \\ \int_{z_{j-1}}^{z_j} \mathbf{\Lambda}_{B,j}\widetilde{\mathbf{n}}_j^{\mathsf{T}} dz + \int_{-h}^{z_{j-1}} \mathbf{\Lambda}_{B,j}\left(\frac{\partial \boldsymbol{\phi}_{j-1}^{p}}{\partial x}\right)^{\mathsf{T}} dz - \int_{-h}^{z_j} \mathbf{\Lambda}_{B,j}\left(\frac{\partial \boldsymbol{\phi}_{j}^{p}}{\partial x}\right)^{\mathsf{T}} dz \end{bmatrix}. \quad (3.34)$$

The continuity conditions on the interfaces above side CD ($x = x_j,\ j = N_c + 1, \ldots, N_d$) yield

$$\begin{bmatrix} \int_{z_{j+1}}^{0} \mathbf{\Lambda}_{A,j+1}\mathbf{\Lambda}_{A,j}^{\mathsf{T}} dz & \int_{z_{j+1}}^{0} \mathbf{\Lambda}_{A,j+1}\mathbf{\Lambda}_{B,j}^{\mathsf{T}} dz & -\int_{z_{j+1}}^{0} \mathbf{\Lambda}_{A,j+1}\mathbf{\Lambda}_{A,j+1}^{\mathsf{T}} dz & -\int_{z_{j+1}}^{0} \mathbf{\Lambda}_{A,j+1}\mathbf{\Lambda}_{B,j+1}^{\mathsf{T}} dz \\ \int_{z_j}^{0} \mathbf{\Lambda}_{B,j}\frac{\partial \mathbf{\Lambda}_{A,j}^{\mathsf{T}}}{\partial x} dz & \int_{z_j}^{0} \mathbf{\Lambda}_{B,j}\frac{\partial \mathbf{\Lambda}_{B,j}^{\mathsf{T}}}{\partial x} dz & -\int_{z_j}^{z_{j+1}} \mathbf{\Lambda}_{B,j}\frac{\partial \mathbf{\Lambda}_{A,j+1}^{\mathsf{T}}}{\partial x} dz & -\int_{z_j}^{z_{j+1}} \mathbf{\Lambda}_{B,j}\frac{\partial \mathbf{\Lambda}_{B,j+1}^{\mathsf{T}}}{\partial x} dz \end{bmatrix} \begin{bmatrix} \boldsymbol{A}_{j} \\ \boldsymbol{B}_{j} \\ \boldsymbol{A}_{j+1} \\ \boldsymbol{B}_{j+1} \end{bmatrix}$$

$$= \begin{bmatrix} \int_{z_{j+1}}^{0} \mathbf{\Lambda}_{A,j+1}\left(\boldsymbol{\phi}_{j+1}^{p} - \boldsymbol{\phi}_{j}^{p}\right)^{\mathsf{T}} dz \\ \int_{z_j}^{z_{j+1}} \mathbf{\Lambda}_{B,j}\widetilde{\mathbf{n}}_j^{\mathsf{T}} dz + \int_{z_{j+1}}^{0} \mathbf{\Lambda}_{B,j}\left(\frac{\partial \boldsymbol{\phi}_{j+1}^{p}}{\partial x}\right)^{\mathsf{T}} dz - \int_{z_j}^{0} \mathbf{\Lambda}_{B,j}\left(\frac{\partial \boldsymbol{\phi}_{j}^{p}}{\partial x}\right)^{\mathsf{T}} dz \end{bmatrix}. \quad (3.35)$$

It should be noted that only the continuity of normal velocity is required on $x = x_{N_d}$ and the matrix form is

$$\begin{bmatrix} \int_{z_{N_d}}^{0} \mathbf{\Lambda}_{B,N_d}\frac{\partial \mathbf{\Lambda}_{A,N_d}^{\mathsf{T}}}{\partial x}dz & \int_{z_{N_d}}^{0} \mathbf{\Lambda}_{B,N_d}\frac{\partial \mathbf{\Lambda}_{B,N_d}^{\mathsf{T}}}{\partial x}dz \end{bmatrix} \begin{bmatrix} \boldsymbol{A}_{N_d} \\ \boldsymbol{B}_{N_d} \end{bmatrix} = \int_{z_{N_d}}^{0} \mathbf{\Lambda}_{B,N_d}\widetilde{\mathbf{n}}_{N_d}^{\mathsf{T}}dz - \int_{z_{N_d}}^{0} \mathbf{\Lambda}_{B,N_d}\left(\frac{\partial \boldsymbol{\phi}_{N_d}^{p}}{\partial x}\right)^{\mathsf{T}}dz. \tag{3.36}$$

In addition, special attention should be given to the interfaces that are adjacent to open domains ($j = 1$ and $j = N_c$). They are summarized as follows:

$$\begin{bmatrix} -\int_{-h}^{z_2} \mathbf{\Lambda}_{B,2}\mathbf{\Lambda}_{A,1}^{\mathsf{T}}dz & \int_{-h}^{z_2} \mathbf{\Lambda}_{B,2}\mathbf{\Lambda}_{A,2}^{\mathsf{T}}dz & \int_{-h}^{z_2} \mathbf{\Lambda}_{B,2}\mathbf{\Lambda}_{B,2}^{\mathsf{T}}dz \\ \int_{-h}^{0} \mathbf{\Lambda}_{A,1}\frac{\partial \mathbf{\Lambda}_{A,1}^{\mathsf{T}}}{\partial x}dz & -\int_{-h}^{z_2} \mathbf{\Lambda}_{A,1}\frac{\partial \mathbf{\Lambda}_{A,2}^{\mathsf{T}}}{\partial x}dz & -\int_{-h}^{z_2} \mathbf{\Lambda}_{A,1}\frac{\partial \mathbf{\Lambda}_{B,2}^{\mathsf{T}}}{\partial x}dz \end{bmatrix} \begin{bmatrix} \boldsymbol{A}_1 \\ \boldsymbol{A}_2 \\ \boldsymbol{B}_2 \end{bmatrix} = \begin{bmatrix} -\int_{-h}^{z_2} \mathbf{\Lambda}_{B,2}\left(\boldsymbol{\phi}_2^{p}\right)^{\mathsf{T}}dz \\ \int_{z_2}^{0} \mathbf{\Lambda}_{A,1}\widetilde{\mathbf{n}}_2^{\mathsf{T}}dz + \int_{-h}^{z_2} \mathbf{\Lambda}_{A,1}\left(\frac{\partial \boldsymbol{\phi}_2^{p}}{\partial x}\right)^{\mathsf{T}}dz \end{bmatrix}, \tag{3.37}$$

$$\begin{bmatrix} -\int_{-h}^{z_{N_c-1}} \mathbf{\Lambda}_{A,N_c-1}\mathbf{\Lambda}_{A,N_c-1}^{\mathsf{T}}dz & -\int_{-h}^{z_{N_c-1}} \mathbf{\Lambda}_{A,N_c-1}\mathbf{\Lambda}_{B,N_c-1}^{\mathsf{T}}dz & \int_{-h}^{z_{N_c-1}} \mathbf{\Lambda}_{A,N_c-1}\mathbf{\Lambda}_{B,N_c}^{\mathsf{T}}dz & 0 & 0 \\ 0 & 0 & \int_{z_{N_c+1}}^{0} \mathbf{\Lambda}_{A,N_c+1}\mathbf{\Lambda}_{B,N_c}^{\mathsf{T}}dz & -\int_{z_{N_c+1}}^{0} \mathbf{\Lambda}_{A,N_c+1}\mathbf{\Lambda}_{A,N_c+1}^{\mathsf{T}}dz & -\int_{z_{N_c+1}}^{0} \mathbf{\Lambda}_{A,N_c+1}\mathbf{\Lambda}_{B,N_c+1}^{\mathsf{T}}dz \\ -\int_{-h}^{z_{N_c-1}} \mathbf{\Lambda}_{B,N_c}\frac{\partial \mathbf{\Lambda}_{A,N_c-1}^{\mathsf{T}}}{\partial x}dz & -\int_{-h}^{z_{N_c-1}} \mathbf{\Lambda}_{B,N_c}\frac{\partial \mathbf{\Lambda}_{B,N_c-1}^{\mathsf{T}}}{\partial x}dz & \int_{-h}^{0} \mathbf{\Lambda}_{B,N_c}\frac{\partial \mathbf{\Lambda}_{B,N_c}^{\mathsf{T}}}{\partial x}dz & -\int_{z_{N_c+1}}^{0} \mathbf{\Lambda}_{B,N_c}\frac{\partial \mathbf{\Lambda}_{A,N_c+1}^{\mathsf{T}}}{\partial x}dz & -\int_{z_{N_c+1}}^{0} \mathbf{\Lambda}_{B,N_c}\frac{\partial \mathbf{\Lambda}_{B,N_c+1}^{\mathsf{T}}}{\partial x}dz \end{bmatrix}$$

$$\cdot \begin{bmatrix} \boldsymbol{A}_{N_c-1} \\ \boldsymbol{B}_{N_c-1} \\ \boldsymbol{B}_{N_c} \\ \boldsymbol{A}_{N_c+1} \\ \boldsymbol{B}_{N_c+1} \end{bmatrix} = \begin{bmatrix} \int_{-h}^{z_{N_c-1}} \mathbf{\Lambda}_{A,N_c-1}\left(\boldsymbol{\phi}_{N_c-1}^{p}\right)^{\mathsf{T}}dz \\ \int_{z_{N_c+1}}^{0} \mathbf{\Lambda}_{A,N_c+1}\left(\boldsymbol{\phi}_{N_c+1}^{p}\right)^{\mathsf{T}}dz \\ \int_{z_{N_c-1}}^{z_{N_c+1}} \mathbf{\Lambda}_{B,N_c}\widetilde{\mathbf{n}}_{N_c}^{\mathsf{T}}dz + \int_{-h}^{z_{N_c-1}} \mathbf{\Lambda}_{B,N_c}\left(\frac{\partial \boldsymbol{\phi}_{N_c-1}^{p}}{\partial x}\right)^{\mathsf{T}}dz + \int_{z_{N_c+1}}^{0} \mathbf{\Lambda}_{B,N_c}\left(\frac{\partial \boldsymbol{\phi}_{N_c+1}^{p}}{\partial x}\right)^{\mathsf{T}}dz \end{bmatrix}. \tag{3.38}$$

Assembling Eq. (3.33) – (3.38) results in a system of linear equations, from which all the unknown coefficients $\boldsymbol{A}_j$ and $\boldsymbol{B}_j$, $(j = 1, 2, \ldots, N_d)$ can be determined. It is worth mentioning that the left-hand side of these equations depends only on the fluid domain discretization and wave frequency, while all terms related to the platform motion and incident wave, arising from both the non-homogeneous body-surface boundary condition $\widetilde{\mathbf{n}}_j$ (Eq. (3.8)) and the particular potential solutions $\boldsymbol{\phi}_j^p$ (Eq. (3.18) and (3.23)), appear only on the right-hand side of the equations. Therefore, the left-hand sides are only required to be calculated once for all three radiation problems and one diffraction problem at each wave frequency. This efficient matrix form effectively avoids the unnecessary recomputation of all terms for each of the four problems as done in existing analytical methods [146]. The left-hand side integrals are also greatly simplified thanks to the orthogonal properties of the eigenfunctions (Eq. (3.15), (3.20), and (3.26)).

For practical computation, the infinite series appearing within the integrals of equations Eq. (3.13), (3.19), (3.22) and (3.24) are truncated, and only the first N modes are included. This leads to $(N_d - 1) \times N \times 4 \times 2$ equations, where N_d denotes the total number of fluid subdomains, N the eigenfunction truncation number, 4 the sum of three radiation and one diffraction potentials $\boldsymbol{\phi}$, and two the continuity conditions of pressure and normal velocity on each fluid interface. After solving the total $(N_d - 1) \times N \times 4 \times 2$ coefficients, the analytical expressions for the velocity potentials in each fluid subdomain can be obtained according to Eq. (3.13), (3.21), and (3.22).

3.3.4 Integration of wave forces

Upon getting the expressions for three radiation potentials $\boldsymbol{\phi}_R$ and a diffraction potential ϕ_D in each fluid subdomain, the hydrodynamic force coefficients of the floating platform around its center of gravity (x_0, z_0), as described in Eq. (3.11), can be calculated as follows:

$$\boldsymbol{\lambda}(\omega) = \rho \boldsymbol{I}_{\phi_R}^{Re}, \;\; \boldsymbol{\mu}(\omega) = -\rho\omega \boldsymbol{I}_{\phi_R}^{Re}, \;\; \mathbf{K}_e(i\omega) = -\rho i\omega \boldsymbol{I}_{\phi_{ID}}, \tag{3.39}$$

where $\boldsymbol{I}_{\phi_R}$ denotes the radiation integrals, involving the calculation on four groups of body-surface boundaries:

$$\begin{aligned}\underset{3\times3}{\boldsymbol{I}_{\phi_R}}(\omega) = &\sum_{j=1}^{N_b-1}\int_{z_{j+1}}^{z_j}\overline{\mathbf{n}}_{\mathbf{v}j}(z)\left[\boldsymbol{\phi}_R(x_{j+1},z)\right]^{\mathsf{T}}dz \\ &+\sum_{j=N_b+1}^{N_d}\int_{z_{j-1}}^{z_j}\overline{\mathbf{n}}_{\mathbf{v}j}(z)\left[\boldsymbol{\phi}_R(x_j,z)\right]^{\mathsf{T}}dz \\ &+\sum_{j=2}^{N_c-1}\int_{x_{j+1}}^{x_j}\overline{\mathbf{n}}_{\mathbf{h}j}(x)\left[\boldsymbol{\phi}_R(x,z_j)\right]^{\mathsf{T}}dx \\ &+\sum_{j=N_c+1}^{N_d}\int_{x_{j-1}}^{x_j}\overline{\mathbf{n}}_{\mathbf{h}j}(x)\left[\boldsymbol{\phi}_R(x,z_j)\right]^{\mathsf{T}}dx,\end{aligned}\tag{3.40}$$

and $\boldsymbol{I}_{\phi_{ID}}$ denotes the diffraction integral:

$$\begin{aligned}\underset{3\times1}{\boldsymbol{I}_{\phi_{ID}}}(\omega) = &\sum_{j=1}^{N_b-1}\int_{z_{j+1}}^{z_j}\overline{\mathbf{n}}_{\mathbf{v}j}(z)\left[\phi_I(x_{j+1},z)+\phi_D(x_{j+1},z)\right]dz \\ &+\sum_{j=N_b+1}^{N_d}\int_{z_{j-1}}^{z_j}\overline{\mathbf{n}}_{\mathbf{v}j}(z)\left[\phi_I(x_j,z)+\phi_D(x_j,z)\right]dz \\ &+\sum_{j=2}^{N_c-1}\int_{x_{j+1}}^{x_j}\overline{\mathbf{n}}_{\mathbf{h}j}(x)\left[\phi_I(x,z_j)+\phi_D(x,z_j)\right]dx \\ &+\sum_{j=N_c+1}^{N_d}\int_{x_{j-1}}^{x_j}\overline{\mathbf{n}}_{\mathbf{h}j}(x)\left[\phi_I(x,z_j)+\phi_D(x,z_j)\right]dx.\end{aligned}\tag{3.41}$$

Note that the integration interval associated with the vertical boundary of the fluid subdomain Ω_{N_c} is $[z_{N_c-1}, z_{N_c+1}]$. The augmented direction vectors on the vertical, horizontal boundaries of the different groups of fluid subdomains are calculated by:

$$\begin{aligned}\overline{\mathbf{n}}_{\mathbf{v}j}(z) &= \begin{cases}\begin{bmatrix}-1 & 0 & -(z-z_0)\end{bmatrix}^{\mathsf{T}}, & j=1,2,\ldots,N_b-1\\ \begin{bmatrix}1 & 0 & (z-z_0)\end{bmatrix}^{\mathsf{T}}, & j=N_b+1,N_b+2,\ldots,N_d,\end{cases} \\ \overline{\mathbf{n}}_{\mathbf{h}j}(x) &= \begin{cases}\begin{bmatrix}0 & 1 & -(x-x_0)\end{bmatrix}^{\mathsf{T}}, & j=2,3,\ldots,N_c-1\\ \begin{bmatrix}0 & -1 & (x-x_0)\end{bmatrix}^{\mathsf{T}}, & j=N_c+1,N_c+2,\ldots,N_d,\end{cases}\end{aligned}\tag{3.42}$$

respectively.

3.4 Numerical formulation: 2D boundary element method

Most existing boundary element codes, such as WAMIT [131] and NEMOH [96], utilize the free-surface Green's function to simplify the linear wave-platform BVP (Eq. (3.7)) into boundary integral equations, which involve discretized elements only on the body surface $\overline{S}_B$. However, these codes are typically developed for generic 3D problems, and only a few are open-source. In this work, the 2D BEM formulation proposed by Meylan [90] is adopted, in which the simple Green's function

$$g(\mathrm{P},\mathrm{Q}) = \frac{1}{2\pi}\ln\frac{1}{r_{\mathrm{PQ}}} \tag{3.43}$$

is applied on all boundaries. $g(\mathrm{P},\ \mathrm{Q})$ describes the wave potential at point P due to a point source of strength -1 placed at point Q [97], where r_{PQ} is the distance between the two points. Modifications to the original 2D BEM formulation and MATLAB codes open-sourced in [90] have been made to improve computational efficiency. In addition, the calculation of hydrostatic and hydrodynamic forces, which is not included in the original BEM code, is proposed in this work with a corresponding MATLAB implementation developed.

3.4.1 Boundary integral equations

Based on Green's theorem, the potential functions $\boldsymbol{\phi} = \begin{bmatrix}\phi_R^{surge} & \phi_R^{heave} & \phi_R^{pitch} & \phi_D\end{bmatrix}^{\mathsf{T}}$ at an observation point P in the fluid domain, which is sufficiently close to the fluid boundary, can be determined from the boundary integral equation:

$$\frac{1}{2}\boldsymbol{\phi}(\mathrm{P}) = \oint_S \frac{\partial\boldsymbol{\phi}(\mathrm{Q})}{\partial n}\cdot g(\mathrm{P},\mathrm{Q})dS(\mathrm{Q}) - \oint_S \boldsymbol{\phi}(\mathrm{Q})\cdot\frac{\partial g(\mathrm{P},\mathrm{Q})}{\partial n}dS(\mathrm{Q}), \tag{3.44}$$

where Q is defined as a dummy point on the closed fluid boundary surfaces $S = \overline{S}_F \cup \overline{S}_B \cup S_\infty \cup S_D$. According to the expressions for boundary conditions in the frequency domain under the linear potential flow assumption (Eq. (3.7)), $\frac{\partial}{\partial n}\boldsymbol{\phi}$ is known on the body surface ($\overline{S}_B$) and the sea bed (S_D), and the relation between $\boldsymbol{\phi}$ and $\frac{\partial}{\partial n}\boldsymbol{\phi}$ is known on the free surface ($\overline{S}_F$) and the far field (S_∞). Hence, the boundary integral equation (Eq. (3.44)) can be rewritten as equations with $\boldsymbol{\phi}$ as the only unknowns on all fluid boundaries.

To alleviate the integration burden along the free surface extending to a sufficiently far field ($|x| \gg 0$), the fluid domain is truncated retaining the domain between two vertical interfaces S_- and S_+, located at $x = x_L$ on the left side and $x = x_R$ on the right of the floating platform. The potential functions in the outer regions can be represented as a sum of eigenfunctions with unknown coefficients. Take the right open region ($x > x_R,\ -h \leq z \leq 0$)

as example, the general expression for $\phi_+(x,z,\omega)$ has the same form as Eq. (3.13), and for practical computation, only the first N modes are taken into account:

$$\phi_+ = \sum_{n=1}^{N} A_{+,n}\Lambda_{+,n}(x,z,\omega) = \sum_{n=1}^{N} A_{+,n}e^{-\beta_{+,n}(x-x_R)}\frac{\cos\left[\beta_{+,n}\left(z+h\right)\right]}{\cos\left(\beta_{+,n}h\right)}, \tag{3.45}$$

where $\beta_{+,n} = \beta_{1,n}$, and $\Lambda_{+,n} = \Lambda_{A,1,n}$. Continuity of pressure and velocity conditions are enforced on the interface between the inner and outer regions ($x = x_R$):

$$\phi(x_R,z,\omega) = \phi_+(x_R,z,\omega) = \sum_{n=1}^{N} A_{+,n}\Lambda_{+,n}(x_R,z,\omega), \tag{3.46}$$

$$\left.\frac{\partial\phi}{\partial x}\right|_{x=x_R} = \left.\frac{\partial\phi_+}{\partial x}\right|_{x=x_R} = -\sum_{n=1}^{N}\beta_{+,n}A_{+,n}\Lambda_{+,n}(x_R,z,\omega). \tag{3.47}$$

Multiplying both sides of Eq. (3.46) by its eigenfunctions $\Lambda_{+,n}(x_R,z,\omega)$ and integrating over $[-h,0]$, one can obtain the expression for $A_{+,n}$. Plugging $A_{+,n}$ into Eq. (3.47) yields the new relation between ϕ and $\frac{\partial}{\partial n}\phi$ on S_+:

$$\frac{\partial\phi}{\partial x}(x_R,z,\omega) = -\sum_{n=1}^{N}\frac{\beta_{+,n}}{C_{+,n}}\left\{\int_{-h}^{0}\phi(x_R,z',\omega)\Lambda_{+,n}(x_R,z',\omega)dz'\right\}\Lambda_{+,n}(x_R,z,\omega), \tag{3.48}$$

where $C_{+,n} = C_{1,n}$ and the expression is given in Eq. (3.16). The ϕ and $\frac{\partial}{\partial n}\phi$ relation on S_- is the same as Eq. (3.48) under the assumption of constant water depth.

3.4.2 Discretization of integral equations

In practice, the closed boundaries appearing in the integral equations of Eq. (3.44) are discretized. As illustrated in Fig. 3.4, the fluid boundaries are approximated by N_e line elements, with the endpoints (geometry points) of the j^{th} element represented as (x_j,z_j) and (x_{j+1},z_{j+1}). The geometry points are labelled counter-clockwise across all fluid boundaries. N_e is the sum of N_- elements on the left boundary S_-, N_+ on the right boundary S_+, N_F on the free surface $\overline{S}_F$, N_D on the sea bed S_D, and N_B on the wetted body surface $\overline{S}_B$. Note that although a barge-type floating platform is shown in Fig. 3.4, the BEM formulation described in this work applies to platforms with arbitrary geometry.

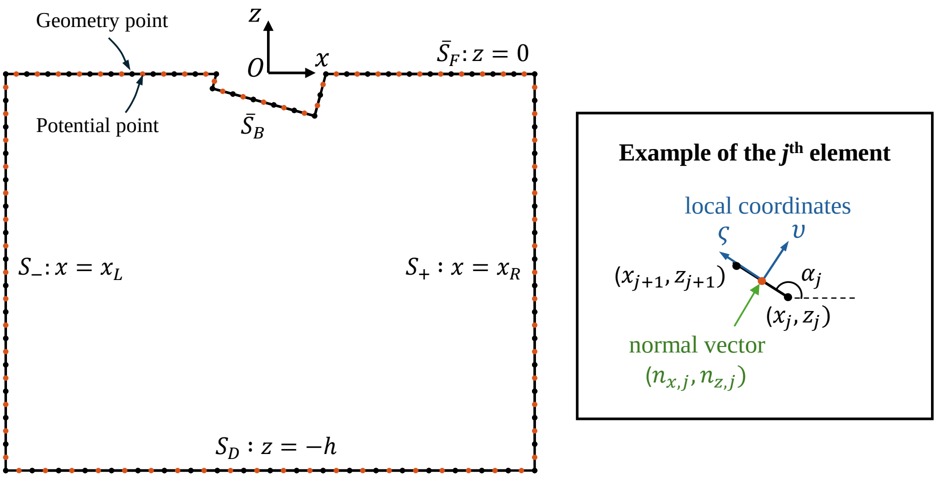

Fig. 3.4 Discretization of the fluid boundaries in the 2D BEM formulation.

The body surface boundary condition $\widetilde{\mathbf{n}}$ at the j^{th} element ($j = 1, 2, \ldots, N_B$) can be determined from Eq. (3.8) as:

$$\widetilde{\boldsymbol{n}}_j = \begin{bmatrix} n_{x,j} \\ n_{z,j} \\ (\frac{z_j + z_{j+1}}{2} - z_0)n_{x,j} - (\frac{x_j + x_{j+1}}{2} - x_0)n_{z,j} \\ -\frac{\partial \phi_I(\frac{x_j+x_{j+1}}{2}, \frac{z_j+z_{j+1}}{2}, \omega)}{\partial x} n_{x,j} - \frac{\partial \phi_I(\frac{x_j+x_{j+1}}{2}, \frac{z_j+z_{j+1}}{2}, \omega)}{\partial z} n_{z,j} \end{bmatrix}, \tag{3.49}$$

in which (x_0, z_0) is the center of gravity, and the components of normal vector can be calculated given the coordinates of the associated geometry points:

$$n_{x,j} = \frac{z_{j+1} - z_j}{\Delta s_j}, \; n_{z,j} = -\frac{x_{j+1} - x_j}{\Delta s_j}, \tag{3.50}$$

where Δs_j denotes the length of the j^{th} element $\Delta s_j = \sqrt{(x_{j+1} - x_j)^2 + (z_{j+1} - z_j)^2}$. To simplify subsequent integration calculations, local coordinates (ς, υ) are defined on each element. As illustrated in the example of the j^{th} element in Fig. 3.4, the rotation angle between the $x - z$ and $\varsigma - \upsilon$ coordinate systems is calculated by $\alpha_j = \tan^{-1}\left(\frac{z_{j+1} - z_j}{x_{j+1} - x_j}\right)$. The midpoint of the k^{th} element, with endpoints at (x_k, z_k) and (x_{k+1}, z_{k+1}), can then be expressed in the $\varsigma - \upsilon$ coordinates of the j^{th} element as:

$$\begin{pmatrix} \varsigma_{j,k} \\ \upsilon_{j,k} \end{pmatrix} = \begin{bmatrix} \cos\alpha_j & \sin\alpha_j \\ \sin\alpha_j & -\cos\alpha_j \end{bmatrix} \begin{pmatrix} \frac{x_k + x_{k+1}}{2} - \frac{x_j + x_{j+1}}{2} \\ \frac{z_k + z_{k+1}}{2} - \frac{z_j + z_{j+1}}{2} \end{pmatrix}. \tag{3.51}$$

The velocity potential $\boldsymbol{\phi}$ and its derivative with respect to the normal to the boundary direction $\frac{\partial}{\partial n}\boldsymbol{\phi}$ are both assumed to be constant over each element and are represented by their values at the midpoint of each element (potential point). As explained in Section 3.4.1, $\frac{\partial}{\partial n}\boldsymbol{\phi}$ can be eliminated from the integral equations given either the values of $\frac{\partial}{\partial n}\boldsymbol{\phi}$ or the relation between $\frac{\partial}{\partial n}\boldsymbol{\phi}$ and $\boldsymbol{\phi}$ on the boundaries:

$$\left[\begin{matrix}\vdots\\ \vdots\\ \dfrac{\partial}{\partial n}\boldsymbol{\phi}^{\mathsf{T}}\\ \vdots\\ \vdots\end{matrix}\right]_{N_e\times 4}=\left[\begin{matrix}\mathbf{R}_- & & & & \\ & \mathbf{R}_+ & & & \\ & & \frac{\omega^2}{g}\mathbf{I} & & \\ & & & \mathbf{0} & \\ & & & & \mathbf{0}\end{matrix}\right]_{N_e\times N_e}\left[\begin{matrix}\vdots\\ \vdots\\ \boldsymbol{\phi}^{\mathsf{T}}\\ \vdots\\ \vdots\end{matrix}\right]_{N_e\times 4}+\left[\begin{matrix}\mathbf{0}_{N_-\times 4}\\ \mathbf{0}_{N_+\times 4}\\ \mathbf{0}_{N_F\times 4}\\ \mathbf{0}_{N_D\times 4}\\ \widetilde{\mathbf{n}}^{\mathsf{T}}_{N_B\times 4}\end{matrix}\right]_{N_e\times 4}. \tag{3.52}$$

The five row blocks from top to bottom represent the boundary conditions on the left boundary, right boundary, free surface, sea bed, and wetted body surface, respectively. The dimension of the potential matrix $\boldsymbol{\phi}$ is $N_e\times 4$, meaning the potential values on all N_e elements for each of the 4 BVP problems (3 wave radiation problems and 1 diffraction problem). The matrix $\mathbf{R}_-$ represents the relation between $\frac{\partial}{\partial n}\boldsymbol{\phi}$ and $\boldsymbol{\phi}$ on the left boundary, and $\mathbf{R}_+$ on the right boundary. Usually the two boundaries are discretized in the same manner, which gives $N_- = N_+$ and $\mathbf{R}_- = \mathbf{R}_+$. Denoting both of them as $\mathbf{R}$, R_{jk} $(j,k = 1,2,\ldots,N_L)$ can be calculated from Eq. (3.48) as follows:

$$\begin{aligned}R_{jk}&=-\sum_{n=1}^{N}\frac{\beta_{+,n}}{C_{+,n}}\left\{\int_{z_k}^{z_{k+1}}\Lambda_{+,n}(x_R,z',\omega)dz'\right\}\Lambda_{+,n}(x_R,\frac{z_j+z_{j+1}}{2},\omega)\\&=-\sum_{n=1}^{N}\frac{2\beta_{+,n}\left\{\sin\left[\beta_{+,n}(z_k+h)\right]-\sin\left[\beta_{+,n}(z_{k+1}+h)\right]\right\}\cos\left[\beta_{+,n}\left(\frac{z_j+z_{j+1}}{2}+h\right)\right]}{\cos\left(\beta_{+,n}h\right)\sin\left(\beta_{+,n}h\right)+\beta_{+,n}h}.\end{aligned} \tag{3.53}$$

Substituting the equations of $\frac{\partial}{\partial n}\boldsymbol{\phi}$ (Eq. (3.52)) into the boundary integral equation, as described in Eq. (3.44), one can obtain a set of linear algebraic equations with $N_e\times 4$ equations and the same number of unknowns $\boldsymbol{\phi}$:

$$\left\{\frac{1}{2}\mathbf{I}+\mathbf{G}_n-\mathbf{G}\left[\begin{matrix}\mathbf{R} & & & & \\ & \mathbf{R} & & & \\ & & \frac{\omega^2}{g}\mathbf{I} & & \\ & & & \mathbf{0} & \\ & & & & \mathbf{0}\end{matrix}\right]\right\}_{N_e\times N_e}\left[\begin{matrix}\vdots\\ \vdots\\ \boldsymbol{\phi}^{\mathsf{T}}\\ \vdots\\ \vdots\end{matrix}\right]_{N_e\times 4}=\mathbf{G}\left[\begin{matrix}\mathbf{0}_{N_-\times 4}\\ \mathbf{0}_{N_+\times 4}\\ \mathbf{0}_{N_F\times 4}\\ \mathbf{0}_{N_D\times 4}\\ \widetilde{\mathbf{n}}^{\mathsf{T}}_{N_B\times 4}\end{matrix}\right]_{N_e\times 4}, \tag{3.54}$$

where the matrix **G** represents the integral of the simple Green's function (Eq. (3.43)) and $\mathbf{G}_n$ represents the integral of its normal derivative. Thanks to the conversion into the local $\varsigma - \upsilon$ coordinate system, the integration calculation is greatly simplified. Take an example of any arbitrary two elements j and k ($j,k = 1,2,\ldots,N_e$), the influence of all points of the j^{th} element on the midpoint of the k^{th} element can be integrated analytically as:

$$
\begin{aligned}
G_{kj} &= -\frac{1}{4\pi}\int_{-\frac{\Delta s_j}{2}}^{\frac{\Delta s_j}{2}} \ln\left[(\varsigma-\varsigma_{j,k})^2+(\upsilon-\upsilon_{j,k})^2\right] d\varsigma \\
&= \begin{cases}
\dfrac{\Delta s_j}{2\pi}, & \varsigma_{j,k}=0,\ \upsilon_{j,k}=0 \\[2ex]
-\dfrac{\Delta s_j}{2\pi}\ln\left(\upsilon_{j,k}^2\right), & \varsigma_{j,k}=0,\ \upsilon_{j,k}\neq 0 \\[2ex]
\dfrac{\Delta s_j}{2\pi} - \dfrac{\left(\frac{\Delta s_j}{2}+\varsigma_{j,k}\right)\ln\left(\frac{\Delta s_j}{2}+\varsigma_{j,k}\right)^2+\left(\frac{\Delta s_j}{2}-\varsigma_{j,k}\right)\ln\left(\frac{\Delta s_j}{2}-\varsigma_{j,k}\right)^2}{4\pi}, & \varsigma_{j,k}\neq 0,\ \upsilon_{j,k}=0 \\[2ex]
\dfrac{\Delta s_j}{2\pi} - \upsilon_{j,k}G_{n,kj} - \dfrac{\left(\frac{\Delta s_j}{2}+\varsigma_{j,k}\right)\ln\left[\left(\frac{\Delta s_j}{2}+\varsigma_{j,k}\right)^2+\upsilon_{j,k}{}^2\right]}{4\pi} & \\
\qquad -\dfrac{\left(\frac{\Delta s_j}{2}-\varsigma_{j,k}\right)\ln\left[\upsilon_{j,k}{}^2+\left(\frac{\Delta s_j}{2}-\varsigma_{j,k}\right)^2\right]}{4\pi}, & \varsigma_{j,k}\neq 0,\ \upsilon_{j,k}\neq 0,
\end{cases}
\end{aligned}
\tag{3.55}
$$

and

$$
\begin{aligned}
G_{n,kj} &= -\frac{1}{4\pi}\int_{-\frac{\Delta s_j}{2}}^{\frac{\Delta s_j}{2}} \frac{\partial}{\partial \upsilon}\ln\left[(\varsigma-\varsigma_{j,k})^2+(\upsilon-\upsilon_{j,k})^2\right] d\varsigma \\
&= -\frac{1}{2\pi}\int_{-\frac{\Delta s_j}{2}}^{\frac{\Delta s_j}{2}} \frac{(\upsilon-\upsilon_{j,k})}{(\varsigma-\varsigma_{j,k})^2+(\upsilon-\upsilon_{j,k})^2} d\varsigma \\
&= \begin{cases}
0, & \upsilon_{j,k}=0 \\[2ex]
\dfrac{\tan^{-1}\left(\frac{\frac{\Delta s_j}{2}-\varsigma_{j,k}}{\upsilon_{j,k}}\right)+\tan^{-1}\left(\frac{\frac{\Delta s_j}{2}+\varsigma_{j,k}}{\upsilon_{j,k}}\right)}{2\pi}, & \upsilon_{j,k}\neq 0.
\end{cases}
\end{aligned}
\tag{3.56}
$$

Note that the analytical integrals of Eq. (3.55) and (3.56) avoid the typical singularity issue in the numerical integration.

After determining the matrices **R**, **G**, $\mathbf{G}_n$, and $\widetilde{\mathbf{n}}$ from Eq. (3.53), Eq. (3.55), Eq. (3.56), and Eq. (3.49), respectively, the system of linear equations in Eq. (3.54) can be solved using the Gauss elimination method. The solutions $\boldsymbol{\phi}$ are obtained at a specified wave frequency ω for all potential points on the fluid boundaries. It is important to note that the solutions $\boldsymbol{\phi}$ for the wave radiation problems are complex values due to the purely imaginary eigenvalue component $\beta_{+,1} = ik$, which is involved in $\mathbf{R}$ in Eq. (3.53) through the boundary conditions on S_- and S_+. Given that these two boundaries can be placed arbitrarily far from the floating platform, the wave radiation damping effect, which is only related to the imaginary part of $\boldsymbol{\phi}$ (see Eq. (3.11)), is found to originate solely from the far-field radiation boundary condition. This observation is consistent with the transient analysis of the wave-platform interaction problem under the potential flow theory, in which the energy generated by the disturbances of the floating platform is radiated outwards and dissipated on the far-field boundaries [87].

It is also worth mentioning that the concatenation of $\frac{\partial}{\partial n}\boldsymbol{\phi}$ and $\boldsymbol{\phi}$ for three radiation problems and one diffraction problem in both Eq. (3.52) and (3.54) is due to the fact that the matrices $\mathbf{G}$, $\mathbf{G}_n$, and the coefficient matrix diag$\left(\mathbf{R}_-,\ \mathbf{R}_+,\ \frac{\omega^2}{g}\mathbf{I},\ \mathbf{0},\ \mathbf{0}\right)$ depend only on the coordinates of the discretized boundaries and the wave frequency. Therefore, they only need to be calculated once at each frequency, and the results can be applied to all four problems. This approach, suggested in this work, reduces unnecessary computational costs present in the original BEM code [90], where the coefficient matrix is recalculated for each problem.

3.4.3 Integration of wave forces

Once obtaining the solutions to $\boldsymbol{\phi} = \begin{bmatrix}\phi_R^{surge} & \phi_R^{heave} & \phi_R^{pitch} & \phi_D\end{bmatrix}^\mathsf{T}$ on all N_B elements of the wetted body-surface boundary $\overline{S}_B$ for both the radiation and diffraction problems, the hydrodynamic force coefficients listed in Eq. (3.11) can be computed simply through the following matrix multiplications:

$$\begin{aligned}
\underset{3\times3}{\boldsymbol{\lambda}(\omega)} &= \rho \underset{3\times N_B}{\overline{\mathbf{n}}_{ds}} \begin{bmatrix} \vdots & \vdots & \vdots \\ \phi_{R,j}^{surge} & \phi_{R,j}^{heave} & \phi_{R,j}^{pitch} \\ \vdots & \vdots & \vdots \end{bmatrix}_{N_B\times3}^{Re}, \\
\underset{3\times3}{\boldsymbol{\mu}(\omega)} &= -\rho\omega \underset{3\times N_B}{\overline{\mathbf{n}}_{ds}} \begin{bmatrix} \vdots & \vdots & \vdots \\ \phi_{R,j}^{surge} & \phi_{R,j}^{heave} & \phi_{R,j}^{pitch} \\ \vdots & \vdots & \vdots \end{bmatrix}_{N_B\times3}^{Im}, \\
\underset{3\times1}{\mathbf{K}_e(i\omega)} &= -\rho i\omega \underset{3\times N_B}{\overline{\mathbf{n}}_{ds}} \begin{bmatrix} \vdots \\ \left(\phi_{I,j}+\phi_{D,j}\right) \\ \vdots \end{bmatrix}_{N_B\times1},
\end{aligned} \tag{3.57}$$

where

$$\overline{\mathbf{n}}_{ds} = \begin{bmatrix} \cdots & n_{x,j}\Delta s_j & \cdots \\ \cdots & n_{z,j}\Delta s_j & \cdots \\ \cdots & \left[(\frac{z_j + z_{j+1}}{2} - z_0) n_{x,j} - (\frac{x_j + x_{j+1}}{2} - x_0) n_{z,j} \right] \Delta s_j & \cdots \end{bmatrix}_{3 \times N_B} . \tag{3.58}$$

The buoyancy forces can be calculated by integrating the static pressure over the body surface $\overline{S}_B$, which can be expressed separately for the surge, heave and pitch DoFs as follows:

$$\begin{aligned} \mathbf{F}_b &= \mathbf{F}_{b0} - \mathbf{K}_{hs}\boldsymbol{\xi} \\ &= \begin{bmatrix} 0 \\ \rho g A_0 \\ -\rho g A_0 (x_{buoy} - x_0) \end{bmatrix} - \begin{bmatrix} 0 & 0 & 0 \\ 0 & \rho g l_0 & -\rho g l_x \\ 0 & -\rho g l_x & \rho g l_{xx} + \rho g A_0 (z_{buoy} - z_0) \end{bmatrix} \begin{bmatrix} \xi_1 \\ \xi_3 \\ \xi_5 \end{bmatrix} . \end{aligned} \tag{3.59}$$

Note that the moment is again calculated around the center of gravity (x_0, z_0). In Eq. (3.59), A_0 denotes the submergence area of the floating platform, which can be calculated numerically given the normal vector distribution (Eq. (3.50)) and the coordinates of geometry points on $\overline{S}_B$ either along the Ox or Oz axis:

$$A_0 = \iint_{\overline{S}_B} dxdz = -\sum_{j=1}^{N_B} \frac{x_j + x_{j+1}}{2} n_{x,j}\Delta s_j = -\sum_{j=1}^{N_B} \frac{z_j + z_{j+1}}{2} n_{z,j}\Delta s_j . \tag{3.60}$$

The geometrical characteristics l_0, l_x, l_{xx} related to the waterline $(x_{N_B+1} < x < x_1)$ can be easily calculated from:

$$\begin{aligned} l_0 &= \int_{x_{N_B+1}}^{x_1} dx = x_1 - x_{N_B+1}, \\ l_x &= \int_{x_{N_B+1}}^{x_1} (x - x_0) dx = \frac{(x_1 - x_0)^2 - (x_{N_B+1} - x_0)^2}{2}, \\ l_{xx} &= \int_{x_{N_B+1}}^{x_1} (x - x_0)^2 dx = \frac{(x_1 - x_0)^3 - (x_{N_B+1} - x_0)^3}{3}. \end{aligned} \tag{3.61}$$

The center of buoyancy (x_{buoy}, z_{buoy}) in Eq. (3.59) are determined using the following equations:

$$
\begin{aligned}
x_{buoy} &= \frac{\iint_{\overline{S}_B} x dx dz}{A_0} = \frac{-\sum_{j=1}^{N_B} \frac{x_j + x_{j+1}}{2} \frac{z_j + z_{j+1}}{2} n_{z,j} \Delta s_j}{A_0}, \\
z_{buoy} &= \frac{\iint_{\overline{S}_B} z dx dz}{A_0} = \frac{-\sum_{j=1}^{N_B} \frac{x_j + x_{j+1}}{2} \frac{z_j + z_{j+1}}{2} n_{x,j} \Delta s_j}{A_0}.
\end{aligned}
\tag{3.62}
$$

3.5 Cross validation of codes

The linear boundary value problem for an arbitrary platform's wetted surface $\overline{S}_B$ can be solved using either the analytical approach developed in Section 3.3 or the numerical BEM approach described in Section 3.4. To cross-validate both methods, three cases of rectangular, trapezoidal, and triangular submergence, as illustrated in Fig. 3.2, are examined in this section. The hydrodynamic force coefficients obtained from both methods are compared for each case. The rectangular and trapezoidal submergence cases are based on a floating platform with the same cross-section as the middle section of the ITI-Barge platform [63], having a width of 40 m, a height of 10 m, and a draft of 4 m under its static equilibrium position, without the moonpool. When the platform displacement in surge, heave, and pitch Dofs is $\xi_1 = \xi_3 = \xi_5 = 0$, the platform is in its upright position, and the submergence area is rectangular, as shown in Fig. 3.2(a). This corresponds to the equilibrium position of the example NREL 5-MW ITI-Barge floating wind turbine introduced in Section 2.5. When the platform is displaced to $\xi_1 = 0$ m, $\xi_3 = -2$ m, $\xi_5 = 10^\circ$, the submergence area becomes trapezoidal, as shown in Fig. 3.2(b), representing a possible movement of the example FWT under combined wind and wave actions. For the third case, a special 45-45-90 triangular submergence as shown in Fig. 3.2(c) is selected, with a width of 40 m, a height of 40 m, a draft of 20 m and a platform displacement of $\xi_1 = \xi_3 = 0$ m, $\xi_5 = 45^\circ$. Although such triangular submergence is unlikely to occur on the example FWT, it serves as a useful test for the robustness of both the analytical and numerical methods. In all three cases, the water depth is set to $h = 150$ m.

3.5.1 Simple case of upright platform: surge-pitch coupled

Both the analytical and numerical formulations require the roots $\beta_{1,n}$, $(n = 1, 2, \ldots, N)$ of the wave dispersion relation (Eq. (3.14)) in open fluid domains. These roots include one imaginary root $\beta_{1,1} = ik$ and a truncated set of real roots $\beta_{1,2}, \ldots, \beta_{1,N}$. Solving this transcendental equation analytically is challenging. In this work, a numerical method is adopted using the MATLAB function `fsolve`. It is important to note that poor initial guesses for the real roots can cause convergence issues in the numerical algorithm, potentially resulting in false or missing roots and eventually inaccurate solutions to the wave-platform BVP. To overcome this issue, the qualitative insight that each real root $\beta_{1,n}$ is bounded by $(n-\frac{3}{2})\pi < \beta_{1,n}h < (n-1)\pi$ [87] is leveraged, and the mean value $(n-\frac{5}{4})\pi/h$ is used as the initial guess for each real root. A truncated number $N = 30$ of roots are calculated across the wave frequency range of $\omega = 0 \sim 5$ rad/s, and the results are plotted in Fig. 3.5. It can be found that the roots vary continuously with the increase of wave frequency, and they are all bounded within $\left(\frac{(n-3/2)\pi}{h}, \frac{(n-1)\pi}{h}\right)$.

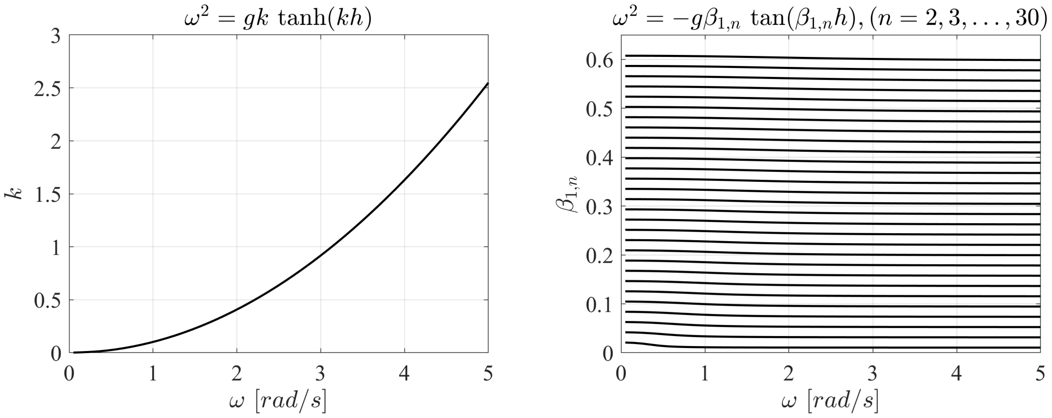

Fig. 3.5 Roots of wave dispersion relation with $h = 150$ m, $g = 9.81$ m/s^2.

Considering the assumption made in the 2D numerical BEM method in Section 3.4.2 that the potential ϕ on each element is assumed to be constant and represented by its midpoint value, the element length Δs must be sufficiently small to ensure accurate numerical results. The suggested Δs is $\frac{1}{8}$ of the shortest wave length being considered. This section presents a convergence test on Δs to validate the accuracy of the numerical solution. The non-zero added mass coefficients λ_{ij}, $(i, j = 1, 3, 5)$ and radiation damping coefficients μ_{ij} calculated using five different sets of element lengths are compared in Fig. 3.6. The finest discretization, referred to as "Mesh5", features an element length Δs of 0.05 m on the body surface $\overline{S}_B$, 0.25 m on the free surface $\overline{S}_F$, and 0.5 m on the sea bed S_D and truncated vertical boundaries $S_\pm$. Coarser discretizations are obtained by scaling the Δs of "Mesh5" on all boundaries uniformly by factors of $2, 4, 6,$ and 8, resulting in meshes labelled as "Mesh4", "Mesh3","Mesh2", and "Mesh1", respectively. As shown in Fig. 3.6, the BEM solutions converge as Δs decreases from "Mesh1" to "Mesh5", with "Mesh5" providing the most accurate results. Further reduction in Δs for "Mesh5" is anticipated to diminish the numerical oscillations even more, but it would increase the simulation time. Therefore, "Mesh5" is selected as the optimal discretization for subsequent BEM analyses. Additionally, other convergence tests were conducted concerning the location of the $S_{\pm}$ boundaries and the number of eigenfunctions truncation N in the analytical representation of potentials in open fluid domains (Eq. (3.45)). The left and right boundary location of $x = \pm 50$ m on both sides and $N = 30$ eigenfunctions were found to yield satisfactory accuracy for hydrodynamic coefficients.

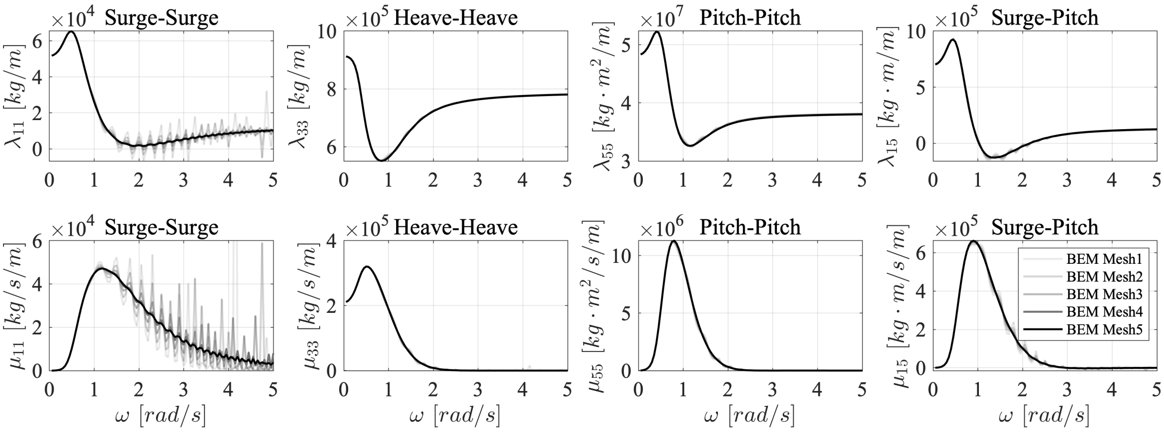

Fig. 3.6 BEM convergence test of the upright platform. Coarse to fine discretization from Mesh1 to Mesh5.

The analytical approach developed in this work is implemented using the Symbolic Math Toolbox in MATLAB. As depicted in Fig. 3.2(a), the rectangular submergence requires only three fluid subdomains in the analytical formulation (Eq. (3.33) – (3.38)), resulting in a system of $4N$ linear equations for each radiation/diffraction problem. The surge-surge, heave-heave, pitch-pitch and surge-pitch added mass ($\lambda_{11}, \lambda_{33}, \lambda_{55}, \lambda_{15}$) and radiation damping ($\mu_{11}, \mu_{33}, \mu_{55}, \mu_{15}$) coefficients calculated using the analytical method, with eigenfunction truncation numbers $N = 10, 20, 30$, are plotted in Fig. 3.7. These results are compared with those obtained using the BEM with "Mesh5" discretization. Notably, due to Green's theorem, the pitch-surge added mass and radiation damping are identical to the surge-pitch ones, i.e., $\lambda_{51} = \lambda_{15}$, $\mu_{51} = \mu_{15}$, and thus they are not repeated in Fig. 3.7. Other couplings not shown here are the surge-heave and heave-pitch couplings, which are effectively zero ignoring minor numerical errors (i.e., $\lambda_{13} = \lambda_{31} = 0$, $\lambda_{35} = \lambda_{53} = 0$, and $\mu_{13} = \mu_{31} = 0$, $\mu_{35} = \mu_{53} = 0$). The amplitude and phase angle of the wave excitation force ($K_{e,j}$) in the three DoFs, calculated using both the analytical method and BEM, are compared in 3.8. The comparisons in Fig. 3.7 and 3.8 demonstrate that the analytical results converge towards the BEM results as more truncated modes are included. Furthermore, the analytical method avoids the oscillations observed in the high-frequency range, a common issue in the BEM due to its sensitivity to mesh resolution, as demonstrated in Fig. 3.6.

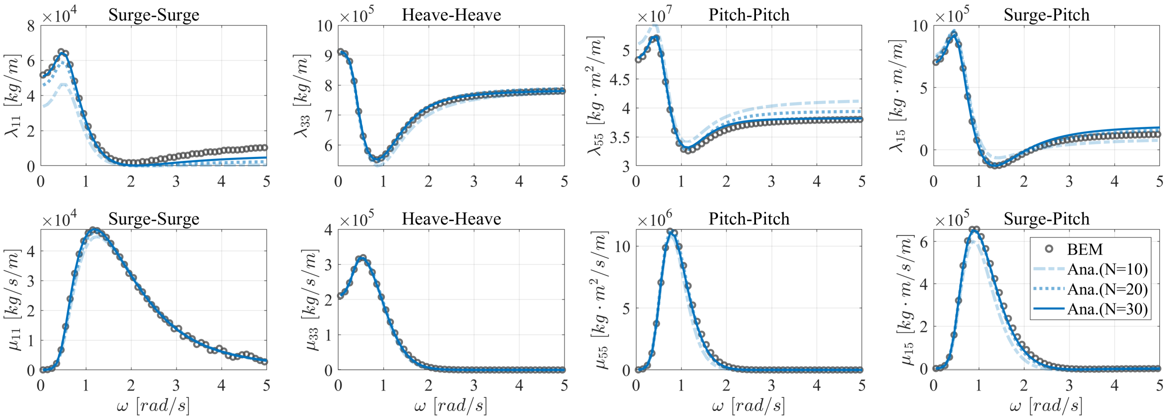

Fig. 3.7 BEM vs. analytical results of the upright platform: added mass (λ_{ij}) and radiation damping (μ_{ij}) coefficients in surge-surge, heave-heave, pitch-pitch and surge-pitch couplings.

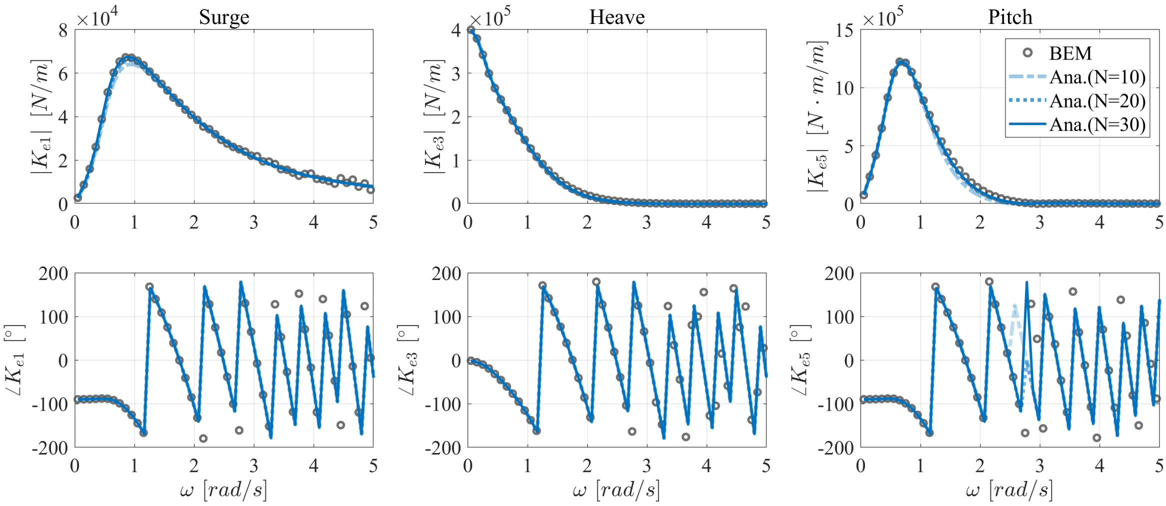

Fig. 3.8 BEM vs. analytical results of the upright platform: amplitude and phase angle of wave excitation force (K_{ej}) coefficients.

The radiated wave velocity fields induced by unit body velocity in surge (ϕ_R^{surge}), heave (ϕ_R^{heave}), and pitch (ϕ_R^{pitch}) DoF at the wave frequency of 1 rad/s are calculated using the analytical method, as shown in Fig. 3.9. As the influence of platform movements decays with increasing water depth, only the velocity field above $z = -30$ m is plotted. It can be observed from Fig. 3.9 that under the rectangular submergence that is symmetrical about the Oz axis, the surge- and pitch-radiation velocity fields are anti-symmetrical, while the heave-radiation field is symmetrical about Oz. This symmetry explains the zero surge-heave and heave-pitch couplings, while non-zero surge-pitch coupling in the added mass and radiation damping results as shown in Fig. 3.7. Moreover, it can be found that the continuity conditions of the normal (horizontal) velocity on the vertical interfaces at $x = \pm 20$ m are not satisfied pointwise. Instead, they are enforced in the weighted residuals form via the Galerkin method, in which the eigenfunctions are taken as weights, such as in Eq. (3.32). This leads to an unrealistic discontinuity in the wave flow across the two vertical interfaces, as shown in Fig. 3.9.

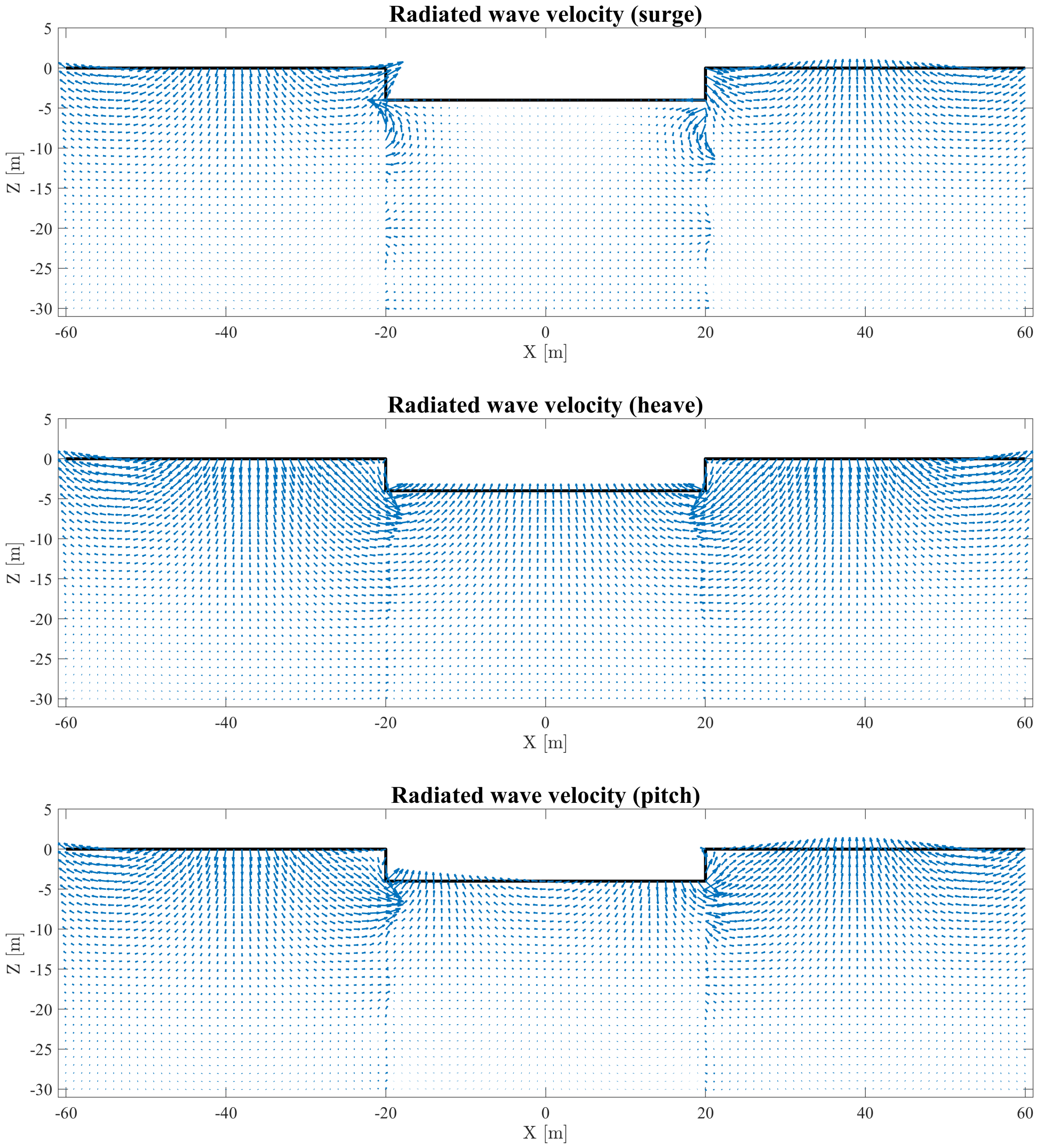

Fig. 3.9 Radiated wave velocity field induced by unit surge, heave, pitch velocity of the upright platform at wave frequency $\omega = 1$ rad/s.

The diffracted wave velocity field (ϕ_D) induced by the incident wave with unit wave amplitude (ϕ_I), as well as the combined field of incident and diffracted waves ($\phi_I + \phi_D$) at the wave frequency $\omega = 1$ rad/s, are depicted in Fig. 3.10. The plots reveal a strong harmonic pattern in both the ϕ_D and $\phi_I + \phi_D$ fields along the Ox direction. This harmonic behavior is a direct result of the e^{-ikx} term in the expression of ϕ_I (Eq. (3.5)). Moreover, the wave velocity normal to the body surface in the $\phi_I + \phi_D$ field is found to be effectively zero. This is attributed to the boundary condition imposed in the diffraction problem, which is expected to negate the influence of the incident wave (ϕ_I) on the body surface, ensuring that the total velocity field ($\phi_I + \phi_D$) satisfies the boundary condition of no normal flow across the surface of the floating platform. Note again that the continuity conditions on the two vertical interfaces are satisfied in the Galerkin weighted residuals form, which explains the slight normal velocity components on the body surface.

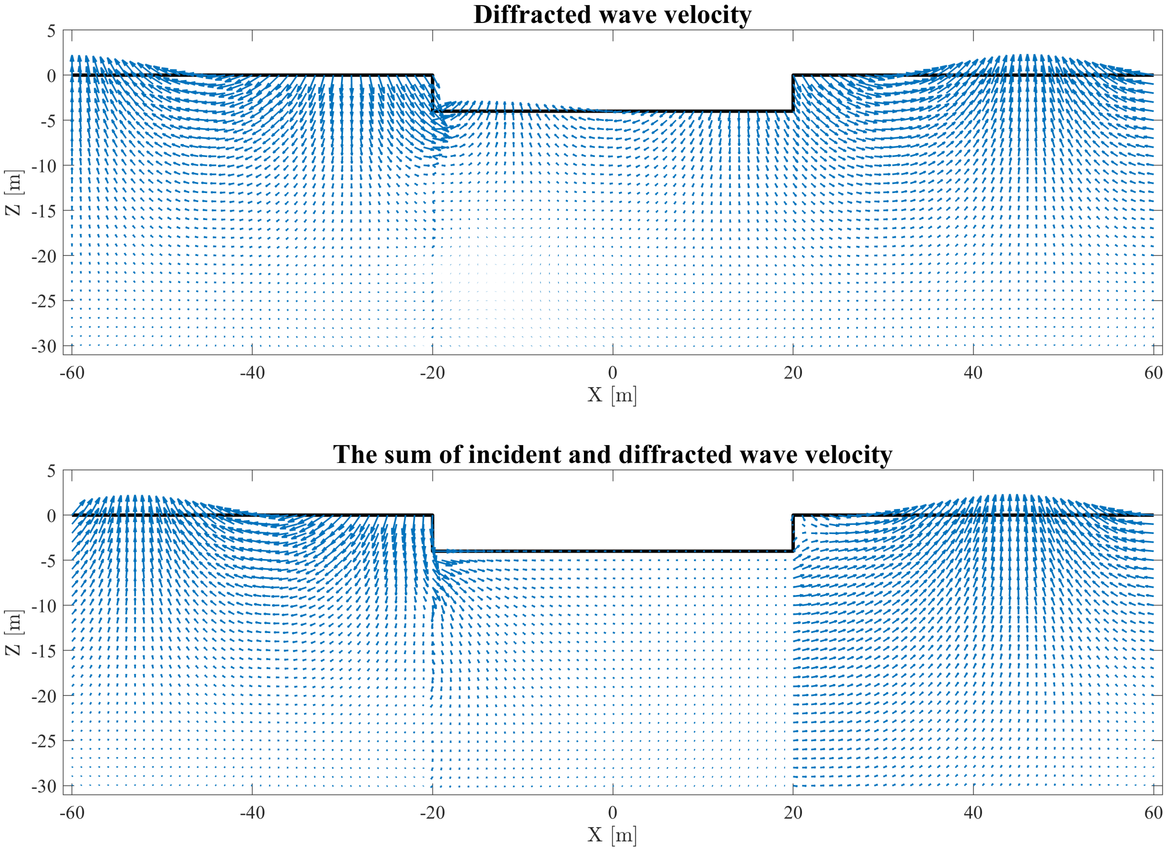

Fig. 3.10 Diffracted wave velocity field, and the sum of incident and diffracted wave field of the upright platform at wave frequency $\omega = 1$ rad/s.

3.5.2 Generic case of tilted platform: surge-heave-pitch all coupled

In this section, a generic trapezoidal submergence case is examined. Convergence tests concerning both the step discretization of the fluid domain and the number of eigenfunction truncations are performed. Fig. 3.11 illustrates the discretization for three cases, each with a different number of steps along the sides AB, BC, and CD of the trapezoidal submergence. The roots for the wave dispersion relation in left and right open domains (Eq. (3.14)) remain the same as those shown in Fig. 3.5. When the step number on side CD is non-zero, new wave dispersion relations (Eq. (3.25)) are solved numerically to find the roots $\beta_{j,n}$, where $j = N_c + 1, \dots, N_d$ and $n = 1, 2, \dots, N$. Note that the first root is imaginary and is denoted as $\beta_{j,1} = ik_j$. Fig. 3.12 presents the first 30 roots of this new dispersion equation with one step on side CD ($z_j = -1.647$ m), and shows how these roots vary with wave frequency. The real roots are found to be significantly larger than those in Fig. 3.5, which can be attributed to the considerable difference in the height of the fluid domains (1.647 m vs.150 m). However, the imaginary root is not affected much by the fluid height.

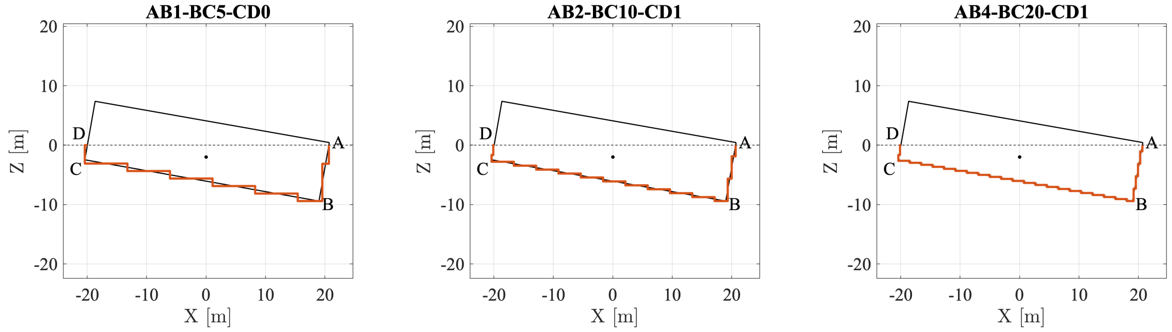

Fig. 3.11 Step discretization of a generically tilted platform.

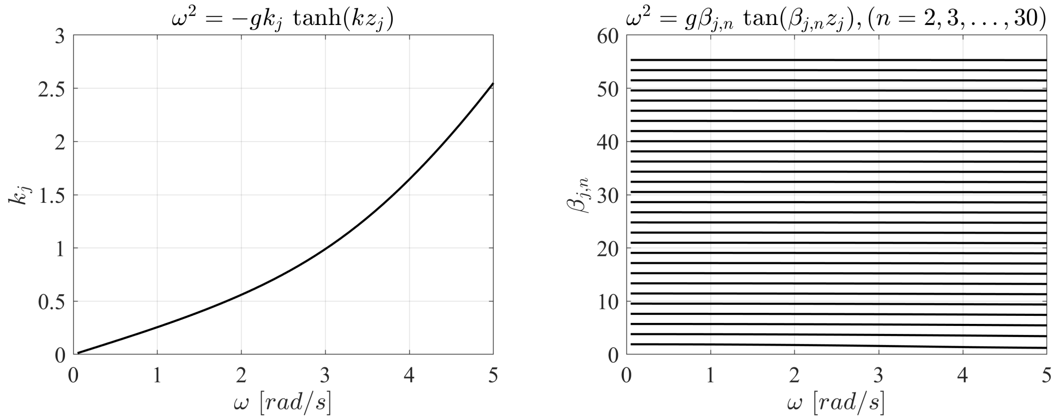

Fig. 3.12 Roots of the dispersion relation with $z_j = -1.647$ m, $g = 9.81$ m/s^2.

Given the coordinates of all steps (x_j, z_j) and the eigenfunctions truncation number N, the system of linear equations can be analytically formulated according to Eq. (3.33) – (3.38) for each of the three discretization examples illustrated in Fig. 3.11. Take the step discretization labelled "AB4-BC20-CD1" as an example, the total $N_d = 28$ fluid subdomains and $N = 30$ truncation modes yield $27 \times 30 \times 4 \times 2 = 6480$ unknowns and equations for each wave frequency. The solutions to these systems of equations yield the added mass, radiation damping, and wave excitation force coefficients, which are presented in Fig. 3.13 – 3.15. For cross-validation, the results obtained from the numerical BEM with the "Mesh5" discretization are also included. The comparison shows that the analytical results increasingly align with the numerical BEM results as the step discretization becomes finer and the eigenfunction truncation number N increases. This trend of convergence verifies the accuracy and reliability of the analytical approach when sufficient discretization and eigenfunction truncations are employed.

Moreover, unlike the rectangular submergence case discussed in Section 3.5.1, the generic trapezoidal submergence does not exhibit the same symmetric characteristics. As a result, all three DoFs (surge, heave, and pitch) are coupled, leading to non-zero coupling coefficients in the surge-heave and heave-pitch interactions, as shown in Fig. 3.14. These additional coupling effects, especially the negative added mass (λ_{35}) and negative radiation damping (μ_{13}, μ_{35}) coefficients that can be observed within some wave frequency ranges, can potentially affect the dynamics of the floating platform significantly, and thus must be handled carefully in the nonlinear dynamic analysis.

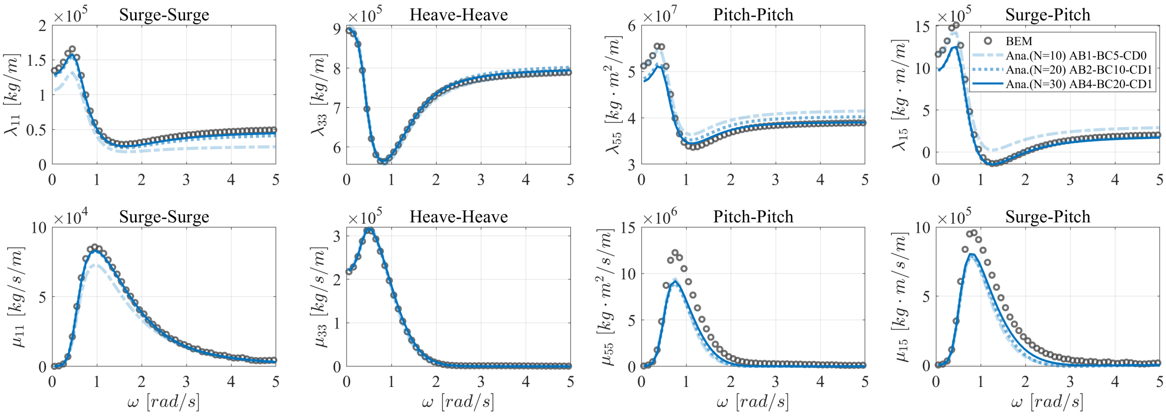

Fig. 3.13 BEM vs. analytical results of a generically tilted platform: added mass (λ_{ij}) and radiation damping (μ_{ij}) in surge-surge, heave-heave, pitch-pitch and surge-pitch couplings.

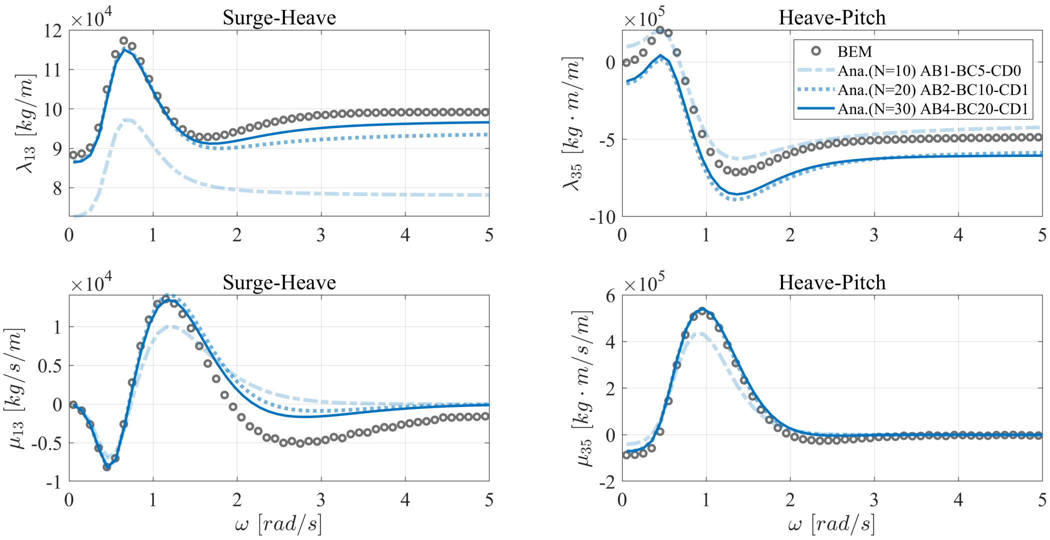

Fig. 3.14 BEM vs. analytical results of a generically tilted platform: added mass (λ_{ij}) and radiation damping (μ_{ij}) in surge-heave and heave-pitch couplings.

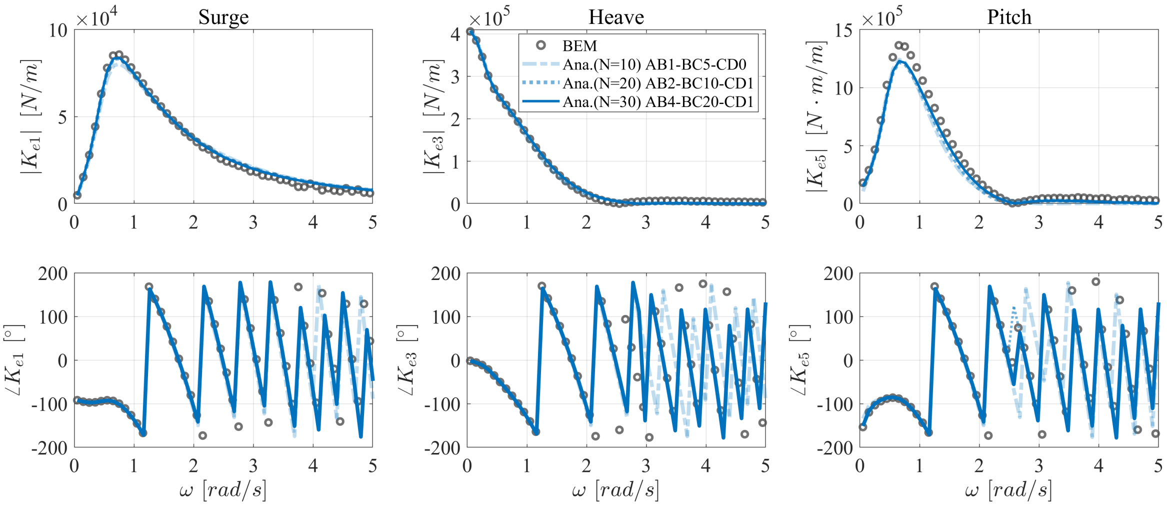

Fig. 3.15 BEM vs. analytical results of a generically tilted platform: amplitude and phase angle of wave excitation force (K_{ej}) coefficients.

Despite further attempts to refine the analytical results by increasing the step discretization and the number of eigenfunctions truncation, the accuracy does not improve significantly. This is due to several factors related to the way the continuity conditions are enforced along the mixed vertical boundary of the body surface and the fluid domain. In the analytical formulation, the continuity of pressure and velocity is enforced in the Galerkin weighted residuals form across these boundaries. For instance, consider the velocity continuity condition along the vertical boundary at $x = x_2$, as expressed in Eq. (3.32). The right-hand side of this condition is the sum of integrals over two segments: $[-h, z_2]$ in the fluid domain and $[z_2, 0]$ on the vertical body step. In the discretization example labelled as "AB4-BC20-CD1", these segments are $[-150, -1.0463]$ m and $[-1.0463, 0]$ m, respectively. The latter segment, corresponding to the body, accounts for only about 0.7% of the entire integral range due to the fine discretization. However, the potential solutions on this small segment directly impact the resultant hydrodynamic forces, making the accuracy of these integrals crucial. Given the small contribution from the body segment relative to the fluid domain in the integral calculation, the influence of potential values on the body can be underrepresented, which hinders further improvement of the analytical results even with increased discretization and eigenfunctions included.

To address this issue, it is suggested that a z-dependent additional weight function be applied to the integrals, giving more emphasis to the body boundaries. However, introducing such a weight function must be done carefully. An inappropriate choice can disrupt the orthogonality of the eigenfunctions, which is beneficial in reducing the number of eigenfunctions needed for accurate solutions. Therefore, further investigation is necessary to propose a suitable weight function that enhances the accuracy of the analytical method without imposing a significant computational burden.

3.5.3 Special case of tilted platform: surge-pitch coupled

A special 45-45-90 triangular submergence case is investigated in this section. As shown in Fig. 3.16, three discretization examples are considered, each with a different number of steps along the AB and BC sides. These examples are combined with various numbers of truncated eigenfunctions $N = 10, 20, 30$, and are calculated using the analytical method. The resultant added mass, radiation damping, and wave excitation force coefficients are plotted in Fig. 3.17 and 3.18, in which the numerical BEM results are shown for comparison.

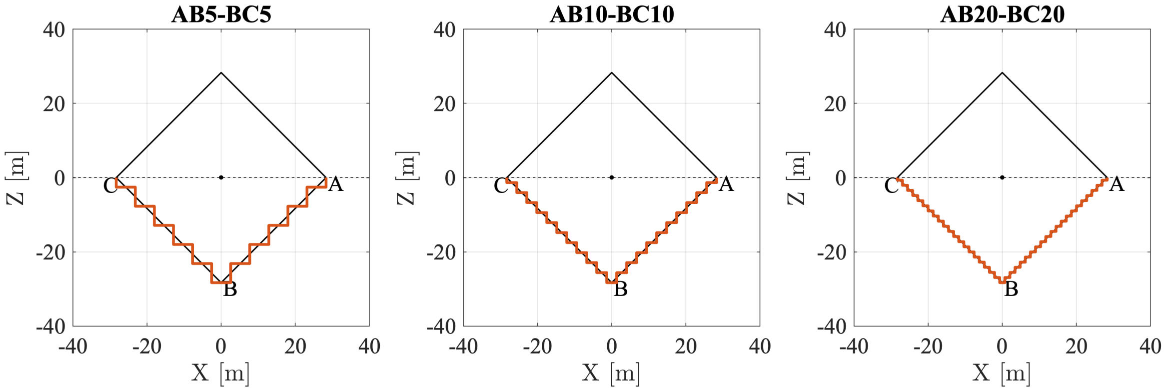

Fig. 3.16 Step discretization of the special 45-45-90 triangular submergence.

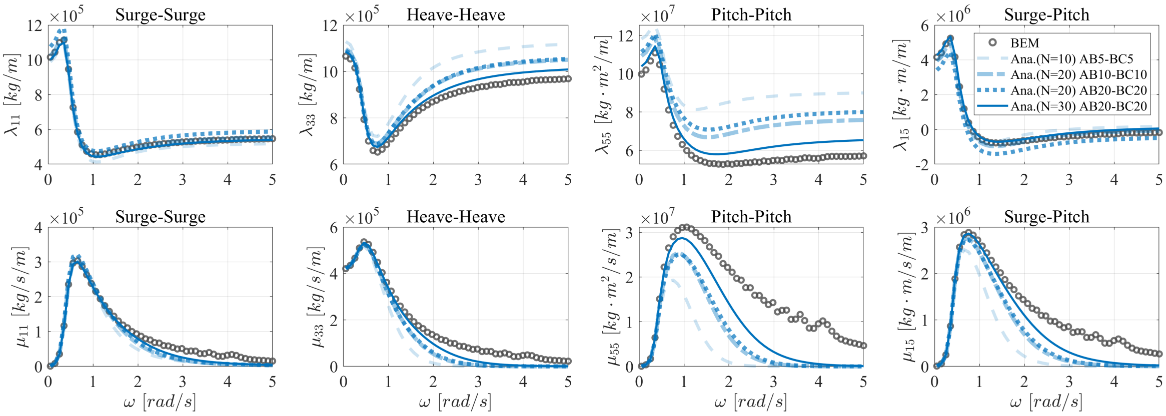

Fig. 3.17 BEM vs. analytical results of a specially tilted platform: added mass (λ_{ij}) and radiation damping (μ_{ij}) in surge-surge, heave-heave, pitch-pitch and surge-pitch couplings.

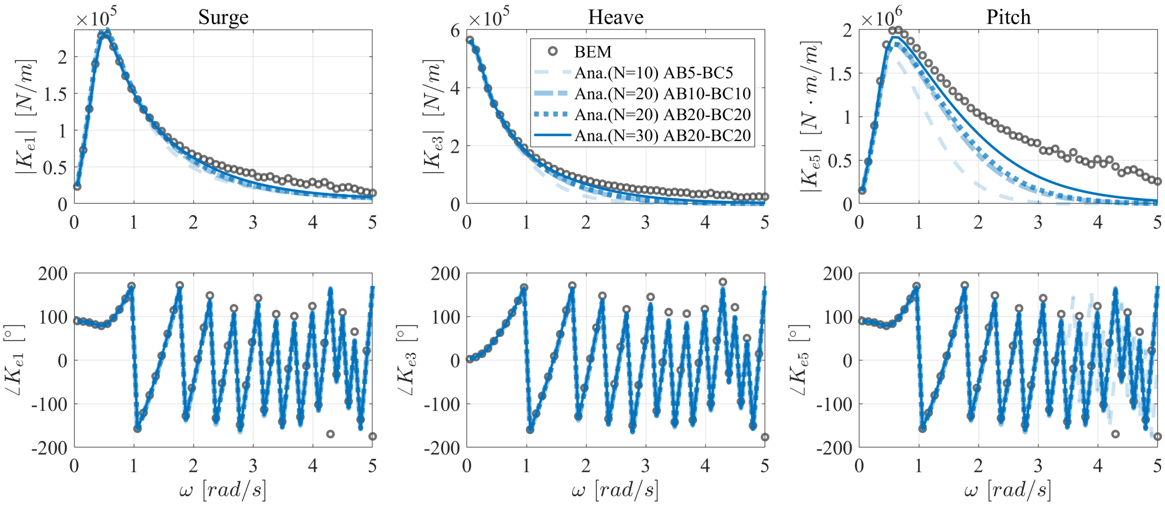

Fig. 3.18 BEM vs. analytical results of a specially tilted platform: amplitude and phase angle of wave excitation force (K_{ej}) coefficients.

As observed in previous cases, the analytical results tend to converge toward the numerical BEM results as both the step discretization and the eigenfunctions truncation number N are increased. However, the number of truncation modes should be compatible with the number of step discretization for better performance of the analytical method. As can be observed in Fig. 3.17 and 3.18, the “AB20-BC20” discretization with only $N = 20$ truncated modes shows similar or even slightly worse results compared to the coarser “AB10-BC10” discretization with $N = 20$, whereas the “AB20-BC20” discretization with an increased $N = 30$ significantly improve the analytical results. That being said, the effects of increasing steps and truncated modes are limited, as discussed in Section 3.5.2, and the discrepancies between the analytical and BEM methods remain.

Interestingly, the geometric symmetry of the 45-45-90 triangle and the symmetric discretized steps on both AB and BC sides, lead to similar coupling effects of the added mass and radiation damping coefficients, as those discussed in Section 3.5.1. More specifically, the couplings between the surge-heave (λ_{13}, μ_{13}) and heave-pitch (λ_{35}, μ_{35}) DoFs no longer exist, which verifies again the robustness of both the analytical and BEM formulations.

3.6 Computational efficiency

The computational efficiency of the analytical and numerical methods is compared in this section. Table 3.1 presents CPU times for both methods under upright ($\xi_3 = 0$ m, $\xi_5 = 0°$) and tilted ($\xi_3 = -2$ m, $\xi_5 = 10°$) platform poses at wave frequency $\omega = 1$ rad/s. The “Mesh5” discretization as described in Section 3.5.1 is used for the BEM solver. Three truncation modes of the eigenfunctions are examined for the analytical solver, which are compatible with three step discretizations used in the tilted platform pose, as depicted in Fig. 3.11.

Table 3.1 Comparison of CPU time for BEM vs. analytical solutions ($\omega = 1$ rad/s).

Platform poses	BEM (Mesh5)	Analytical		
		N=10	N=20	N=30
Upright platform	1.8s	(AB0-BC1-CD0) 0.3s	(AB0-BC1-CD0) 0.9s	(AB0-BC1-CD0) 2.2s
Tilted platform	2s	(AB1-BC5-CD0) 1.8s	(AB2-BC10-CD1) 42s	(AB4-BC20-CD1) 403s

It can be found from Table 3.1 that, when the platform is upright, the analytical solver performs comparably to BEM even with $N = 30$ truncated modes. However, for the tilted platform, CPU time increases significantly as step approximations and truncated modes increase. Thus, while the analytical method is computationally efficient and provides valuable physical insights for upright platforms, the BEM solver is recommended for tilted platform scenarios due to its superior computational efficiency.

3.7 Conclusions

An analytical formulation to address the 2D linear wave-platform boundary value problem for wetted platform surfaces of arbitrary geometry is developed in this work. The non-orthogonal body-surface boundaries, which prevent the direct use of the method of separation of variables, are approximated by a series of horizontal and vertical steps. The standard eigenfunction expansion matching method is applied to the discretized fluid subdomains. A system of linear equations is then derived, from which the unknown coefficients of the eigenfunctions are calculated and the potentials in the entire fluid domain are determined. A 2D numerical BEM formulation that employs the simple Green's function and truncated fluid domains is adopted for the cross-validation of the analytical approach. This work provides a detailed description of the 2D BEM methodology, which has not been comprehensively documented in previous literature. The calculation of hydrodynamic and hydrostatic forces from both the analytical and numerical potential solutions is also included.

Three examples of barge-type platform submergence cases, i.e., rectangular, trapezoidal, and 45-45-90 triangular shapes, which correspond to different platform positions, are examined. The added mass, radiation damping and wave excitation force coefficients calculated using both analytical and numerical methods are compared for each case. For the rectangular submergence when the platform is in its static equilibrium position, the analytical results show excellent agreement with the numerical BEM results across a wide range of frequencies. For non-rectangular geometries when the platform is tilted, it is found that the analytical results generally converge towards the BEM results as the step discretization becomes finer and the number of truncated eigenfunctions is increased, and more truncated eigenfunctions are required for finer step discretization. However, this comes at the expense of significantly higher computational costs compared to the BEM code. The limitations of the developed analytical formulation are also discussed. Specifically, the analytical results do not improve with further increases in step discretization and eigenfunction truncation. This is attributed to challenges in enforcing the mixed boundary condition at the interface between fluid subdomains, where the influence of the body segment is underrepresented. Further research on an appropriate weighting function that emphasizes the body segment is suggested.

The influence of platform position on its hydrodynamic behaviour has also been revealed from the examples. The barge-type floating platform in its static equilibrium position shows no coupling between the surge-heave and heave-pitch added mass and radiation damping coefficients, due to the symmetry of the body submergence area. However, when the platform is tilted, unless the submergence area is perfectly symmetric, the generally asymmetric body submergence introduces non-zero surge-heave and heave-pitch couplings in the added mass and radiation damping. Some of them are even negative and are anticipated to affect the platform dynamics and eventually the global dynamic response of the FWT. This geometric nonlinear effect, induced by the variation of the platform submergence, will be taken into account in the subsequent nonlinear dynamic analysis of FWTs.

Overall, this work demonstrates that the proposed analytical method can reliably solve the linear wave-platform BVP for various body submergence geometries, often providing results comparable to the numerical BEM approach. Particularly in cases involving simple rectangular submergence, the analytical method offers superior computational efficiency and deeper insight into potential flow physics. It is important to note that the proposed analytical method is applicable not only to the FWTs studied in this work, but also to a broad range of floating structures, especially those exhibiting pronounced 2D flow characteristics, such as floating breakwaters of different shapes, floating bridge piers, and vessels.

Chapter 4

Linear Parameter-varying Model for Geometrically Nonlinear FWT Hydrodynamics

4.1 Introduction

The compliance of floating platforms can result in large displacements and rotations for floating wind turbines (FWT) under combined wind and wave actions. For instance, DNVGL-RP-0286 [26] specifies a maximum allowable tilting angle of up to 10° for operating and 15° for non-operating FWTs at the tower top. In contrast, the tilt for their bottom-fixed counterparts is limited to just 0.5°. Such substantial platform motion poses novel challenges for FWTs due to the geometrically nonlinear wave-platform interaction effects. This phenomenon has been reported by Antonutti et al. [4], who observed a 10% increase in the pitch response of the 5-MW Dutch Tri-floater FWT when the platform is subjected to a constant platform inclination of 6° in the downwind direction from its equilibrium position. Similarly, Li and Bachynski [76] reported a 17% reduction in the vertical wave diffraction force on the 5-MW OC6 semi-submersible FWT when the platform is fixed at a 5° inclination. These findings suggest that evaluating hydrodynamics around the equilibrium platform position, as done using the conventional linear potential flow theory, may lead to inaccurate analyses. Popular FWT simulation tools, such as OpenFAST [101] and HWAC2 [50], which employ such linear assumptions, exhibit notable limitations in handling large platform motions.

The geometrically nonlinear effects in wave-platform interactions can be evaluated using various modelling assumptions, which are categorized into different levels of complexity, as summarized in the following Fig. 4.1.

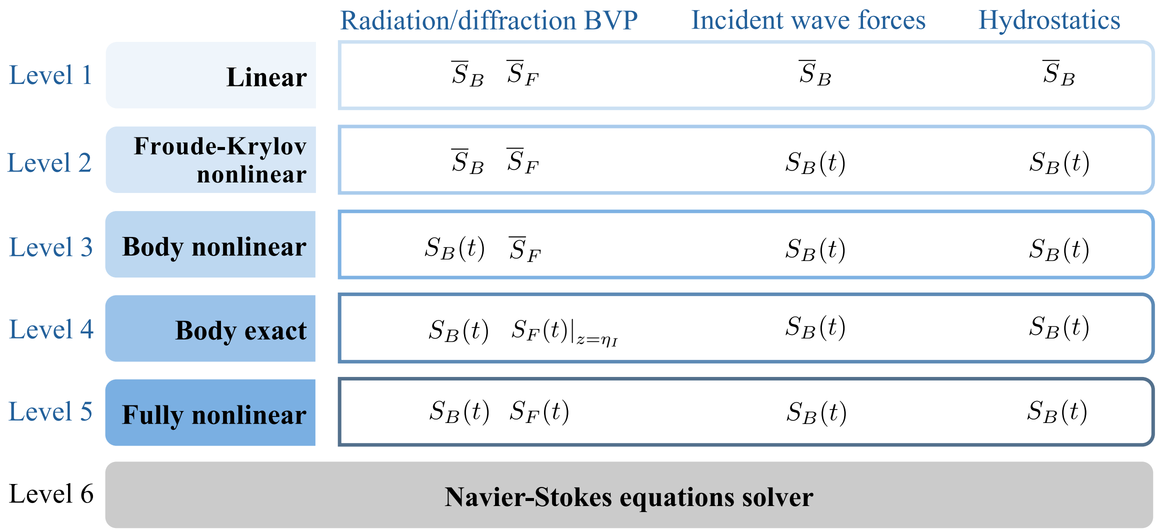

		Radiation/diffraction BVP	Incident wave forces	Hydrostatics
Level 1	**Linear**	$\overline{S}_B$ $\overline{S}_F$	$\overline{S}_B$	$\overline{S}_B$
Level 2	**Froude-Krylov nonlinear**	$\overline{S}_B$ $\overline{S}_F$	$S_B(t)$	$S_B(t)$
Level 3	**Body nonlinear**	$S_B(t)$ $\overline{S}_F$	$S_B(t)$	$S_B(t)$
Level 4	**Body exact**	$S_B(t)$ $S_F(t)\|_{z=\eta_I}$	$S_B(t)$	$S_B(t)$
Level 5	**Fully nonlinear**	$S_B(t)$ $S_F(t)$	$S_B(t)$	$S_B(t)$
Level 6	**Navier-Stokes equations solver**			

Fig. 4.1 6 levels of increasing modelling complexity for wave-platform interactions.

This classification of Fig. 4.1 is adapted from ship hydrodynamics [52]. The conventional linear method, designated as **Level 1**, is commonly employed by FWT simulation tools. It solves the wave-platform boundary value problem (BVP) using up to a second-order perturbation expansion around the mean free surface ($\overline{S}_F : z = 0$) and a first-order perturbation around the mean wetted body surface ($\overline{S}_B$). In this method, all hydrostatic and hydrodynamic forces are computed relative to the mean platform position $\overline{S}_B$.

Level 2 introduces weak geometric nonlinearity by evaluating incident wave forces and hydrostatics around the instantaneous body surface ($S_B(t)$), while still defining the BVP on the stationary boundaries of $\overline{S}_B$ and $\overline{S}_F$. For instance, Philippe et al. [104] reported slightly larger platform motions for the 5-MW Dutch Tri-floater FWT using the **Level 2** modelling compared to **Level 1**. This method captures some nonlinear effects without a significant increase in computational cost. Building on **Level 2**, **Level 3** solves the BVP using the instantaneous body surface $S_B(t)$, with $S_B(t)$ being re-meshed and potentials being re-calculated at each time step. This method captures more accurate geometrically nonlinear effects, at the expense of significantly increased computational cost. Chan et al. [16] applied this body-nonlinear approach to the 5-MW MIT/NREL TLP FWT and reported larger surge diffraction forces compared to those predicted by OpenFAST.

Given that the real free-surface boundary can differ considerably from $\overline{S}_F : z = 0$ under large platform motions, **Level 4** modifies $\overline{S}_F$ to follow the prescribed incident wave profile ($S_F(t) : z = \eta_I$), assuming that the generated waves are smaller than η_I. This allows for a more accurate representation of the associated wave effects. Further, **Level 5** eliminates all linear assumptions and solves the BVP on an unknown free surface boundary $S_F(t)$, which is updated at each time step and offers even higher accuracy. For example, Yu et al. [141] developed a fully-nonlinear potential solver for the 5-MW OC4 semi-submersible FWT and demonstrated good agreement with the experimental data of the wave field. The potential flow theory methods in **Levels 2** $\sim$ **5** are effective in capturing nonlinear wave-platform interaction effects to varying degrees. However, when viscous effects become significant, solving the Navier-Stokes equations using Computational Fluid Dynamics (CFD) tools is necessary, categorized as **Level 6** in Fig. 4.1. For example, Nematbakhsh et al. [94] developed a CFD model to study a 5-MW spar-type FWT under severe sea states, successfully capturing large platform rotation (10°) and strong nonlinear effects, such as full submergence of the platform and tether slacking, which are challenging to predict using linearized models such as OpenFAST.

The computational cost increases exponentially from **Level 1** to **6**. For instance, a 250-second simulation using a CFD model (**Level 6**) with a time step of 0.0016s on an Intel E5-2687W 3.10 GHz machine can take up to 480 hours (20 days) to complete, while a linear potential solver (**Level 1**) only requires around 4 hours on a less powerful Intel X5660 2.80 GHz machine [95]. Although the fully-nonlinear solver (**Level 5**) is more efficient than CFD, it remains computationally intensive, taking approximately 30 hours for a 120-second simulation on an Intel E5-2670 2.5 GHz machine [67]. The substantial computational demand of these high-fidelity models becomes even more pronounced when the aerodynamics and structural flexibility are incorporated [3, 124]. For example, a 1-hour CFD-FEM simulation for a FWT requires as much as 3×10^4 core hours [43].

Given these substantial computational costs, high-fidelity models are generally reserved for final verification and fine-tuning of the FWT design, while the linear method is widely recommended in FWT design guidelines for the preliminary design and optimization [20, 26]. During the early design phases, thousands of simulations are required to assess FWT performance under various environmental and operational conditions, making computational efficiency a top priority. However, the inherent limitations of the linear assumption can result in design candidates that are later found suboptimal and even infeasible, causing costly delays and design changes in the final stage [121]. To bridge the gap between accuracy and efficiency, it is essential to use reliable nonlinear models that can capture the dominant FWT hydrodynamics with realistic computational costs in early design phases [42].

Efforts have been made to practically capture the geometric nonlinearity arising from the time-varying wetted body surface $S_B(t)$, as represented by **Level 3** in Fig. 4.1. One notable approach is the offline method proposed by Rajendran et al. [108], where nonlinear hydrodynamics for ships are studied. In this approach, the hydrodynamic coefficients of added mass, radiation damping and wave-radiation impulse response functions are precalculated for various ship positions and stored in a database. During simulation, these coefficients are interpolated at each time step based on the instantaneous ship motion. Although this method effectively captures nonlinear hydrodynamic bending moments, as validated through a scaled model test [108], the convolution integral using impulse response functions remains time-consuming. The alternative state-space representation, commonly used in linear hydrodynamics, is appealing due to its efficiency and compatibility with control system design [35]. This has motivated recent research into using state-space models to represent nonlinear wave radiation forces. For instance, Schubert et al. [114] investigated the application of linear parameter-varying (LPV) systems to capture the pose-dependent radiation forces for wave energy converters (WECs). This approach involves identifying a set of state-space models at various WEC positions, and then using state-space interpolation to estimate the real-time radiation forces. While this method offers a practical solution to approximate geometric nonlinearity, it introduces a critical challenge: state-basis incoherency. The state-space basis is typically chosen arbitrarily by the identification algorithm, resulting in inconsistent bases for models identified at different WEC positions. Direct interpolation of these incoherent models can lead to inaccurate predictions [61, 81]. This state-basis incoherency issue is a known pitfall in stochastic-subspace identification [17] and LPV modelling [130, 23]. It could be a contributing factor to the large discrepancies observed between the WEC behaviour predicted by the LPV model and high-fidelity CFD results, as reported by Schubert et al. [114]. Notably, no specific treatment to ensure state-basis coherency was mentioned in their work, highlighting a key area for further development.

In this work, a novel LPV modelling framework is developed to evaluate the nonlinear FWT hydrodynamics following **Level 3** assumptions in Fig. 4.1, except that the incident wave forces are simplified to be computed on the mean wetted body surface $\overline{S}_B$. The radiation/diffraction BVPs are solved for a grid of specified platform heave and pitch positions using the validated 2D Boundary Element Method (BEM) code. State-space models are then estimated at each grid point using a subspace identification algorithm. To address the basis incoherency issue for subsequent model interpolation, a black-box approach based on the balanced realization and an automatic state-basis correction technique is proposed. Additionally, a novel gray-box approach is developed, which assigns physical meaning to the state vector through a finite-element formulation of the wave-platform interaction system, inherently ensuring basis coherency. The LPV state-space models representing the nonlinear wave radiation forces, along with other pose-dependent hydrodynamic effects, are implemented in Matlab/Simulink and validated against the standard **Level 3** body-nonlinear potential solver on the benchmark van Daalen cylinder model [128]. The validated LPV model is then integrated with other physical domains of the Simulink FWT model, as described in Section 2.3, and the nonlinear hydrodynamic effects on the global dynamic behaviour of an example 5-MW ITI-Barge FWT under various loading conditions are investigated.

4.2 Linear parameter-varying (LPV) modelling

In this section two methods will be discussed, themed as black- and gray- box respectively. The black-box LPV modelling framework involves three main steps: **identification**, **transformation**, and **interpolation**. For wave-platform interaction, wave radiation frequency response samples are obtained at specified platform positions and are used for the identification of the underlying state-space system. These identified state-space models are then transformed to ensure coherence in the state basis. With a set of coherent state-space models corresponding to various platform positions, a grid-based LPV state-space system is constructed, from which the geometric nonlinearity due to platform movement can be approximated through interpolation. In contrast, the gray-box LPV modelling framework follows a process of **identification**, **optimization**, and **interpolation**. Here, state-basis coherence is automatically guaranteed by using states with physical meanings, at the expense of introducing a nonlinear optimization problem. The detailed procedures for each LPV framework are elaborated in the following subsections.

4.2.1 Local state-space identification

In this work, the stochastic subspace state-space system identification (N4SID) algorithm is used to estimate from frequency response samples $\mathbf{K}(i\omega_k)$ a state-space realization of the system:

$$\begin{cases} \dot{\mathbf{x}}(t) = \mathbf{A}\mathbf{x}(t) + \mathbf{B}\mathbf{u}(t) \\ \mathbf{y}(t) = \mathbf{C}\mathbf{x}(t) + \mathbf{D}\mathbf{u}(t). \end{cases} \tag{4.1}$$

where $\mathbf{x}$ is a chosen state basis used to describe the system, $\mathbf{u}$ denotes the system input and $\mathbf{y}$ the output. Specifically, for the wave radiation force evaluation, $\mathbf{K}(i\omega_k)$ corresponds to the wave-radiation frequency response $\mathbf{K}_r(i\omega_k)$, which is derived from added mass $\boldsymbol{\lambda}(\omega_k)$ and radiation damping $\boldsymbol{\mu}(\omega_k)$, as expressed in Eq. (2.4). These hydrodynamic coefficients are obtained by solving the linear wave-platform BVP (Eq. (3.7)), either analytically or numerically, as detailed in Section 3.2. The frequency response $\mathbf{K}_r$ describes the relationship between the platform's rigid-body velocity $\dot{\boldsymbol{\xi}}$ (input) and the resulting wave radiation damping force $\mathbf{F}_r$ (output).

The direct application of the N4SID algorithm to the continuous-time frequency response samples $\mathbf{K}(i\omega_k)$ can lead to numerical ill-conditioning, due to the computation of high powers of $i\omega_k$. To address this issue, the continuous-time samples $\mathbf{K}(i\omega_k)$ are first converted into discrete-time samples $\mathbf{K}_d(e^{i\omega_{d,k}})$ using the bilinear transformation:

$$\mathbf{K}(i\omega_k) = \mathbf{K}\left(\frac{2(e^{i\omega_{d,k}}-1)}{T_{sp}(e^{i\omega_{d,k}}+1)}\right) = \mathbf{K}_d(e^{i\omega_{d,k}}), \tag{4.2}$$

where T_{sp} denotes the sampling period, which rescales the continuous-time frequency ω_k to a corresponding discrete-time frequency $\omega_{d,k} = 2\arctan(\frac{\omega_k T_{sp}}{2})$ such that $\omega_{d,k} \in [0,\pi]$. Accordingly, the continuous-time wave-radiation state-space model (Eq. (2.6)) is converted to the following discrete-time form:

$$\begin{cases} \mathbf{x}_d(t_d+1) = \mathbf{A}_d\mathbf{x}_d(t_d) + \mathbf{B}_d\dot{\boldsymbol{\xi}}(t_d) \\ \mathbf{y}(t_d) = \mathbf{C}_d\mathbf{x}_d(t_d) + \mathbf{D}_d\dot{\boldsymbol{\xi}}(t_d), \end{cases} \tag{4.3}$$

with the corresponding discrete-time frequency response function expressed as follows:

$$\underset{l\times m}{\mathbf{K}_d}(e^{i\omega_d}) = \underset{l\times n}{\mathbf{C}_d}\left(e^{i\omega_d}\underset{n\times n}{\mathbf{I}} - \underset{n\times n}{\mathbf{A}_d}\right)^{-1}\underset{n\times m}{\mathbf{B}_d} + \underset{l\times m}{\mathbf{D}_d}, \tag{4.4}$$

where l,m,n denotes the number of outputs, inputs and states, respectively. The objective now is to estimate a discrete-time state-space realization $[\mathbf{A}_d, \mathbf{B}_d, \mathbf{C}_d, \mathbf{D}_d]$ from the discrete-time frequency response samples $\mathbf{K}_d(e^{i\omega_{d,k}})$. The process involves the following steps.

- **Step 1: deriving the data equation**

  By applying the discrete-time Fourier transform (DTFT) to Eq. (4.3) and replacing the state-space model input $\dot{\boldsymbol{\xi}}$ with an identity matrix of size m, i.e., $\mathbf{I}_{m\times m}$, the resulting state-space model produces the frequency response function $\mathbf{K}_d(e^{i\omega_d})$ as the output:

  $$\begin{cases} e^{i\omega_d}\mathbf{X}_d(\omega_d) = \mathbf{A}_d\mathbf{X}_d(\omega_d) + \mathbf{B}_d \\ \mathbf{K}_d(e^{i\omega_d}) = \mathbf{C}_d\mathbf{X}_d(\omega_d) + \mathbf{D}_d. \end{cases} \tag{4.5}$$

  Eq. (4.5), evaluated with different time shifts $(0,1,2,\ldots,p)$ and frequency samples $(\omega_{d,k}, k = 1,2,\ldots,q)$, can be stacked into the following system of equations:

$$\underbrace{\begin{bmatrix} \mathbf{K}_{d,1} & \mathbf{K}_{d,2} & \dots & \mathbf{K}_{d,q} \\ e^{i\omega_{d,1}}\mathbf{K}_{d,1} & e^{i\omega_{d,2}}\mathbf{K}_{d,2} & \dots & e^{i\omega_{d,q}}\mathbf{K}_{d,q} \\ \vdots & \vdots & \ddots & \vdots \\ e^{i(p-1)\omega_{d,1}}\mathbf{K}_{d,1} & e^{i(p-1)\omega_{d,2}}\mathbf{K}_{d,2} & \dots & e^{i(p-1)\omega_{d,q}}\mathbf{K}_{d,q} \end{bmatrix}}_{\substack{\overline{\mathbf{K}} \\ lp\times mq}} = \underbrace{\begin{bmatrix} \mathbf{C}_d \\ \mathbf{C}_d\mathbf{A}_d \\ \vdots \\ \mathbf{C}_d{\mathbf{A}_d}^{p-1} \end{bmatrix}}_{\substack{\mathscr{O} \\ lp\times n}} \underbrace{\begin{bmatrix} \mathbf{X}_{d,1} & \mathbf{X}_{d,2} & \dots & \mathbf{X}_{d,q} \end{bmatrix}}_{\substack{\overline{\mathbf{X}} \\ n\times mq}}$$

$$+ \underbrace{\begin{bmatrix} \mathbf{D}_d & \mathbf{0} & \dots & \mathbf{0} \\ \mathbf{C}_d\mathbf{B}_d & \mathbf{D}_d & \dots & \mathbf{0} \\ \vdots & \vdots & \ddots & \vdots \\ \mathbf{C}_d{\mathbf{A}_d}^{p-2}\mathbf{B}_d & \mathbf{C}_d{\mathbf{A}_d}^{p-3}\mathbf{B}_d & \dots & \mathbf{D}_d \end{bmatrix}}_{\substack{\mathbf{\Gamma} \\ lp\times mp}} \underbrace{\begin{bmatrix} \mathbf{I}_m & \mathbf{I}_m & \dots & \mathbf{I}_m \\ e^{i\omega_{d,1}}\mathbf{I}_m & e^{i\omega_{d,2}}\mathbf{I}_m & \dots & e^{i\omega_{d,q}}\mathbf{I}_m \\ \vdots & \vdots & \ddots & \vdots \\ e^{i(p-1)\omega_{d,1}}\mathbf{I}_m & e^{i(p-1)\omega_{d,2}}\mathbf{I}_m & \dots & e^{i(p-1)\omega_{d,q}}\mathbf{I}_m \end{bmatrix}}_{\substack{\overline{\mathbf{W}} \\ mp\times mq}}. \tag{4.6}$$

In this equation, $\mathbf{K}_{d,k} = \mathbf{K}_d(e^{i\omega_k})$, $\mathbf{X}_{d,k} = \mathbf{X}_d(\omega_k)$, $\mathscr{O}$ denotes the extended observability matrix, and $\mathbf{\Gamma}$ the Toeplitz matrix. Eq. (4.6) can be rewritten into its real-valued form:

$$\underbrace{\begin{bmatrix} \overline{\mathbf{K}}^{Re} & \overline{\mathbf{K}}^{Im} \end{bmatrix}}_{\mathscr{G}} = \mathscr{O} \underbrace{\begin{bmatrix} \overline{\mathbf{X}}^{Re} & \overline{\mathbf{X}}^{Im} \end{bmatrix}}_{\mathscr{X}} + \mathbf{\Gamma} \underbrace{\begin{bmatrix} \overline{\mathbf{W}}^{Re} & \overline{\mathbf{W}}^{Im} \end{bmatrix}}_{\mathscr{W}}, \tag{4.7}$$

which is the data equation commonly used by most subspace-based identification algorithms.

- **Step 2: estimating $\mathbf{A}_d$ and $\mathbf{C}_d$**

  The state-space matrices $\mathbf{A}_d$ and $\mathbf{C}_d$ can be extracted from the extended observability matrix $\mathscr{O}$. To eliminate the influence of $\mathbf{\Gamma}\mathscr{W}$ in Eq. (4.7), the projector onto the nullspace of $\mathscr{W}$, calculated by $\mathscr{W}^{\perp} = \mathbf{I} - \mathscr{W}^{\mathsf{T}}(\mathscr{W}\mathscr{W}^{\mathsf{T}})^{-1}\mathscr{W}$, is multiplied on both sides of Eq. (4.7), resulting in $\mathscr{G}\mathscr{W}^{\perp} = \mathscr{O}\mathscr{X}\mathscr{W}^{\perp}$. It can be shown that when the state-space realization is minimal and $p \geq n$, $\mathscr{O}$ has full rank of n. The range space of $\mathscr{G}\mathscr{W}^{\perp}$ coincides with the range space of $\mathscr{O}$ [86]. Following standard subspace identification procedures, the singular value decomposition (SVD) is then applied to $\mathscr{G}\mathscr{W}^{\perp}$:

$$\mathscr{G}\mathscr{W}^{\perp} = \begin{bmatrix} \mathbf{U}_n & \mathbf{U}_0 \end{bmatrix} \begin{bmatrix} \mathbf{\Sigma}_n & \mathbf{0} \\ \mathbf{0} & \mathbf{\Sigma}_0 \end{bmatrix} \begin{bmatrix} \mathbf{V}_n^{\mathsf{T}} \\ \mathbf{V}_0^{\mathsf{T}} \end{bmatrix}. \tag{4.8}$$

  The matrix $\mathbf{U}_n$, corresponding to the first n largest singular values, provides an estimate of the rank of $\mathscr{O}$. This estimated $\widehat{\mathscr{O}}$ is related to the original $\mathscr{O}$ through a similarity transformation, such that $\widehat{\mathscr{O}} = \mathscr{O}\mathbf{T}$, where $\mathbf{T}$ is not uniquely defined. For instance, $\mathbf{T} = \mathscr{X}\mathscr{W}^{\perp}\mathbf{V}_n\mathbf{\Sigma}_n^{-1}$ if one takes $\widehat{\mathscr{O}} = \mathbf{U}_n$, and $\mathbf{T} = \mathscr{X}\mathscr{W}^{\perp}\mathbf{V}_n\mathbf{\Sigma}_n^{-1/2}$ if $\widehat{\mathscr{O}} = \mathbf{U}_n\mathbf{\Sigma}_n^{1/2}$, etc. Whatever the case, the estimates for $\widehat{\mathbf{A}}_d$ and $\widehat{\mathbf{C}}_d$ can be derived from the estimated $\widehat{\mathscr{O}}$ by

$$\widehat{\mathbf{A}}_d = (\mathbf{J}_1\widehat{\mathscr{O}})^{\dagger}\mathbf{J}_2\widehat{\mathscr{O}}, \quad \widehat{\mathbf{C}}_d = \mathbf{J}_3\widehat{\mathscr{O}}, \tag{4.9}$$

where $\mathbf{J}_1 = [\mathbf{I}_{l(p-1)}\ \mathbf{0}_{l(p-1)\times l}]$, $\mathbf{J}_2 = [\mathbf{0}_{l(p-1)\times l}\ \mathbf{I}_{l(p-1)}]$, $\mathbf{J}_3 = [\mathbf{I}_l\ \mathbf{0}_{l\times l(p-1)}]$, and $\dagger$ denotes the Moore-Penrose pseudo-inverse.

It should be highlighted that the meaning of this transformation matrix corresponds to the use of a specific state basis, which will generally be a transformation of the basis indicated in Eq. (4.1).

- **Step 3: estimating $\mathbf{B}_d$ and $\mathbf{D}_d$**

  Once the estimates of $\mathbf{A}_d$ and $\mathbf{C}_d$ are obtained, the matrices $\mathbf{B}_d$ and $\mathbf{D}_d$ can be determined by solving a linear least-squares problem based on Eq. (4.4):

$$\widehat{\mathbf{B}}_d, \widehat{\mathbf{D}}_d = \arg \min_{\mathbf{B}_d, \mathbf{D_d}} \sum_{k=1}^{q} \left\| \mathbf{K}_{d,k} - \widehat{\mathbf{C}}_d \left(e^{i\omega_{d,k}}\mathbf{I} - \widehat{\mathbf{A}}_d \right)^{-1} \mathbf{B}_d - \mathbf{D}_d \right\|_F^2, \tag{4.10}$$

  given that the frequency response $\mathbf{K}_{d,k}$ remains invariant with similarity transformations.

The estimated discrete-time state-space matrices $[\widehat{\mathbf{A}}_d, \widehat{\mathbf{B}}_d, \widehat{\mathbf{C}}_d, \widehat{\mathbf{D}}_d]$ can then be converted back to the continuous-time matrices $[\widehat{\mathbf{A}}, \widehat{\mathbf{B}}, \widehat{\mathbf{C}}, \widehat{\mathbf{D}}]$ via the bilinear transformation:

$$\begin{aligned} \widehat{\mathbf{A}} &= \frac{2}{T_{sp}}(\widehat{\mathbf{A}}_d + \mathbf{I})^{-1}(\widehat{\mathbf{A}}_d - \mathbf{I}), \quad & \widehat{\mathbf{B}} &= \frac{2}{\sqrt{T_{sp}}}(\widehat{\mathbf{A}}_d + \mathbf{I})^{-1}\widehat{\mathbf{B}}_d, \\ \widehat{\mathbf{C}} &= \frac{2}{\sqrt{T_{sp}}}\widehat{\mathbf{C}}_d(\widehat{\mathbf{A}}_d + \mathbf{I})^{-1}, \quad & \widehat{\mathbf{D}} &= \widehat{\mathbf{D}}_d - \widehat{\mathbf{C}}_d(\widehat{\mathbf{A}}_d + \mathbf{I})^{-1}\widehat{\mathbf{B}}_d. \end{aligned} \tag{4.11}$$

It is important to note that the estimated system matrices $[\widehat{\mathbf{A}}, \widehat{\mathbf{B}}, \widehat{\mathbf{C}}, \widehat{\mathbf{D}}]$ obtained through the above steps differ from the original system matrices by a similarity transformation: $\widehat{\mathbf{A}} = \mathbf{T}^{-1}\mathbf{A}\mathbf{T}$, $\widehat{\mathbf{B}} = \mathbf{T}^{-1}\mathbf{B}$, $\widehat{\mathbf{C}} = \mathbf{C}\mathbf{T}$, $\widehat{\mathbf{D}} = \mathbf{D}$. As mentioned in **Step 2**, this is a consequence of the algorithm choosing a transformed state basis. The transformation matrix $\mathbf{T}$ is not uniquely defined, amongst other factors it requires the definition of a reference basis, e.g., in mechanics problems the physical basis is often used. Additionally, popular N4SID-based identification algorithms, such as the MATLAB function `ssest` used in this work, include a subsequent refinement step using the prediction error minimization approach. This refinement alters all entries in the system matrices $[\widehat{\mathbf{A}}, \widehat{\mathbf{B}}, \widehat{\mathbf{C}}, \widehat{\mathbf{D}}]$, making it even more difficult to track

$\mathbf{T}$, which is required to recover the state-space model in terms of the reference basis. As a result, state-space models independently identified from the frequency response samples at different platform positions generally have different state-space bases. When these models are assembled into an interpolation array for the LPV modelling, it is critical to convert them to a common state basis or compensate for the instantaneous change of the state vectors when the state basis is changed. If no provision is taken, the evolution of the states over time and more crucially the resulting outputs (radiation damping forces $\mathbf{F}_r$ in this work) will be erroneous.

4.2.2 State-basis coherency

The objective of this subsection is to transform all locally identified state-space models, each along arbitrary state bases chosen by the identification algorithm, into models using a coherent state basis. This coherent basis remains consistent across different platform positions, allowing the transformed state-space models to be constructed into an interpolation array for the evaluation of nonlinear hydrodynamic effects.

4.2.2.1 Definition of state-basis coherency

The true dynamics of the wave radiation damping effect, which accounts for the time-varying wetted platform surface $S_B(t)$, are simplified as an LPV state-space system expressed as follows:

$$\begin{cases} \dot{\mathbf{x}}(t) = \mathbf{A}(\mathbf{p}(t))\mathbf{x}(t) + \mathbf{B}(\mathbf{p}(t))\dot{\boldsymbol{\xi}}(t) \\ \mathbf{y}(t) = \mathbf{C}(\mathbf{p}(t))\mathbf{x}(t) + \mathbf{D}(\mathbf{p}(t))\dot{\boldsymbol{\xi}}(t), \end{cases} \tag{4.12}$$

where the system matrices $[\mathbf{A}, \mathbf{B}, \mathbf{C}, \mathbf{D}]$ are functions of a time-varying scheduling parameter vector $\mathbf{p}(t)$. In this work, $\mathbf{p}(t)$ is defined as the platform pose, i.e., its displacement and rotation, for the ease of interpolation. Assuming that a set of platform poses $\mathbf{p}_i$, $(i = 1, 2, \ldots, N_p)$ is chosen and the state-space models locally identified at each $\mathbf{p}_i$ are transformed to share a coherent state basis $[\widehat{\mathbf{A}}_i, \widehat{\mathbf{B}}_i, \widehat{\mathbf{C}}_i, \widehat{\mathbf{D}}_i]$, these linear models can be constructed into a grid-based LPV model, allowing for interpolation based on instantaneous platform position.

Ensuring state-basis coherency is essential for the proposed grid-based LPV modelling approach to provide an accurate approximation of the underlying wave-radiation LPV system, as defined in Eq. (4.12). However, different definitions of "state-basis coherency" have been used in the literature. These definitions, as summarized by Zhang et al. [143], are adapted here as follows:

Strict Coherency: A set of state-space models $[\widehat{\mathbf{A}}_i, \widehat{\mathbf{B}}_i, \widehat{\mathbf{C}}_i, \widehat{\mathbf{D}}_i]$ is strictly coherent with respect to the LPV system (Eq. (4.12)) at $\mathbf{p} = \mathbf{p}_i$ if there exists a non-singular transformation matrix $\mathbf{T}$ that is common to all local models $(i = 1, 2, \ldots, N_p)$, such that

$$\widehat{\mathbf{A}}_i = \mathbf{T}^{-1}\mathbf{A}(\mathbf{p}_i)\mathbf{T}, \quad \widehat{\mathbf{B}}_i = \mathbf{T}^{-1}\mathbf{B}(\mathbf{p}_i), \quad \widehat{\mathbf{C}}_i = \mathbf{C}(\mathbf{p}_i)\mathbf{T}, \quad \widehat{\mathbf{D}}_i = \mathbf{D}(\mathbf{p}_i). \tag{4.13}$$

Relaxed Coherency: A set of state-space models $[\widehat{\mathbf{A}}_i, \widehat{\mathbf{B}}_i, \widehat{\mathbf{C}}_i, \widehat{\mathbf{D}}_i]$ is considered coherent with respect to the LPV system (Eq. (4.12)) at $\mathbf{p} = \mathbf{p}_i$ if there exists a matrix-valued function $\mathbf{T}_i = \mathbf{T}(\mathbf{p}_i)$ specific to each local model, such that

$$\widehat{\mathbf{A}}_i = \mathbf{T}_i^{-1}\mathbf{A}(\mathbf{p}_i)\mathbf{T}_i, \quad \widehat{\mathbf{B}}_i = \mathbf{T}_i^{-1}\mathbf{B}(\mathbf{p}_i), \quad \widehat{\mathbf{C}}_i = \mathbf{C}(\mathbf{p}_i)\mathbf{T}_i, \quad \widehat{\mathbf{D}}_i = \mathbf{D}(\mathbf{p}_i). \tag{4.14}$$

As pointed out in [143], Eq. (4.13), which uses a common transformation matrix $\mathbf{T}$ for all local models, is the only definition that ensures exact state-basis coherency, thereby preserving the input-output behaviour of the original LPV system. In contrast, Eq. (4.14), as a less stringent condition, does not guarantee the same input-output behaviour after interpolation. However, the relaxed consistency condition enables a more straightforward and efficient application of the black-box method. Various forms of black-box LPV modelling have been investigated, such as the balanced-basis form, controllable canonical form, modal form, and pole-zero form, etc [61]. Conversely, achieving strict state-basis coherency is only possible under global structural assumptions, which requires employing the gray-box method that is less frequently investigated.

4.2.2.2 Black-box method: balanced basis

Among the various forms used in black-box LPV modelling, the balanced form is preferable due to its superior numerical conditioning and ease of automation [82, 61]. The balanced form makes use of the controllability and observability properties of a linear system, which can be quantified for a continuous-time state-space representation using the controllability Gramian $\mathscr{W}_c$ and observability Gramian $\mathscr{W}_o$ as follows:

$$\mathscr{W}_c = \int_0^\infty e^{\mathbf{A}\tau}\mathbf{B}\mathbf{B}^\intercal e^{\mathbf{A}^\intercal\tau}\,d\tau, \quad \mathscr{W}_o = \int_0^\infty e^{\mathbf{A}^\intercal\tau}\mathbf{C}^\intercal\mathbf{C}e^{\mathbf{A}\tau}\,d\tau. \tag{4.15}$$

The controllability and observability properties can be visualized using ellipsoids in the state space: the controllability ellipsoid is defined as $\{\mathbf{x}\,|\,\mathbf{x}^\intercal\mathscr{W}_c^{-1}\mathbf{x} \leq 1\}$, and the observability ellipsoid as $\{\mathbf{x}\,|\,\mathbf{x}^\intercal\mathscr{W}_o^{-1}\mathbf{x} \leq 1\}$. A similarity transformation $\mathbf{T}_b$, which transforms the two ellipsoids into a common ellipsoid whose principal axes coincide with the state coordinate axes, is called the balanced transformation. This transformation is mathematically defined as $\mathbf{T}_b^{-1}\mathscr{W}_c\mathbf{T}_b^{-\intercal} = \mathbf{T}_b^\intercal\mathscr{W}_o\mathbf{T}_b = \mathbf{\Sigma}_b$, where $\mathbf{\Sigma}_b$ is a diagonal matrix containing decreasing singular values. The matrix $\mathbf{T}_b$ can be determined as follows: first, apply the Cholesky decomposition

$\mathscr{W}_c = \mathbf{L}_c\mathbf{L}_c^\intercal$ and $\mathscr{W}_o = \mathbf{L}_o\mathbf{L}_o^\intercal$, then compute the SVD of $\mathbf{L}_o^\intercal\mathbf{L}_c = \mathbf{U}_b\mathbf{\Sigma}_b\mathbf{V}_b^\intercal$, and finally obtain $\mathbf{T}_b = \mathbf{L}_c\mathbf{V}_b\mathbf{\Sigma}_b^{-1/2}$ and $\mathbf{T}_b^{-1} = \mathbf{\Sigma}_b^{-1/2}\mathbf{U}_b^\intercal\mathbf{L}_o^\intercal$. This balanced transformation reorders the state-basis vector such that the states are ordered from the most controllable and observable to the least. To illustrate this method, a simple 2-state model expressed as follows is taken as an example:

$$\mathbf{A} = \begin{bmatrix} -0.6 & 0.3 \\ -0.4 & -0.1 \end{bmatrix}, \ \mathbf{B} = \begin{bmatrix} 1 \\ 3 \end{bmatrix}, \ \mathbf{C} = \begin{bmatrix} 1 & 2 \end{bmatrix}, \ \mathbf{D} = 0. \tag{4.16}$$

Its controllability and observability Gramians are

$$\mathscr{W}_c = \begin{bmatrix} 4.6825 & 7.6984 \\ 7.6984 & 14.2063 \end{bmatrix}, \ \mathscr{W}_o = \begin{bmatrix} 2.6587 & -2.7381 \\ -2.7381 & 11.7857 \end{bmatrix}, \tag{4.17}$$

respectively. Their corresponding ellipsoids are shown in Fig. 4.2. It is evident that the most controllable direction is difficult to observe, and vice versa. Applying the balanced transformation, $\mathbf{T}_b = \begin{bmatrix} 0.5920 & 0.7231 \\ 1.1024 & 0.0919 \end{bmatrix}$ yields the following balanced state-space model:

$$\mathbf{A}_b = \begin{bmatrix} -0.3348 & -0.2403 \\ 0.2403 & -0.3652 \end{bmatrix}, \ \mathbf{B}_b = \begin{bmatrix} 2.7968 \\ -0.9068 \end{bmatrix}, \ \mathbf{C}_b = \begin{bmatrix} 2.7968 & 0.9068 \end{bmatrix}, \ \mathbf{D}_b = 0, \tag{4.18}$$

with identical diagonal controllability and observability Gramians:

$$\overline{\mathscr{W}}_c = \overline{\mathscr{W}}_o = \mathbf{\Sigma}_b = \begin{bmatrix} 11.6814 & 0 \\ 0 & 1.1259 \end{bmatrix}. \tag{4.19}$$

The transformed ellipsoids, shown in Fig. 4.2, coincide perfectly as expected, and their principal axes are aligned with the state bases x_1 and x_2. Both the most controllable and most observable directions are now along the state x_1.

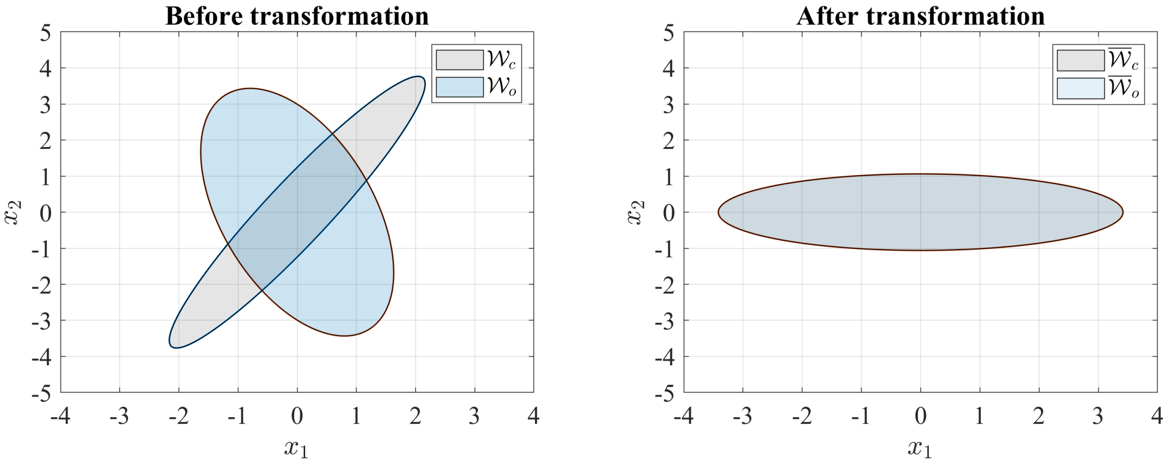

Fig. 4.2 Controllability and observability ellipsoids of the example state-space model (Eq. (4.16)) before and after the balanced transformation.

As concluded by Moore [92], the uniqueness of the balanced transformation $\mathbf{T}_b$ depends on whether the eigenvalues of the Gramian product $\mathscr{W}_c\mathscr{W}_o$ are distinct. When the eigenvalues are distinct, the columns of $\mathbf{T}_b$ are uniquely determined except for a potential sign change of ±1. However, if the eigenvalues are repeated, the columns of $\mathbf{T}_b$ can be arbitrarily rotated, making the transformation non-unique. In the balanced-form LPV modelling approach proposed by [61], the eigenvalues are monitored to ensure basis coherency. If distinct eigenvalues are detected, the sign of the columns is corrected if necessary. In cases where repeated eigenvalues lead to non-uniqueness, the corresponding local state-space models are discarded to avoid inconsistencies in subsequent interpolation.

However, in a practical implementation, the states of the identified models may be swapped by the identification algorithm. This state swapping complicates basis correction, making it more challenging than merely adjusting sign changes for distinct eigenvalues. To address this issue, this work proposes an automatic state correction method capable of handling both sign changes and state swapping. The proposed method relies on the assumption that the intervals between the grid of platform positions are sufficiently small. Under this assumption, adjacent locally identified state-space models and their corresponding balanced-form models should be similar. This proximity allows the pseudo similarity transformation between two adjacent models, $\widetilde{\mathscr{T}}_{b,i/i+1}$, to serve as an indicator for detecting and correcting both sign changes and state swapping in the state basis.

Given two adjacent state-space models that have been transformed into the balanced bases $[\mathbf{A}_{b,i}, \mathbf{B}_{b,i}, \mathbf{C}_{b,i}, \mathbf{D}_{b,i}]$ and $[\mathbf{A}_{b,i+1}, \mathbf{B}_{b,i+1}, \mathbf{C}_{b,i+1}, \mathbf{D}_{b,i+1}]$, the pseudo similarity relation associated with $\widetilde{\mathscr{T}}_{b,i/i+1}$ can be expressed as follows:

$$\mathbf{A}_{b,i+1} \approx \widetilde{\mathscr{T}}_{b,i/i+1}^{-1}\mathbf{A}_{b,i}\widetilde{\mathscr{T}}_{b,i/i+1}, \quad \mathbf{B}_{b,i+1} \approx \widetilde{\mathscr{T}}_{b,i/i+1}^{-1}\mathbf{B}_{b,i}, \quad \mathbf{C}_{b,i+1} \approx \mathbf{C}_{b,i}\widetilde{\mathscr{T}}_{b,i/i+1}. \tag{4.20}$$

This set of equations is linear in terms of $\widetilde{\mathscr{T}}_{b,i/i+1}$, and one can estimate it by solving the following standard linear least-squares problem:

$$\begin{bmatrix} \mathbf{I} \otimes \mathbf{A}_{b,i} - \mathbf{A}_{b,i+1}^{\mathsf{T}} \otimes \mathbf{I} \\ \mathbf{B}_{b,i+1}^{\mathsf{T}} \otimes \mathbf{I} \\ \mathbf{I} \otimes \mathbf{C}_{b,i} \end{bmatrix} vec\left\{\widetilde{\mathscr{T}}_{b,i/i+1}\right\} \approx \begin{pmatrix} \mathbf{0} \\ vec\left\{\mathbf{B}_{b,i}\right\} \\ vec\left\{\mathbf{C}_{b,i+1}\right\} \end{pmatrix}, \tag{4.21}$$

where $\otimes$ denotes the Kronecker product and $vec\{\cdot\}$ represents the vectorization of a matrix. The effectiveness of this newly proposed basis correction method will be demonstrated in subsequent sections through various test cases and performance evaluations.

4.2.2.3 Gray-box method: physical basis

As mentioned in Section 4.2.2.1, strict state-basis coherency requires prior knowledge of the dynamic system. To this end, the finite element formulation of the linear wave-platform interaction problem, as proposed by [7] and [71], is employed in this work to construct a gray-box state-space model. This model uses a state basis with physical interpretations, specifically wave radiation potentials and their time derivatives.

For the convenience of discussion, the 2D linear wave-platform BVP described in Section 3.2.2 is reiterated here, with the far-field boundary condition on S_∞ replaced by the modified time-domain Orlanski's radiation condition, as detailed in [71].

$$\begin{cases} \nabla^2 \Phi_R = 0, & \mathbf{X} \in \Omega \\ \dfrac{\partial \Phi_R}{\partial z} + \dfrac{1}{g}\dfrac{\partial^2 \Phi_R}{\partial t^2} = 0, & \mathbf{X} \in \overline{S}_F : \; z = 0 \\ \dfrac{\partial \Phi_R}{\partial \mathbf{n}} = V_n, & \mathbf{X} \in \overline{S}_B \\ \dfrac{\partial \Phi_R}{\partial z} = 0, & \mathbf{X} \in S_D : \; z = -h \\ \dfrac{\partial \Phi_R}{\partial \mathbf{n}} + \dfrac{1}{c_p}\dfrac{\partial \Phi_R}{\partial t} = 0, & \mathbf{X} \in S_\infty \\ \Phi_R\big|_{t=0} = 0, \; \dfrac{\partial \Phi_R}{\partial t}\bigg|_{t=0} = 0, & \end{cases} \tag{4.22}$$

where $V_n = \dot{\boldsymbol{\xi}} \cdot \overline{\mathbf{n}}$ denotes the normal velocity on the platform surface pointing outward from the fluid, $\dot{\boldsymbol{\xi}} = [\dot{\xi}_1 \;\; \dot{\xi}_3 \;\; \dot{\xi}_5]^{\mathsf{T}}$ denotes the platform's rigid-body velocity, and $c_p = c_p(t)$ is the time-varying phase velocity of radiated waves crossing the far-field boundaries S_∞.

According to Bai [7], solving the well-posed BVP of Eq. (4.22) with the mixed boundary conditions in the form of $\frac{\partial \Phi_R}{\partial \mathbf{n}} + \alpha \Phi_R = \beta$, where α and β are known functions, is equivalent to finding a velocity potential Φ_R that makes the functional

$$\mathscr{F}(\Phi_R) \equiv \int_\Omega \frac{1}{2}(\nabla\Phi_R)^2 d\Omega + \int_{\bar{S}_F \bigcup \bar{S}_B \bigcup S_D \bigcup S_\infty} \left(\frac{1}{2}\alpha\Phi_R^2 - \beta\Phi_R\right) dS \tag{4.23}$$

stationary, i.e., $\delta\mathscr{F}(\Phi_R) = 0$. This leads to an integral equation

$$\begin{aligned}\delta\mathscr{F} &= \int_\Omega \nabla\Phi_R \cdot \nabla\delta\Phi_R d\Omega + \int_{\bar{S}_F \bigcup \bar{S}_B \bigcup S_D \bigcup S_\infty} (\alpha\Phi_R\delta\Phi_R - \beta\delta\Phi_R) dS \\ &= \int_\Omega \nabla\Phi_R \cdot \nabla\delta\Phi_R d\Omega + \frac{1}{g}\int_{\bar{S}_F} \frac{\partial^2\Phi_R}{\partial t^2}\delta\Phi_R dS + \frac{1}{c_p}\int_{S_\infty} \frac{\partial\Phi_R}{\partial t}\delta\Phi_R dS - \int_{\bar{S}_B} V_n\delta\Phi_R dS \\ &= 0,\end{aligned} \tag{4.24}$$

where the variation $\delta\Phi_R$ satisfies the same governing equation and boundary conditions as Φ_R (Eq. (4.22)), and it is assumed that $\delta\nabla\Phi_R = \nabla\delta\Phi_R$.

Following the standard finite element method, the computational domain Ω can be discretized, and the velocity potential Φ_R throughout Ω can be approximated by the inner product of the shape functions $\mathbf{N}$ and the nodal values of the potential $\boldsymbol{\varphi}$, which is expressed as follows:

$$\Phi_R(x,z,t) = \mathbf{N}(x,z) \cdot \boldsymbol{\varphi}(t). \tag{4.25}$$

Substituting Eq. (4.25) into Eq. (4.24) yields the equations of motion (EoM) for the fluid subsystem:

$$\mathbf{M}_f\ddot{\boldsymbol{\varphi}}(t) + \mathbf{C}_f\dot{\boldsymbol{\varphi}}(t) + \mathbf{K}_f\boldsymbol{\varphi}(t) = \mathbf{F}_f, \tag{4.26}$$

where $\mathbf{M}_f$, $\mathbf{C}_f$, and $\mathbf{K}_f$ denote the mass, damping, and stiffness matrices of the fluid subsystem, respectively, and $\mathbf{F}_f$ represents the load vector due to the platform motion. Their detailed expressions are summarized as follows:

$$\begin{gathered}\mathbf{M}_f = \frac{1}{g}\int_{\bar{S}_F} \mathbf{N}\mathbf{N}^\intercal dS, \quad \mathbf{C}_f = \frac{1}{c_p}\int_{S_\infty} \mathbf{N}\mathbf{N}^\intercal dS, \quad \mathbf{K}_f = \int_\Omega \nabla\mathbf{N} \cdot \nabla\mathbf{N}^\intercal d\Omega, \\ \mathbf{F}_f = \int_{\bar{S}_B} \mathbf{N}V_n dS = \int_{\bar{S}_B} \mathbf{N}\bar{\mathbf{n}}^\intercal dS \cdot \dot{\boldsymbol{\xi}}.\end{gathered} \tag{4.27}$$

The 2^{nd}-order differential equation of the fluid subsystem is derived from the linear wave-platform BVP (Eq. (4.22)), which assumes small platform displacements around the wetted body surface $\bar{S}_B$ at a specified platform position. Consequently, when the platform undergoes generic movements, the EoMs (Eq. (4.26)) are expected to remain accurate only over a short time duration, during which both the phase velocity c_p and the normal velocity on the platform surface V_n are assumed to be constant. This leads to a set of differential equations with constant coefficients and external forces, enabling the derivation of a linear state-space model with a physical basis of nodal potentials.

The structure of the mass, damping and stiffness matrices of the fluid subsystem, i.e., the location of non-zero entries, is more important than their exact values. To illustrate the state-space representation, a simple example of finite element discretization for the fluid subsystem is used, as shown in Fig. 4.3. The nodal potentials in the fluid subsystem are categorized as $\boldsymbol{\varphi}_1$, $\boldsymbol{\varphi}_2$, $\boldsymbol{\varphi}_3$, and $\boldsymbol{\varphi}_4$, representing nodes on the free surface ($\overline{S}_F$), the far-field boundary (S_∞), the platform wetted surface ($\overline{S}_B$), and all other nodes on the sea bed and within the fluid domain, respectively. By applying the standard finite element formulation to the discretized fluid domain, the resultant structure of the mass, damping, stiffness matrices and the force vector can be obtained, as shown in Fig. 4.4.

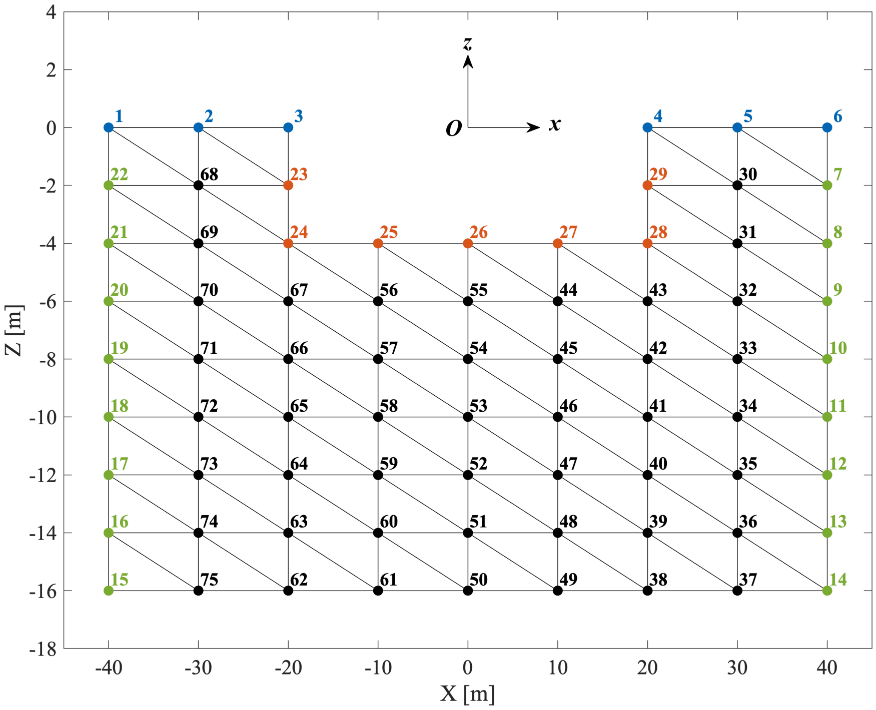

Fig. 4.3 A simple finite element mesh for the fluid subsystem. Nodes 1 $\sim$ 6 represent potentials on the free surface, nodes 7 $\sim$ 22 on the artificial far-field boundary, nodes 23 $\sim$ 29 on the platform wetted surface, and nodes 30 $\sim$ 75 on the sea bed or in the inner fluid domain.

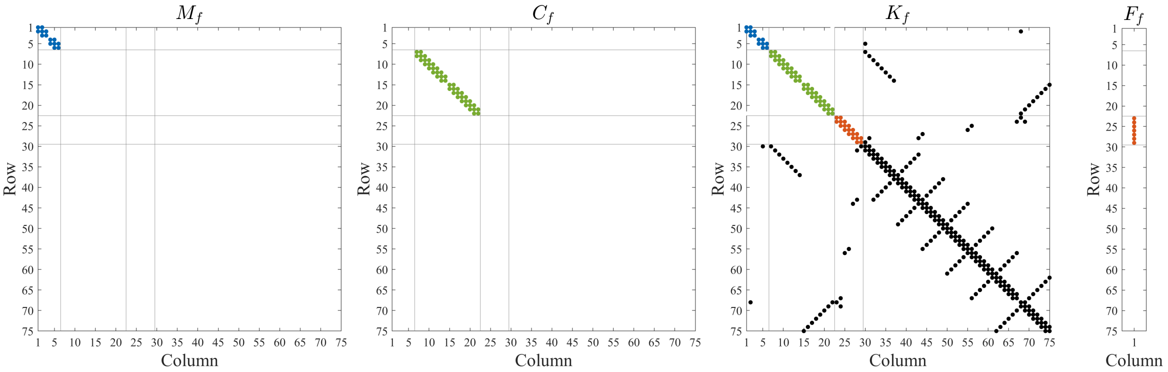

Fig. 4.4 The structure of mass, damping, stiffness matrices and the force vector obtained from the example finite element mesh. Only the location of non-zero entries is shown.

As indicated in Eq. (4.27), the fluid inertia effect is only present on the free surface boundary $\overline{S}_F$, leading to non-zero entries in the mass matrix $\mathbf{M}_f$ corresponding to $\boldsymbol{\varphi}_1$ nodes, as depicted in Fig. 4.4. Similarly, the damping effect originates exclusively from the far-field boundary S_∞, producing non-zero entries in the damping matrix $\mathbf{C}_f$ associated with $\boldsymbol{\varphi}_2$ nodes. The force exerted by the fluid, represented by $\mathbf{F}_f$, is transferred to the platform through $\boldsymbol{\varphi}_3$ nodes located on the platform surface $\overline{S}_B$. In contrast, the fluid stiffness matrix $\mathbf{K}_f$ accounts for contributions from nodes across the entire fluid domain, resulting in a symmetric and non-singular matrix structure. This distinction in matrix structures highlights the unique roles of the fluid nodes in the overall dynamic behaviour of the fluid subsystem.

Given the structure of $\mathbf{M}_f, \mathbf{C}_f, \mathbf{K}_f$ and $\mathbf{F}_f$ (Fig. 4.4), the EoMs for the fluid subsystem can be expressed as the following differential-algebraic system of equations (DAE):

$$\begin{bmatrix} \mathbf{M}_{f,11} & \mathbf{0} & \mathbf{0} & \mathbf{0} \\ \mathbf{0} & \mathbf{0} & \mathbf{0} & \mathbf{0} \\ \mathbf{0} & \mathbf{0} & \mathbf{0} & \mathbf{0} \\ \mathbf{0} & \mathbf{0} & \mathbf{0} & \mathbf{0} \end{bmatrix} \begin{pmatrix} \ddot{\boldsymbol{\varphi}}_1 \\ \ddot{\boldsymbol{\varphi}}_2 \\ \ddot{\boldsymbol{\varphi}}_3 \\ \ddot{\boldsymbol{\varphi}}_4 \end{pmatrix} + \begin{bmatrix} \mathbf{0} & \mathbf{0} & \mathbf{0} & \mathbf{0} \\ \mathbf{0} & \mathbf{C}_{f,22} & \mathbf{0} & \mathbf{0} \\ \mathbf{0} & \mathbf{0} & \mathbf{0} & \mathbf{0} \\ \mathbf{0} & \mathbf{0} & \mathbf{0} & \mathbf{0} \end{bmatrix} \begin{pmatrix} \dot{\boldsymbol{\varphi}}_1 \\ \dot{\boldsymbol{\varphi}}_2 \\ \dot{\boldsymbol{\varphi}}_3 \\ \dot{\boldsymbol{\varphi}}_4 \end{pmatrix}$$

$$+ \begin{bmatrix} \mathbf{K}_{f,11} & \mathbf{0} & \mathbf{0} & \mathbf{K}_{f,14} \\ \mathbf{0} & \mathbf{K}_{f,22} & \mathbf{0} & \mathbf{K}_{f,24} \\ \mathbf{0} & \mathbf{0} & \mathbf{K}_{f,33} & \mathbf{K}_{f,34} \\ \mathbf{K}_{f,41} & \mathbf{K}_{f,42} & \mathbf{K}_{f,43} & \mathbf{K}_{f,44} \end{bmatrix} \begin{pmatrix} \boldsymbol{\varphi}_1 \\ \boldsymbol{\varphi}_2 \\ \boldsymbol{\varphi}_3 \\ \boldsymbol{\varphi}_4 \end{pmatrix} = \begin{pmatrix} \mathbf{0} \\ \mathbf{0} \\ \mathbf{F}_{f,3} \\ \mathbf{0} \end{pmatrix}, \tag{4.28}$$

In this system, the differential equations are associated with $\boldsymbol{\varphi}_1$ and $\boldsymbol{\varphi}_2$, representing the dynamic balance of mass and energy within the fluid domain. The algebraic constraints are associated with $\boldsymbol{\varphi}_3$ and $\boldsymbol{\varphi}_4$, imposing equilibrium conditions of fluid velocity and pressure. While a descriptor state-space formulation can be directly derived from the DAE as discussed in Moarref and Jovanovic [91], it requires specialized system identification techniques to handle the mixed differential and algebraic nature of the equations. In this work, the algebraic constraints in the DAE (Eq. (4.28)) are eliminated, resulting in a standard state-space representation that involves only the differential equations. This approach simplifies the modelling process and facilitates the application of conventional system identification algorithms.

From the algebraic constraints in Eq. (4.28), the variables $\boldsymbol{\varphi}_3$ and $\boldsymbol{\varphi}_4$ can be expressed in terms of $\boldsymbol{\varphi}_1$, $\boldsymbol{\varphi}_2$ and the force $\mathbf{F}_{f,3}$ as follows:

$$\begin{aligned}
\boldsymbol{\varphi}_3 &= \left(\mathbf{K}_{f,33} - \mathbf{K}_{f,34}\mathbf{K}_{f,44}^{-1}\mathbf{K}_{f,43}\right)^{-1}\left(\mathbf{F}_{f,3} + \mathbf{K}_{f,34}\mathbf{K}_{f,44}^{-1}\mathbf{K}_{f,41}\boldsymbol{\varphi}_1 + \mathbf{K}_{f,34}\mathbf{K}_{f,44}^{-1}\mathbf{K}_{f,42}\boldsymbol{\varphi}_2\right), \\
\boldsymbol{\varphi}_4 &= -\mathbf{K}_{f,44}^{-1}\left(\mathbf{K}_{f,41}\boldsymbol{\varphi}_1 + \mathbf{K}_{f,42}\boldsymbol{\varphi}_2 + \mathbf{K}_{f,43}\boldsymbol{\varphi}_3\right).
\end{aligned} \tag{4.29}$$

Substituting Eq. (4.29) into the differential equations in Eq. (4.28) yields a system of ordinary differential equations (ODE):

$$\begin{bmatrix} \mathbf{M}_{f,11} & \mathbf{0} \\ \mathbf{0} & \mathbf{0} \end{bmatrix} \begin{pmatrix} \ddot{\boldsymbol{\varphi}}_1 \\ \ddot{\boldsymbol{\varphi}}_2 \end{pmatrix} + \begin{bmatrix} \mathbf{0} & \mathbf{0} \\ \mathbf{0} & \mathbf{C}_{f,22} \end{bmatrix} \begin{pmatrix} \dot{\boldsymbol{\varphi}}_1 \\ \dot{\boldsymbol{\varphi}}_2 \end{pmatrix} + \begin{bmatrix} \mathbf{E}_{11} & \mathbf{E}_{12} \\ \mathbf{E}_{21} & \mathbf{E}_{22} \end{bmatrix} \begin{pmatrix} \boldsymbol{\varphi}_1 \\ \boldsymbol{\varphi}_2 \end{pmatrix} = \begin{pmatrix} \mathbf{Q}_1 \\ \mathbf{Q}_2 \end{pmatrix} \dot{\boldsymbol{\xi}}, \tag{4.30}$$

where $\mathbf{E}_{11}, \mathbf{E}_{12}, \mathbf{E}_{21}, \mathbf{E}_{22}, \mathbf{Q}_1$ and $\mathbf{Q}_2$ represent non-zero blocks whose exact values are not of interest in this context. The input to the fluid subsystem is defined as the platform's rigid-body velocity $\dot{\boldsymbol{\xi}}$, which is related to the force $\mathbf{F}_f$ as described in Eq. (4.27). Defining the state vector as $\mathbf{x}_p = \left(\boldsymbol{\varphi}_1^\intercal \ \dot{\boldsymbol{\varphi}}_1^\intercal \ \boldsymbol{\varphi}_2^\intercal\right)^\intercal$, the 2^{nd}-order ODE of Eq. (4.30) can be conveniently rewritten into the following state-space form:

$$\begin{pmatrix} \dot{\boldsymbol{\varphi}}_1 \\ \ddot{\boldsymbol{\varphi}}_1 \\ \dot{\boldsymbol{\varphi}}_2 \end{pmatrix} = \begin{bmatrix} \mathbf{0} & \mathbf{I} & \mathbf{0} \\ -\mathbf{M}_{f,11}^{-1}\mathbf{E}_{11} & \mathbf{0} & -\mathbf{M}_{f,11}^{-1}\mathbf{E}_{12} \\ -\mathbf{C}_{f,22}^{-1}\mathbf{E}_{21} & \mathbf{0} & -\mathbf{C}_{f,22}^{-1}\mathbf{E}_{22} \end{bmatrix} \begin{pmatrix} \boldsymbol{\varphi}_1 \\ \dot{\boldsymbol{\varphi}}_1 \\ \boldsymbol{\varphi}_2 \end{pmatrix} + \begin{bmatrix} \mathbf{0} \\ \mathbf{M}_{f,11}^{-1}\mathbf{Q}_1 \\ \mathbf{C}_{f,22}^{-1}\mathbf{Q}_2 \end{bmatrix} \dot{\boldsymbol{\xi}}. \tag{4.31}$$

The physical interpretation of $\mathbf{x}_p$ is as follows: the potential values at selected free-surface nodes ($\boldsymbol{\varphi}_1$), the time derivatives of the selected free-surface nodes ($\dot{\boldsymbol{\varphi}}_1$), and the potential values at selected far-field boundary nodes ($\boldsymbol{\varphi}_2$). Once these node locations are determined, a unique state basis is established, which remains unchanged regardless of the platform position. The zero blocks in Eq. (4.31), corresponding to the relations between $\ddot{\boldsymbol{\varphi}}_1$ and $\dot{\boldsymbol{\varphi}}_1$, as well as between $\dot{\boldsymbol{\varphi}}_2$ and $\dot{\boldsymbol{\varphi}}_1$, originate from the damping matrix in Eq. (4.30). To accommodate various damping mechanisms, these strict requirements of zeros blocks are relaxed without altering the physical meaning of the states $\mathbf{x}_p$. The resulting wave-radiation state-space model can then be represented as follows:

$$\underbrace{\begin{pmatrix}\dot{\boldsymbol{\varphi}}_1\\ \ddot{\boldsymbol{\varphi}}_1\\ \dot{\boldsymbol{\varphi}}_2\end{pmatrix}}_{\dot{\mathbf{x}}_p}=\underbrace{\begin{bmatrix}\mathbf{0}&\mathbf{I}&\mathbf{0}\\ \mathbf{A}_{21}&\mathbf{A}_{22}&\mathbf{A}_{23}\\ \mathbf{A}_{31}&\mathbf{A}_{32}&\mathbf{A}_{33}\end{bmatrix}}_{\mathbf{A}_p}\underbrace{\begin{pmatrix}\boldsymbol{\varphi}_1\\ \dot{\boldsymbol{\varphi}}_1\\ \boldsymbol{\varphi}_2\end{pmatrix}}_{\mathbf{x}_p}+\underbrace{\begin{bmatrix}\mathbf{0}\\ \mathbf{B}_2\\ \mathbf{B}_3\end{bmatrix}}_{\mathbf{B}_p}\dot{\boldsymbol{\xi}},\tag{4.32}$$

where both the state matrix $\mathbf{A}_p$ and input matrix $\mathbf{B}_p$ are constant.

The selection of the state basis $\mathbf{x}_p$ allows for the output of all variables related to the linear wave-platform BVP. Among these variables, the wave radiation force $\mathbf{F}_r$ is of primary interest for the evaluation of platform dynamics. $\mathbf{F}_r$ can be calculated from $-\rho\int_{\bar{S}_B}\dot{\boldsymbol{\varphi}}_3\bar{\mathbf{n}}\,dS$, as described in Section 3.2.3. According to Eq. (4.27) and (4.29), $\dot{\boldsymbol{\varphi}}_3$ is a function of the state variables $\boldsymbol{\varphi}_1,\dot{\boldsymbol{\varphi}}_1,\boldsymbol{\varphi}_2$, the velocity input $\dot{\boldsymbol{\xi}}$, and the platform acceleration $\ddot{\boldsymbol{\xi}}$. As discussed in Section 2.2.1, the mapping from $\dot{\boldsymbol{\xi}}$ to $\mathbf{F}_r$ is characterized by a strict proper wave radiation frequency response function $\mathbf{K}_r(i\omega)$, which implies that no direct feedthrough exists in the wave radiation state-space model. Furthermore, the term associated with $\ddot{\boldsymbol{\xi}}$ corresponds to an infinite-frequency added mass effect. Since this effect is commonly handled separately, it is not included in the wave-radiation state-space representation. Therefore, the output equation of $\mathbf{F}_r$ in the state-space representation only involves the states $\boldsymbol{\varphi}_1,\dot{\boldsymbol{\varphi}}_1$ and $\boldsymbol{\varphi}_2$.

To accurately capture the dynamics of the 2D wave-platform interaction system, the finite element mesh should be sufficiently dense. This typically results in a high number of states, which is much larger than the number of output forces — only 3 for the 2D problem. For the purposes of the basis transformation, additional outputs are required apart from the wave radiation force $\mathbf{F}_r$. In this work, the nodal potentials $\boldsymbol{\varphi}_1$ and $\boldsymbol{\varphi}_2$ are added to complement $\mathbf{F}_r$ outputs, yielding the output equations in the following state-space form:

$$\underbrace{\begin{pmatrix}\boldsymbol{\varphi}_1\\ \boldsymbol{\varphi}_2\\ \mathbf{F}_r\end{pmatrix}}_{\mathbf{y}}=\underbrace{\begin{bmatrix}\mathbf{I}&\mathbf{0}&\mathbf{0}\\ \mathbf{0}&\mathbf{0}&\mathbf{I}\\ \mathbf{C}_{31}&\mathbf{C}_{32}&\mathbf{C}_{33}\end{bmatrix}}_{\mathbf{C}_p}\underbrace{\begin{pmatrix}\boldsymbol{\varphi}_1\\ \dot{\boldsymbol{\varphi}}_1\\ \boldsymbol{\varphi}_2\end{pmatrix}}_{\mathbf{x}_p},\tag{4.33}$$

where the output matrix $\mathbf{C}_p$ is constant.

In summary, the state-space matrices defined using the physical basis $\mathbf{x}_p=\begin{pmatrix}\boldsymbol{\varphi}_1^\mathsf{T} & \dot{\boldsymbol{\varphi}}_1^\mathsf{T} & \boldsymbol{\varphi}_2^\mathsf{T}\end{pmatrix}^\mathsf{T}$ have the following structure:

$$\mathbf{A}_p=\begin{bmatrix}\mathbf{0}&\mathbf{I}&\mathbf{0}\\ \mathbf{A}_{21}&\mathbf{A}_{22}&\mathbf{A}_{23}\\ \mathbf{A}_{31}&\mathbf{A}_{32}&\mathbf{A}_{33}\end{bmatrix},\ \mathbf{B}_p=\begin{bmatrix}\mathbf{0}\\ \mathbf{B}_2\\ \mathbf{B}_3\end{bmatrix},\ \mathbf{C}_p=\begin{bmatrix}\mathbf{I}&\mathbf{0}&\mathbf{0}\\ \mathbf{0}&\mathbf{0}&\mathbf{I}\\ \mathbf{C}_{31}&\mathbf{C}_{32}&\mathbf{C}_{33}\end{bmatrix}.\tag{4.34}$$

The identified state-space model $[\widehat{\mathbf{A}},\widehat{\mathbf{B}},\widehat{\mathbf{C}}]$ is related to the physical state-space model $[\mathbf{A}_p,\mathbf{B}_p,\mathbf{C}_p]$ by the following relation:

$$\widehat{\mathbf{A}} = \mathbf{T}^{-1}\mathbf{A}_p\mathbf{T}, \quad \widehat{\mathbf{B}} = \mathbf{T}^{-1}\mathbf{B}_p, \quad \widehat{\mathbf{C}} = \mathbf{C}_p\mathbf{T}, \tag{4.35}$$

where $\mathbf{T}$ denotes a transformation matrix that can convert the algorithmically chosen state basis $\mathbf{x}$ to the physical basis $\mathbf{x}_p$ through:

$$\mathbf{x}_p = \mathbf{T}\mathbf{x}. \tag{4.36}$$

Substituting Eq. (4.34) into Eq. (4.35) yields the following relations:

$$\begin{gathered}
\begin{bmatrix}\mathbf{T}_1\\ \mathbf{T}_2\\ \mathbf{T}_3\end{bmatrix}\widehat{\mathbf{A}} = \begin{bmatrix}\mathbf{0} & \mathbf{I} & \mathbf{0}\\ \mathbf{A}_{21} & \mathbf{A}_{22} & \mathbf{A}_{23}\\ \mathbf{A}_{31} & \mathbf{A}_{32} & \mathbf{A}_{33}\end{bmatrix}\begin{bmatrix}\mathbf{T}_1\\ \mathbf{T}_2\\ \mathbf{T}_3\end{bmatrix} \Rightarrow \mathbf{T}_2 = \mathbf{T}_1\widehat{\mathbf{A}},\\
\begin{bmatrix}\mathbf{T}_1\\ \mathbf{T}_2\\ \mathbf{T}_3\end{bmatrix}\widehat{\mathbf{B}} = \begin{bmatrix}\mathbf{0}\\ \mathbf{B}_2\\ \mathbf{B}_3\end{bmatrix} \Rightarrow \mathbf{T}_1\widehat{\mathbf{B}} = 0,\\
\begin{bmatrix}\widehat{\mathbf{C}}_1\\ \widehat{\mathbf{C}}_2\\ \widehat{\mathbf{C}}_3\end{bmatrix} = \begin{bmatrix}\mathbf{I} & \mathbf{0} & \mathbf{0}\\ \mathbf{0} & \mathbf{0} & \mathbf{I}\\ \mathbf{C}_{31} & \mathbf{C}_{32} & \mathbf{C}_{33}\end{bmatrix}\begin{bmatrix}\mathbf{T}_1\\ \mathbf{T}_2\\ \mathbf{T}_3\end{bmatrix} \Rightarrow \mathbf{T}_1 = \widehat{\mathbf{C}}_1, \mathbf{T}_3 = \widehat{\mathbf{C}}_2,
\end{gathered} \tag{4.37}$$

from which one can extract the transformation matrix $\mathbf{T}$:

$$\mathbf{T} = \begin{bmatrix}\widehat{\mathbf{C}}_1\\ \widehat{\mathbf{C}}_1\widehat{\mathbf{A}}\\ \widehat{\mathbf{C}}_2\end{bmatrix}, \tag{4.38}$$

and an implicit constraint:

$$\widehat{\mathbf{C}}_1\widehat{\mathbf{B}} = 0, \tag{4.39}$$

which are both expressed in terms of the blocks of the estimated state-space matrices. To satisfy strict state-basis coherency (Eq. (4.13)), the transformation matrix $\mathbf{T}$ must remain the same for all local models, leading to the following constrained nonlinear programming problem:

$$\mathbf{A}_{opt}, \mathbf{B}_{opt}, \mathbf{C}_{3,opt} = \arg \min_{\mathbf{A},\mathbf{B},\mathbf{C}_3} \sum_{k=1}^{q} \left\| \mathbf{K}(i\omega_k) - \begin{bmatrix} \widehat{\mathbf{C}}_{1,ref} \\ \widehat{\mathbf{C}}_{2,ref} \\ \mathbf{C}_3 \end{bmatrix} (i\omega_k \mathbf{I} - \mathbf{A})^{-1} \mathbf{B} \right\|_F^2 ,$$
$$\text{such that} \begin{cases} \widehat{\mathbf{C}}_{1,ref}\mathbf{A} = \widehat{\mathbf{C}}_{1,ref}\widehat{\mathbf{A}}_{ref} \\ \widehat{\mathbf{C}}_{1,ref}\mathbf{B} = 0, \end{cases} \tag{4.40}$$
$$\text{with the initial guess of } [\mathbf{A},\mathbf{B},\mathbf{C}_3] \text{ as } [\widehat{\mathbf{A}}_{ref},\widehat{\mathbf{B}}_{ref},\widehat{\mathbf{C}}_{3,ref}].$$

In this problem, $\mathbf{K}(i\omega_k)$ is an augmented frequency response samples matrix, which takes the platform velocity $\dot{\boldsymbol{\xi}}$ as input and outputs the potentials $\boldsymbol{\varphi}_1$, $\boldsymbol{\varphi}_2$, and the wave radiation force $\mathbf{F}_r$. $[\widehat{\mathbf{A}}_{ref},\widehat{\mathbf{B}}_{ref},\widehat{\mathbf{C}}_{ref}]$ is the state-space model identified at a reference platform position, which is used to provide an initial guess for the optimization iteration, as well as to define a transformation matrix $\mathbf{T}$ that remains unchanged for the optimization of state-space models at each platform position. The solution $[\mathbf{A}_{opt},\mathbf{B}_{opt},\mathbf{C}_{opt}]$ obtained for each platform position is thus related to the corresponding physical state-space model $[\mathbf{A}_p,\mathbf{B}_p,\mathbf{C}_p]$ through a fixed transformation $\mathbf{T}$. According to Eq. (4.36), this ensures strict state-basis coherency and hence guarantees that the interpolation of a set of $[\mathbf{A}_{opt},\mathbf{B}_{opt},\mathbf{C}_{opt}]$ models yields the same input-output behaviour as the original physical LPV system.

4.2.3 Grid-based LPV interpolation

The grid-based LPV modelling framework proposed in this work to capture the geometrically nonlinear wave-radiation dynamics caused by large platform motions are summarized in Fig. 4.5. The platform is constrained to planar movements, specifically in the surge (ξ_1), heave (ξ_3) and pitch (ξ_5) DoFs. Given that the wave radiation frequency response function $\mathbf{K}_r$ remains unchanged for pure surge motion (ξ_1), only heave displacement (ξ_3) and pitch rotation (ξ_5) are selected as the scheduling parameters $\mathbf{p}$ for the LPV system.

In the black-box LPV modelling approach, independent state-space **identification** is performed on the wave radiation frequency response samples calculated at each linearized platform position $\mathbf{p}_i = (\xi_3, \xi_5)$, as illustrated in Fig. 4.5(a). The locally identified state-space model, denoted as $[\widehat{\mathbf{A}}_i,\widehat{\mathbf{B}}_i,\widehat{\mathbf{C}}_i]$ ($i = 1,2,\ldots,N_p$), each undergoes a balanced **transformation** $\mathbf{T}_{b,i}$ followed by the basis correction algorithm, ensuring relaxed basis coherency, as discussed in Section 4.2.2.2. The resulting coherent state-space models $[\mathbf{A}_{b,i},\mathbf{B}_{b,i},\mathbf{C}_{b,i}]$ are then organized into an **interpolation** array based on the grid points of $\mathbf{p}_i$ ($i = 1,2,\ldots,N_p$), as shown in Fig. 4.5(a). For the gray-box LPV modelling approach, which utilizes the newly proposed physical basis, the **identification** step only involves a reference state-space model to initialize the subsequent **optimization**. By solving the nonlinear programming problem defined in Eq. (4.40) at each grid point of platform position $\mathbf{p}_i$ $(i = 1, 2, \ldots, N_p)$, local state-space models with a strictly coherent basis, denoted as $[\mathbf{A}_{opt,i}, \mathbf{B}_{opt,i}, \mathbf{C}_{opt,i}]$, are organized into an **interpolation** array, as shown in Fig. 4.5(b).

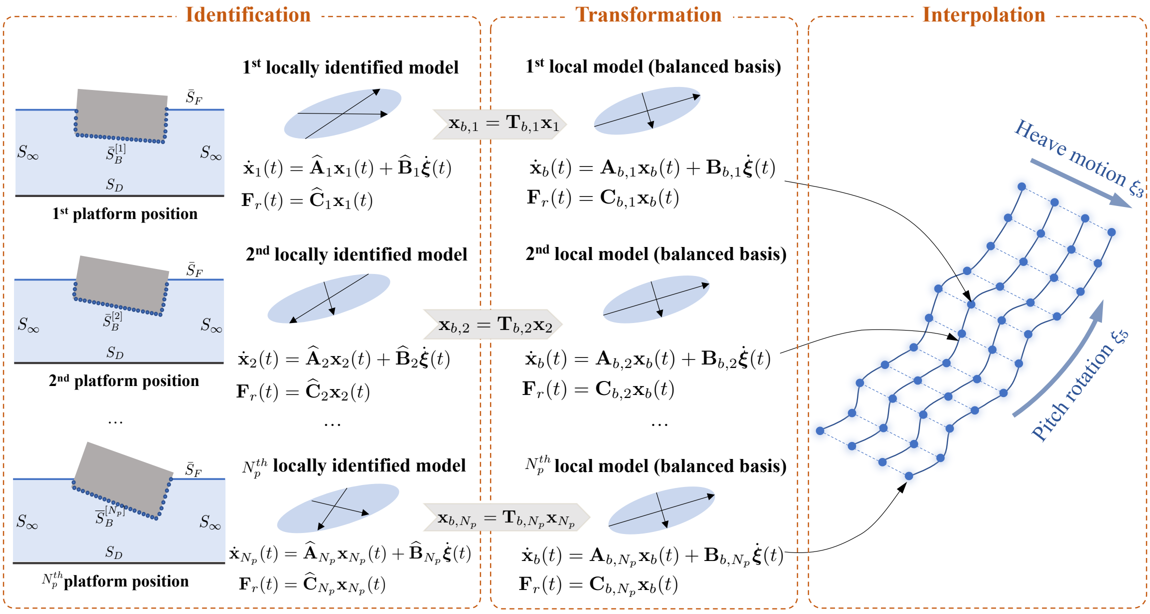

(a) Black-box balanced basis

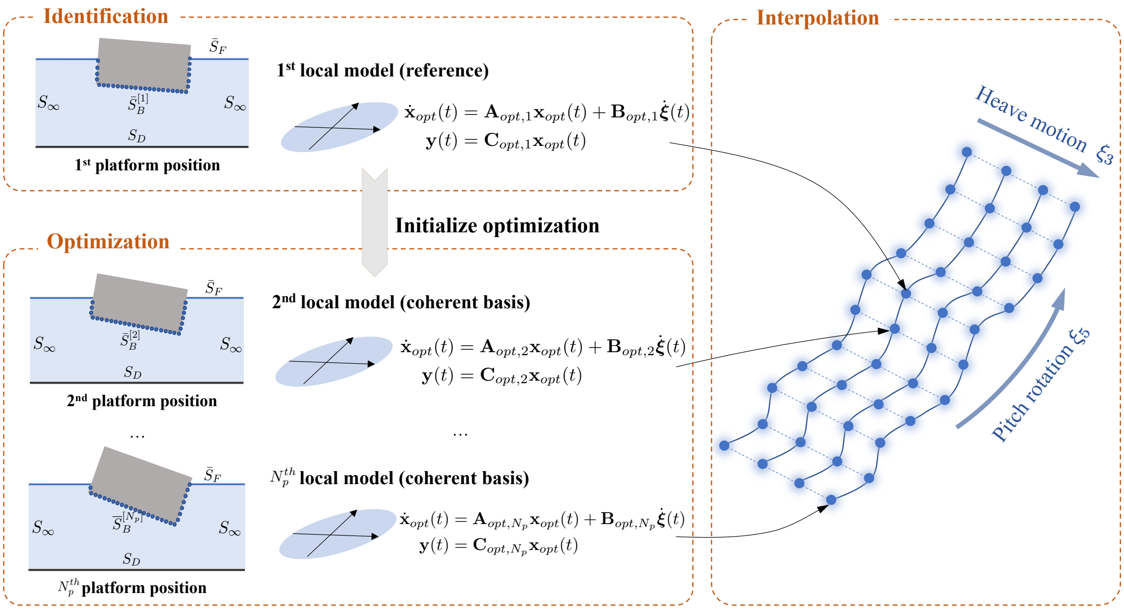

(b) Gray-box (optimized) physical basis

Fig. 4.5 Grid-based linear parameter-varying modelling approach.

4.3 Code verification: van Daalen 2D cylinder

The black-box and gray-box LPV modelling approaches described in Section 4.2 are validated using the van Daalen benchmark model [128]. This benchmark model consists of a 2D rectangular cylinder that freely oscillates on the still water surface in a numerical wave tank, starting from an initial rotation angle θ_0. The geometry of the floating cylinder and the numerical wave tank is depicted in Fig. 4.6. The gravity center of the cylinder is fixed at the origin O, which restricts its motion to rotation only around the y-axis. Environmental parameters and mechanical properties of the cylinder are also listed in Fig. 4.6. Non-reflecting far-field boundary conditions are applied on the left and right walls of the numerical tank.

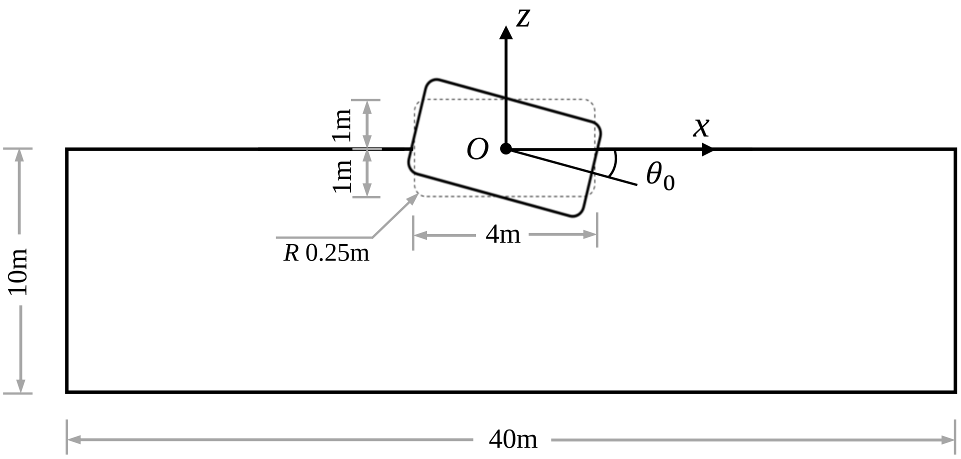

Environmental parameters
Gravity constant g = 9.81 m/s^2 Water density ρ = 1000 kg/m^3
Cylinder properties
Mass m_v = 3973.15 kg Moment of inertia around y axis I_v = 6541.12 kg·m^2

Fig. 4.6 Freely oscillating 2D van Daalen cylinder in a numerical wave tank.

In the work of van Daalen [128], the geometrically nonlinear wave radiation effects due to large cylinder rotations are evaluated using a body-nonlinear potential solver. This solver handles the wave-body interaction BVP at each time step on the instantaneous wetted body surface $S_B(t)$ and the mean free surface $\overline{S}_F$, and calculates the hydrostatic forces over $S_B(t)$. These assumptions correspond to **Level 3** in Fig. 4.1. The obtained nonlinear cylinder responses from [128] provide a reliable reference for assessing the accuracy and performance of the proposed black-box and gary-box LPV modelling approaches.

4.3.1 Nonlinear water-cylinder interaction system

The nonlinear EoM that couples the fluid subsystem with the rigid-body dynamics of the floating cylinder in the rotation DoF can be expressed as follows:

$$I_v \ddot{\theta}(t) = \int_{S_B(t)} \left[-\rho \left(\frac{\partial \Phi}{\partial t} + \frac{1}{2} |\nabla \Phi|^2 + gz \right) \right] \cdot (\mathbf{r} \times \mathbf{n}) \, dS, \tag{4.41}$$

where I_v denotes the moment of inertia of the cylinder, θ the cylinder's rotation angle, ρ the fluid density, $\Phi(x,z,t)$ the potential function of the fluid domain, g the gravity constant, $\mathbf{r}$ the position vector of a point on the wetted body surface S_B, and $\mathbf{n}$ the normal vector pointing outward from the fluid domain. In van Daalen's work [128], the potential function Φ at time t is solved from the water-cylinder interaction BVP defined on the wetted surface $S_B(t)$. Using the solution for Φ at t, the cylinder's rotation angle and the corresponding wetted surface S_B at the next time step $t+dt$ can be determined from Eq. (4.41). This iterative approach enables accurate calculation of the geometrically nonlinear effects caused by the time-varying wetted body surface during cylinder oscillations.

The free oscillations of the 2D cylinder, calculated from the nonlinear EoM by van Daalen [128], are presented in Fig. 4.7 for three different initial rotation angles, θ_0. For the purpose of comparison, the response amplitudes are normalized by their respective θ_0 values. The primary observations from Fig. 4.7 are that the oscillation period of the cylinder decreases as θ_0 increases, and the responses decay slightly faster for higher θ_0 values. These findings suggest that the nonlinear effects become more pronounced with larger cylinder rotations. The trends will be used to verify the proposed LPV modelling approaches in the subsequent subsections.

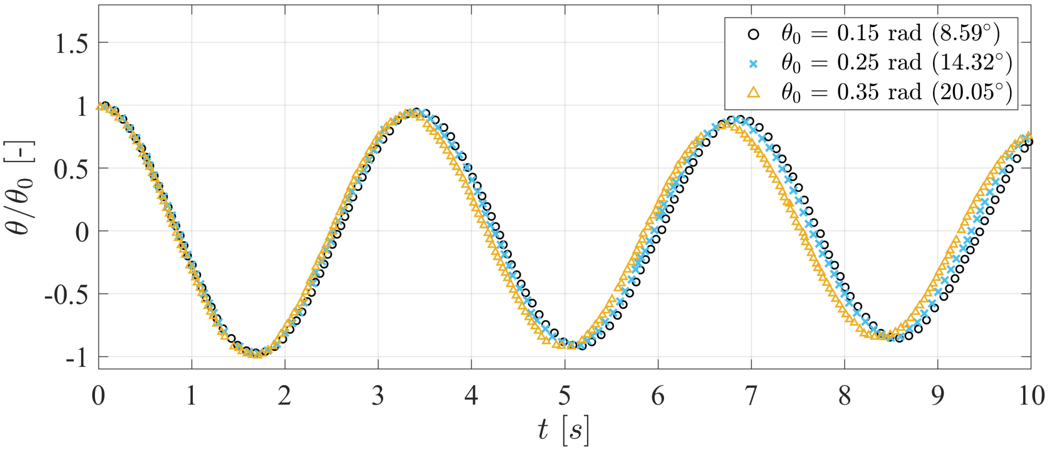

Fig. 4.7 Normalized responses of the 2D floating cylinder under three different initial rotations of 0.15, 0.25, and 0.35 rad reproduced from van Daalen [128].

4.3.2 LPV modelling of the van Daalen cylinder

The grid-based LPV modelling methodology proposed in Section 4.2 is applied to the van Daalen 2D cylinder to evaluate its effectiveness in capturing the geometrically nonlinear dynamics. A set of rotation angles θ_i $(i = 1, 2, \ldots, N_i)$ is selected as grid points, around which the nonlinear water-cylinder BVP is linearized. The EoM for the i^{th} local linear model can be formulated as follows:

$$[I_v + \lambda_{\infty,i}]\,\ddot{\theta}(t) = F_{b,i}(t) - F_{r,i}(t), \tag{4.42}$$

where $\lambda_{\infty,i}$ denotes the infinite-frequency added mass for the i^{th} local model, $F_{b,i}$ the dynamic buoyancy force, and $F_{r,i}$ the wave radiation damping force. According to Section 2.2.1, the wave radiation damping force $F_{r,i}$ can be calculated in two ways: (1) using the convolution integral expressed as follows:

$$F_{r,i}(t) = \int_0^t k_{r,i}(t-\tau)\dot{\theta}(\tau)d\tau, \tag{4.43}$$

where $k_{r,i}(t)$ is the impulse response function determined at the i^{th} rotation angle, and (2) using the following state-space model:

$$\begin{cases} \dot{\mathbf{x}}_i(t) = \widehat{\mathbf{A}}_i\mathbf{x}_i(t) + \widehat{\mathbf{B}}_i\dot{\theta}(t) \\ F_{r,i}(t) = \widehat{\mathbf{C}}_i\mathbf{x}_i(t), \end{cases} \tag{4.44}$$

where the state-space matrices $[\widehat{\mathbf{A}}_i, \widehat{\mathbf{B}}_i, \widehat{\mathbf{C}}_i]$ are identified from the wave-radiation frequency response samples $K_{r,i}(i\omega_k)$, as outlined in Section 4.2.1. The EoM described in Eq. (4.42) is only valid within the immediate vicinity of the i^{th} cylinder rotation angle θ_i. In this subsection, the rotation-dependence of key parameters — the infinite-frequency added mass $\lambda_{\infty,i}$, dynamic buoyancy $F_{b,i}$, and wave radiation damping force $F_{r,i}$ — is first analyzed. They are then incorporated into the dynamic analysis of the cylinder through direct interpolations.

Interpolating the wave radiation damping force $F_{r,i}$ using the state-space representation requires addressing the state-basis incoherency issue, as detailed in Section 4.2.2.1. To overcome this challenge, both the black-box and gray-box LPV modelling approaches proposed in this work are implemented to ensure basis coherency across all grid points θ_i $(i = 1, 2, \ldots, N_i)$. While the convolution integral (Eq. (4.43)) is computationally less efficient compared to the state-space representation (Eq. (4.44)), it is inherently free from the basis-incoherency issue. As such, the nonlinear convolution integral method, featuring the interpolation of impulse response functions $k_{r,i}$, is used as a benchmark in the nonlinear analysis of the van Daalen cylinder to evaluate the performance of the proposed LPV modelling approaches.

4.3.2.1 Local linear models

A series of rotation angles θ_i in the range of $[-30^\circ, 30^\circ]$, with an interval of 0.5°, are selected to calculate the local linear models for the van Daalen cylinder. The 2D BEM code described in Section 3.4 is adopted. It reformulates the wave-platform BVP (Eq. (3.7)) linearized at a specific cylinder rotation into boundary integral equations, from which a system of linear algebraic equations are obtained after the boundary discretization. The virtual far-field boundaries are placed at -50 m and 50 m on the left and right sides, respectively. A mesh size of 0.01 m is used for the wetted body surface to ensure accurate force coefficients solution, while a coarser mesh size of 0.1 m is used for all other boundaries to reduce computational costs.

Fig. 4.8 illustrates the variation of the infinite-frequency added mass λ_∞ and dynamic buoyancy force F_b with the grid point of rotation θ_i. It can be observed that as the cylinder rotates, these values undergo significant changes compared to those at the equilibrium position ($\theta = 0$). The most notable variation occurs in the infinite-frequency added mass λ_∞ when $|\theta|$ exceeds 24°, as shown in Fig. 4.8. This abrupt change is attributed to the sudden alteration of the submerged geometry of the cylinder as θ increases from 20° to 30°, with the bottom left corner of the body crossing over the free-surface, as shown in Fig. 4.9.

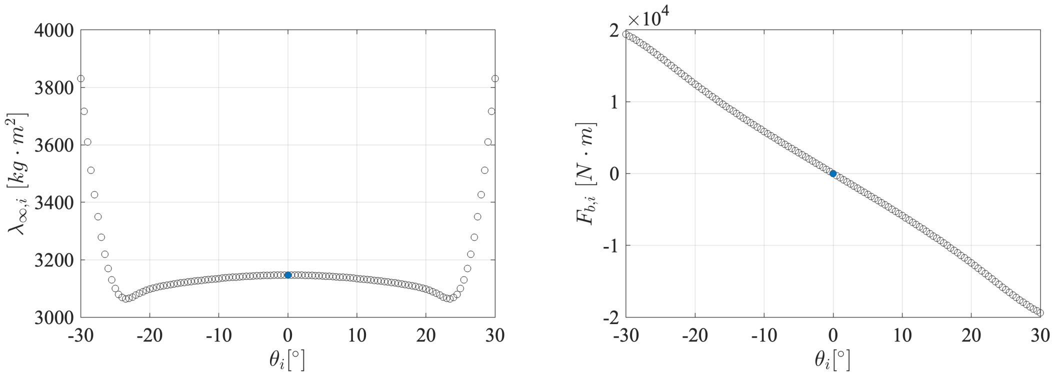

Fig. 4.8 Variation of infinite-frequency added mass (λ_∞) and dynamic buoyancy force (F_b) with the rotation angle ranging $-30^\circ \sim 30^\circ$. The filled dots represent the values calculated at the equilibrium position ($\theta = 0^\circ$).

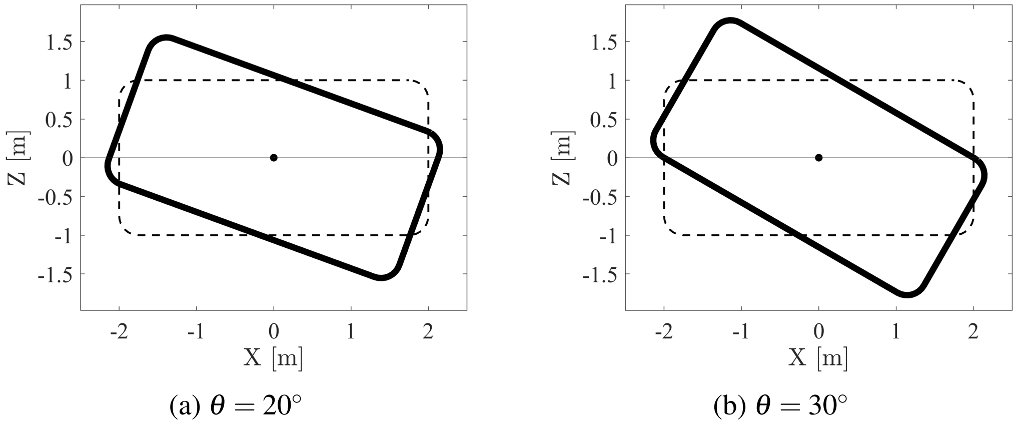

(a) $\theta = 20°$ (b) $\theta = 30°$

Fig. 4.9 Comparison of the van Daalen cylinder submergence at 20° and 30°.

For this preliminary investigation of the LPV modelling approach, the cylinder's rotation is restricted to a moderate range of $[-20°, 20°]$ selected from the original grid points, to avoid abrupt changes that could pose challenges to the LPV interpolation process. This range of rotation angles results in a total of 81 local linear BVPs. Fig. 4.10 illustrates the variation of the wave radiation impulse response $k_r(t)$ and frequency response $K_r(i\omega)$ samples as functions of the rotation angle θ_i. Again, notable changes can be observed compared to the values at the equilibrium position ($\theta = 0°$). Additionally, both Fig. 4.8 and Fig. 4.10 demonstrate symmetry for positive and negative rotation angles. The observed variations in the additional inertia, hydrostatic, and radiation damping properties, even for small changes in rotation angle, are expected to influence the overall cylinder dynamics. This underscores the importance of accurately capturing these geometrically nonlinear effects to ensure the reliability of the LPV model.

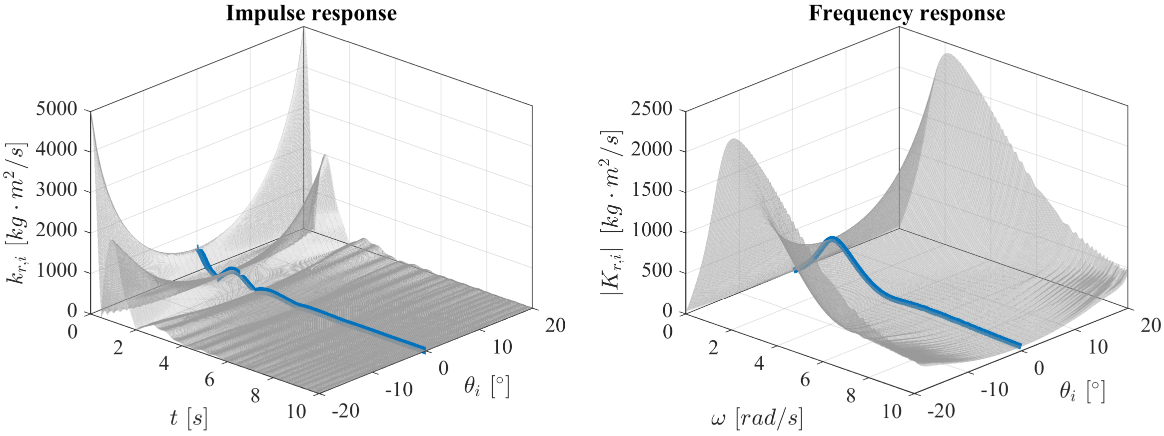

Fig. 4.10 Variation of wave radiation impulse response ($k_r(t)$) and frequency response amplitude ($|K_r(i\omega)|$) with the rotation angles of $-20° \sim 20°$. The thick blue curves represent the values calculated at the equilibrium position ($\theta = 0°$).

4.3.2.2 Black-box LPV modelling

The **identification-transformation-interpolation** procedure of the black-box LPV modelling framework, as illustrated in Fig. 4.5(a), is applied to the van Daalen floating cylinder. Each step of this procedure is detailed in this subsection, and the resulting free oscillations of the cylinder under various initial rotation angles are compared against the benchmark results shown in Fig. 4.7 from [128] to verify the accuracy of the proposed LPV modelling approach.

The local linear state-space models corresponding to 81 grid points of the cylinder rotation angle θ_i are identified independently from their frequency response samples using the N4SID algorithm, as described in Section 4.2.1. Fig. 4.11 presents the identification results for three example rotation angles: 0°, 10° and 20°. The fitting quality is compared for three different state numbers ($n = 2,4,6$). It can be found that the 4-state model sufficiently captures the dominant resonance behaviour of the wave radiation effect for each local linear model. Therefore, a state number of 4 is chosen for the subsequent black-box LPV modelling to ensure both accuracy and computational efficiency.

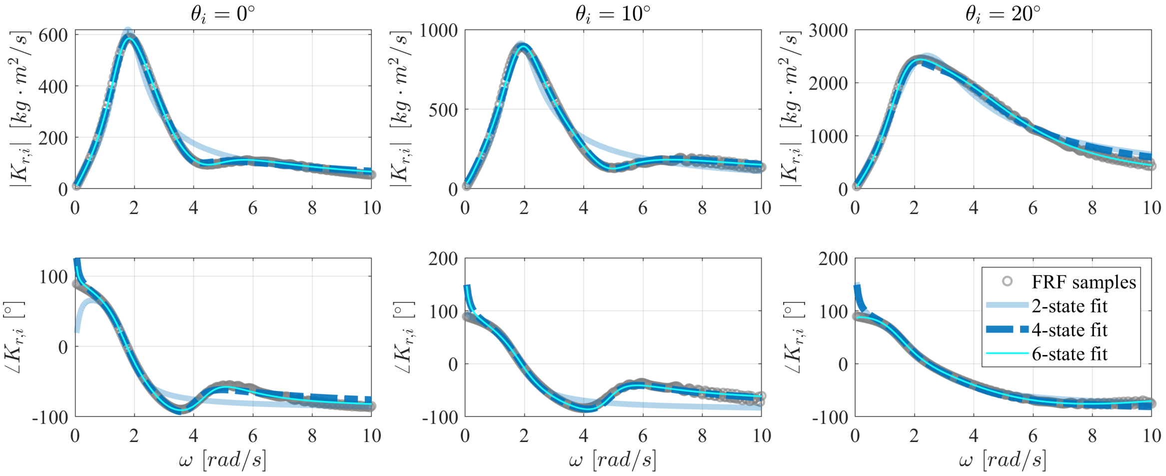

Fig. 4.11 Comparison of the amplitude ($|K_r(i\omega)|$) and phase angle ($\angle K_r(i\omega)|$) of the frequency response functions (FRF) calculated from the BEM code for three rotation angles (0°, 10° and 20°) and the estimated wave radiation state-space models using three different numbers of states ($n = 2,4,6$).

The location of system poles in the real-imaginary plane provides important information about the dynamic characteristics of a linear state-space system. Therefore, the poles of the 81 local state-space models $[\widehat{\mathbf{A}}_i, \widehat{\mathbf{B}}_i, \widehat{\mathbf{C}}_i]$ ($i = 1,2,\ldots,81$) are investigated to illustrate the geometrically nonlinear effects of the wave-radiation problem. The eigenvalue decomposition is applied to each identified system matrix $\widehat{\mathbf{A}}_i$ to obtain the corresponding system poles for each rotation angle θ_i. The evolution of these poles as θ_i varies from $-20°$ and 20° is shown in Fig. 4.12. The 4-state model features 2 complex conjugate pairs of poles that capture the two resonance peaks at around 2 rad/s and approximately 6 $\sim$ 8 rad/s, as illustrated in the example frequency response samples for $\theta_i = 0^\circ$ and 10° in Fig. 4.11. As the absolute value of θ_i increases from 0° to 19°, the 2 pairs of poles gradually move away from the imaginary axis, indicating an increase in both the natural frequencies and damping ratios of the wave radiation process. However, when $|\theta_i|$ reaches 19.5°, the poles begin to shift back towards the imaginary axis, with a noticeable change at $\theta_i = 20^\circ$. This shift corresponds to a fundamental change in the frequency responses, as shown in Fig. 4.11, where only one predominant resonance peak is observed at $\theta_i = 20^\circ$. These observations highlight the nonlinear nature of the wave radiation dynamic process when the floating cylinder undergoes large rotation angles and their impact on the system's dynamic characteristics.

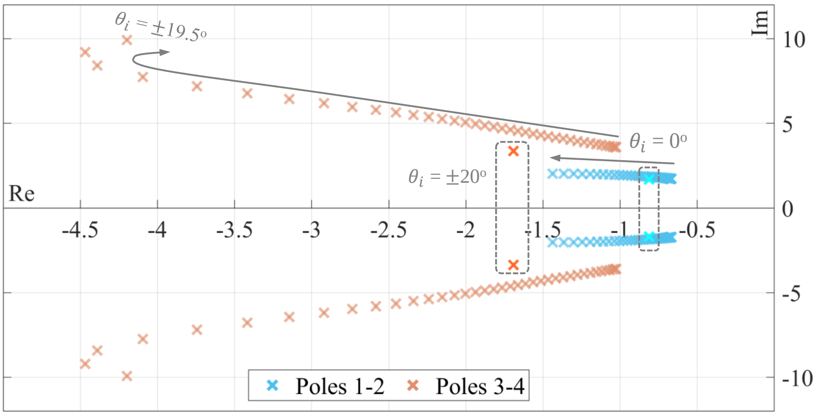

Fig. 4.12 The evolution of poles with the cylinder rotation angles θ_i between -20° to 20°.

The abrupt change in the poles' locations at $\theta_i = \pm 20^\circ$ can potentially lead to instability in the LPV interpolation. Therefore, these outliers are discarded to ensure model stability and consistency. To automate the detection of outliers, a technique based on the Modal Assurance Criterion (MAC) is proposed in this work. The MAC provides a measure of similarity between two mode shapes, with MAC=1 indicating identical mode shapes and MAC close to 0 indicating very different mode shapes. Taking the mode shapes corresponding to the equilibrium position, $\boldsymbol{\psi}_0$, as a reference, the MAC values evaluating the similarity between $\boldsymbol{\psi}_0$ and the mode shapes $\boldsymbol{\psi}_i$ at all rotation angles θ_i can be calculated as follows:

$$\mathrm{MAC}\{\boldsymbol{\psi}_0, \boldsymbol{\psi}_i\} = \frac{\left|\boldsymbol{\psi}_0^H \boldsymbol{\psi}_i\right|^2}{\left(\boldsymbol{\psi}_0^H \boldsymbol{\psi}_0\right)\left(\boldsymbol{\psi}_i^H \boldsymbol{\psi}_i\right)}, \tag{4.45}$$

where $()^H$ denotes the conjugate transpose. The resulting MAC matrix for the 4-state model across 81 rotation angles θ_i is presented in Fig. 4.13. The MAC is shown to successfully detect the extremes $\theta_i = \pm 20^\circ$ at which the MAC values are much smaller than 1, implying that their mode shapes are distinct from the reference. The performance of the subsequent LPV interpolation is susceptible to this abrupt mode-shape change. To focus on the LPV implementation and simplify the discussion, this extreme angle of $\pm 20^\circ$ and the corresponding state-space models are excluded from the interpolation array in this work.

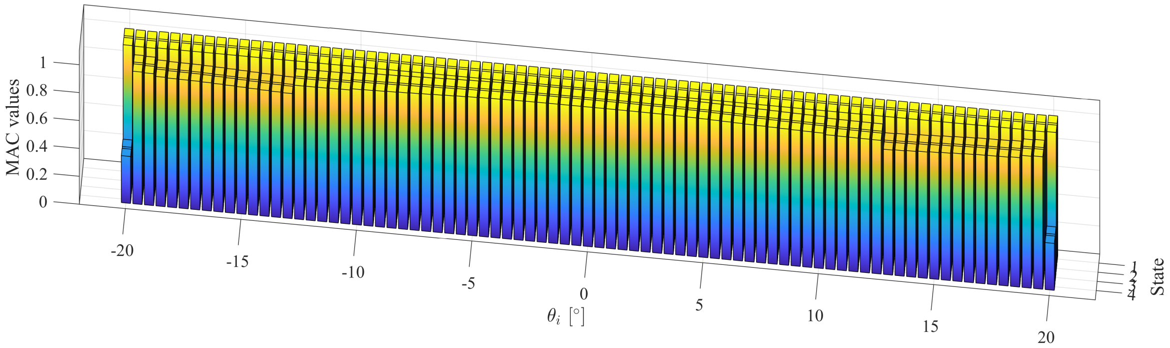

Fig. 4.13 MAC values for different cylinder rotation angles $\theta_i = -20^\circ \sim 20^\circ$.

As mentioned in Section 4.2.2.1, the identified state-space models $[\widehat{\mathbf{A}}_i, \widehat{\mathbf{B}}_i, \widehat{\mathbf{C}}_i]$ $(i = 2, 3, \ldots, 80)$ typically have different state bases. To ensure basis-coherency for reliable LPV interpolation, they are transformed onto the balanced basis, according to the proposed black-box LPV modelling approach described in Section 4.2.2.2. The eigenvalues of the product of the controllability and observability Gramians, $\mathscr{W}_c \mathscr{W}_o$, for rotation angles between -19.5° to 19.5° are shown in Fig. 4.14. The four distinct eigenvalues vary smoothly with the cylinder rotation, indicating that the balanced basis is theoretically unique up to sign changes. In practice, state-swapping can also occur between different identified models. Both the sign changes and state swap should be corrected to ensure coherency across all local models.

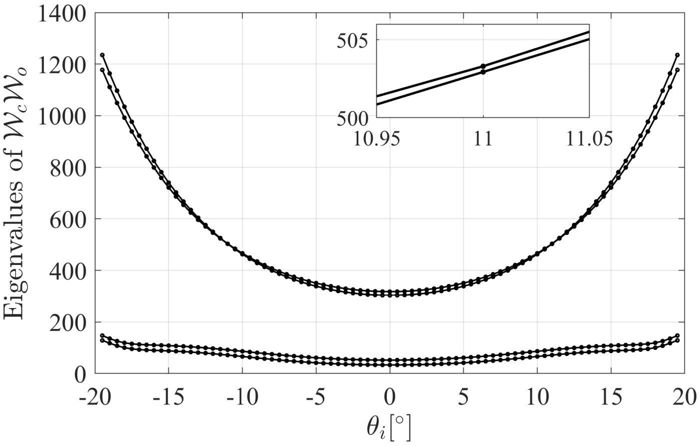

Fig. 4.14 Eigenvalues of the products of Gramians as θ_i varies between -19.5° and 19.5°.

The automatic basis correction method proposed in Eq. (4.21) is implemented. For example, consider two adjacent models at rotation angles $\theta_{17} = -11.5^\circ$ and $\theta_{18} = -11^\circ$. The state-space matrices for these two models, which have been transformed to the balanced form, are listed as follows:

$$\mathbf{A}_{b,17} = \begin{bmatrix} 0.000 & 1.929 & 0.001 & 0.004 \\ -1.929 & -1.289 & -0.392 & -1.530 \\ 0.001 & 0.392 & -0.111 & -5.627 \\ -0.004 & -1.530 & 5.627 & -4.170 \end{bmatrix}, \mathbf{B}_{b,17} = \begin{bmatrix} -0.074 \\ -36.753 \\ 4.581 \\ -24.915 \end{bmatrix}, \mathbf{C}_{b,17} = \begin{bmatrix} 0.074 \\ -36.753 \\ -4.581 \\ -24.915 \end{bmatrix}^{\mathsf{T}}, \tag{4.46}$$

$$\mathbf{A}_{b,18} = \begin{bmatrix} -1.254 & -1.916 & 0.400 & -1.488 \\ 1.916 & 0.000 & 0.000 & -0.001 \\ -0.400 & 0.000 & -0.117 & 5.511 \\ -1.488 & 0.001 & -5.511 & -4.044 \end{bmatrix}, \mathbf{B}_{b,18} = \begin{bmatrix} 35.524 \\ -0.020 \\ 4.634 \\ 24.095 \end{bmatrix}, \mathbf{C}_{b,18} = \begin{bmatrix} 35.524 \\ 0.020 \\ -4.634 \\ 24.095 \end{bmatrix}^{\mathsf{T}}, \tag{4.47}$$

Substituting them into Eq. (4.21), the similarity transformation matrix $\widetilde{\mathbf{T}}_{b,17/18}$ can be calculated as follows:

$$\widetilde{\mathbf{T}}_{b,17/18} = \begin{bmatrix} -0.005 & -0.999 & 0.000 & 0.003 \\ -0.999 & -0.005 & -0.006 & 0.000 \\ 0.006 & 0.001 & 0.999 & -0.005 \\ -0.001 & 0.004 & 0.006 & -0.999 \end{bmatrix}, \tag{4.48}$$

whose entries are close to 0 and ±1, and it can be rounded off to the following matrix:

$$\mathbf{T}_{b,17/18} = \begin{bmatrix} 0 & -1 & 0 & 0 \\ -1 & 0 & 0 & 0 \\ 0 & 0 & 1 & 0 \\ 0 & 0 & 0 & -1 \end{bmatrix}. \tag{4.49}$$

This matrix indicates the changes in the state basis from the model at θ_{17} to the model at θ_{18}. Specifically, it shows that the first two states are swapped and their signs are changed, and the sign of the fourth state is also changed. With the transformation matrix $\mathbf{T}_{b,17/18}$, the model $[\mathbf{A}_{b,18}, \mathbf{B}_{b,18}, \mathbf{C}_{b,18}]$ can be converted to the following form with entries similar to those of the model $[\mathbf{A}_{b,17}, \mathbf{B}_{b,17}, \mathbf{C}_{b,17}]$ presented in Eq. (4.46):

$$\widetilde{\mathbf{A}}_{b,18} = \begin{bmatrix} -0.000 & 1.916 & -0.000 & -0.001 \\ -1.916 & -1.254 & -0.400 & -1.488 \\ -0.000 & 0.400 & -0.117 & -5.511 \\ 0.001 & -1.488 & 5.511 & -4.044 \end{bmatrix}, \widetilde{\mathbf{B}}_{b,18} = \begin{bmatrix} 0.020 \\ -35.524 \\ 4.634 \\ -24.095 \end{bmatrix}, \widetilde{\mathbf{C}}_{b,18} = \begin{bmatrix} -0.020 \\ -35.524 \\ -4.634 \\ -24.095 \end{bmatrix}^{\mathsf{T}}. \tag{4.50}$$

Fig. 4.15 compares the variation of each entry in the state-space models $[\mathbf{A}_{b,i}, \mathbf{B}_{b,i}, \mathbf{C}_{b,i}]$ ($i = 2, 3, \ldots, 80$) with cylinder rotation angles θ_i before and after the basis correction. It is evident that the state-space matrices prior to correction exhibit abrupt jumps due to the sign changes and state swapping, which can cause instability in the subsequent LPV interpolation. Applying the basis correction technique (Eq. (4.21)) consecutively to two adjacent state-space models $[\mathbf{A}_{b,i}, \mathbf{B}_{b,i}, \mathbf{C}_{b,i}]$ and $[\mathbf{A}_{b,i+1}, \mathbf{B}_{b,i+1}, \mathbf{C}_{b,i+1}]$ with i varying from 2 to 79, all local models are transformed to the basis used in the model $[\mathbf{A}_{b,2}, \mathbf{B}_{b,2}, \mathbf{C}_{b,2}]$. Consequently, a smooth and continuous variation of each matrix entry is achieved, as shown in Fig. 4.15, indicating successful alignment of all local models across the entire range of rotation angles. As the transformation matrix changes with i, this technique only guarantees relaxed state coherency as defined in Eq. (4.14).

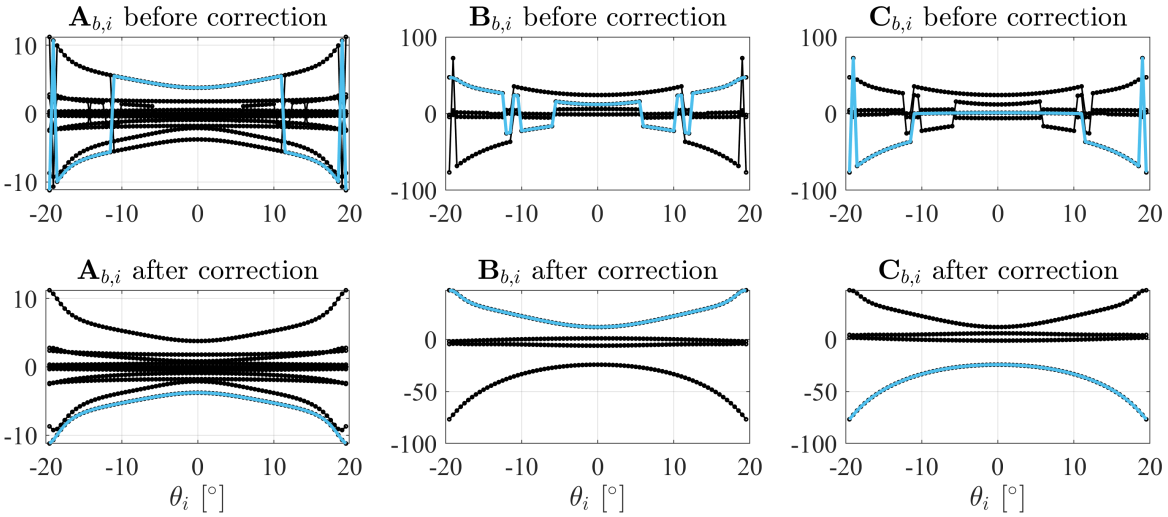

Fig. 4.15 Variation of entries in the state-space matrices $[\mathbf{A}_{b,i}, \mathbf{B}_{b,i}, \mathbf{C}_{b,i}]$ with θ_i varying between $-19.5°$ to $19.5°$. One example entry is highlighted for each of the three matrices.

The grid-based LPV interpolation is implemented in Simulink for the van Daalen floating cylinder. Its framework as well as visualization are presented in Fig. 4.16. The gravity center of the cylinder is connected to the world frame on the water surface via a `Revolute Joint`, which only allows rotational motion. The rotation angle θ, angular velocity $\dot{\theta}$, and angular acceleration $\ddot{\theta}$ are measured from this joint. Simulink `1D Lookup Table` blocks are used to describe the variation of the dynamic buoyancy force $F_{b,i}$ and infinite-frequency added mass $\lambda_{\infty,i}$ over the range of rotation angles θ_i from $-19.5°$ to $19.5°$, as shown in Fig. 4.8. The local state-space models with corrected balanced basis, as presented in Fig. 4.15, are pre-specified in the `LPV System` block at corresponding θ_i. During the simulation, linear interpolation is implemented to determine the instantaneous values of F_b, λ_∞, and the state-space matrices $[\mathbf{A}_b, \mathbf{B}_b, \mathbf{C}_b]$ based on the current rotation angle θ. The additional inertia effect is computed by multiplying λ_∞ with the acceleration $\ddot{\theta}$. The interpolated state-space model $[\mathbf{A}_b, \mathbf{B}_b, \mathbf{C}_b]$ receives the velocity $\dot{\theta}$ as input to calculate the wave radiation damping force F_r.

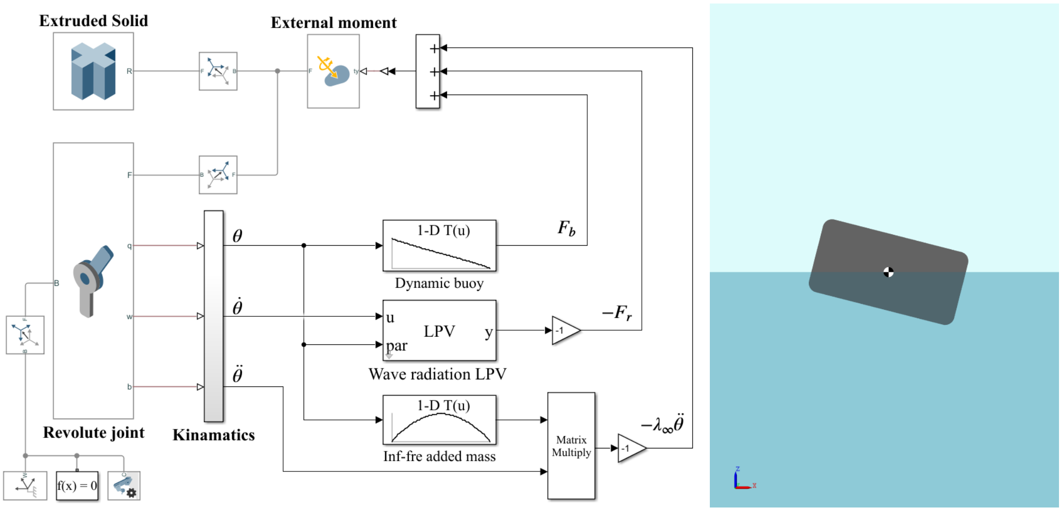

(a) Simulink framework (b) Visualization

Fig. 4.16 The LPV modelling for the van Daalen cylinder in Simulink.

Free oscillation tests of the van Daalen floating cylinder under different initial rotation angles θ_0 are simulated using the Simulink LPV model, as illustrated in Fig. 4.16. The normalized rotational responses θ/θ_0 for initial angles of 0.15 rad, 0.25 rad and 0.35 rad are presented in Fig. 4.17. Compared to van Daalen's nonlinear BEM simulation results shown in Fig. 4.7, a similar trend of decreased oscillation period and increased damping with increasing θ_0 is observed, indicating that the proposed LPV black-box model effectively captures the general nonlinear behaviour of the water-cylinder system.

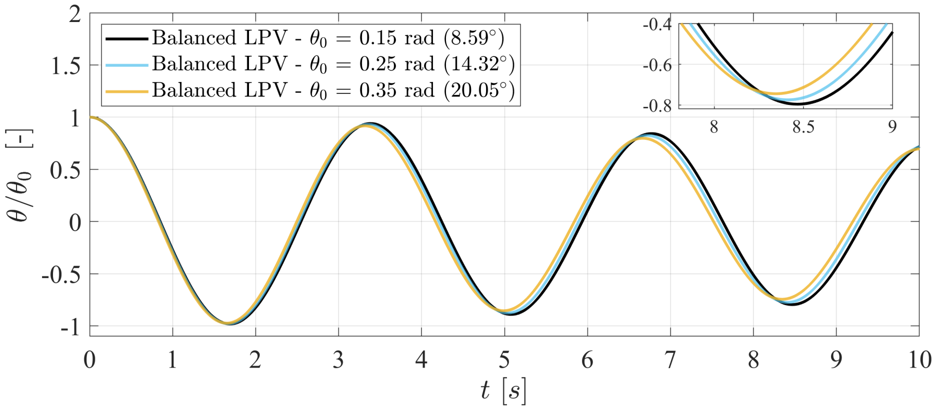

Fig. 4.17 Normalized rotational responses of the van Daalen floating cylinder under three different initial rotation angles of 0.15, 0.25, and 0.35 rad simulated by the Simulink black-box LPV model.

However, it is worth mentioning that the absolute values of the Simulink responses do not coincide exactly with van Daalen's results, as shown in Fig. 4.18 for the comparison of both responses under $\theta_0 = 0.35$ rad. The discrepancy is primarily due to the neglect of the second-order term $-\frac{1}{2}\rho|\nabla\Phi|^2$ in the hydrodynamic pressure computation of the Simulink LPV model, whereas its effect is included in van Daalen' work, as shown in Eq. (4.41).

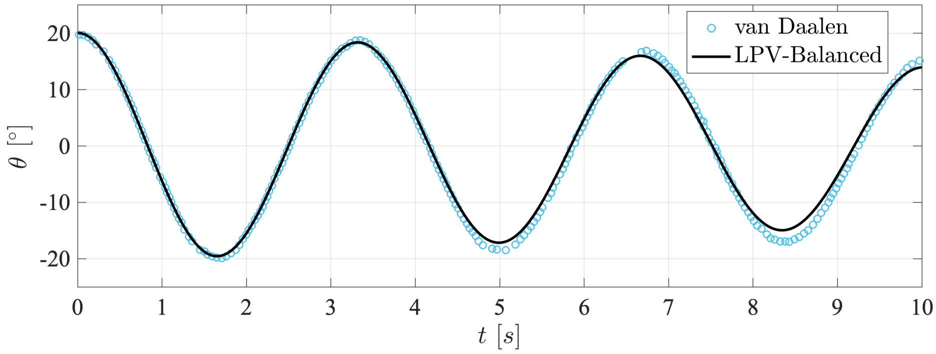

Fig. 4.18 Comparison of van Daalen cylinder's rotational responses under initial rotation angle of 0.35 rad (20°) simulated by the body-nonlinear solver used in van Daalen [128] and Simulink black-box LPV model.

Fig. 4.19 shows the wave radiation force F_r, which is the output of the LPV system in the Simulink model, for the three initial rotation angles. When $\theta_0 = 0.15$ rad, F_r exhibits an almost simple harmonic form. As θ_0 increases to 0.25 rad, the crests and troughs of F_r become flatter, indicating more modes involved in the system dynamics. At $\theta_0 = 0.35$ rad, the higher-order oscillations are clearly observed. These results again demonstrate the capability of the Simulink LPV model to capture the dynamic variation of the water-cylinder system caused by large rotations.

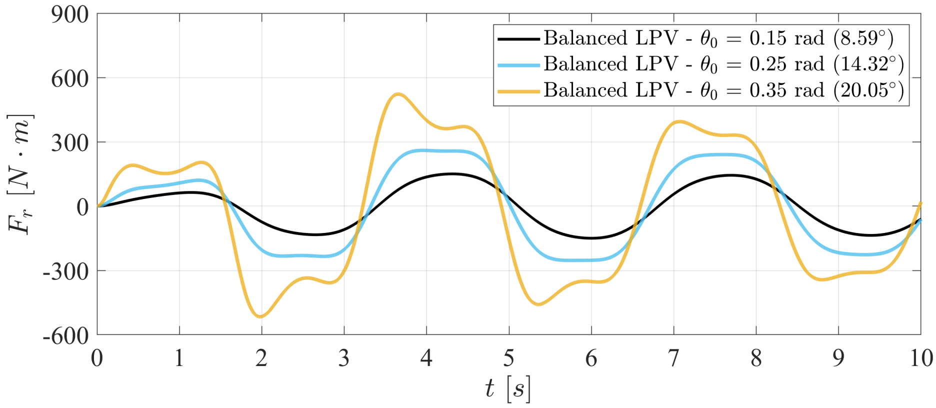

Fig. 4.19 Wave radiation force F_r of the van Daalen floating cylinder under three different initial rotations of 0.15, 0.25, and 0.35 rad simulated by the Simulink black-box LPV model.

4.3.2.3 Gray-box LPV modelling

In this subsection, the gray-box LPV modelling approach illustrated in Fig. 4.5(b) is applied to the van Daalen cylinder to capture the geometric nonlinearity of the water-cylinder system. This gray-box method is characterized by the use of a physical state basis derived from the finite element formulation. Free oscillations of the cylinder simulated using various modelling assumptions are compared to evaluate the performance of the newly proposed gray-box LPV modelling approach.

As described in Eq. (4.40), a constrained nonlinear optimization problem is required to be solved at each grid point θ_i to obtain a set of state-space models $[\mathbf{A}_{opt}, \mathbf{B}_{opt}, \mathbf{C}_{opt}]$. This set of models can be transformed to the proposed physical state-space form $[\mathbf{A}_p, \mathbf{B}_p, \mathbf{C}_p]$ (Eq. (4.34)) using a transformation matrix $\mathbf{T}$ that remains invariant across all rotation angles θ_i. As such, the strict state-basis coherency defined in Section 4.2.2.1 is ensured, which is critical for achieving reliable LPV interpolation.

According to the output equation of the physical state-space representation, as expressed in Eq. (4.33), the required outputs include the potentials on the free surface ($\boldsymbol{\varphi}_1$), the potentials on the virtual far-field boundary ($\boldsymbol{\varphi}_2$), and the wave radiation damping force ($\mathbf{F}_r$). To capture these outputs, potential sensors are deployed on the free surface (denoted as ε) and the virtual far-field boundary (denoted as Γ) in the developed 2D BEM code, alongside the conventional force sensor described in Section 3.4. The deployment of these sensors enables the computation of an augmented frequency response function $\mathbf{K}(i\omega)$, which includes the free-surface potential frequency response $\mathbf{K}_\varepsilon$, far-field potential frequency response $\mathbf{K}_\Gamma$, and wave radiation force frequency response $\mathbf{K}_r$. This augmented frequency response $\mathbf{K}(i\omega)$ will be used in the identification and optimization steps of the LPV modelling. The sensor deployment strategy is illustrated in Fig. 4.20. To ensure that the identified state-space models retain the symmetry property of the wave-radiation frequency response, as shown in Fig. 4.10, the sensors must be positioned symmetrically about the earth-fixed reference frame Oxz.

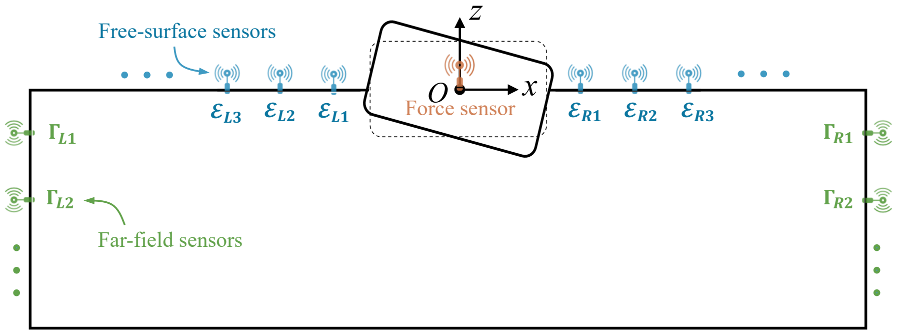

Fig. 4.20 Sensor deployment for forces, free-surface potentials and far-field potentials.

The identification of a reference state-space model is necessary to provide initial guesses for the optimization problem, as described in Eq. (4.40). This process involves two key technical considerations: (1) determining an appropriate number of states, and (2) selecting a reference grid point θ_{ref}. The number of states in the physical state-space model depends on the number of potential sensors. According to the state equation of the physical state-space model described in Eq. (4.32), each free-surface sensor corresponds to 2 states, while each far-field sensor corresponds to 1 state. Regarding the reference grid point, while it may seem intuitive to select the equilibrium position ($\theta = 0^\circ$), this choice leads to an ill-conditioned physical state-space model due to the resulting singular $\mathbf{T}$ matrix. The singularity arises because the far-field sensors positioned at the same vertical level, such as Γ_{L1} and Γ_{R1}, are not independent when the fluid domain is perfectly symmetric about the Oz axis. To overcome this issue, a non-zero θ_{ref} is selected as the reference point. In this subsection, three LPV models with different state numbers (n) are computed, with their corresponding θ_{ref} and sensor locations listed in Table 4.1. Their performance and accuracy will be investigated in the following analysis to assess the impact of these choices on the overall LPV model.

Table 4.1 Reference grid point θ_{ref} and sensors location for different numbers of states.

Number of states (n)	θ_{ref}	Free-surface sensors (ε)	Far-field sensors (Γ)
8	1°	±4 m	-2 m, -4 m
12	0.5°	±3 m, ±4 m	-2 m, -6 m
16	1°	±3 m, ±4 m, ±5 m	-2 m, -8 m

To illustrate the optimization process, the $n = 8$ configuration in Table 4.1 is taken as an example. This configuration consists of 2 free-surface sensors (4 states) and 4 far-field sensors (4 states). The state-space model identified from the augmented frequency response samples at $\theta_{ref} = 1^\circ$ is selected as the reference model. Initialized with this reference state-space model $[\mathbf{A}_{ref}, \mathbf{B}_{ref}, \mathbf{C}_{ref}]$, the optimization problem described in Eq. (4.40) is solved independently for each grid point θ_i ranging from -20° to 20°. The frequency responses of the resultant optimized state-space models $[\mathbf{A}_{opt}, \mathbf{B}_{opt}, \mathbf{C}_{opt}]$ are compared with the corresponding frequency response samples obtained from the 2D BEM solver in Fig. 4.21 for θ_{ref} and $\theta = \pm 10^\circ$. The large differences in the amplitude of the force and potential frequency responses introduce challenges in the optimization computation. To overcome this, scaling factors of 10^3 and 1.67×10^3 are applied to the original frequency response samples associated with the potentials on the free surface K_ε and far field K_Γ, respectively.

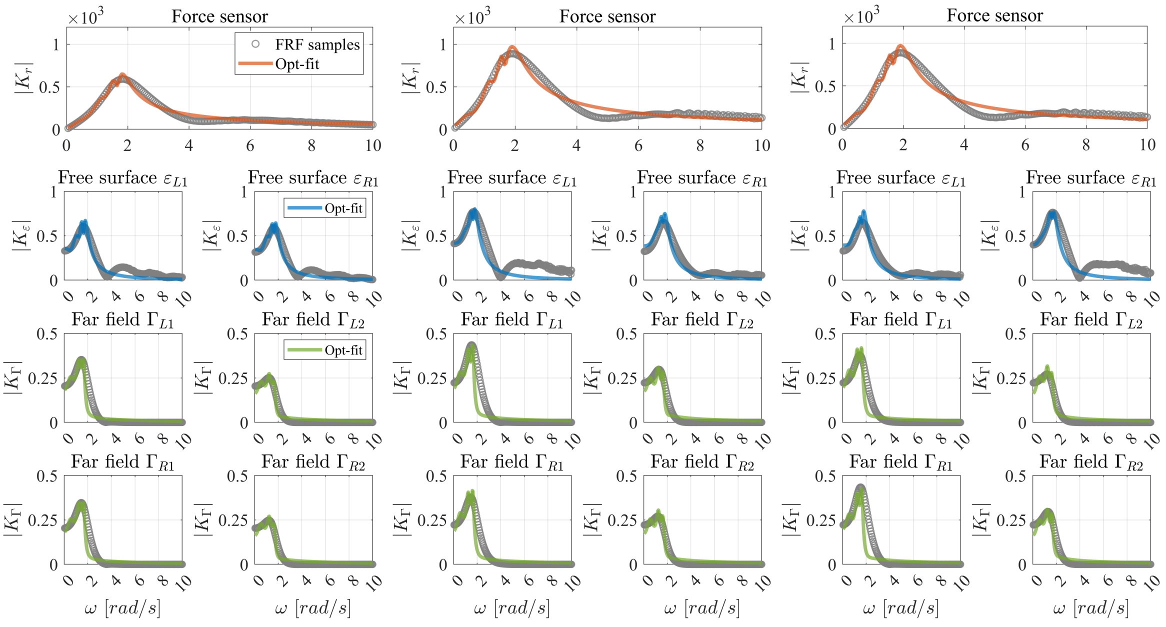

(a) Reference: $\theta = 1^\circ$ (b) Example 1: $\theta = 10^\circ$ (c) Example 2: $\theta = -10^\circ$

Fig. 4.21 The optimized state-space estimation of the wave radiation force frequency response samples (K_r), and the potential frequency response samples on the free surface (K_ε) and far field (K_Γ) for the van Daalen cylinder under the rotation of 1° and $\pm 10^\circ$.

Fig. 4.21 indicates that the state number of 8 is sufficient to capture the dominant resonances of the water-cylinder dynamic system. Moreover, the optimized state-space models exhibit the expected symmetry in K_r and K_Γ, and anti-symmetry in K_ε for positive and negative rotation angles. These symmetry properties validate the effectiveness of the optimization process in accurately representing the system's dynamic characteristics. With the collection of optimized state-space models, the physical state-space models $[\mathbf{A}_p, \mathbf{B}_p, \mathbf{C}_p]$ can be computed for each grid point θ_i using Eq. (4.35) and 4.38. The system matrices of the physical state-space model at an example grid point of 10° are presented below:

$$\mathbf{A}_{p,10^\circ} = \begin{bmatrix} 0 & 0 & 1 & 0 & 0 & 0 & 0 & 0 \\ 0 & 0 & 0 & 1 & 0 & 0 & 0 & 0 \\ -13.89 & -10.84 & 2.39 & 3.47 & 35.84 & -6.88 & 39.89 & -11.64 \\ 11.83 & 8.91 & -3.01 & -4.05 & -34.87 & 6.67 & -38.91 & 11.43 \\ 38.43 & 37.05 & 5.07 & 6.00 & -186.32 & -20.56 & -209.47 & 6.87 \\ 21.73 & 20.38 & 4.25 & 4.90 & -41.53 & -127.59 & -57.54 & -108.52 \\ -36.94 & -35.56 & -4.81 & -5.73 & 172.54 & 32.22 & 195.10 & 5.48 \\ -20.56 & -19.21 & -4.03 & -4.67 & 30.63 & 136.99 & 46.18 & 118.43 \end{bmatrix},$$

$$\mathbf{B}_{p,10^\circ} = \begin{bmatrix} 0 \\ 0 \\ 1342.30 \\ -1238.40 \\ -154.48 \\ -152.02 \\ 150.40 \\ 148.08 \end{bmatrix}, \mathbf{C}_{p,10^\circ} = \begin{bmatrix} 1 & 0 & 0 & 0 & 0 & 0 & 0 & 0 \\ 0 & 1 & 0 & 0 & 0 & 0 & 0 & 0 \\ 0 & 0 & 0 & 0 & 1 & 0 & 0 & 0 \\ 0 & 0 & 0 & 0 & 0 & 1 & 0 & 0 \\ 0 & 0 & 0 & 0 & 0 & 0 & 1 & 0 \\ 0 & 0 & 0 & 0 & 0 & 0 & 0 & 1 \\ -7.04 & -7.55 & -0.01 & -0.77 & 60.03 & -82.44 & 58.90 & -80.98 \end{bmatrix}, \tag{4.51}$$

which adhere to the specified structure in Eq. (4.34), as expected. This demonstrates the success of the proposed algorithm in imposing the state-space representations at all grid points to use a unified physical basis, which is critical for achieving accurate LPV interpolation in subsequent steps.

The performance of the physical state-space model is evaluated for different state numbers. Fig. 4.22 compares the fitting of the wave radiation force frequency response (K_r) at $\theta = 8^\circ$ using physical state-space models with $n = 8$, $n = 12$, $n = 16$ states against the samples obtained from the 2D BEM code. For reference, the K_r estimated using the $n = 4$ balanced-form state-space model, as shown in Fig. 4.11, is also included. The results indicate that increasing the state number improves the fitting quality of the physical state-space models, with the $n = 16$ model providing the closest match to the BEM samples. The gray-box physical-basis model requires a larger number of states compared to the black-box balanced-form model ($n = 4$) because it includes additional potential sensors for more comprehensive representation. In contrast, the black-box balanced-form model only handles the single-input single-output (SISO) frequency response K_r in the van Daalen model. As a result, while the gray-box model provides a naturally coherent state basis, it introduces greater model complexity, which must be considered when choosing the appropriate model configuration for practical applications.

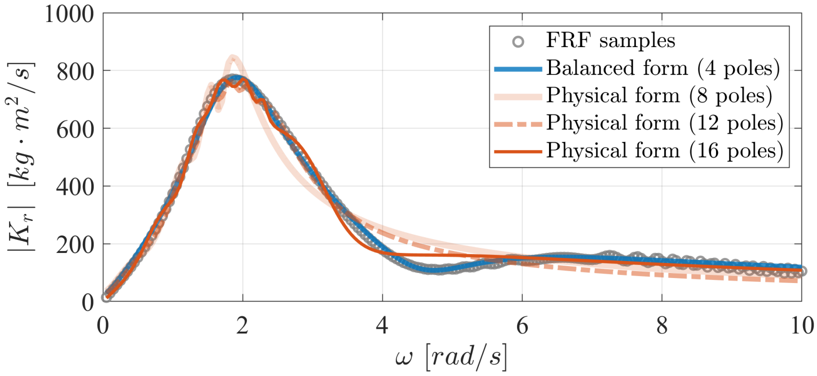

Fig. 4.22 Comparison of the wave radiation force frequency response (K_r) at $\theta = 8°$ calculated from the BEM code, the physical state-space models using three different numbers of states ($n = 8, 12, 16$), and the balanced-form state-space model using 4 states.

The ability of the proposed physical-form state-space model in capturing the variation of the van Daalen cylinder's dynamic characteristics with rotation angles is investigated by analyzing the evolution of system poles in the real-imaginary plane. Fig. 4.23 shows the evolution of poles for physical state-space models using $n = 8$, $n = 12$, $n = 16$ states over the rotation ranges of $-18° \sim 18°$, $-12° \sim 12°$ and $-10° \sim 10°$, respectively. Models outside of these ranges are considered outliers and have been eliminated to maintain a relatively smooth variation of poles, which is essential for subsequent LPV interpolation. Interestingly, the $n = 8$ and $n = 12$ models contain only complex conjugate poles, indicating a consistent dynamic response within these rotation ranges. In contrast, for the $n = 16$ model, a shift between real and complex conjugate poles is observed as the rotation angle changes. This shift suggests that a higher number of states is able to capture more intricate dynamics of the system. However, it also introduces additional complexity, whose impact on the interpolation process will be studied later.

Fig. 4.24 shows the variation of entries in the matrices $[\mathbf{A}_{opt}, \mathbf{B}_{opt}, \mathbf{C}_{opt}]$ of the optimized state-space models and matrices $[\mathbf{A}_p, \mathbf{B}_p, \mathbf{C}_p]$ of the transformed physical state-space models as functions of the cylinder's rotation angles θ_i. While both model collections are constructed along a coherent state basis, the optimized form generally exhibits better numerical conditioning compared to the physical form. Therefore, the optimized form is recommended for use in the subsequent LPV interpolation to ensure a more stable and accurate model representation.

Regarding the number of states, different behaviours are observed in the variation of matrices $\mathbf{A}_{opt}$ and $\mathbf{B}_{opt}$ for different state numbers. When $n = 8$ is used, the matrices tend to exhibit anti-symmetry with respect to the rotation angles, whereas for $n = 12$ and $n = 16$ models, the matrices show a symmetric variation. This change in symmetry suggests that the system dynamics are captured differently depending on the number of states, which

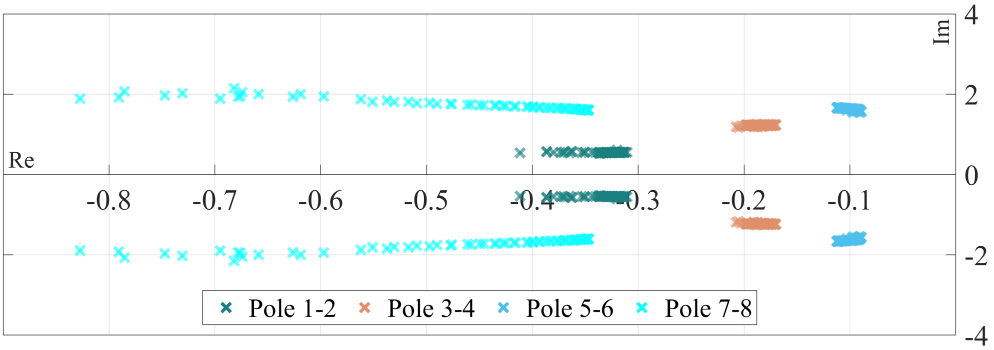

(a) 8 poles ($n = 8$)

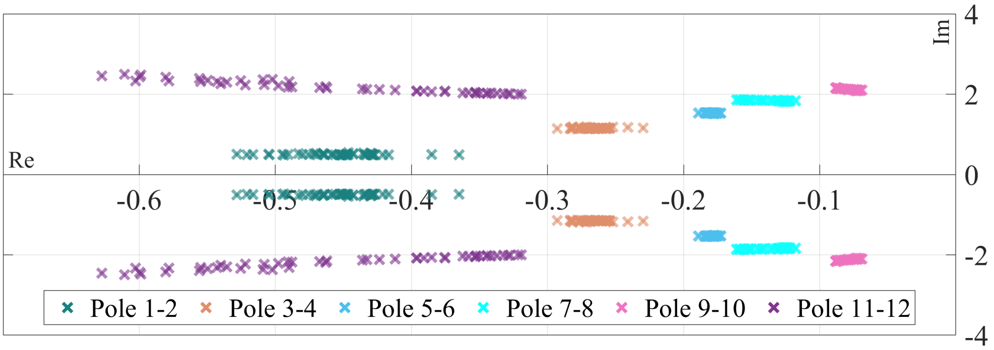

(b) 12 poles ($n = 12$)

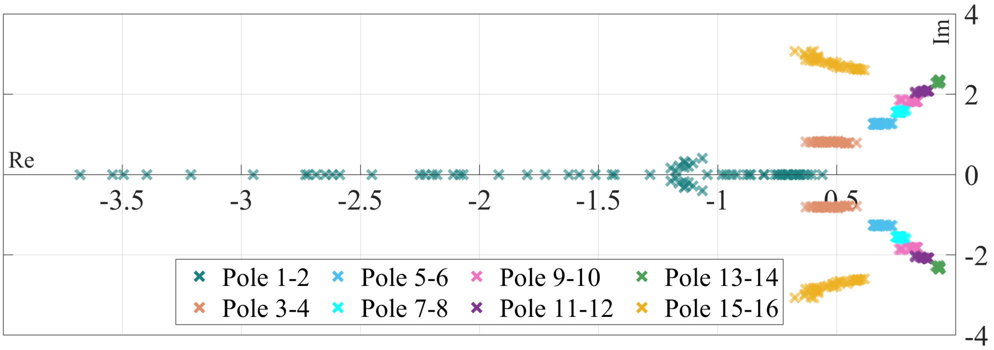

(c) 16 poles ($n = 16$)

Fig. 4.23 The evolution of poles of the physical state-space models under different rotations.

can affect the results of the later interpolation process. This behaviour is likely occurring from the identification process rather than the transformation, as similar observations are of considerations in stabilization methods [109]. Additionally, with a higher number of states ($n = 16$), fewer oscillations are observed in the entries of the state-space matrices, which is theoretically preferable for interpolation. The symmetric trends and smooth variations of the state-space matrices provide confidence in the ability of the proposed physical-form LPV modelling approach to capture the geometrically nonlinear dynamics of the example water-cylinder system.

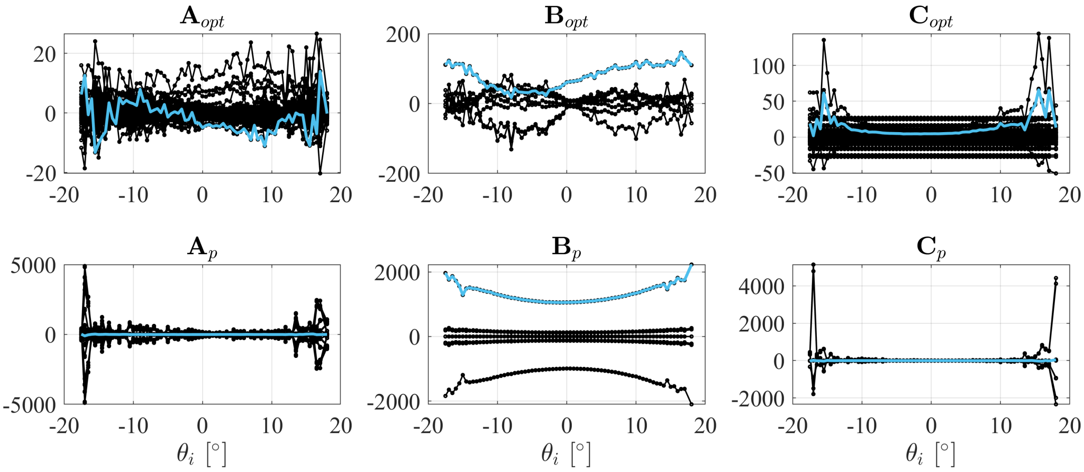

(a) 8 poles ($n = 8$)

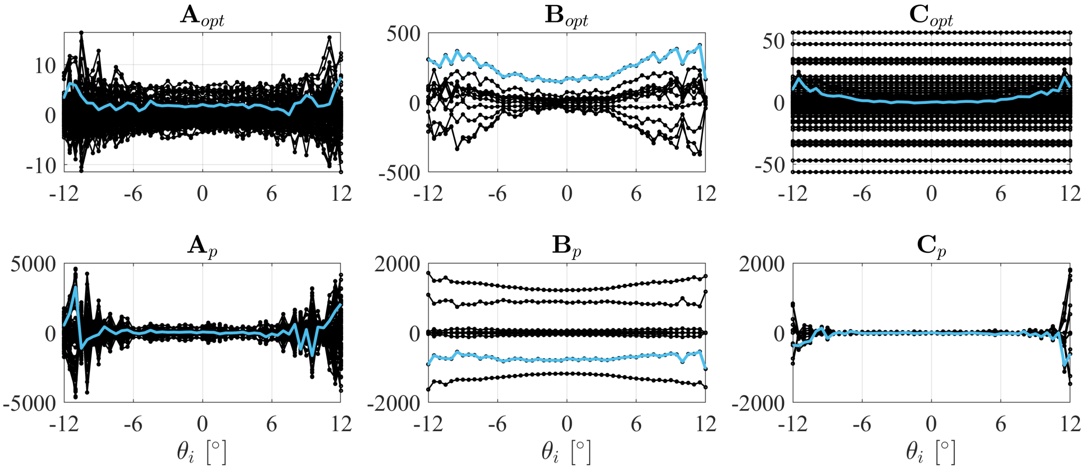

(b) 12 poles ($n = 12$)

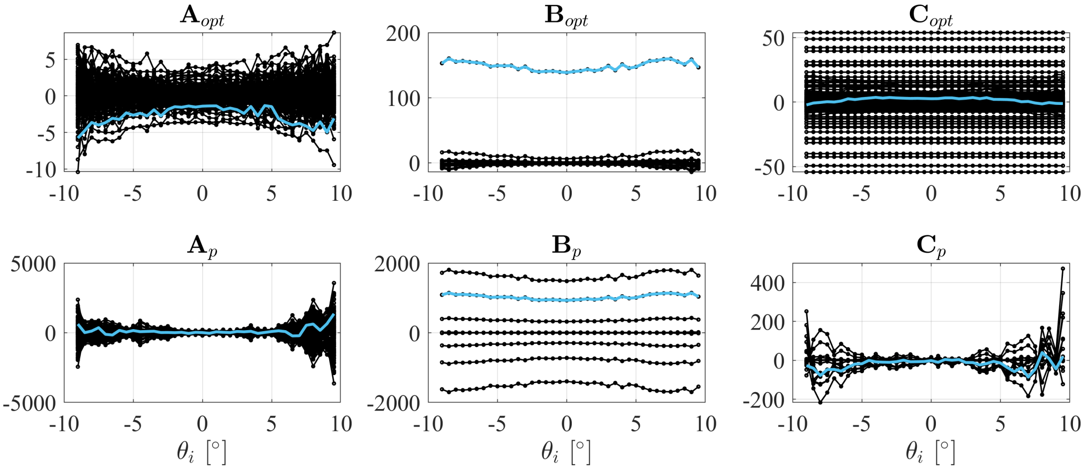

(c) 16 poles ($n = 16$)

Fig. 4.24 The variation of entries to the system matrices for the optimized $[\mathbf{A}_{opt}, \mathbf{B}_{opt}, \mathbf{C}_{opt}]$ and physical $[\mathbf{A}_p, \mathbf{B}_p, \mathbf{C}_p]$ state-space models with rotation angles θ_i.

The Simulink modelling framework for the van Daalen floating cylinder, as illustrated in Fig. 4.16, is used to evaluate the performance and accuracy of the proposed gray-box LPV modelling approach. The free rotational response of the cylinder is simulated using various modelling assumptions for each component of the hydrodynamic forces, as summarized in Table 4.2. The optimized state-space models with $n = 8$, $n = 12$, and $n = 16$ states, along with their corresponding grid points of rotation angles, are individually specified in the Simulink model. The rotation-dependence of the dynamic buoyancy force F_b and the infinite-frequency added mass λ_∞ is accounted for using interpolation, and this configuration is referred to as "LPV" model in Table 4.2. For closer evaluation of the geometrically nonlinear effects of the water-cylinder system, the LPV model is compared against conventional purely linear models, partly-nonlinear and nonlinear convolution integral models. The linear models use either the convolution integral or state-space representation to compute the wave-radiation damping force F_r, with the corresponding impulse response $k_r(t)$ or the state-space representation, as well as F_b and λ_∞, all evaluated at the equilibrium position ($\theta = 0°$), as detailed in Section 2.2.1.1. The partly-nonlinear convolution integral model considers the rotation-dependence of F_b and λ_∞ while retaining the linear F_r. In contrast, the nonlinear convolution integral model incorporates all nonlinear forces with k_r interpolated at each time instant for the evaluation of nonlinear F_r. This nonlinear model serves as the benchmark for assessing the accuracy of the proposed LPV modelling approach because it is free from state-basis incoherency issues.

Table 4.2 Assumptions for different models.

	Linear conv	Linear ss	Partly-nonlinear conv	Nonlinear conv	LPV
Buoyancy F_b	linear	linear	nonlinear	nonlinear	nonlinear
Infinite-frequency added mass λ_∞	linear	linear	nonlinear	nonlinear	nonlinear
Wave radiation force F_r	linear	linear	linear	nonlinear	nonlinear

conv: convolution integral; ss: state-space model.

Fig. 4.25 compares the rotational responses of the van Daalen cylinder under an initial rotation angle $\theta_0 = 20°$ simulated by the Simulink model using the various models listed in Table 4.2. The responses calculated using the balanced-form LPV model, as described in Fig. 4.17, is also included. The results show that the LPV models and the nonlinear model exhibit shorter oscillation periods and higher damping effects compared to the purely linear models. This indicates the presence of nonlinearities in the water-cylinder interaction dynamics, due to the time-varying wetted body surface. However, the different LPV models, whether using the balanced form or the optimized physical form with different state numbers, all show minimal deviation from the nonlinear model. This demonstrates the ability of the proposed LPV modelling approaches in accurately capturing the geometric nonlinearities. The partly-nonlinear response shows a similar period to the nonlinear response but has a decay rate comparable to that of the purely linear responses. This suggests that the oscillation period is primarily influenced by the dynamic buoyancy force F_b and the infinite-frequency added mass λ_∞. Fig. 4.26 compares the wave radiation forces F_r simulated using the various models. The nonlinear and LPV models show higher F_r amplitudes compared to the partly-nonlinear and purely linear models. This explains the increased damping effect, due to radiation energy loss, when the rotation-dependence of F_r is taken into account.

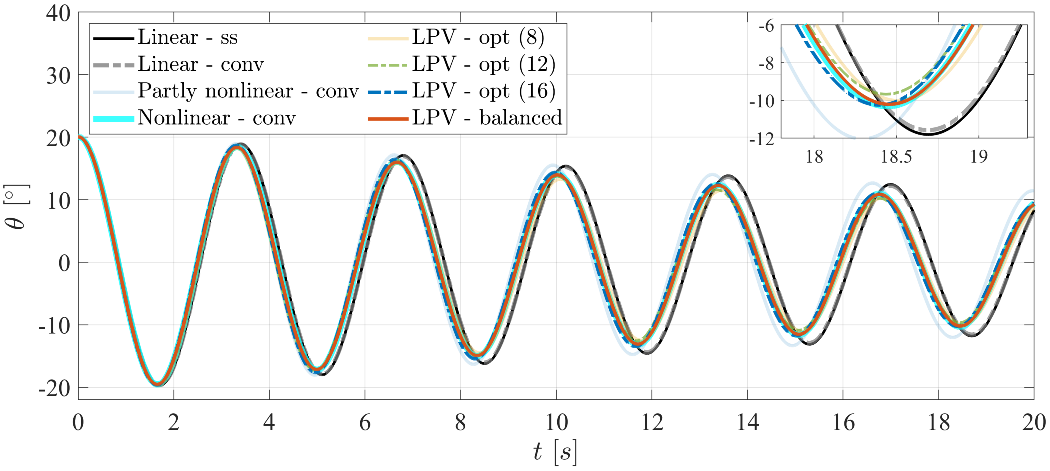

Fig. 4.25 Comparison of van Daalen cylinder's rotational responses θ under the initial rotation angle $\theta_0 = 20^\circ$ simulated using different modelling assumptions.

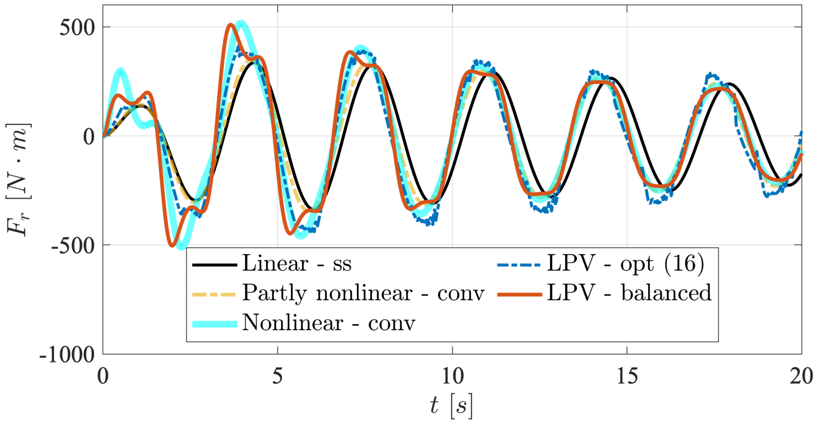

Fig. 4.26 Comparison of van Daalen cylinder's wave radiation damping force F_r under the initial rotation angle $\theta_0 = 20^\circ$ simulated using different modelling assumptions.

4.3.3 Nonlinear analysis

To further investigate the influence of geometric nonlinearity on the dynamic response of the system, a nonlinear analysis is conducted on the van Daalen floating cylinder. In this analysis, the numerical frequency sweep method, which is commonly used for nonlinear systems, is adopted. A total of 40 sinusoidal excitation signals, characterized by the moment about the y-axis (M_y), are selected with unevenly spaced excitation frequencies (f_{exc}) ranging from 0.0608 Hz to 0.5556 Hz. Fine frequency intervals are set around 0.3 Hz, which corresponds to the estimated rotational natural frequency of the cylinder from the free oscillation results in Fig. 4.25. For each of the 40 excitation signals, the mean moment value is fixed at 2000 $N \cdot m$, while the amplitude is set to 500 $N \cdot m$.

For the sweep-up (down) test, as illustrated in Fig. 4.27, the excitation signal with the lowest (highest) frequency is initially applied to the right side of the `External moment` block in the Simulink model (Fig. 4.16) to excite the cylinder from rest. The rotational response of the cylinder is simulated using a specified model, as listed in Table 4.2. A sufficiently long simulation time is used for each frequency to ensure that the response converges to the steady state. Afterwards, without interrupting the simulation, the excitation frequency is increased (decreased) to the next value, until all frequency cases are completed.

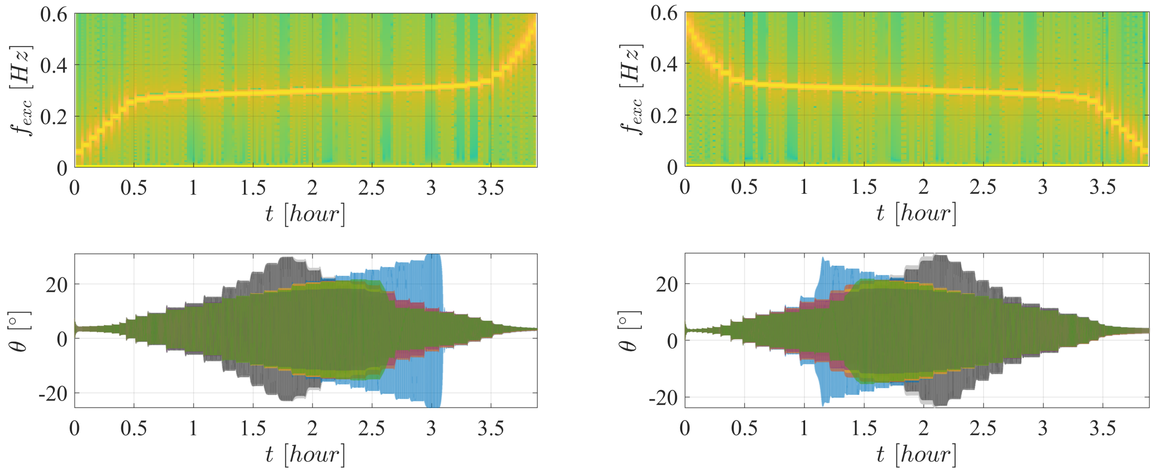

(a) Sweep up

(b) Sweep down

Fig. 4.27 Spectrograms of the numerical frequency sweep-up and down excitation signals, and comparison of the cylinder's rotational responses calculated from various models. Refer to Fig. 4.28 for the legends of these models.

After individually simulating the floating cylinder using different model assumptions for both frequency sweep-up and down tests, the resulting rotational responses are compared in Fig. 4.27. The steady-state rotational amplitudes under each excitation frequency (f_{exc})

are extracted and plotted against f_{exc} in the pseudo frequency response shown in Fig. 4.28. The solid lines represent the frequency responses obtained from the frequency sweep-up test using 6 different models, while the dashed lines show the results from the sweep-down tests. These test cases provide a comprehensive view of the nonlinear behaviour of the floating cylinder under varying excitation frequencies and help evaluate the impact of different model assumptions on the system's response.

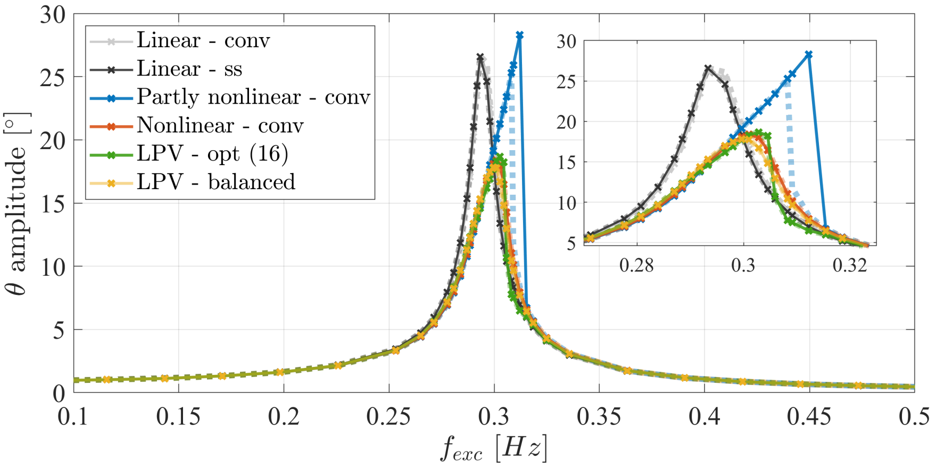

Fig. 4.28 Pseudo frequency responses of the van Daalen cylinder calculated from various models under the frequency sweep-up (solid lines) and down (dashed lines) tests.

From Fig. 4.28, it can be observed that only including the nonlinear infinite-frequency added mass λ_∞ and buoyancy F_b, as in the partly-nonlinear model, results in an increase in the natural frequency by approximately 6.5% compared to the purely linear models (0.293 Hz v.s. 0.312 Hz). This hardening effect is consistent with the shortened oscillation period observed from the partly-nonlinear model in Fig. 4.25. Further incorporating the nonlinear radiation force F_r through either the nonlinear convolution integral model or LPV models slightly increases the natural frequency but significantly reduces the resonance peak. This indicates a considerable increase in damping effect when geometric nonlinearity is accounted for, which has also been reflected in the time-domain free oscillation results shown in Fig. 4.25. The good agreement between the two LPV models and the nonlinear convolution integral model again verifies the effectiveness of both the black-box balanced and gray-box physical modelling approaches to accurately capture the system's nonlinear dynamics.

The frequency responses from the sweep-up and down tests in Fig. 4.28 do not show appreciable differences for most models, except for the partly nonlinear convolution integral model. In this case, jumps occur at different frequencies during the sweep-up and sweep-down tests, indicating the presence of bifurcation which is a typical phenomenon in nonlinear systems. It is important to note that the cylinder's rotation angle can reach as large as

30° when resonance occurs for the partly-nonlinear model. As plotted in Fig. 4.8, the infinite-frequency added mass (λ_∞) experiences an abrupt jump when θ increases to around $\pm 24°$, which can contribute to the observed bifurcation behaviour. In contrast, due to higher damping effects, the resonance peaks of the LPV models occur within a range of rotation angles where λ_∞ exhibits only mild variation, preventing bifurcation under this excitation moment amplitude. This comparison highlights the significant influence of each nonlinear hydrodynamic component on the overall system response. Neglecting or misrepresenting any of these components can lead to fundamentally different dynamic predictions.

4.4 LPV modelling of the floating wind turbine

The LPV modelling methodology, which has been verified on the van Daalen floating cylinder, is applied to the platform of floating wind turbines (FWT) in this section. For this study, only 2D movements of the FWT platform are considered. Both the black-box method using the balanced-form basis and the gray-box method with the newly proposed physical basis are explored. The platform responses of the LPV models are simulated in Simulink for an example NREL 5-MW ITI-Barge FWT under irregular wave excitation. Additionally, the geometrically nonlinear effects are investigated for both wave-only and simultaneous wind-wave excitation scenarios. These analyses aim to evaluate the accuracy and robustness of the LPV models in capturing the complex nonlinear hydrodynamics of the FWT system.

4.4.1 LPV modelling

This section provides a detailed description of the procedures used for the LPV modelling of FWT hydrodynamics. Specifically, the **identification-transformation-interpolation** procedure for the black-box LPV method and the **identification-optimization-interpolation** procedure for the gray-box LPV method, as illustrated in Fig. 4.5, are explained in depth. Their integration with the Simulink FWT model, developed in Section 2.3, is also introduced.

4.4.1.1 Local linear models

To generate local linear models for the FWT platform hydrodynamics, a 2D grid is defined with heave displacements (ξ_3) ranging from -2 m to 2 m with an interval of 0.1 m, and pitch rotations (ξ_5) ranging from $-10°$ to $10°$ with an interval of 0.5°. This grid is selected to capture the variation in hydrodynamic coefficients over a broad range of platform positions. The 2D BEM code developed in Section 3.4 is used to numerically solve the BVP linearized at each specified platform pose (ξ_3, ξ_5).

Fig. 4.29 shows the resulting infinite-frequency added mass ($\boldsymbol{\lambda}_\infty$) for all couplings of three DoFs in the 2D space — surge, heave and pitch — along with the dynamic buoyancy force ($\mathbf{F}_b$) for these DoFs. The results indicate significant variations in $\boldsymbol{\lambda}_\infty$ and $\mathbf{F}_b$ with the platform's heave displacement (ξ_3) and pitch rotation (ξ_5). An exception is observed in the buoyancy $\mathbf{F}_b$ for the surge DoF, which remains zero across the entire grid. The wave-radiation damping effect, represented by either the frequency response function ($\mathbf{K}_r(i\omega)$) or impulse response function ($\mathbf{k}_r(t)$), also varies with the platform position, as shown in Fig. 4.30 and 4.31, respectively.

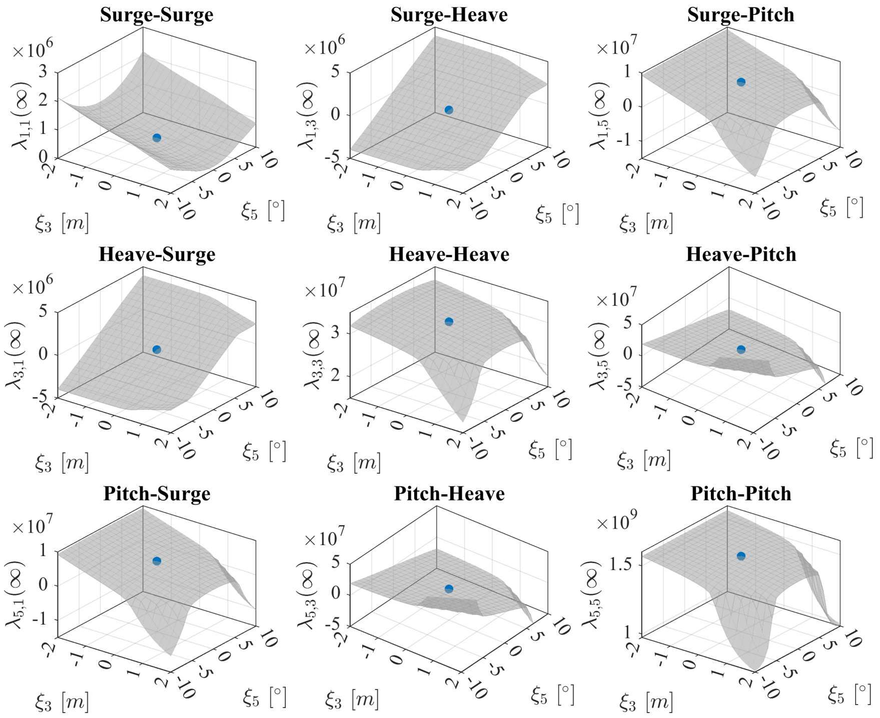

(a) Infinite-frequency added mass ($\boldsymbol{\lambda}_\infty$).

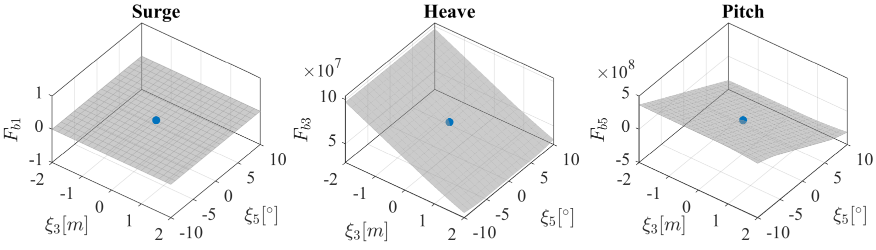

(b) Buoyancy force ($\mathbf{F}_b$).

Fig. 4.29 Variation of the infinite-frequency added mass ($\boldsymbol{\lambda}_\infty$) and dynamic buoyancy force ($\mathbf{F}_b$) of the 2D ITI-Barge FWT platform under the heave displacements ξ_3 of -2 m $\sim$ 2 m and pitch rotations ξ_5 of $-10° \sim 10°$. The filled dots represent the values calculated at the equilibrium position ($\xi_3 = 0$ m, $\xi_5 = 0°$).

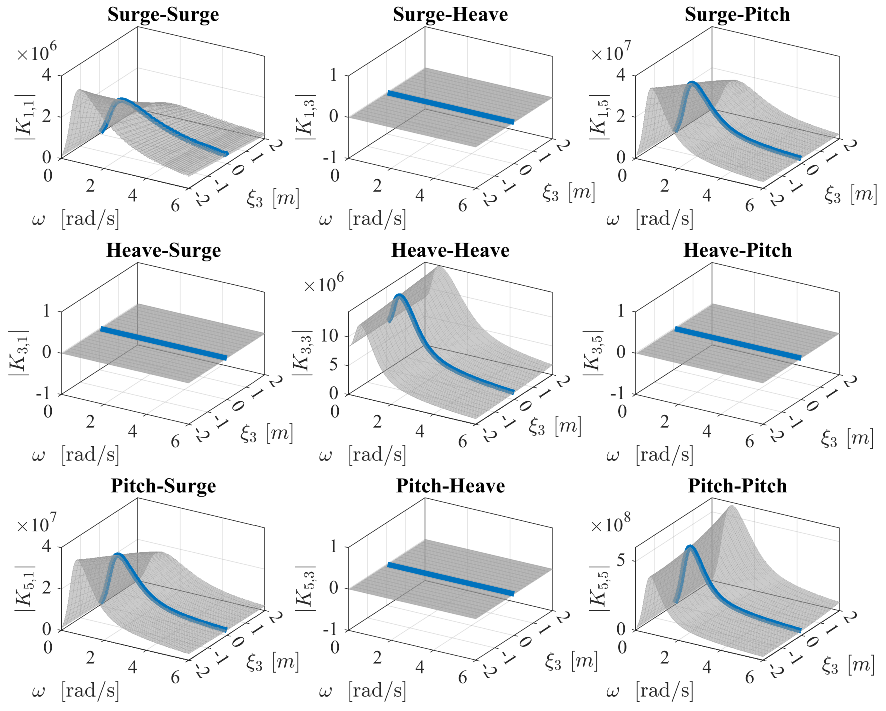

(a) Fixed pitch $\xi_5 = 0°$, varying heave ξ_3 of -2 m $\sim$ 2 m.

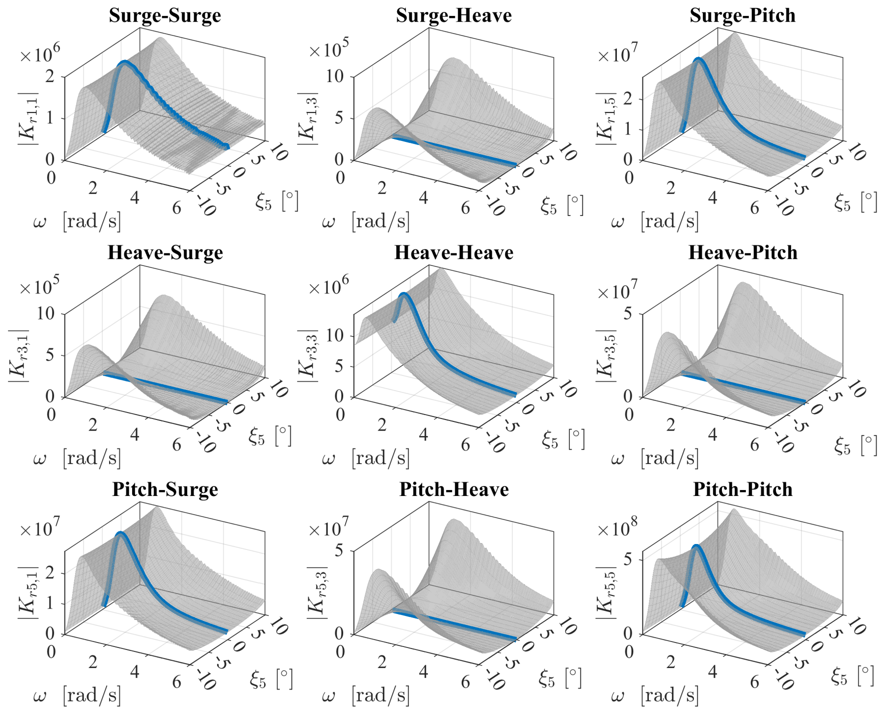

(b) Fixed heave $\xi_3 = 0$ m, varying pitch ξ_5 of $-10° \sim 10°$.

Fig. 4.30 Variation of wave radiation force frequency response $\mathbf{K}_r(i\omega)$ of the 2D ITI-Barge FWT platform with platform positions. The thick blue curves represent the values calculated at the equilibrium position ($\xi_3 = 0$ m, $\xi_5 = 0°$).

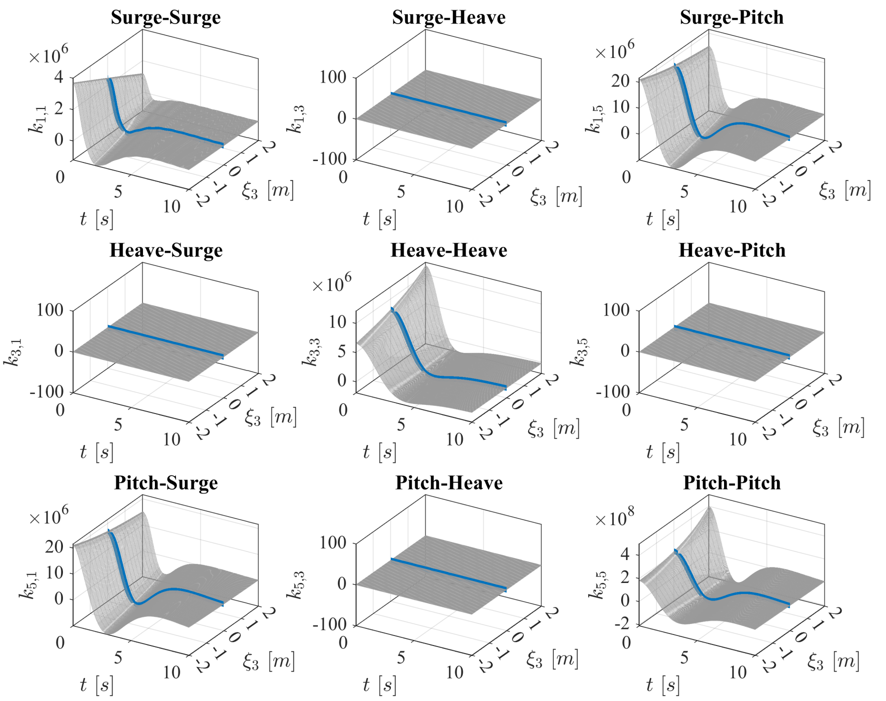

(a) Fixed pitch $\xi_5 = 0°$, varying heave ξ_3 of -2 m $\sim$ 2 m.

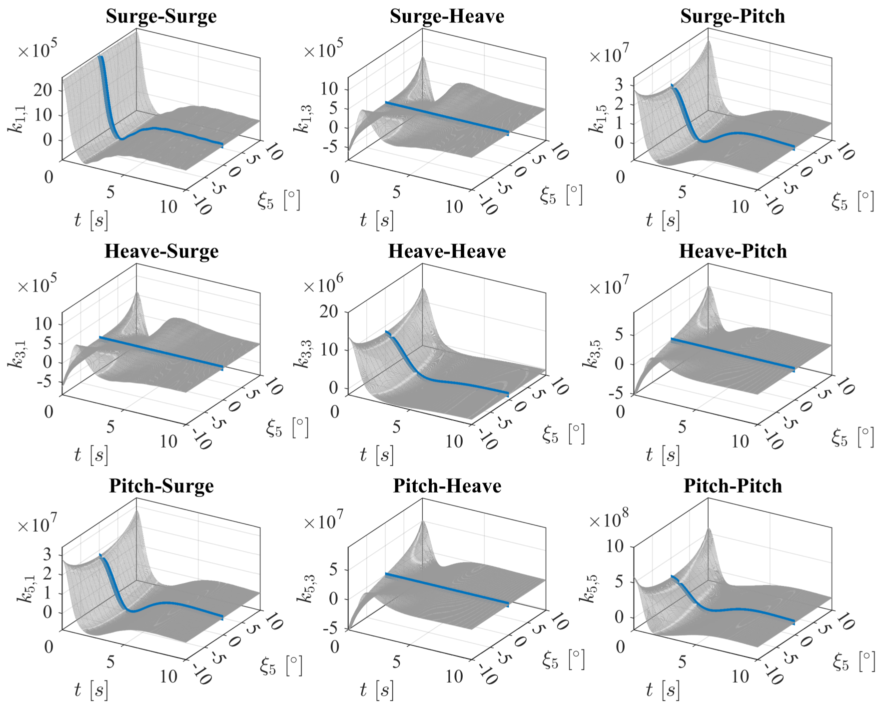

(b) Fixed heave $\xi_3 = 0$ m, varying pitch ξ_5 of $-10° \sim 10°$.

Fig. 4.31 Variation of wave radiation force impulse response $\mathbf{k}_r(t)$ of the 2D ITI-Barge FWT platform with platform positions. The thick blue curves represent the values calculated at the equilibrium position ($\xi_3 = 0\ \text{m}, \xi_5 = 0°$).

As shown in Fig. 4.30(a) and Fig. 4.31(a), when the platform's pitch rotation ξ_5 is fixed at 0° and only the heave displacement ξ_3 varies, the cross-coupling terms of both $\mathbf{k}_r(t)$ and $\mathbf{K}_r(i\omega)$ remain zeros, which is attributed to the geometric symmetry of the barge platform about the Oz axis. However, once the platform is tilted, breaking this symmetry, the cross-coupling terms become non-zero, as shown in Fig. 4.30(b) and Fig. 4.31(b). Additionally, both the wave radiation functions $\mathbf{k}_r$ and $\mathbf{K}_r$ show symmetry with respect to positive and negative rotation angles, as expected. These variations in the hydrodynamic coefficients with platform position must be accurately captured in the LPV modelling to ensure reliable predictions of the FWT dynamics.

4.4.1.2 Black-box LPV modelling

In the black-box LPV modelling approach, the 3-input 3-output wave radiation force frequency response matrix $\mathbf{K}_r$ is used to identify the local state-space models at each specified grid point of the platform position. The frequency-domain subspace identification algorithm described in Section 4.2.1 is applied to $\mathbf{K}_r$ to obtain the state-space models. Fig. 4.32 compares the frequency responses of the identified state-space models with different numbers of states (6, 8 and 10) against the frequency response samples computed from the 2D BEM code at two example platform positions. The results show that the model using 8 states provides a better overall representation for $\mathbf{K}_r$ compared to the 6-state model for both examples. Further increasing the state number to 10 improves the fitting at the platform position of $\xi_3 = -2$ m, $\xi_5 = 8°$, but results in a poorer fit at $\xi_3 = 0.6$ m, $\xi_5 = 8°$. Given these observations, the state-space model with 8 states is selected for more robust identification results across different platform positions.

It is worth noting that when the platform's heave displacement ξ_3 and the pitch rotation $|\xi_5|$ exceed the thresholds 0.8 m and 9°, the platform's submergence area changes shape from a trapezoid to a triangle. This fundamentally alters the envelope shape of the frequency response function $\mathbf{K}_r$, leading to significant changes in the pole locations of the identified state-space models. To avoid the instability caused by such abrupt changes, the grid points for the platform position are restricted to $\xi_3 \in [-2\text{ m}, 0.65\text{ m}]$ and $\xi_5 \in [-8°, 8°]$. Fig. 4.33 plots the evolution of poles for the identified state-space models within this selected range of heave displacements (ξ_3) and pitch rotations (ξ_5).

As shown in Fig. 4.33(a), when the platform moves upward with the rotation fixed at $\xi_5 = 0°$, the 4 pairs of complex conjugate poles consistently shift to the left side of the real-imaginary plane. This indicates an increase in natural frequencies and damping ratios. However, when $\xi_5 \neq 0$, the poles' shifts are no longer monotonic, and the poles' evolution paths with heave ξ_3 vary distinctly at different fixed rotation ξ_5. Similarly, Fig. 4.33(b) shows that for different fixed heave values ξ_3, the poles' evolution with rotation ξ_5 tends to be more scattered as ξ_3 increases. Furthermore, the poles corresponding to negative rotation angles (e.g. $\xi_5 = -8^\circ$ labelled as "**+**") and positive angles (e.g. $\xi_5 = 8^\circ$ labelled as bold "×") overlap, reflecting the inherent symmetry of $\mathbf{K}_r$ as shown in Fig. 4.30(b). The slight mismatches between "**+**" and "×" in Fig. 4.33(b) are introduced by numerical oscillations in the BEM results. The smooth variations in the poles of the identified state-space models provide further evidence of the geometric nonlinearity in the wave radiation effect, which can be captured by the selected range of grid points.

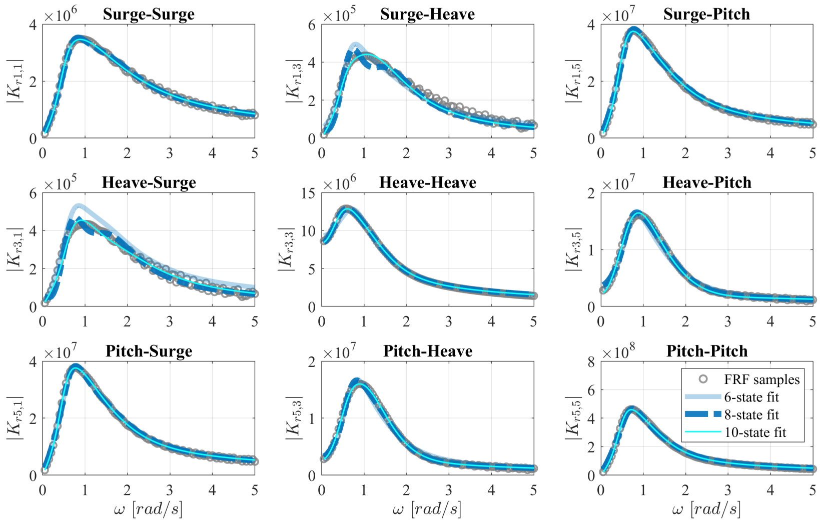

(a) Platform position: $\xi_3 = -2$ m, $\xi_5 = 8^\circ$

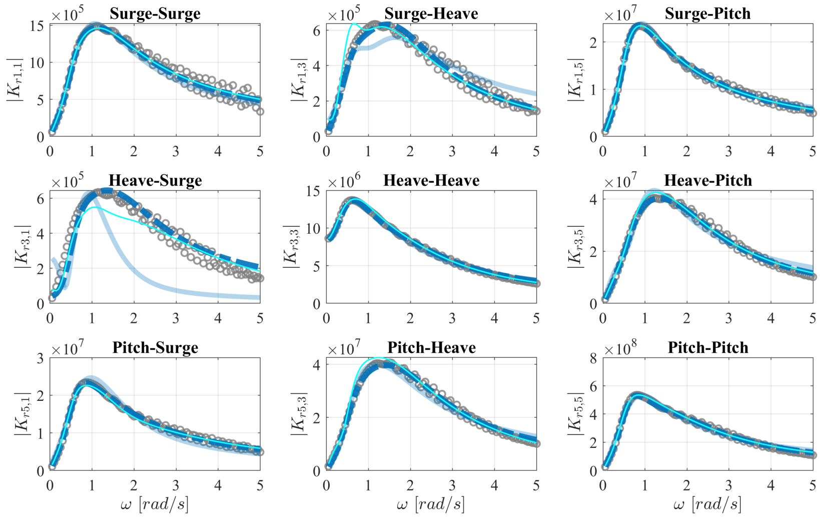

(b) Platform position: $\xi_3 = 0.6$ m, $\xi_5 = 8^\circ$

Fig. 4.32 Comparison of wave radiation frequency response ($\mathbf{K}_r$) at two example platform positions calculated from the BEM code and state-space models using $n = 6, 8, 10$ states.

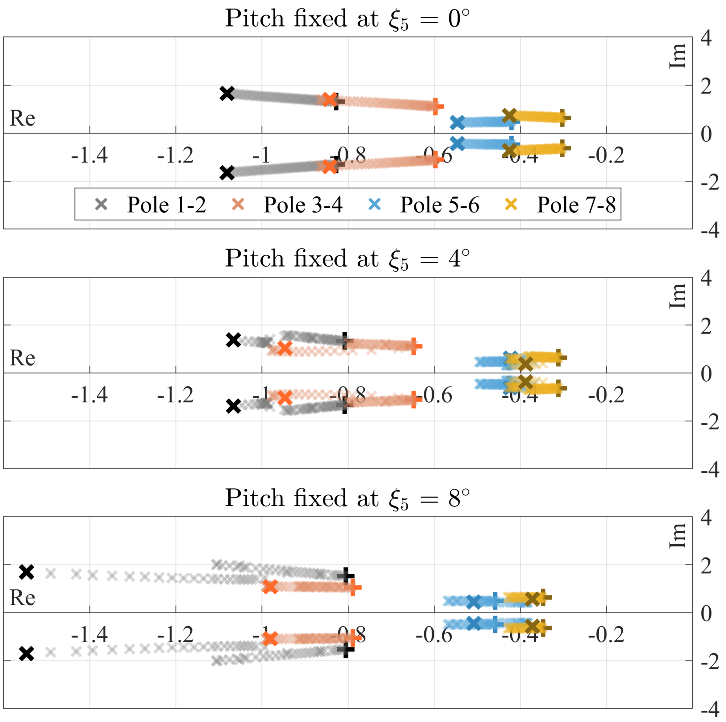

(a) Varying with heave from -2 m to 0.65 m

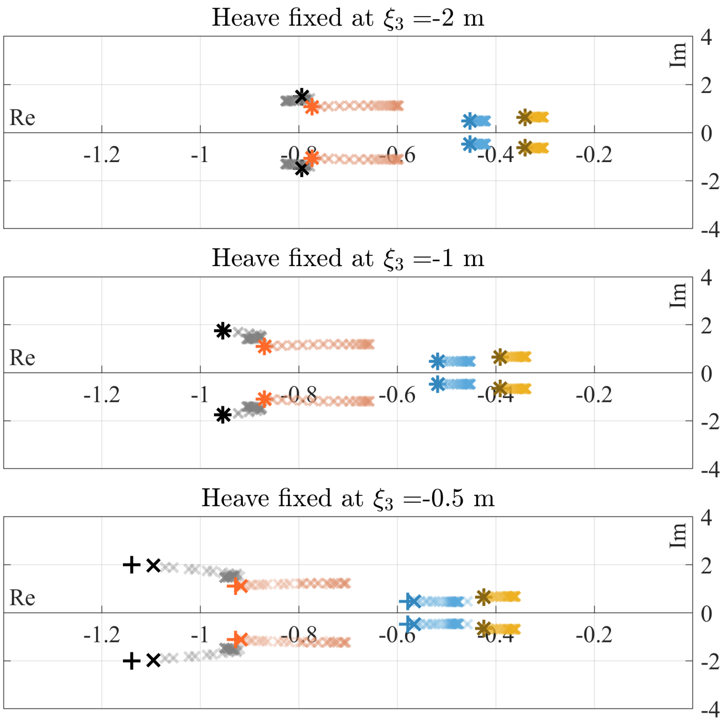

(b) Varying with pitch from $-8°$ to $8°$

Fig. 4.33 The evolution of poles of the identified state-space models under different heave displacements and pitch rotations. Bold "+" and "×" labels represent the poles corresponding to the smallest and largest platform displacement values, respectively.

The identified state-space models, each with algorithmically chosen state basis, are transformed to the balanced basis and then corrected to ensure basis coherency, as described in Section 4.2.2.2. To evaluate the uniqueness of the balanced coordinates, the 8 eigenvalues of the Gramian products $\mathscr{W}_c\mathscr{W}_o$ are computed for each locally identified state-space model. The variations of these eigenvalues with respect to the heave ξ_3 and pitch ξ_5 platform displacements are shown in Fig. 4.34. These eigenvalues are found to be distinct across the entire range of platform positions. Hence, the balanced coordinates are guaranteed to be unique up to a sign change and a shift between states. To achieve basis coherency, the automatic basis correction algorithm proposed in Section 4.2.2.2 is applied to align the state bases of the state-space models in the balanced form $\mathbf{A}_b, \mathbf{C}_b, \mathbf{C}_b$ at different platform positions. This step is crucial for ensuring that the local models can be interpolated for a reliable LPV representation of the FWT hydrodynamics.

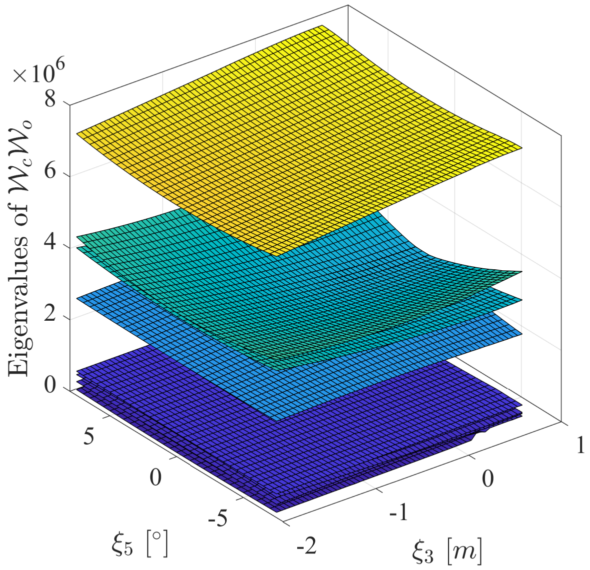

Fig. 4.34 Eigenvalues of the products of Gramians with the heave displacement ξ_3 ranging from -2 m to 0.65 m and the pitch rotation ξ_5 from $-8°$ to $8°$.

Fig. 4.35 compares the entries of the $[\mathbf{A}_b, \mathbf{C}_b, \mathbf{C}_b]$ matrices before and after basis correction. The comparison shows that random sign changes have been successfully corrected by the developed algorithm, and the entries of the system matrices exhibit smooth variations with the platform motion after basis correction. Notably, when the pitch rotation ξ_5 is fixed at $0°$, all matrix entries show monotonic variations as the platform moves upward in the heave ξ_3 direction, which is consistent with the pole evolution trends observed in Fig. 4.33(a). On the other hand, when the heave position ξ_3 is fixed at -1 m, the entries corresponding to positive and negative pitch rotation angles ξ_5 exhibit either symmetric or anti-symmetric behaviour. This satisfactorily reflects the inherent symmetry characteristics of the wave radiation frequency response $\mathbf{K}_r$. These transformed state-space models, with smooth and consistent variations in the matrix entries, are now prepared for use in the LPV interpolation process, which will be detailed later.

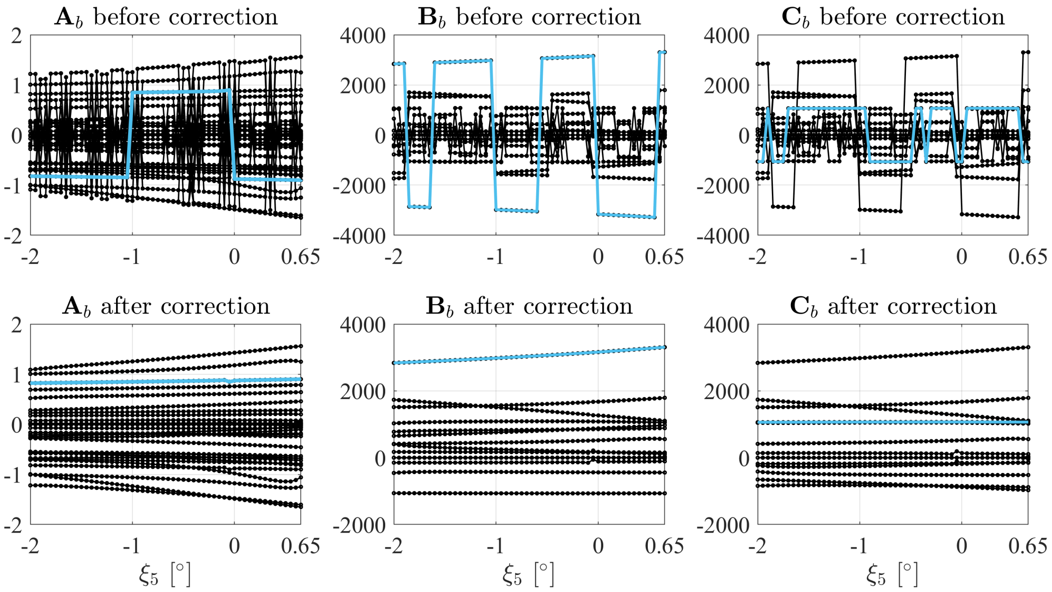

(a) Pitch fixed at $\xi_5 = 0°$, heave ξ_3 varies between -2 m $\sim$ 0.65 m

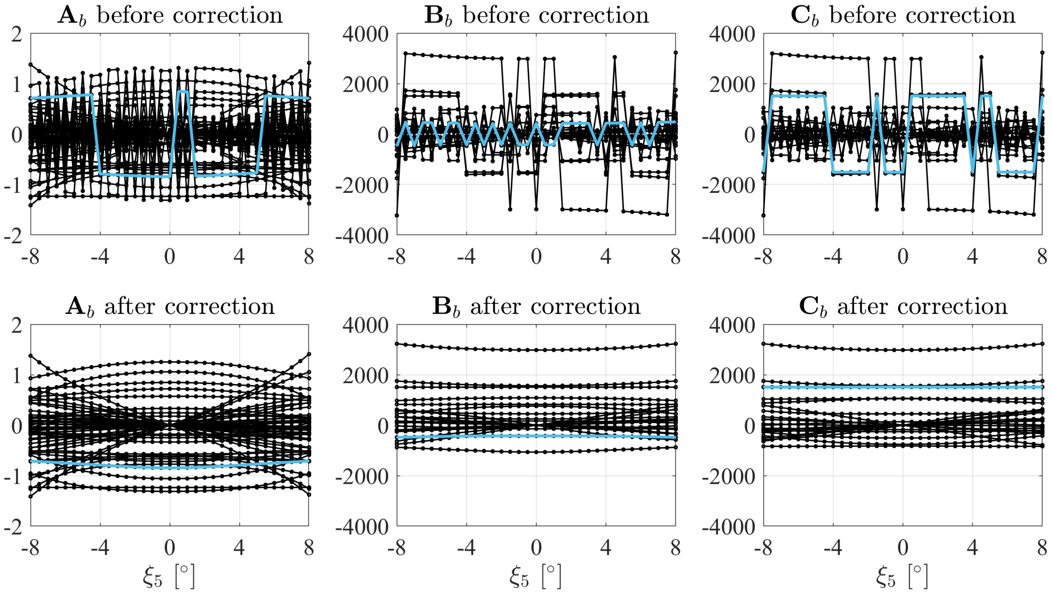

(b) Heave fixed at $\xi_3 = -1$ m, pitch ξ_5 varies between $-8° \sim 8°$.

Fig. 4.35 Variation of the entries of the state-space matrices $[\mathbf{A}_b, \mathbf{B}_b, \mathbf{C}_b]$ before and after basis correction, with different heave displacements ξ_3 and pitch rotations ξ_5. One example entry is highlighted for each of the three matrices.

4.4.1.3 Gray-box LPV modelling

In this subsection, the gray-box method using the physical form state-space model, as proposed in Section 4.2.2.3, is applied to model the geometrically nonlinear wave radiation effect for FWTs. To construct the physical state space model (Eq. (4.32), (4.33)), free-surface potential sensors and far-field potential sensors are required in addition to the conventional wave radiation force $\mathbf{F}_r$ sensors used in the black-box method described in Section 4.4.1.2.

The $\boldsymbol{\varphi}_2$ sensors are placed on the truncated far-field boundaries ($x = \pm x_\Gamma$) in the numerical BEM code. The choice of boundary truncation location is critical for accurately capturing the far-field frequency response samples, which directly affect the estimation of the proposed physical state-space model. To determine the optimal truncation location, the values obtained for the platform being in its equilibrium position from the analytical method, which provides accurate potential solutions $\boldsymbol{\varphi}_2(x,z,\omega)$ (Section 3.5.1), is used as a benchmark. Fig. 4.36 compares the analytical and numerical BEM results for $\boldsymbol{\varphi}_2$ at the vertical level $z_\Gamma = -80$ m and wave frequency $\omega = 0.1$ rad/s under different truncation location x_Γ. The results indicate that $\boldsymbol{\varphi}_2$ outputs converge as x_Γ increases, and the BEM results show good agreement with the analytical solution. Based on this comparison, $x_\Gamma = 200$ m is chosen as the optimal truncation location, ensuring both accurate $\boldsymbol{\varphi}_2$ computation and computational efficiency.

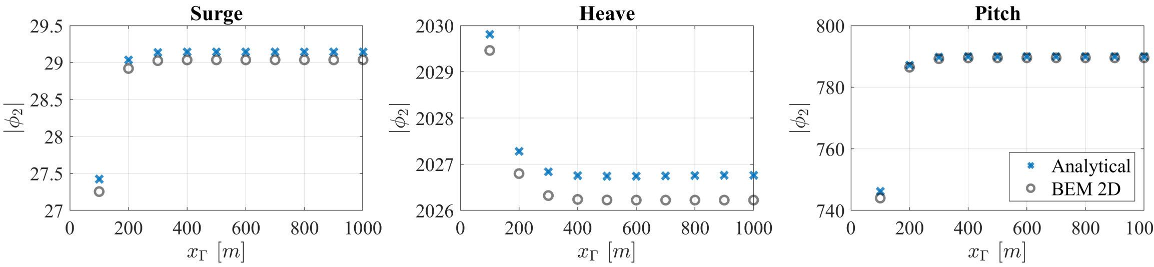

Fig. 4.36 Comparison of the analytical and numerical BEM solutions to the far-field potential φ_2 at $z_\Gamma = -80$ m with different far-field truncation location x_Γ. The platform is at its equilibrium position and the wave frequency is 0.1 rad/s.

The frequency response matrices used to identify the physical state-space model are constructed by concatenating the free-surface potential frequency response $\mathbf{K}_\varepsilon(i\omega_k)$ of size $N_1 \times 3$, the far-field potential frequency response $\mathbf{K}_\Gamma(i\omega_k)$ of size $N_2 \times 3$, and the wave radiation force frequency response $\mathbf{K}_r(i\omega_k)$ of size 3×3, where N_1 and N_2 are the number of free-surface and far-field potential sensors, respectively. This results in an augmented frequency response matrix $\mathbf{K}(i\omega_k)$ of size $(N_1 + N_2 + 3) \times 3$. In this work, $N_1 = 4$ free-surface potential sensors are placed $x_\varepsilon = \pm 24$ m and ± 28 m, while $N_2 = 8$ far-field potential sensors are set at $z_\Gamma = -50$ m, -60 m, -70 m and -80 m along the previously determined boundary truncation $x_\Gamma = \pm 200$ m. These sensors are used to construct the augmented frequency response matrices $\mathbf{K}_r(i\omega_k)$ for each platform position.

The constrained nonlinear optimization problem defined in Eq. (4.40) is solved to obtain all local state-space models in the physical form. The platform position at heave $\xi_3 = 0$ m and pitch $\xi_5 = 3^\circ$ is selected as the reference model for initialization. Due to the large amplitude differences in the frequency responses corresponding to different sensors in different DoFs, as shown in the numerical BEM results in Fig. 4.37, scaling is applied to improve fitting quality. The heave-heave wave-radiation frequency response $|K_{r3,3}|$ is used as the reference for scaling. The scaling factors for the surge and pitch DoFs for both inputs (velocity) and outputs (force) are set to 1 and 0.1, respectively, resulting in a scaling matrix of $[1\ 1\ 0.1;\ 1\ 1\ 0.1;\ 0.1\ 0.1\ 0.01]$, which is multiplied to $\mathbf{K}_r$ obtained from the BEM code. Similarly for the potentials frequency response, scaling vectors of $[10^4\ 3.33\times10^3\ 10^3]^\intercal$ and $[3.33\times10^4\ 3.33\times10^3\ 3.33\times10^3]^\intercal$ are multiplied to $\mathbf{K}_\varepsilon$ and $\mathbf{K}_\Gamma$, respectively.

Fig. 4.37 shows the optimization results for one example local model. Good agreement can be observed between the frequency responses calculated from the optimized state-space model $[\mathbf{A}_{opt}, \mathbf{B}_{opt}, \mathbf{C}_{opt}]$ and those obtained from the BEM code. Additionally, the proposed state-space model accurately captures the singularities at $\omega = 0$ in the heave DoF, which are present in both the potential frequency responses $\mathbf{K}_\varepsilon$ and $\mathbf{K}_\Gamma$. These results demonstrate the effectiveness of the physical-form state-space model in capturing the complex hydrodynamic behaviour of the wave-platform interaction system for FWTs.

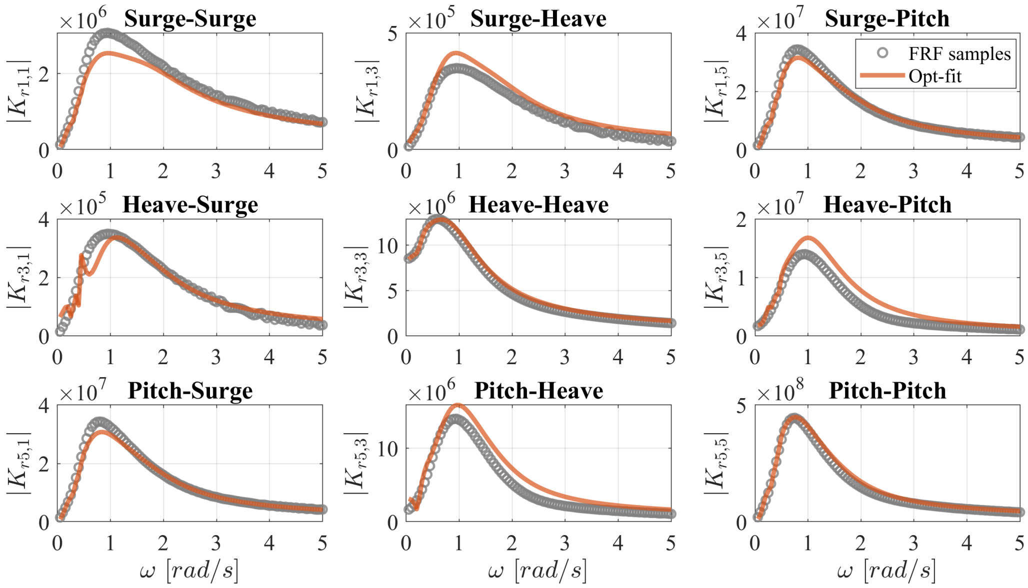

(a) Wave radiation force frequency response.

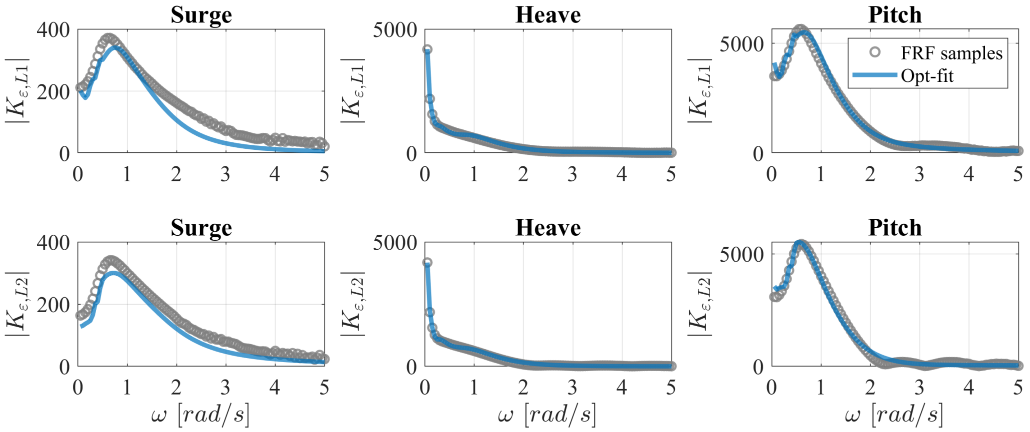

(b) Free-surface potential frequency responses at $x_{\varepsilon,L1} = -24$ m and $x_{\varepsilon,L2} = -28$ m.

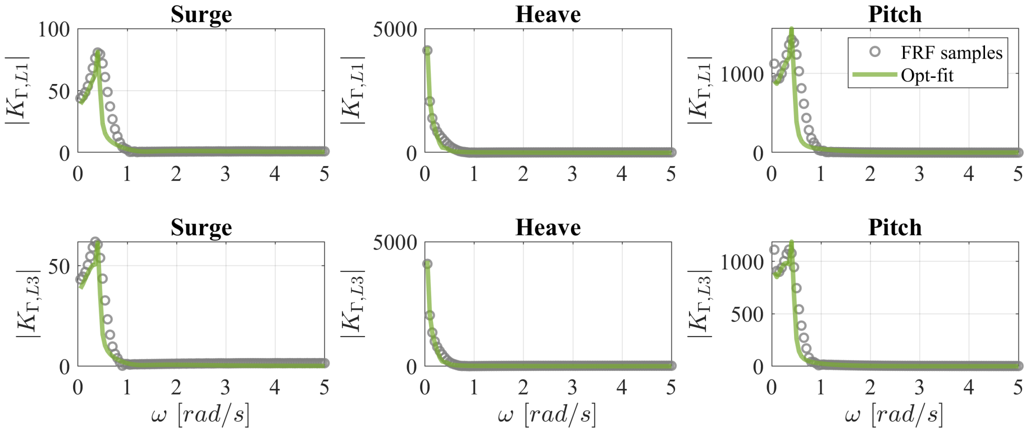

(c) Far-field potential frequency responses at $z_{\Gamma,L1} = -50$ m and $z_{\Gamma,L3} = -70$ m.

Fig. 4.37 Comparison of the wave radiation force frequency response ($\mathbf{K}_r$), and the potential frequency response on the free surface ($\mathbf{K}_\varepsilon$) and the far field ($\mathbf{K}_\Gamma$) from the optimized state-space model and BEM code at the platform position of heave $\xi_3 = -1$ m and pitch $\xi_5 = 6°$.

To evaluate the capability of the physical state-space model in capturing the variation of the dynamic characteristics for the FWT system, the evolution of poles of the optimized state-space models is analyzed. According to the structure of the physical state equation described in Eq. (4.31), the total number of states is given by $N_1 \times 2 + N_2 = 16$ for the sensors deployment strategy described above. The evolution of the 16 poles with different heave displacements under three fixed pitch rotation angles are shown in Fig. 4.38. In contrast to the black-box method, where only complex conjugate poles are present (see Fig. 4.33), the larger number of states used in the gray-box model introduces real poles. This is particularly necessary due to the singularities at $\omega = 0$ in the potential frequency responses, which require one or more poles to be sufficiently close to the imaginary axis. This condition is satisfied by the presence of a real pole, labeled as "Pole 1" in Fig. 4.38.

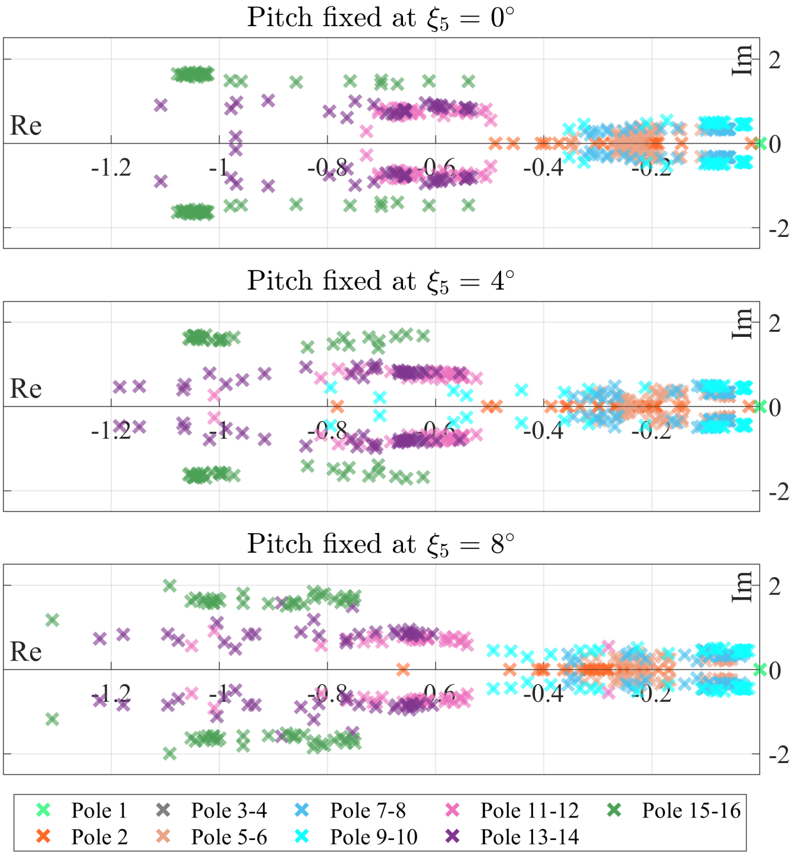

Fig. 4.38 The evolution of poles of the optimized physical state-space models with the platform heave displacements ξ_3 from -2 m to 1 m under three fixed pitch rotations (ξ_5).

The evolution of the poles with varying heave displacements ξ_3 demonstrates relatively smooth paths, which is expected for linear systems obtained by nearby linearizations of an underlying smooth non-linear system. This implies that the optimization process successfully captures the nonlinear dynamic characteristics of the wave-platform system. However, as the pitch rotation angle ξ_5 increases, the poles tend to deviate more, reflecting the increased complexity of the system dynamics. This rapid change is also observed in Fig. 4.39, where the variations in the entries of the optimized state-space matrices $[\mathbf{A}_{opt}, \mathbf{B}_{opt}, \mathbf{C}_{opt}]$ and the physical state-space matrices $[\mathbf{A}_p, \mathbf{B}_p, \mathbf{C}_p]$ are compared. Fig. 4.39(a) shows the variations with different heave displacements ξ_3 under a fixed pitch rotation ξ_5, while Fig. 4.39(b) shows the variations with different pitch rotations ξ_5 under a fixed heave position ξ_3.

Again, it can be found that the entries of the matrices for the physical state-space models are changing more rapidly than those of the optimized state-space models. The large difference in magnitude between $[\mathbf{A}_{opt}, \mathbf{B}_{opt}, \mathbf{C}_{opt}]$ and $[\mathbf{A}_p, \mathbf{B}_p, \mathbf{C}_p]$ arises from the ill-conditioning of the transformation matrix $\mathbf{T}$ (see Eq. (4.35)). This ill-conditioning is a consequence of deploying sensors at the same vertical levels on the left and right far-field boundaries. While this sensor placement preserves the symmetry in the frequency response functions for positive and negative platform pitch rotations, it also causes the corresponding rows of $\mathbf{T}$ to be nearly linearly dependent. As a result, $\mathbf{T}$ has a very large condition number, and eventually leads to an ill-conditioned set of $\mathbf{A}_p, \mathbf{B}_p, \mathbf{C}_p$ matrices.

Therefore, the optimized models $[\mathbf{A}_{opt}, \mathbf{B}_{opt}, \mathbf{C}_{opt}]$ are selected for subsequent LPV interpolation. Additionally, no clear trend is observed in the entries of the matrices $[\mathbf{A}_{opt}, \mathbf{B}_{opt}, \mathbf{C}_{opt}]$ as the platform rotates under fixed heave displacement, as shown in Fig. 4.39(b). This lack of trend might be attributed to the limited number of states used in the model. Although increasing the number of states could improve the model's ability to capture complex dynamics, it also complicates the nonlinear optimization process, making it more likely to yield suboptimal solutions. In this work, a state number of 16 is chosen as a compromise between model accuracy and computational feasibility. The performance of this model will be further discussed in subsequent sections.

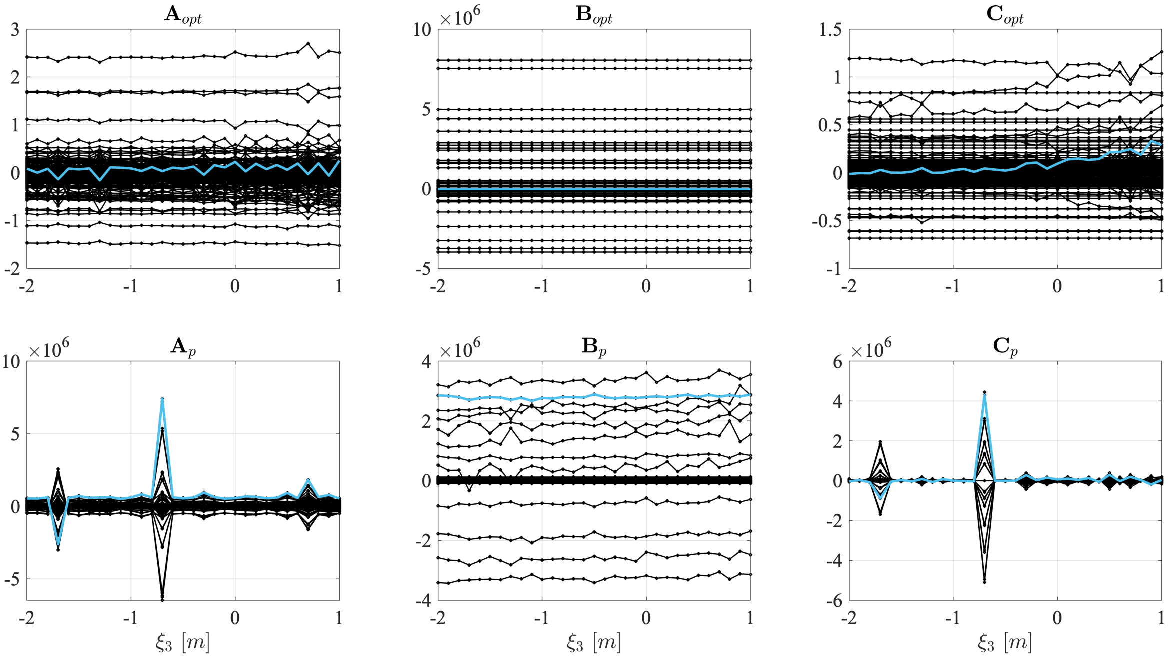

(a) Pitch fixed at $\xi_5 = 6°$, heave ξ_3 varies from -2 m to 1 m

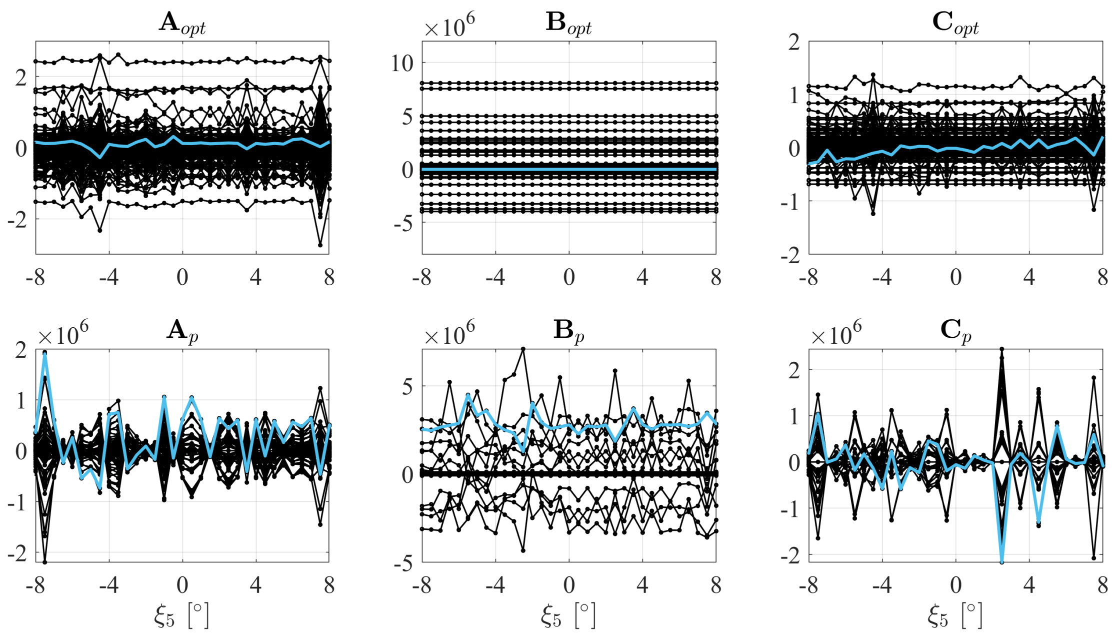

(b) Heave fixed at $\xi_3 = 0$ m, pitch ξ_5 varies from $-8°$ to $8°$.

Fig. 4.39 Variation of the matrix entries of the optimized state-space models $[\mathbf{A}_{opt}, \mathbf{B}_{opt}, \mathbf{C}_{opt}]$ and physical state-space models $[\mathbf{A}_p, \mathbf{B}_p, \mathbf{C}_p]$ with different platform heave (ξ_3) and pitch (ξ_5) displacements.

4.4.1.4 Simulink implementation

The proposed grid-based LPV method for FWT hydrodynamics modelling is implemented in Simulink and integrated with other physical domains in the Simulink FWT model developed in Section 2.3. This integration allows for a comprehensive evaluation of the nonlinear FWT dynamics by coupling the hydrodynamic, aerodynamic, structural, and control subsystems within a unified simulation environment. To constrain the platform motion to a 2D space with 3 DoFs of surge (ξ_1), heave (ξ_3) and pitch (ξ_5), the `6-DOF Joint` used in the original Simulink FWT model, as illustrated in Fig. 2.9, is replaced with a `Planar Joint` as shown in Fig. 4.40. The blade and tower structural dynamic, aerodynamic, and control subsystems from the original Simulink FWT model are retained.

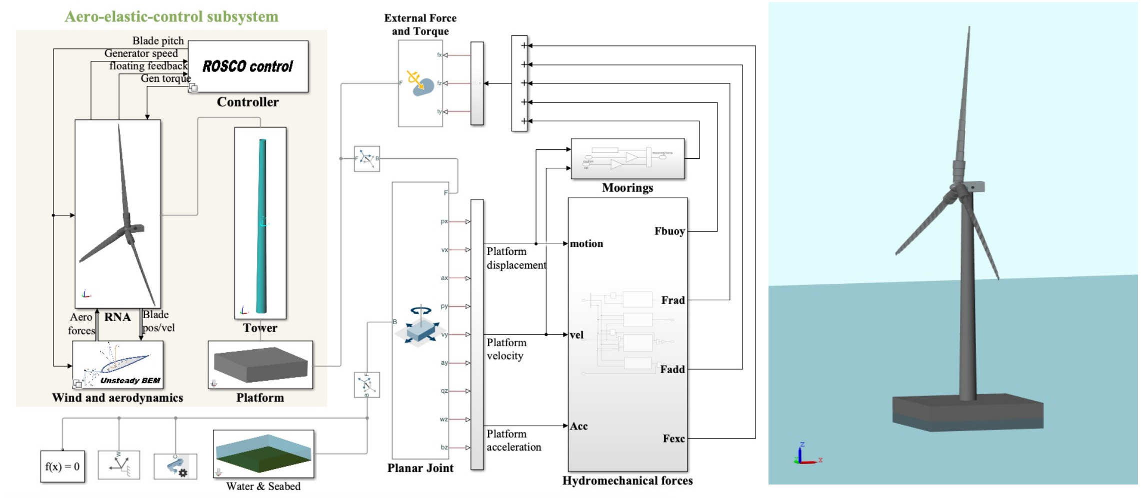

Fig. 4.40 Simulink implementation of the FWT system with nonlinear hydrodynamics.

Given the large platform movements typically experienced by FWTs, the original mooring restoring effect represented by a linear stiffness matrix K_{moor} (described in Section 2.3.3) is insufficient for accurately modelling the mooring restoring forces, and hence is replaced by a nonlinear mooring subsystem. According to Masciola et al. [84], the nonlinear mooring forces are calculated by solving the nonlinear catenary equations for specified combinations of surge (ξ_1), heave (ξ_3), and pitch (ξ_5) displacements. The variation of nonlinear mooring forces with respect to platform displacements is plotted in Fig. 4.41. The results indicate that the surge restoring force exhibits a much stronger nonlinear effect compared to the heave and pitch forces. For comparison, the linear mooring stiffness K_{moor} effect in surge is also plotted in Fig. 4.41. As expected, the linear force is tangential to the nonlinear force at zero surge displacement (ξ_1). To incorporate these nonlinear mooring forces into the Simulink FWT model, 3D interpolation arrays are defined separately for each of the three mooring forces using `n-D Lookup Table` Simulink blocks within the mooring subsystem. These interpolation arrays use the instantaneous platform displacements as inputs to calculate the nonlinear mooring forces in real time during the simulation. In this work, the mooring damping force is still assumed to be linear and is represented by a constant damping matrix C_{moor}, as described in Section 2.3.3.

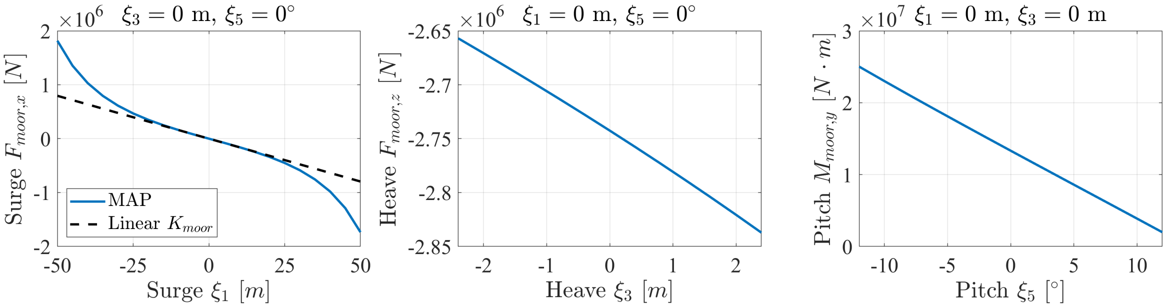

Fig. 4.41 Nonlinear mooring line restoring forces.

To accommodate large platform motions in the FWT hydrodynamic calculation, the linear hydrodynamic subsystem in the original Simulink FWT model is replaced by a nonlinear subsystem. This modification ensures that the wave-platform interactions are represented more realistically, especially when the platform experiences significant heave (ξ_3) and pitch (ξ_5) displacements. The framework for the nonlinear FWT hydrodynamics modelling is illustrated in Fig. 4.42. The nonlinear hydrodynamic properties of the dynamic buoyancy force ($\mathbf{F}_b$) and infinite-frequency added mass ($\boldsymbol{\lambda}_\infty$) that are computed at different heave and pitch displacements, as shown in Fig. 4.29, are incorporated into 2D interpolation arrays using `n-D Lookup Table` blocks within the nonlinear hydrodynamic subsystem in Simulink (Fig. 4.42). This allows for real-time updates of these hydrodynamic properties based on the instantaneous platform displacements. It is important to note that in this work, the wave excitation forces are still calculated from the hydrodynamic coefficients obtained by linearizing the BVP around the equilibrium platform position, as described in Section 2.3.3, and the geometric nonlinearity due to the time-varying wetted body surface is not taken into account.

The LPV modelling methodology for the wave radiation damping effect, using either the black-box or gray-box method as described in Sections 4.4.1.2 and 4.4.1.3, respectively, is implemented in Simulink using the `LPV System` block, as highlighted in Fig. 4.42. This block allows for real-time evaluation of the nonlinear wave radiation damping forces $\mathbf{F}_r$, by linearly interpolating the coherent state-space matrices based on the instantaneous platform displacements in heave (ξ_3) and pitch (ξ_5).

For the black-box LPV model, the balanced-form state-space matrices $[\mathbf{A}_b, \mathbf{B}_b, \mathbf{C}_b]$ obtained after basis correction (illustrated in Fig. 4.35) are constructed into a 2D interpolation array. This array is configured in the `LPV System` block, with the grid points of ξ_3 and ξ_5 displacements specified to determine the real-time nonlinear wave radiation damping force $\mathbf{F}_r$ based on the instantaneous platform position. Similarly, the gray-box LPV model implementation uses the optimized state-space matrices $[\mathbf{A}_{opt}, \mathbf{B}_{opt}, \mathbf{C}_{opt}]$ and their corresponding ξ_3

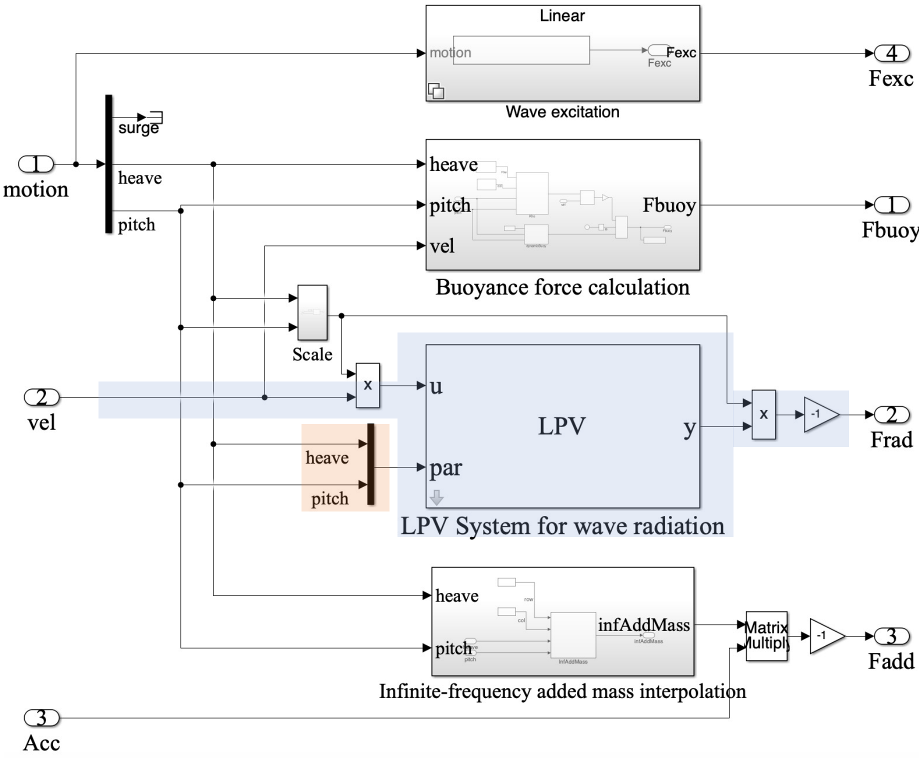

Fig. 4.42 Simulink nonlinear hydrodynamic subsystem using LPV modelling approach.

and ξ_5 grid points, as shown in Fig. 4.39. These matrices are defined within the `LPV System` block to compute the nonlinear radiation damping forces $\mathbf{F}_r$. It is important to note that the state-space models identified from the scaled frequency response samples must be rescaled to their original amplitude. This is achieved by applying a scaling factor of $[1\ 1\ 10]^\intercal$ for both the input (platform velocity) and output (wave radiation force).

Overall, integrating the nonlinear mooring and hydrodynamic subsystems within the Simulink FWT model significantly enhances its ability to capture the complex nonlinear dynamics of the entire FWT system under large platform motions. The updated FWT model enables a comprehensive evaluation of the global dynamic behaviour of the FWT system under various environmental and operational conditions, especially in scenarios where the conventional mooring and hydrodynamic models with linear assumptions may fall short.

4.4.2 Irregular wave response analysis

To assess the effectiveness of the proposed LPV modelling methodology, wave response analysis is performed on the Simulink model of the example NREL 5-MW ITI-Barge FWT. The study utilizes an irregular wave condition defined by the Jonswap spectrum, with a significant wave height of 5 m and a peak-spectral period of 10 s, to generate the wave excitation forces ($\mathbf{F}_e$) based on Eq. (2.5). This wave condition represents a typical moderate sea state, making it ideal for evaluating the platform's nonlinear response under moderately large motions that are likely to induce complex dynamic behaviour. The time histories of the wave excitation forces $\mathbf{F}_e$ in the surge, heave, and pitch DoFs are plotted in Fig. 4.43. These forces are applied to the Simulink FWT model to excite platform motions and analyze its response. To focus exclusively on the geometrically nonlinear platform response, the FWT model is configured with simplified assumptions of rigid blades and tower, and with the aerodynamic and control subsystems disabled.

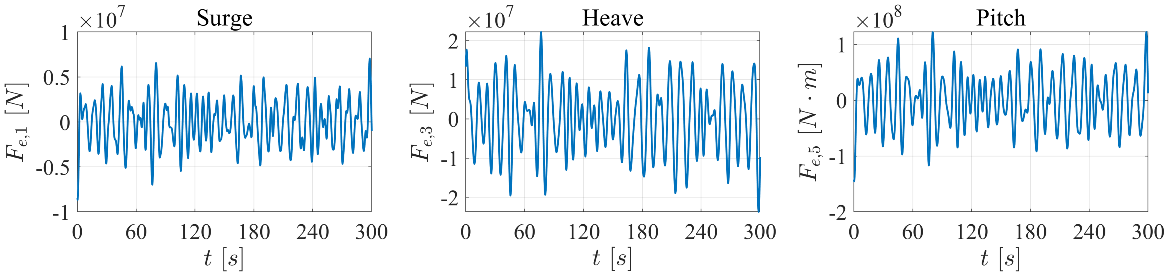

Fig. 4.43 Wave excitation forces $\mathbf{F}_e$ for the irregular wave response analysis.

Fig. 4.44 compares the platform responses calculated using OpenFAST, a Simulink model with purely linear hydrodynamics, and Simulink models with nonlinear hydrodynamics employing either the nonlinear convolution integral method or various LPV methods for the wave radiation damping force computation. The LPV methods differ in their state-basis transformation strategies: the inconsistent form uses the identified state-space models with algorithmically chosen state bases that are generally incoherent (labelled as "LPV-inconsistent"), the balanced form ensures relaxed basis coherency through balanced transformation and basis correction (labelled as "LPV-balanced"), and the optimized physical form guarantees a strictly coherent basis tied to physical parameters of the system and well numerical-conditioning (labelled as "LPV-opt"). This comparison illustrates how these state-basis choices influence the LPV models' ability to capture nonlinear platform hydrodynamics accurately.

The results presented in Fig. 4.44 show that the linear Simulink model is in excellent agreement with OpenFAST, further validating its accuracy in representing linear hydrodynamics. However, when geometric nonlinearities are considered, the nonlinear platform surge responses (ξ_1) estimated by the nonlinear convolution method and LPV methods, whether using balanced or optimized physical forms, deviate significantly from the linear response, whereas the differences in heave (ξ_3) and pitch (ξ_5) responses are relatively small. These large discrepancies in surge are attributed to the combined effects of multiple nonlinear factors: the

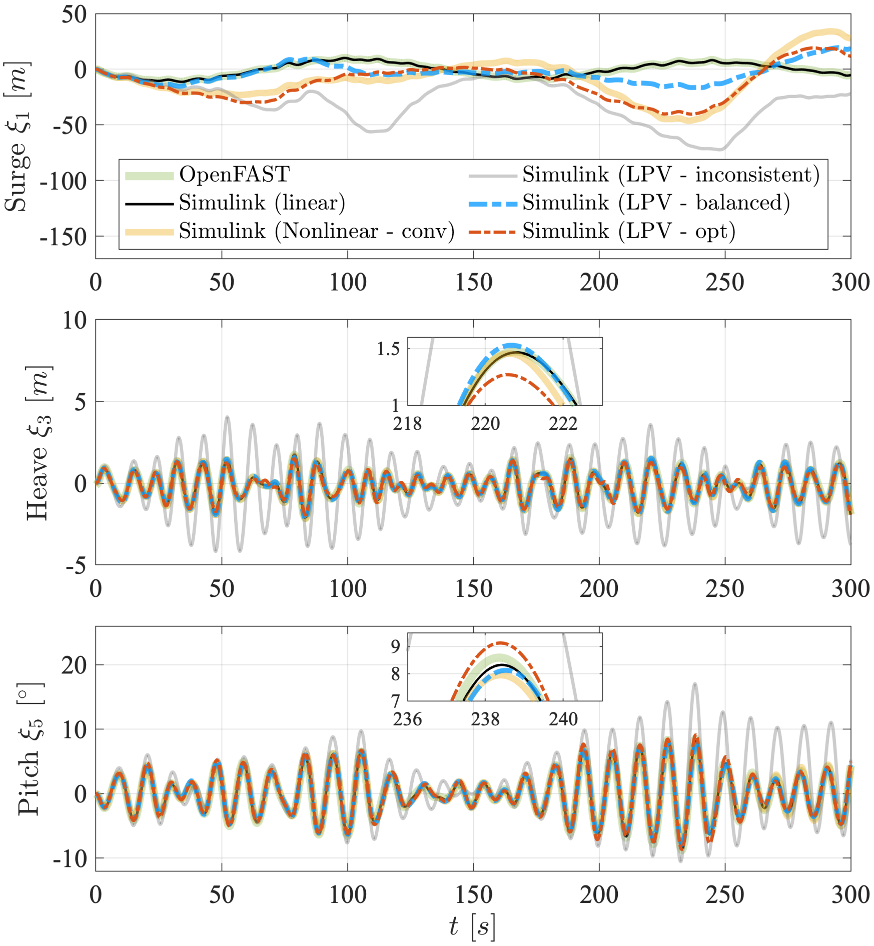

Fig. 4.44 Platform responses of the 5MW ITI-Barge FWT calculated from OpenFAST and various Simulink models, under the wave excitation force shown in Fig. 4.43.

nonlinear mooring restoring force ($\mathbf{F}_{moor}$) shown in Fig. 4.41, the pose-dependent additional inertia ($\boldsymbol{\lambda}_\infty$) shown in Fig. 4.29(a), and the pose-dependent wave radiation damping ($\mathbf{F}_r$) shown in Fig. 4.30. The restoring force in the surge DoF relies primarily on the highly compliant mooring lines, resulting in a very low effective stiffness in the surge direction for the nonlinear wave-platform system. Consequently, for such a nonlinear system characterized by a weak attractor, even minor differences in the wave radiation damping force $\mathbf{F}_r$ occurring from different LPV models can lead to substantial discrepancies in surge responses.

As can be found in Fig. 4.44, both the LPV-balanced and the LPV-optimized models show good agreement with the benchmark nonlinear convolution model, indicating that the proposed LPV modelling provides a coherent state basis capable of capturing the geometric nonlinearity. Additionally, the LPV-optimized model predicts the surge response more accurately compared to the LPV-balanced model. In contrast, the LPV approach using the originally identified state-space models without ensuring state-basis coherency results in significantly larger and erroneous platform responses, as observed in Fig. 4.44. This outcome emphasizes the critical importance of using a coherent state basis when applying LPV modelling to represent nonlinear wave-platform interactions. Ignoring this requirement can lead to inaccurate platform hydrodynamics, undermining the reliability of the overall dynamic analysis for FWTs.

Additionally, the proposed LPV modelling approach offers a significant advantage in computational efficiency, as shown in Table 4.3 for a 300-s simulation of the irregular wave response analysis. The computational efficiency of LPV models is comparable to the linear model, while the nonlinear convolution solver is significantly more computationally expensive. The higher-fidelity body-nonlinear potential solver described in Fig. 4.1 can take several hours to complete the same simulation. This favorable trade-off between accuracy and computational efficiency makes the proposed LPV method an effective and practical tool for evaluating nonlinear FWT dynamics during the early stages of design, where thousands of simulations are required to explore various configurations and design parameters.

Table 4.3 Comparison of wave-platform solvers (300-s simulation).

	Linear	LPV balanced	LPV opt physics	Nonlinear conv
No. states	8	8	16	/
CPU time	70s	82s	86s	13 min

4.4.3 Nonlinear analysis

Nonlinear analysis using numerical frequency sweep tests, similar to the approach applied to the van Daalen floating cylinder described in Section 4.3.3, is conducted on the Simulink model of the example 5-MW ITI-Barge FWT. The primary objective is to evaluate the influence of geometric nonlinearities on the overall dynamic behaviour of the FWT platform. Both wave-only and combined wind-wave tests are carried out to investigate the nonlinear coupling effects under various environmental loading conditions. A wind-only test is also conducted for the purpose of comparison.

4.4.3.1 Wind-only excitation

A constant wind speed of 11.4 m/s (i.e., the rated wind speed for NREL 5-MW turbines) is applied uniformly across the entire rotor span, simulating the steady-state aerodynamic loading condition. The aerodynamic forces on each blade are calculated using the dynamic blade-element momentum method, as detailed in Fig. 2.7. The ROSCO control strategy, as described in Fig. 2.8, is implemented to regulate the blade pitch. For this study, the floating feedback loop in the ROSCO control subsystem is disabled to avoid control-induced damping. To isolate the hydrodynamic response and simplify the analysis, the blades and tower are assumed to be rigid. The OpenFAST model of the example FWT is configured with similar settings of the aerodynamic and control modules as in the Simulink model, to provide a reference as a standard FWT simulation tool adopting linear hydrodynamics.

Fig. 4.45 presents the platform responses and turbine opration conditions under the wind-only excitation, calculated using OpenFAST as well as Simulink models with linear, nonlinear convolution integral, LPV-balanced, and LPV-optimized assumptions. It can be found that the discrepancies between all models are not pronounced due to the small platform heave and pitch motions under wind-only excitation. In this case, the linear potential flow assumption remains valid, and a purely linear model is sufficient to capture the dominant FWT dynamics.

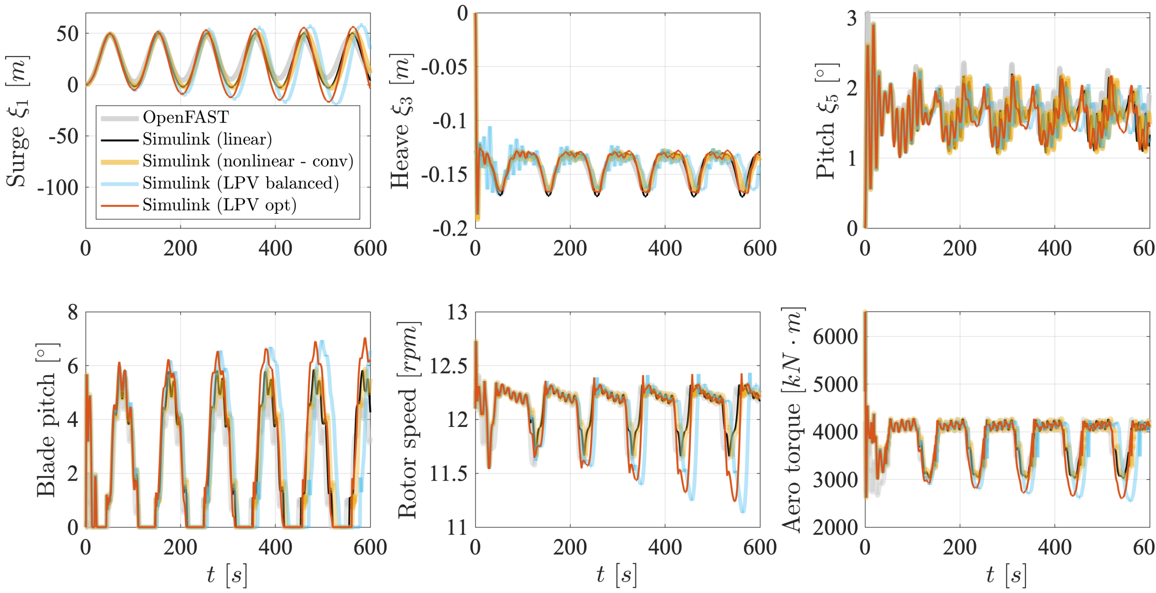

Fig. 4.45 Platform responses of the example FWT under a constant wind excitation with the wind speed of 11.4 m/s.

4.4.3.2 Wave-only excitations

A total of 34 sinusoidal waves with a wave height of 4 m and wave periods ranging from 6.28s to 209.44s, corresponding to wave frequencies between 0.0048 Hz and 0.1592 Hz, are selected to generate wave excitation forces. These sinusoidal forces at various wave frequencies are applied one at a time to the platform centroid in the Simulink model. The blades and tower are assumed to be rigid, and the aerodynamic and control subsystems are disabled. For each wave frequency, the simulation is run for a sufficiently long duration to allow the platform responses to reach steady state, ensuring that accurate response amplitudes are extracted. The aim is to provide a comprehensive evaluation of the FWT's hydrodynamic behaviour over a wide frequency range and help identify platform resonances and nonlinear effects.

Fig. 4.46 presents the platform responses calculated from both OpenFAST and the Simulink models with various assumptions under a wave period of 11.97 s (0.0835 Hz). The wave excitation frequency used in Fig. 4.46 is close to the platform's pitch resonance frequency of 0.0841 Hz, as shown in the eigenanalysis results in Table.2.3. Consequently, a peak in the pitch response amplitude can be observed in the pseudo frequency response plot obtained from a frequency sweep test, as shown in Fig. 4.47. Additionally, it can be seen in Fig. 4.47 that the platform's surge resonance frequency of 0.0071 Hz is successfully captured, while the heave resonance at 0.1274 Hz is not having a very distinct peak in the corresponding frequency response plot.

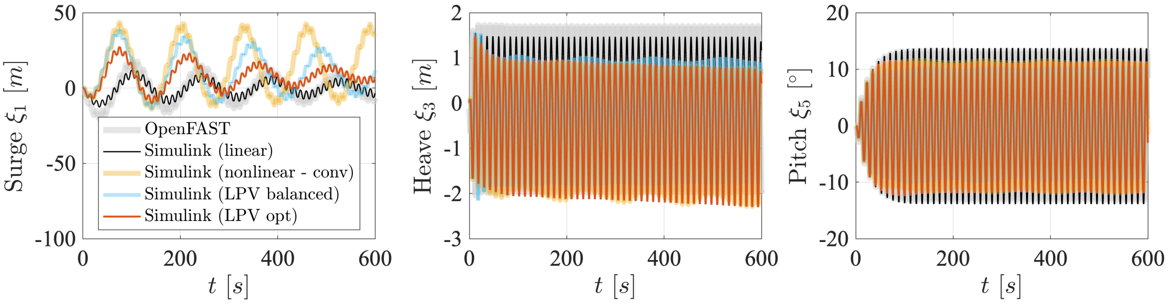

Fig. 4.46 Platform responses of the example FWT under a regular wave excitation with the wave height of 4 m and period of 11.97s.

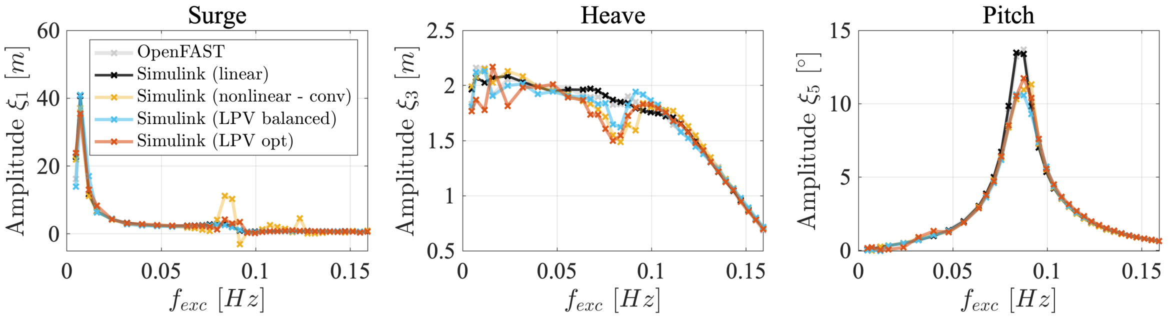

Fig. 4.47 Pseudo frequency responses of the example FWT under regular wave excitations with the frequencies ranging from 0.0048 Hz to 0.1592 Hz.

Regarding the resonance amplitudes, the nonlinear hydrodynamic models are found to reduce the peak pitch response by approximately 20% when compared to the linear model. The heave response amplitude corresponding to the pitch resonance frequency (0.0835 Hz) is also reduced by around 20%. These findings suggest an increased damping effect when the geometric nonlinearity in the wave-platform interaction is considered. Additionally, the LPV-optimized model shows slightly larger damping than the LPV-balanced and nonlinear convolution models, especially in the surge response.

4.4.3.3 Combined wind-wave excitations

The frequency sweep analysis is repeated for the example FWT under simultaneous wind and wave excitations to investigate the combined effects on the nonlinear platform dynamics. Similar to the wave-only simulations, the blades and tower are set to be rigid.

Fig. 4.48 compares the platform responses, turbine operating conditions, and aerodynamic torque calculated from both OpenFAST and the Simulink models with various assumptions at a wave period of 11.97s. Periodic oscillations in the aerodynamic torque are observed in the simulation results of Fig. 4.48, which correspond to fluctuations in the blade pitch angle and rotor speed. These oscillations can be attributed to frequent transitions between the two control regions corresponding to the wind speeds above and below the rated speed, induced by the platform pitch motion. The fluctuations in platform rotation cause the relative wind speed experienced by the rotor to change dynamically, triggering frequent control adjustments. These oscillations are much larger in the OpenFAST results compared to the Simulink models, which may be due to differences in the coupling methods of the aerodynamic and control subsystems in the two modelling environments. OpenFAST's coupling appears to be more sensitive to platform motions than the Simulink model. Nonetheless, the overall platform responses between the two models remain fairly consistent.

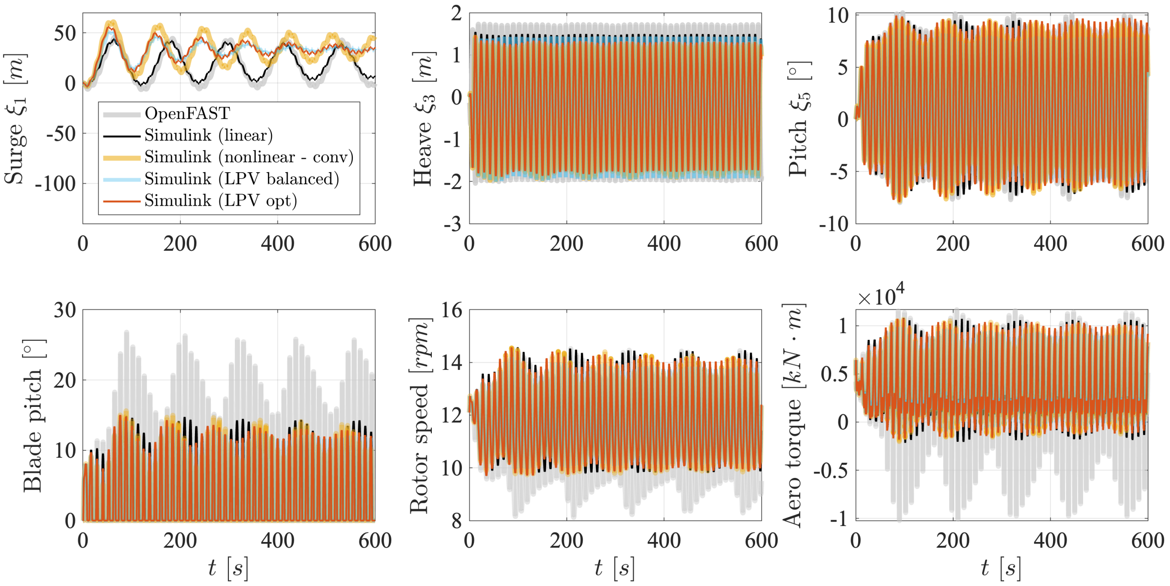

Fig. 4.48 Platform responses of the example FWT under simultaneous constant wind speed of 11.4 m/s and regular wave excitation with the height of 4 m and period of 11.97s.

As demonstrated in Fig. 4.48, incorporating geometrically nonlinear hydrodynamics in the wind-wave analysis does not significantly alter the pitch amplitude compared to the linear response. This contrasts with the wave-only analysis results shown in Fig. 4.46, where nonlinear effects result in noticeable changes in the platform response. This discrepancy is further illustrated in the pseudo frequency responses presented in Fig. 4.49, which compare wave-only (dashed curves) and combined wind-wave (solid curves) frequency responses. While nonlinear hydrodynamics significantly influence the platform pitch responses in the wave-only scenario, their effect is less pronounced in the presence of wind. This is primarily due to the dominant effect of the aerodynamic forces on the platform pitch dynamics. In contrast, the heave amplitude, approximately around the pitch resonance frequency, is consistently reduced irrespective of wind, which is attributed to the negligible aerodynamic forces acting in the vertical direction.

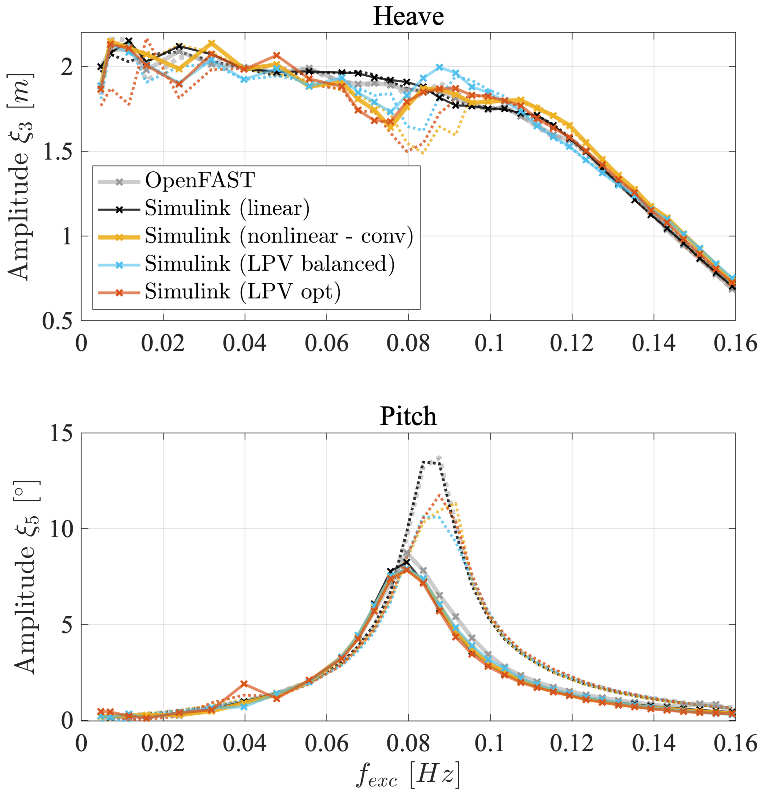

Fig. 4.49 Pseudo frequency responses of the example FWT under simultaneous constant wind speed of 11.4 m/s and regular wave excitation with the frequency ranging from 0.0048 Hz to 0.1592 Hz. Thick curves represent wind-wave responses, while dashed curves represent wave-only responses.

Another important observation from Fig. 4.49 is that the presence of wind suppresses the platform pitch resonance amplitudes whereas amplifies the heave amplitudes in the Simulink nonlinear models compared to the wave-only responses, as shown in Fig. 4.49. Additionally, the pitch resonance frequency decreases when wind is present. The suppression in pitch resonance amplitude is attributed to the well-known aerodynamic damping effect, which introduces additional damping that mitigates platform rotations. In contrast, the increased heave amplitudes, as well as the reduced pitch resonance frequency, suggest complex nonlinear couplings between aerodynamics, platform hydrodynamics, and control systems. These interactions potentially alter the energy distribution between different DoFs, highlighting the importance of accurate nonlinear FWT hydrodynamics modelling to capture the intricate coupled dynamics of FWT systems under realistic environmental and operational conditions.

4.5 Conclusions

A novel LPV modelling methodology to capture the geometrically nonlinear hydrodynamic forces acting on FWTs under large platform motions is proposed in this work. The main contribution is the development of a physical state-space representation derived from a finite element formulation of the wave-platform interaction system. This physical state basis is leveraged to construct a gray-box LPV model that effectively addresses the state-basis incoherency issue. This issue is a common problem in traditional state-space identification methods that results in inconsistent state-space coordinates across different platform positions. In addition to this gray-box approach, an enhanced black-box LPV model featuring the balanced transformation and an automatic basis correction technique is developed to ensure coherent state-space representations across the full range of platform positions.

The effectiveness of the proposed gray-box (physical form) and black-box (balanced form) LPV modelling techniques is verified using the benchmark van Daalen floating cylinder model. Through free oscillation and frequency sweep tests, the LPV models are found to successfully capture the nonlinear effects of decreased oscillation period and increased damping as the cylinder rotation increases. Following the verification, the LPV model with a consistent state basis is integrated with the superstructure, aerodynamic, control, and nonlinear mooring subsystems in the Simulink FWT model to evaluate the impact of geometrically nonlinear hydrodynamics on the global dynamic behaviour of the FWT. Both the balanced form and the physical form LPV models accurately predict the nonlinear platform responses of the example 5-MW ITI-Barge FWT except in the surge DoF, where the very low effective stiffness makes the system sensitive to disturbances. Another significant observation from this work is that using the bases directly obtained from identification algorithms, without further transformation, can lead to erroneous results. This is evident from the significant variations observed in the transformation matrices between the identified and coherent bases over different platform positions.

Additionally, a nonlinear analysis of the Simulink FWT model coupled with the LPV hydrodynamic system is conducted. When subjected to wave excitations alone, the inclusion of geometric nonlinearities reduces the resonance amplitude in the pitch response of the example FWT. However, when wind is present, this effect is significantly diminished due to the dominant aerodynamic damping effect, highlighting the complex interaction between hydrodynamics, aerodynamics, and control systems in the FWT system.

Moreover, the proposed LPV approaches demonstrate significant computational efficiency, requiring only a fraction of the time needed by higher-fidelity body-nonlinear solvers, which involve re-meshing the wetted body surface at each time step. This efficiency, combined with their validated capability to capture nonlinear hydrodynamic effects, makes the LPV method a fast and robust tool for the preliminary design and optimization phases of FWT systems, where numerous design iterations are often necessary. Furthermore, the state-space representation inherent in the LPV system provides additional advantages in control system design, enabling the integration of geometric nonlinearities into the control strategy. This allows for a more accurate representation of varying stiffness and damping properties as the platform undergoes large movements, and contributes to improved overall performance and stability of the FWT system under various operating conditions.

Notably, the proposed LPV modelling aproach may not be applicable to all floating wind turbine concepts. This limitation arises from the fundamental assumption that variations in the scheduling parameter are slow relative to system dynamics, so as to ensure an effective LPV approximation of the original time-varying system. If this assumption is violated, for example, when the platform's natural frequencies exceed the fluid-body resonance frequencies, which is likely on tension-leg platforms stabilized by high-stiffness tendons, the influence of higher-order time derivatives of the scheduling parameter becomes significant. In such cases, the applicability of the proposed LPV model should be carefully re-evaluated.

In conclusion, this research presents a practical and effective solution for modelling nonlinear hydrodynamic forces in FWT systems. It demonstrates that the idea of using linearized systems requires careful consideration of the bases that are used. The study also presents two different ways of choosing a coherent base. Future work will focus on extending the model to fully 3D platform movements and incorporating nonlinear wave excitation forces, which will further enhance its applicability to complex FWT simulations. Moreover, the versatility of the LPV approach makes it suitable for a wide range of engineering applications beyond FWTs, where systems can be represented by a combination of linear models with parameters slowly evolving as a function of measurable variables. This includes applications such as highly elastic mechanical systems parameterized by displacement, aircraft dynamics parameterized by angle of attack, etc.

Chapter 5

Conclusions

This thesis develops a comprehensive modelling framework for the dynamic analysis of FWTs in the Simulink environment. Chapter 2 describes the modelling methodologies and investigation for dominant FWT physics with a comparable fidelity to widely used FWT simulation tools. The wave-platform interaction effects are evaluated around the equilibrium platform position using linear potential flow theory. Chapter 3 addresses the limitations of this conventional linear hydrodynamic model by proposing a novel analytical solution to the 2D wave-platform BVP, which is linearized at an arbitrary platform pose. This sets the stage for using linearized models to investigate nonlinear wave-platform interactions caused by large platform motions in Chapter 4. Finally, Chapter 4 introduces a novel LPV modelling framework to incorporate these linearized models, with black-box and gray-box methods proposed to ensure the state-basis coherency for reliable evaluation of nonlinear hydrodynamic forces. This chapter summarizes the major findings and contributions from each chapter and outlines potential directions for future research.

5.1 Findings and contributions

In Chapter 2, the newly developed Simulink FWT model was found to successfully capture the dominant coupling effects between various physical domains of a FWT system. Specifically, for wave-platform interaction, the newly proposed direct-MIMO subspace state-space identification technique demonstrated accuracy and efficiency in representing wave radiation and excitation effects, compared to conventional multi-SISO methods; for structural modelling, the multibody formulation coupled with Craig-Bampton model reduction technique was demonstrated to accommodate large geometrically nonlinear blade deformations, as validated against the high-fidelity BeamDyn solver in OpenFAST; for aerodynamics calculation, the implemented dynamic inflow and stall models were shown to accurately capture variations in rotor behaviour due to platform pitch rotations; for controls, the employed ROSCO control strategy featuring a floating feedback loop was demonstrated to effectively regulate power output and mitigate platform instability. Furthermore, the above-mentioned important FWT dynamics are investigated holistically in the Simulink model on the example NREL 5-MW ITI-Barge FWT model through a modal analysis and a fully coupled time-domain dynamic analysis under realistic wind and wave excitations. The significant one-way coupling from the platform surge-heave-pitch motions, to the tower fore-aft, and eventually to the blade flapwise vibrations was observed from the analysis results. In addition, the neglected skewed wake effects in the developed Simulink aerodynamic model were shown to have limited impact on the structural and operational responses of the FWT system for below-rated wind conditions. However, their effects should be re-investigated at higher wind speeds.

The Simulink model developed in Chapter 2 contributes to a new FWT simulation alternative for the research community and industry. The model offers flexibility to switch between different modelling fidelities for each subsystem, which is particularly useful for performing multiple simulation tasks, ranging from rapid conceptual design checks to standard design load analyses under various environmental and operational conditions. Moreover, it allows for easy integration with advanced subsystem models, such as the nonlinear hydrodynamic model developed in Chapter 4, and other mechanical, electrical subsystems for a more sophisticated FWT model. It also enables extensive simulation objectives, such as structural health monitoring and control co-design.

In Chapter 3, the newly proposed analytical approach using a step approximation of the body boundaries and eigenfunction expansion method showed good agreement with the numerical boundary element method for an example barge-type platform under the submergence cases of rectangular, trapezoidal, and 45-45-90 triangular shape. The platform rotation was shown to introduce non-zero and even negative surge-heave and heave-pitch couplings in the hydrodynamic coefficients, unless the submergence area is perfectly symmetric, highlighting the importance of considering the time-varying platform submergence when evaluating the wave-platform interaction effects. Moreover, the analytical method offers superior computational efficiency, especially in cases involving simple rectangular submergence.

The major contribution of Chapter 3 is that it provides an alternative to popular numerical boundary element methods for solving the wave-platform BVP. Compared to the numerical analysis results, the analytical results are free from irregular numerical oscillations and they offer deeper insights into the potential flow physics in the entire fluid domain. Another important contribution of the developed analytical method is that it has broad applicability beyond FWTs, including floating breakwaters of different shapes, floating bridge piers, vessels, and other floating structures characterized by 2D flow characteristics.

In Chapter 4, the proposed black-box LPV model based on the balanced realization and an automatic basis correction technique, and the gray-box LPV model based on the physical state-space representation derived from the finite element formulation of the wave-platform interaction system, were shown to effectively address the state-basis incoherency issue. Both LPV models were found to successfully capture nonlinear hydrodynamic effects such as decreased oscillation periods and increased damping at large body rotations on the benchmark van Daalen floating cylinder model. The integration of these LPV models into the Simulink FWT model enabled the evaluation of the impact of geometrically nonlinear hydrodynamics on global FWT behaviour. A significant finding is that the LPV model using the state-space bases directly obtained from identification algorithms, without any further transformation, resulted in erroneous FWT responses, highlighting careful attention to the basis coherency issue. In addition, the newly developed LPV models were shown to accurately predict the reduced resonance amplitude in platform pitch responses under wave-only excitations on the example 5-MW ITI-Barge FWT model. However, under the combined wind-wave excitations, this geometric nonlinearity in the wave-platform interaction was found to be overshadowed by the large aerodynamic damping effects. Moreover, the LPV model demonstrated significant computational efficiency, requiring only a fraction of the time needed by higher-fidelity body-nonlinear solvers.

The major contribution of Chapter 4 is that it provides a practical and effective method to determine the nonlinear hydrodynamic forces acting on FWTs. The LPV framework introduces a system theory perspective for wave-platform interaction. Both the black-box and gray-box LPV models proposed in this chapter can be extended to other dynamic systems, where a set of linear models with parameters evolve as a function of measurable variables, such as highly elastic mechanical systems and aircraft dynamics.

5.2 Future work

The LPV modelling framework proposed in Chapter 4 is currently limited to planar platform motions under aligned wind and wave conditions. However, floating platforms are characterized by 3D movements, largely driven by the asymmetric aerodynamic force distribution on the rotor. The FWT simulation in Chapter 2 observed platform yaw rotation as large as 5° at below-rated wind speeds and 10° at above-rated wind speeds. Future work will focus on extending the LPV model to account for fully 3D platform motions for more realistic FWT dynamics. This will involve generating local linear models using open-source 3D boundary element codes to represent the wave-platform interaction at various 3D platform poses. While the gray-box method proposed in this thesis inherently guarantees basis coherency, it requires potential sensors on a much broader boundary area than the 2D case, posing great challenges for solving the nonlinear optimization problem. In contrast, the black-box method is more promising due to its reliance on just 6 radiation force sensors.

In addition, the present work evaluates the wave excitation effect from the hydrodynamic coefficients calculated around the equilibrium position. Another direction for future research is to develop an LPV model to capture the geometric nonlinearities in the wave excitation model caused by large platform motions. Handling the non-causality of the linearized wave excitation problem will be a key challenge, as detailed in Chapter 2. In addition to interpolating state-space matrices, a pose-dependent negative time delay from frequency-domain state-space identification will need to be considered.

Moreover, the Simulink FWT model requires validation against high-fidelity tools, such as CFD, or experimental data, to ensure its accuracy in capturing geometrically nonlinear hydrodynamics under large 3D platform motions. This future research will help evaluate the capability of the LPV models in estimating nonlinear wave radiation and excitation effects under generic platform movements.

References

[1] N. J. Abbas, J. Jasa, D. S. Zalkind, A. Wright, and L. Pao. Control co-design of a floating offshore wind turbine. *Applied Energy*, 353:122036, 2024.

[2] ABS. Guide for building and classing: Floating offshore wind turbines. *American Bureau of Shipping (ABS)*, 2020.

[3] A. Alkhabbaz, H. Hamza, A. M. Daabo, H.-S. Yang, M. Yoon, A. Koprulu, and Y.-H. Lee. The aero-hydrodynamic interference impact on the nrel 5-mw floating wind turbine experiencing surge motion. *Ocean Engineering*, 295:116970, 2024.

[4] R. Antonutti, C. Peyrard, L. Johanning, A. Incecik, and D. Ingram. The effects of wind-induced inclination on the dynamics of semi-submersible floating wind turbines in the time domain. *Renewable Energy*, 88:83–94, 2016.

[5] Y. H. Bae. Development of a dynamic mooring module feam for fast v8. Technical report, Texas A&M University (TAMU), TX, USA, 2014.

[6] Y. H. Bae and M. Kim. Rotor-floater-tether coupled dynamics including second-order sum–frequency wave loads for a mono-column-tlp-type fowt (floating offshore wind turbine). *Ocean engineering*, 61:109–122, 2013.

[7] K. J. Bai. Diffraction of oblique waves by an infinite cylinder. *Journal of Fluid Mechanics*, 68(3):513–535, 1975.

[8] K. J. Bai and R. W.-C. Yeung. Numerical solutions to free-surface flow problems. In *Proc. 10th Symp. Naval Hydrodyn. Office of Naval Research, 1974*, pages 609–641, 1974.

[9] R. Bergua, A. Robertson, J. Jonkman, E. Branlard, A. Fontanella, M. Belloli, P. Schito, A. Zasso, G. Persico, A. Sanvito, et al. OC6 project phase III: validation of the aerodynamic loading on a wind turbine rotor undergoing large motion caused by a floating support structure. *Wind Energy Science*, 8:465–485, 2023.

[10] Bladed. https://www.dnv.com/services/wind-turbine-design-software-bladed-3775, 2024. Accessed: 2024-04-12.

[11] E. Branlard, B. Jonkman, G. Pirrung, K. Dixon, and J. Jonkman. Dynamic inflow and unsteady aerodynamics models for modal and stability analyses in openfast. In *Journal of Physics: Conference Series*, volume 2265, page 032044. IOP Publishing, 2022.

[12] Y. Cai, H. Zhao, X. Li, and Y. Liu. Aerodynamic analysis for different operating states of floating offshore wind turbine induced by pitching movement. *Energy*, 285:129538, 2023.

[13] Y. Cai, H. Zhao, X. Li, and Y. Liu. Effects of yawed inflow and blade-tower interaction on the aerodynamic and wake characteristics of a horizontal-axis wind turbine. *Energy*, 264:126246, 2023.

[14] C. Cermelli, D. Roddier, and A. Aubault. Windfloat: a floating foundation for offshore wind turbines—part ii: hydrodynamics analysis. In *International Conference on Offshore Mechanics and Arctic Engineering*, volume 43444, pages 135–143, 2009.

[15] C. Cermelli, C. Leroux, S. Díaz Domínguez, and A. Peiffer. Experimental measurements of windfloat 1 prototype responses and comparison with numerical model. In *International Conference on Offshore Mechanics and Arctic Engineering*, volume Volume 10: Ocean Renewable Energy, page V010T09A050. American Society of Mechanical Engineers, 2018.

[16] G. K. Y. Chan, P. D. Sclavounos, J. Jonkman, and G. Hayman. Computation of nonlinear hydrodynamic loads on floating wind turbines using fluid-impulse theory. In *International Conference on Offshore Mechanics and Arctic Engineering*, volume 56574, page V009T09A038. American Society of Mechanical Engineers, 2015.

[17] M. N. Chatzis, E. N. Chatzi, and A. W. Smyth. An experimental validation of time domain system identification methods with fusion of heterogeneous data. *Earthquake Engineering & Structural Dynamics*, 44(4):523–547, 2015.

[18] Z. Chen, X. Wang, Y. Guo, and S. Kang. Numerical analysis of unsteady aerodynamic performance of floating offshore wind turbine under platform surge and pitch motions. *Renewable energy*, 163:1849–1870, 2021.

[19] P. Cheng, Y. Huang, and D. Wan. A numerical model for fully coupled aero-hydrodynamic analysis of floating offshore wind turbine. *Ocean Engineering*, 173: 183–196, 2019.

[20] L. Cottura, R. Caradonna, A. Ghigo, R. Novo, G. Bracco, and G. Mattiazzo. Dynamic modeling of an offshore floating wind turbine for application in the mediterranean sea. *Energies*, 14(1):248, 2021.

[21] R. R. Craig Jr and M. C. Bampton. Coupling of substructures for dynamic analyses. *AIAA journal*, 6(7):1313–1319, 1968.

[22] W. Cummins, W. Iiuhl, and A. Uinm. The impulse response function and ship motions. *David Taylor Model Basin Washington DC*, 1962.

[23] J. De Caigny, R. Pintelon, J. F. Camino, and J. Swevers. Interpolated modeling of lpv systems. *IEEE Transactions on Control Systems Technology*, 22(6):2232–2246, 2014.

[24] J. De Vaal, M. L. Hansen, and T. Moan. Effect of wind turbine surge motion on rotor thrust and induced velocity. *Wind Energy*, 17(1):105–121, 2014.

[25] DNV. Floating wind turbine structures. *DNVGL-ST-0119*, 2018.

[26] DNV. Coupled analysis of floating wind turbines. *DNVGL-RP-0286*, 2019.

[27] DNV. Sesam: Software suite for hydrodynamic and structural analysis of renewable, offshore and maritime structures. Technical report, DNV GL, 2021.

[28] DNV. Energy transition outlook 2024, 2024.

[29] A. J. Dunbar, B. A. Craven, and E. G. Paterson. Development and validation of a tightly coupled cfd/6-dof solver for simulating floating offshore wind turbine platforms. *Ocean Engineering*, 110:98–105, 2015.

[30] O. El Beshbichi, Y. Xing, and M. C. Ong. An object-oriented method for fully coupled analysis of floating offshore wind turbines through mapping of aerodynamic coefficients. *Marine Structures*, 78:102979, 2021.

[31] O. El Beshbichi, Y. Xing, and M. Chen Ong. Modelica-aerodyn: Development, benchmark, and application of a comprehensive object-oriented tool for dynamic analysis of non-conventional horizontal-axis floating wind turbines. *Wind Energy*, 2023.

[32] Equinor. The world's largest floating offshore wind farm officially opened. https://www.equinor.com/news/20230823-hywind-tampen-officially-opened, 2023. Accessed: 2024-09-12.

[33] N. Faedo, Y. Peña-Sanchez, and J. V. Ringwood. Finite-order hydrodynamic model determination for wave energy applications using moment-matching. *Ocean Engineering*, 163:251–263, 2018.

[34] J. Falnes. On non-causal impulse response functions related to propagating water waves. *Applied Ocean Research*, 17(6):379–389, 1995.

[35] M. Farajvand, D. García-Violini, and J. V. Ringwood. Representative linearised models for a wave energy converter using various levels of force excitation. *Ocean Engineering*, 270:113635, 2023.

[36] A. Feng. *Numerical simulation of nonlinear wave-body problem based on desingularized Rankine source and mixed Euler-Lagrange method*. PhD thesis, University of Southampton, 2014.

[37] A. Feng, W. Bai, Y. You, Z.-M. Chen, and W. Price. A rankine source method solution of a finite depth, wave–body interaction problem. *Journal of Fluids and Structures*, 62:14–32, 2016.

[38] A. Fontanella, M. Al, D. Van Der Hoek, Y. Liu, J. Van Wingerden, and M. Belloli. A control-oriented wave-excited linear model for offshore floating wind turbines. In *Journal of Physics: Conference Series*, volume 1618, page 022038. IOP Publishing, 2020.

[39] A. Fontanella, A. Facchinetti, E. Daka, and M. Belloli. Modeling the coupled aero-hydro-servo-dynamic response of 15 mw floating wind turbines with wind tunnel hardware in the loop. *Renewable Energy*, 219:119442, 2023.

[40] S. Fu, Y. Jin, Y. Zheng, and L. P. Chamorro. Wake and power fluctuations of a model wind turbine subjected to pitch and roll oscillations. *Applied Energy*, 253:113605, 2019.

[41] S. Fu, Z. Li, W. Zhu, X. Han, X. Liang, H. Yang, and W. Shen. Study on aerodynamic performance and wake characteristics of a floating offshore wind turbine under pitch motion. *Renewable Energy*, 205:317–325, 2023.

[42] G. Giorgi, S. Sirigu, M. Bonfanti, G. Bracco, and G. Mattiazzo. Fast nonlinear froude–krylov force calculation for prismatic floating platforms: a wave energy conversion application case. *Journal of Ocean Engineering and Marine Energy*, 7(4):439–457, 2021.

[43] H. Gu and H.-C. Chen. Numerical simulation of a semi-submersible fowt platform under calibrated extreme and irregular waves. *Ocean Engineering*, 311:118847, 2024.

[44] B. Guo, R. J. Patton, S. Jin, and J. Lan. Numerical and experimental studies of excitation force approximation for wave energy conversion. *Renewable energy*, 125: 877–889, 2018.

[45] Y. Guo, X. Wang, Y. Mei, Z. Ye, and X. Guo. Effect of coupled platform pitch-surge motions on the aerodynamic characters of a horizontal floating offshore wind turbine. *Renewable Energy*, 196:278–297, 2022.

[46] GWEC. Global wind report 2024. Technical report, Global Wind Energy Council, Belgium, 2024.

[47] M. Hall. Moordyn user's guide. Technical report, Department of Mechanical Engineering, University of Maine, 2015.

[48] M. Hall and A. Goupee. Validation of a lumped-mass mooring line model with deepcwind semisubmersible model test data. *Ocean Engineering*, 104:590–603, 2015.

[49] M. Hansen. *Aerodynamics of wind turbines*. Routledge, 2015.

[50] HAWC2. https://www.hawc2.dk/about-hawc2, 2024. Accessed: 2024-04-12.

[51] Y. He, B. Han, L. Yan, and X. Han. Wave diffraction and radiation problems on a heteroaxial floating structure composed of two cylinders. *Applied Ocean Research*, 144:103915, 2024.

[52] S. Hirdaris, Y. Lee, G. Mortola, A. Incecik, O. Turan, S. Hong, B. Kim, K. Kim, S. Bennett, S. Miao, et al. The influence of nonlinearities on the symmetric hydrodynamic response of a 10,000 teu container ship. *Ocean Engineering*, 111:166–178, 2016.

[53] C. E. Høeg and Z. Zhang. The influence of gyroscopic effects on dynamic responses of floating offshore wind turbines in idling and operational conditions. *Ocean Engineering*, 227:108712, 2021.

[54] J. Huang and R. E. Taylor. Semi-analytical solution for second-order wave diffraction by a truncated circular cylinder in monochromatic waves. *Journal of Fluid Mechanics*, 319:171–196, 1996.

[55] A. Hulme. The wave forces acting on a floating hemisphere undergoing forced periodic oscillations. *Journal of Fluid Mechanics*, 121:443–463, 1982.

[56] IEC. Wind energy generation systems part 3-2: Design requirements for floating offshore wind turbines. *IEC TS 61400-3-2:2019*, 2019.

[57] IRENA. Renewable power generation costs in 2023, 2024.

[58] IRENA. Floating offshore wind outlook, 2024.

[59] A. Jacobsen and M. Godvik. Influence of wakes and atmospheric stability on the floater responses of the hywind scotland wind turbines. *Wind Energy*, 24(2):149–161, 2021.

[60] R. M. Janssen, H. Jansen, and J.-W. van Wingerden. A novel strategy for the identification of radiation force models. In *International Conference on Offshore Mechanics and Arctic Engineering*, volume 45370, page V01AT01A038. American Society of Mechanical Engineers, 2014.

[61] R. Jirasek, T. Schauer, D. Su, T. Nagayama, and A. Bleicher. Experimental linear parameter-varying model identification of an elastic kinetic roof structure. *Engineering Structures*, 297:116986, 2023.

[62] J. Jonkman. Influence of control on the pitch damping of a floating wind turbine. In *46th AIAA aerospace sciences meeting and exhibit*, page 1306, 2008.

[63] J. M. Jonkman. *Dynamics modeling and loads analysis of an offshore floating wind turbine*. University of Colorado at Boulder, 2007.

[64] J. M. Jonkman, G. Hayman, B. Jonkman, R. Damiani, and R. Murray. Aerodyn v15 user's guide and theory manual. Technical report, NREL Report, 2015.

[65] K. E. Kaasen. Consistent state space modelling of hydrodynamic memory. In *International Conference on Offshore Mechanics and Arctic Engineering*, volume 84317, page V001T01A041. American Society of Mechanical Engineers, 2020.

[66] I.-C. Kim, G. Ducrozet, V. Leroy, F. Bonnefoy, Y. Perignon, and S. Delacroix. Numerical and experimental investigation on deterministic prediction of ocean surface wave and wave excitation force. *Applied Ocean Research*, 142:103834, 2024.

[67] S.-J. Kim, M.-H. Kim, and W. Koo. Nonlinear hydrodynamics of freely floating symmetric bodies in waves by three-dimensional fully nonlinear potential-flow numerical wave tank. *Applied Ocean Research*, 113:102727, 2021.

[68] K. Kokkinowrachos, S. Mavrakos, and S. Asorakos. Behaviour of vertical bodies of revolution in waves. *Ocean Engineering*, 13(6):505–538, 1986.

[69] V. Leble and G. Barakos. A coupled floating offshore wind turbine analysis with high-fidelity methods. *Energy Procedia*, 94:523–530, 2016.

[70] C.-H. Lee and P. Sclavounos. Removing the irregular frequencies from integral equations in wave-body interactions. *Journal of Fluid Mechanics*, 207:393–418, 1989.

[71] J. Lee and J. Leonard. A time-dependent radiation condition for transient wave-structure interactions. *Ocean engineering*, 14(6):469–488, 1987.

[72] J.-F. Lee. On the heave radiation of a rectangular structure. *Ocean Engineering*, 22 (1):19–34, 1995.

[73] M. Leimeister, A. Kolios, and M. Collu. Development and verification of an aero-hydro-servo-elastic coupled model of dynamics for fowt, based on the mowit library. *Energies*, 13(8):1974, 2020.

[74] M. Leimeister, A. Kolios, M. Collu, and P. Thomas. Design optimization of the oc3 phase iv floating spar-buoy, based on global limit states. *Ocean Engineering*, 202: 107186, 2020.

[75] J. Leng, Z. Gao, M. C. Wu, T. Guo, and Y. Li. A fluid–structure interaction model for large wind turbines based on flexible multibody dynamics and actuator line method. *Journal of Fluids and Structures*, 118:103857, 2023.

[76] H. Li and E. E. Bachynski. Experimental and numerical investigation of nonlinear diffraction wave loads on a semi-submersible wind turbine. *Renewable Energy*, 171: 709–727, 2021.

[77] C. Linton. Radiation and diffraction of water waves by a submerged sphere in finite depth. *Ocean Engineering*, 18(1-2):61–74, 1991.

[78] X. Liu, Q. Miao, X. Wang, S. Xu, and H. Fan. A novel numerical method for the hydrodynamic analysis of floating bodies over a sloping bottom. *Journal of Marine Science and Technology*, pages 1–19, 2021.

[79] Y. Liu, Q. Xiao, A. Incecik, C. Peyrard, and D. Wan. Establishing a fully coupled cfd analysis tool for floating offshore wind turbines. *Renewable Energy*, 112:280–301, 2017.

[80] Y. Liu, Q. Xiao, A. Incecik, and C. Peyrard. Aeroelastic analysis of a floating offshore wind turbine in platform-induced surge motion using a fully coupled cfd-mbd method. *Wind Energy*, 22(1):1–20, 2019.

[81] Y. Liu, W. Gao, Q. Li, and B. Lu. Oblique projection-based modal matching algorithm for lpv model order reduction of aeroservoelastic systems. *Aerospace*, 10(5):406, 2023.

[82] M. Lovera and G. Mercere. Identification for gain-scheduling: a balanced subspace approach. In *2007 American Control Conference*, pages 858–863. IEEE, 2007.

[83] M. Masciola, J. Jonkman, and A. Robertson. Implementation of a multisegmented, quasi-static cable model. In *The Twenty-third International Offshore and Polar Engineering Conference*. OnePetro, 2013.

[84] M. Masciola, J. Jonkman, and A. Robertson. Implementation of a multisegmented, quasi-static cable model. In *ISOPE International Ocean and Polar Engineering Conference*, pages ISOPE–I. ISOPE, 2013.

[85] E. Masoudi and L. Gan. Diffraction waves on large aspect ratio rectangular submerged breakwaters. *Ocean Engineering*, 209:107474, 2020.

[86] T. McKelvey, H. Akçay, and L. Ljung. Subspace-based multivariable system identification from frequency response data. *IEEE Transactions on Automatic control*, 41(7): 960–979, 1996.

[87] C. C. Mei. *The applied dynamics of ocean surface waves*, volume 1. World scientific, 1989.

[88] F. Meng, W. H. Lio, A. Pegalajar-Jurado, F. Pierella, E. N. Hofschulte, A. G. Santaya, and H. Bredmose. Experimental study of floating wind turbine control on a tetrasub floater with tower velocity feedback gain. *Renewable Energy*, 205:509–524, 2023.

[89] Q. Meng, X. Hua, C. Chen, S. Zhou, F. Liu, and Z. Chen. Analytical study on the aerodynamic and hydrodynamic damping of the platform in an operating spar-type floating offshore wind turbine. *Renewable Energy*, 198:772–788, 2022.

[90] M. Meylan. Boundary element method for the radiation potential in finite depth. https://wikiwaves.org/Boundary_Element_Method_for_the_Radiation_Potential_in_Finite_Depth, 2010. Accessed: 2024-05-01.

[91] R. Moarref and M. R. Jovanovic. Remarks on computing the h 2 norm of incompressible fluids using descriptor state-space formulation. In *2008 American Control Conference*, pages 3064–3069. IEEE, 2008.

[92] B. Moore. Principal component analysis in linear systems: Controllability, observability, and model reduction. *IEEE transactions on automatic control*, 26(1):17–32, 1981.

[93] S. M. Mortensen, K. Laugesen, J. K. Jensen, K. Jessen, and M. Soltani. Experimental verification of the hydro-elastic model of a scaled floating offshore wind turbine. In *2018 IEEE Conference on Control Technology and Applications (CCTA)*, pages 1623–1630. IEEE, 2018.

[94] A. Nematbakhsh, D. J. Olinger, and G. Tryggvason. Nonlinear simulation of a spar buoy floating wind turbine under extreme ocean conditions. *Journal of Renewable and Sustainable Energy*, 6(3):033121, 2014.

[95] A. Nematbakhsh, E. E. Bachynski, Z. Gao, and T. Moan. Comparison of wave load effects on a tlp wind turbine by using computational fluid dynamics and potential flow theory approaches. *Applied Ocean Research*, 53:142–154, 2015.

[96] Nemoh. Nemoh v3.0.2. https://gitlab.com/lheea/Nemoh, 2024. Accessed: 2024-04-12.

[97] J. N. Newman. *Marine hydrodynamics*. The MIT press, 2018.

[98] S. A. Ning. A simple solution method for the blade element momentum equations with guaranteed convergence. *Wind Energy*, 17(9):1327–1345, 2014.

[99] M. Odeh, K. Mohsin, T. Ngo, D. Zalkind, J. Jonkman, A. Wright, A. Robertson, and T. Das. Development of a wind turbine model and simulation platform using an acausal approach: Multiphysics modeling, validation, and control. *Wind Energy*, 26 (9):985–1011, 2023.

[100] S. Ohmatsu. On the irregular frequencies in the theory of oscillating bodies in a free surface. *Paper 48 of the Ship Research Institute, Ship Dynamics Division, Tokyo, Japan*, 1975.

[101] OpenFAST. Openfast documentation v3.5.3. https://openfast.readthedocs.io/en/main/, 2024. Accessed: 2024-04-12.

[102] OrcaFlex. Orcaflex interface. https://www.nrel.gov/wind/nwtc/orcaflex-interface.html. Accessed: 2021-08-20.

[103] T. Perez and T. I. Fossen. Practical aspects of frequency-domain identification of dynamic models of marine structures from hydrodynamic data. *Ocean Engineering*, 38(2-3):426–435, 2011.

[104] M. Philippe, A. Babarit, and P. Ferrant. Aero-hydro-elastic simulation of a semi-submersible floating wind turbine. *Journal of offshore mechanics and Arctic engineering*, 136(2), 2014.

[105] F. Pimenta, D. Ribeiro, A. Román, and F. Magalhães. Modal properties of floating wind turbines: Analytical study and operational modal analysis of an utility-scale wind turbine. *Engineering Structures*, 301:117367, 2024.

[106] R. Porter. On the connection between step approximations and depth-averaged models for wave scattering by variable bathymetry. *The Quarterly Journal of Mechanics and Applied Mathematics*, 73(1):84–100, 2020.

[107] A. Poul and W. He. On the calculation of two-dimensional added mass and damping coefficients by simple green's function technique. *Ocean engineering*, 12(5):425–451, 1985.

[108] S. Rajendran, N. Fonseca, and C. G. Soares. Simplified body nonlinear time domain calculation of vertical ship motions and wave loads in large amplitude waves. *Ocean Engineering*, 107:157–177, 2015.

[109] E. Reynders. System identification methods for (operational) modal analysis: review and comparison. *Archives of Computational Methods in Engineering*, 19:51–124, 2012.

[110] L. Roald, J. Jonkman, and A. Robertson. The Effect of Second-Order Hydrodynamics on a Floating Offshore Wind Turbine. Technical report, National Renewable Energy Laboratory, May 2014.

[111] A. N. Robertson, F. Wendt, J. M. Jonkman, W. Popko, H. Dagher, S. Gueydon, J. Qvist, F. Vittori, J. Azcona, E. Uzunoglu, et al. Oc5 project phase ii: validation of global loads of the deepcwind floating semisubmersible wind turbine. *Energy Procedia*, 137: 38–57, 2017.

[112] Ø. Y. Rogne, T. Moan, and S. Ersdal. Identification of passive state-space models of strongly frequency dependent wave radiation forces. *Ocean engineering*, 92:114–128, 2014.

[113] ROSCO. Rosco documentation, v2.9.0. https://rosco.readthedocs.io/en/latest/, 2024. Accessed: 2024-04-12.

[114] B. W. Schubert, W. S. Robertson, B. S. Cazzolato, and M. H. Ghayesh. Linear and nonlinear hydrodynamic models for dynamics of a submerged point absorber wave energy converter. *Ocean Engineering*, 197:106828, 2020.

[115] K. Shaler, E. Branlard, and A. Platt. Olaf user's guide and theory manual. Technical report, NREL Report, 2020.

[116] M. Sirigu, E. Faraggiana, A. Ghigo, and G. Bracco. Development of most, a fast simulation model for optimisation of floating offshore wind turbines in simscape multibody. In *Journal of Physics: Conference Series*, volume 2257, page 012003. IOP Publishing, 2022.

[117] SS_Fitting. https://www.nrel.gov/wind/nwtc/ss-fitting.html, 2024. Accessed: 2024-04-12.

[118] D. Stockhouse and L. Y. Pao. Multiloop control of floating wind turbines: Tradeoffs in performance and stability. *IEEE Control Systems*, 44(5):63–80, 2024.

[119] D. Stockhouse, M. Pusch, R. Damiani, S. Sirnivas, and L. Pao. Robust multi-loop control of a floating wind turbine. *Wind Energy*, 2023.

[120] D. Stockhouse, M. Phadnis, A. Henry, N. J. Abbas, M. Sinner, M. Pusch, and L. Y. Pao. A tutorial on the control of floating offshore wind turbines: Stability challenges and opportunities for power capture. *IEEE Control Systems*, 44(5):28–57, 2024.

[121] A. Subbulakshmi, M. Verma, M. Keerthana, S. Sasmal, P. Harikrishna, and S. Kapuria. Recent advances in experimental and numerical methods for dynamic analysis of floating offshore wind turbines—an integrated review. *Renewable and Sustainable Energy Reviews*, 164:112525, 2022.

[122] H. Suzuki, Y. Sakai, Y. Yoshimura, H. Houtani, L. H. Carmo, H. Yoshimoto, K. Kamizawa, and R. T. Gonçalves. Non-linear motion characteristics of a shallow draft cylindrical barge type floater for a fowt in waves. *Journal of Marine Science and Engineering*, 9(1):56, 2021.

[123] B. Tagliafierro, M. Karimirad, I. Martínez-Estévez, J. M. Domínguez, G. Viccione, and A. J. Crespo. Numerical assessment of a tension-leg platform wind turbine in intermediate water using the smoothed particle hydrodynamics method. *Energies*, 15 (11):3993, 2022.

[124] S. Tang, B. Sweetman, and J. Gao. Nonlinear effects and dynamic coupling of floating offshore wind turbines using geometrically-exact blades and momentum-based methods. *Ocean Engineering*, 229:108866, 2021.

[125] T. T. Tran and D.-H. Kim. Fully coupled aero-hydrodynamic analysis of a semi-submersible fowt using a dynamic fluid body interaction approach. *Renewable energy*, 92:244–261, 2016.

[126] C.-C. Tsai, W. Tai, T.-W. Hsu, and S.-C. Hsiao. Step approximation of water wave scattering caused by tension-leg structures over uneven bottoms. *Ocean Engineering*, 166:208–225, 2018.

[127] TurbSim. https://www.nrel.gov/wind/nwtc/turbsim.html, 2024. Accessed: 2024-04-12.

[128] E. F. G. van Daalen. *Numerical and theoretical studies of water waves and floating bodies.* PhD thesis, University of Twente, 1993.

[129] G. J. van der Veen, I. J. Couchman, and R. Bowyer. Control of floating wind turbines. In *2012 American Control Conference (ACC)*, pages 3148–3153. IEEE, 2012.

[130] D. Vizer, G. Mercere, O. Prot, and J. Ramos. A local approach framework for black-box and gray-box lpv system identification. In *2013 European Control Conference (ECC)*, pages 1916–1921. IEEE, 2013.

[131] WAMIT. Wamit, inc. the state of the art in wave ineraction analysis. https://www.wamit.com/, 2024. Accessed: 2024-04-12.

[132] L. Wang, R. Bergua, A. Robertson, A. Wright, D. Zalkind, M. Fowler, E. Lenfest, A. Viselli, A. Goupee, and R. Kimball. Experimental investigation of advanced turbine control strategies and load-mitigation measures with a model-scale floating offshore wind turbine system. *Applied Energy*, 355:122343, 2024.

[133] Q. Wang, M. A. Sprague, J. Jonkman, N. Johnson, and B. Jonkman. Beamdyn: A high-fidelity wind turbine blade solver in the fast modular framework. *Wind Energy*, 20(8):1439–1462, 2017.

[134] S. Wang, T. Moan, and A. R. Nejad. A comparative study of fully coupled and de-coupled methods on dynamic behaviour of floating wind turbine drivetrains. *Renewable Energy*, 179:1618–1635, 2021.

[135] C. Yang, L. Xiao, S. Deng, P. Chen, L. Liu, and Z. Cheng. An experimental study on the aerodynamic-induced effects of a semi-submersible floating wind turbine. *Renewable Energy*, page 119930, 2024.

[136] Y. Yang, M. Bashir, C. Michailides, C. Li, and J. Wang. Development and application of an aero-hydro-servo-elastic coupling framework for analysis of floating offshore wind turbines. *Renewable Energy*, 161:606–625, 2020.

[137] R. W. Yeung. Added mass and damping of a vertical cylinder in finite-depth waters. *Applied Ocean Research*, 3(3):119–133, 1981.

[138] R. W.-C. Yeung. A singularity-distribution method for free-surface flow problems with an oscillating body. Technical report, Report No. NA73-6, University of California, Berkeley, 1973.

[139] H. Yu, S. Zheng, Y. Zhang, and G. Iglesias. Wave radiation from a truncated cylinder of arbitrary cross section. *Ocean Engineering*, 173:519–530, 2019.

[140] Z. Yu and J. Falnes. State-space modelling of a vertical cylinder in heave. *Applied Ocean Research*, 17(5):265–275, 1995.

[141] Z. Yu, Q. Ma, X. Zheng, K. Liao, H. Sun, and A. Khayyer. A hybrid numerical model for simulating aero-elastic-hydro-mooring-wake dynamic responses of floating offshore wind turbine. *Ocean Engineering*, 268:113050, 2023.

[142] X. Zeng, Y. Shao, X. Feng, K. Xu, R. Jin, and H. Li. Nonlinear hydrodynamics of floating offshore wind turbines: A review. *Renewable and Sustainable Energy Reviews*, 191:114092, 2024.

[143] Q. Zhang, L. Ljung, and R. Pintelon. On local lti model coherence for lpv interpolation. *IEEE Transactions on Automatic Control*, 65(8):3671–3676, 2019.

[144] Y. Zhang, Y. Song, C. Shen, and N.-Z. Chen. Aerodynamic and structural analysis for blades of a 15mw floating offshore wind turbine. *Ocean Engineering*, 287:115785, 2023.

[145] S. Zheng, W. Gao, Y. Liu, and S. Cheng. Wave diffraction from a truncated cylinder with a moonpool of arbitrary cross-section: A semi-analytical study. *Ocean Engineering*, 237:109573, 2021.

[146] Y. Zheng, Y. You, and Y. Shen. On the radiation and diffraction of water waves by a rectangular buoy. *Ocean engineering*, 31(8-9):1063–1082, 2004.

[147] B. Zhou, Q. Zhang, P. Jin, Y. Li, Y. Liu, S. Zheng, and D. Ning. Geometric asymmetry in the energy conversion and wave attenuation of a power-take-off-integrated floating breakwater. *Ocean Engineering*, 246:110576, 2022.

[148] Y. Zhu, C. Hu, Y. Ma, G. Xie, and Z. Yao. An equation-based method for fully coupled analyses of floating offshore wind turbine based on modelica. *Energy Conversion and Management*, 277:116653, 2023.